Controllable preparation, structural characterization and application of rare earth element - containing layered double hydroxides

Zheng Chang

Numéro d'ordre : D.U. 1681

UNIVERSITE BLAISE PASCAL

(U.F.R. de Recherche Scientifique et Technique)

ECOLE DOCTORALE DES SCIENCES FONDAMENTALES

N° : 494

THESE

Présentée pour obtenir le grade de

DOCTEUR D'UNIVERSITE

(Spécialité : Chimie, Sciences des Matériaux)

Par

Zheng CHANG

Titulaire du Master en Chimie Appliquée obtenu à Pékin

Préparation contrôlée, caractérisation structurale et application d'hydroxydes doubles lamellaires contenant des terres rares.

Soutenue publiquement le 16 Octobre 2006, devant la commission d'examen :

Président :	Mme. J. BRENDLE : Professeur - Mulhouse.
Examinateurs :	M. C. FORANO : Professeur - Clermont-Ferrand.
	Mme. M. de ROY : Professeur - Clermont-Ferrand.
	M. D. G. EVANS : Professeur - Pékin.
	M. F. Z. ZHANG : Professeur - Pékin.
	Mme. M. WEI : Professeur - Pékin.
Invité :	M. P. BOUTINAUD : Professeur - Clermont-Ferrand.

CONTROLLABLE PREPARATION, STRUCTURAL CHARACTERIZATION AND APPLICATION OF RARE EARTH ELEMENT - CONTAINING LAYERED DOUBLE HYDROXIDES

Abstract

Layered double hydroxides (LDHs) and rare earth elements (REEs) have both attracted extensive attention because of their structures and properties. The layered structure of LDHs makes it possible for many functional ions to be incorporated and the uniform dispersion of metal - organic anions in interlayer galleries or metal cations in layers extends the applications of layered materials to a wide variety of fields, whilst the electronic structure of REEs offers many advantages in the areas of optical, magnetic and catalytic materials.

Catalytic wet oxidation (CWO) is a promising technique for destruction of organic pollutants, of which phenol is a simple representative, in water under mild conditions. Common heterogeneous catalysts for CWO can be divided into three series: noble metals, transition metals (especially copper) and rare earths, each of which has their own advantages and shortcomings. Co-existence of two types of catalyst components may show a higher catalytic efficiency. It is, therefore, of interest to prepare hybrid materials based on ZnAl- or CuZnAl-LDHs incorporating rare earth elements such as

Ce or Eu in order to investigate the potential synergistic effect between the two components and the resultant influence on catalytic properties.

A continuous co-precipitation method under steady-state conditions was first developed for the preparation of nanometer-size LDH particles using $Zn_2Al(OH)_6(CO_3)_{0.5}\cdot 2H_2O$ as prototype. The effects of varying the operating conditions on the structural and textural properties of LDHs were studied, including total cation concentration, solvent, residence time, pH and intercalation anion. Increasing either the cation concentration or the fraction of ethylene glycol (EG) in EG/H_2O mixtures affects salt solubility and supersaturation, which results in smaller crystallites, larger surface areas and more amorphous compounds. The new method employs a short residence time of less than 15 min, allows large-scale production and maintains a constant supersaturation level in the reactor, and was shown to be a promising alternative to the conventional batch method.

The second part of this research was to prepare a series of novel REE-containing LDH materials by anion-exchange or co-precipitation methods, and to investigate the effects of varying experimental parameters in order to optimize the product properties. Using the anion-exchange method, pyridine-2,6-dicarboxylic acid (H_2dipic) and diethylenetriaminepentaacetic acid (DTPA) were employed as the ligands in REE-containing complex anions. $[Ce(dipic)_3]^{3-}$ complexes were firstly introduced into ZnAl-NO_3-LDH and other LDH precursors with varying layer metal ions like CuZnAl-NO_3-LDH, and then different REE-containing complexes such as $[Ce(DTPA)]^{2-}$ and $[Eu(dipic)_3]^{3-}$ were incorporated into LDHs. The products were

characterized by many physicochemical techniques, including XRD, IR, UV, ICP, BET, TEM, TG/Mass, *in situ* HT-XRD and XPS.

Ce-containing ZnAl-LDHs prepared by an anion-exchange method with $[Ce(dipic)_3]^{3-}$ were found to be always mixed with a CO_3^{2-}-containing LDH. The intercalation of $[Ce(dipic)_3]^{3-}$ in the layered host was confirmed by an increase in interlayer spacing to 1.24 nm. Geometrical considerations suggest the complex has a tilted orientation between the layers. However, a fraction of the $[Ce(dipic)_3]^{3-}$ anions decomposed into $dipic^{2-}$ and Ce^{3+} (or Ce^{4+}) ions during the exchange process, resulting in formation of a $dipic^{2-}$-containing LDH. Different experimental conditions were optimized, including the host layer composition, charge density and other synthesis parameters such as temperature, pressure, reagent concentration, and reaction time. The most promising product was obtained with a ratio of layer cations $M^{2+}/M^{3+} = 2$, with a $[Ce(dipic)_3]^{3-}$ concentration around 5 mmol/l and an exchange period around 10 h at room temperature. For some other host matrix compositions, the decomposition of $[Ce(dipic)_3]^{3-}$ and co-intercalation of CO_3^{2-} could both be reduced. The interlayer spacing values varied for different layer metals. Another Ce-containing ZnAl-LDH product was synthesized by a ion-exchange process with $[Ce(DTPA)]^{2-}$. The product showed characteristics of a well-crystallized LDH and the interlayer spacing was enlarged to 1.46 nm.

Eu-containing LDHs with $[Eu(dipic)_3]^{3-}$ anions in the interlayer galleries were prepared under the same conditions as for $[Ce(dipic)_3]^{3-}$-intercalated LDHs and the structure and properties of the products were similar. The immobilized luminescent

materials had excellent stability and luminescence properties. Eu^{3+} was used as a structural probe to study the interaction between the layered host and the complex guest by monitoring its luminescence properties. The structural information obtained can reasonably be transposed to $[Ce(dipic)_3]^{3-}$-intercalated LDHs.

On the basis of studies with REE-containing ZnAl-LDH materials, CuZnAl-Ce(dipic)-LDHs with cerium ions located in the interlayer galleries were synthesized by the ion-exchange method. The decomposition of $[Ce(dipic)_3]^{3-}$ and co-intercalation of CO_3^{2-} were relatively insignificant with this host matrix. Another type of CeX-LDHs (where X represents Ce content) was prepared by a co-precipitation method. It was demonstrated that the products were a mixture of CuZnAl-LDH and CeO_2, with cerium uniformly dispersed on the surface of small LDH particles.

Thermal behavior of Ce-containing CuZnAl-LDHs was found to be influenced by the presence of cerium oxides and the temperature of formation of spinel phases was significantly increased. The effects of varying some experimental conditions such as preparation method, layer composition, calcination temperature/time and Ce/Al molar ratio on the specific surface area were investigated. When the product CuZnAl-Ce(dipic)-CLDH with a stoichiometric Ce/Al ratio was calcined at 500 °C for 6 h, a composite Cu-Ce-O solid solution consisting of mixed metal oxides and having a large specific surface area was obtained.

The final part of research was to prepare a series of new catalysts by calcination of Ce-containing CuZnAl-LDHs, to study the catalytic abilities of these materials in the phenol oxidation reaction and investigate the interaction between Cu and Ce centers in

the catalysts. It was shown that the difference in catalytic performances of the two types of Ce-containing CuZnAl-CLDHs is related to the structure and composition of the catalysts. For CuZnAl-Ce(dipic)-CLDHs obtained by calcination of $[Ce(dipic)_3]^{3-}$-intercalated CuZnAl-LDHs, the presence of cerium significantly improved the catalytic activity and control over the product distribution in phenol oxidation. The uniform dispersion of Ce-complexes in the interlayer galleries of the LDH precursors results in the presence of a Cu-Ce synergistic effect in the Cu-Ce-O solid solution. The strong interaction between Cu and Ce enhances the catalyst performance. For CeX-CLDHs obtained by calcination of the mixture of CuZnAl-LDH and CeO_2, the presence of cerium enhanced deep oxidation of phenol and reduced the extent of leaching of metal elements, resulting in improved catalyst selectivity and stability. The interaction between Cu and Ce in the two different phases was weak, not enough to give significant increase in catalytic activity, but sufficient to stabilize the active component, Cu, against leaching.

KEY WORDS: Layered Double Hydroxides (LDHs), Rare Earth Elements (REEs), $[Ce(dipic)_3]^{3-}$, intercalation, catalyst, Cu-Ce synergistic effect

Contents

Abstract····· I

Chapter 1 Introduction

1.1 Layered Double Hydroxides (LDHs)····· 1

1.1.1 Structure and composition····· 1

1.1.2 Properties····· 2

1.1.2.1 Controllable modulation of chemical composition of the layers····· 2

1.1.2.2 Controllable modulation of charge density in the layers····· 3

1.1.2.3 Controllable modulation of nature and orientation of anions in the interlayer galleries····· 3

1.1.2.4 Controllable modulation of particle size and distribution····· 4

1.1.2.5 Basic properties····· 4

1.1.2.6 Thermal stability····· 5

1.1.2.7 Memory effect····· 5

1.1.3 Synthesis methods····· 6

1.1.3.1 Coprecipitation····· 6

1.1.3.2 Anion exchange····· 7

1.1.3.3 Rehydration of calcined LDH precursors····· 7

1.1.3.4 Reaction of LDH-carbonate precursors with acids····· 7

1.1.4 Potential applications····· 8

1.1.4.1 Heterogeneous catalysis and supported catalysis····· 8

1.1.4.2 Sorbents····· 9

1.1.4.3 Functional materials····· 10

1.1.4.4 Decontamination of wastewater····· 11

1.1.5 Calcined LDHs (CLDHs)····· 11

1.2 Rare Earth Elements (REEs)····· 13

1.2.1 Electronic structure····· 13

1.2.2 Properties of cerium and europium····· 13

1.2.2.1 Structure and characterization of cerium oxides····· 13

1.2.2.2 Structure and characterization of cerium complexes····· 15

1.2.2.3 Structure and characterization of europium complexes····· 17

1.2.3 Catalytic applications····· 18

1.2.3.1 CeO_2 as catalyst····· 18

1.2.3.2 CeO_2 as catalyst promoter····· 19

1.2.3.3 Composite catalyst of CuO and CeO_2····· 20

1.3 Research objectives····· 22

1.3.1 Incorporation of REEs into LDHs····· 23

1.3.2 Characterization of REE-containing LDHs····· 24

1.3.3 Discussion of catalytic abilities and mechanism····· 24
1.3.4 Characterization techniques····· 25
1.4 Significance of this work····· 28
1.5 Research aims····· 29
References····· 30
Chapter 2 Controllable Preparation and Structural Characterization of Nanosize ZnAl-LDHs
2.1 Introduction····· 46
2.2 Controllable preparation under steady-state conditions····· 48
2.2.1 Experimental methods····· 48
2.2.2 Experimental conditions····· 50
2.2.3 Characterization techniques····· 52
2.3 Structural and textural characterization····· 53
2.3.1 Common characteristics····· 54
2.3.1.1 Elemental analysis····· 54
2.3.1.2 TEM analysis····· 55
2.3.1.3 IR spectroscopy····· 57
2.3.1.4 BET analysis····· 58
2.3.2 Effect of varying experimental conditions····· 59
2.3.2.1 Effect of varying total salt concentration····· 59
2.3.2.2 Effect of varying solvent····· 60
2.3.2.3 Effect of varying residence time····· 63
2.3.2.4 Effect of varying pH····· 64
2.3.2.5 Effect of varying the anions present in preparation medium····· 65
2.4 Thermal behaviors of materials prepared under steady-state conditions····· 67
2.4.1 *In situ* variable temperature XRD analysis····· 67
2.4.2 TG-DTA analysis····· 69
2.5 Discussion and comparison with the standard preparation method····· 71
2.5.1 Theoretical analysis of the new preparation method····· 71
2.5.2 Comparison with the standard preparation method····· 75
2.6 Conclusion····· 76
References····· 77
Chapter 3 Controllable preparation and structural characterization of LDHs with rare earth complexes intercalated in the interlayer galleries
3.1 Introduction····· 81
3.1.1 General introduction····· 81
3.1.2 Intercalation chemistry of LDHs····· 82
3.2 Controllable preparation of rare earth complexes and rare earth-containing intercalated LDHs····· 85
3.2.1 Experimental conditions····· 85
3.2.1.1 Synthesis of LDHs precursors····· 86
3.2.1.2 Synthesis of rare earth complexes····· 86

3.2.1.3 Synthesis of REE-containing LDHs····· 87
3.2.1.4 Adsorption experiments····· 90
3.2.2 Characterization techniques····· 91
3.3 Structural characterization of $[Ce(dipic)_3]^{3-}$ complex····· 92
3.3.1 Crystal structure····· ····· 92
3.3.2 Composition and structural analysis····· 93
3.3.2.1 NaOH titration analysis····· 93
3.3.2.2 UV spectroscopy····· 94
3.3.2.3 IR spectroscopy····· 95
3.3.2.4 Elemental analysis····· 97
3.3.2.5 TG-DTA analysis····· 98
3.4 Attempted intercalation of $[Ce(dipic)_3]^{3-}$ into ZnAl-LDHs····· 99
3.4.1 Co-precipitation method····· 99
3.4.1.1 Structure characterization····· 99
3.4.1.2 Discussion····· 100
3.4.2 Ion-exchange method····· 103
3.4.2.1 Structural characterization····· 103
3.4.2.1.1 Elemental analysis····· 103
3.4.2.1.2 XRD analysis····· 104
3.4.2.1.3 IR spectroscopy····· 105
3.4.2.1.4 UV spectroscopy····· 106
3.4.2.1.5 Back-exchange experiments····· 108
3.4.2.2 Effect of varying experimental conditions····· 110
3.4.2.2.1 Effect of precursor····· 110
3.4.2.2.2 Effect of temperature/pressure····· 112
3.4.2.2.3 Effect of charge density in the layers····· 115
3.4.2.2.4 Effect of reagent concentration····· 118
3.4.2.3 Adsorption isotherm of $[Ce(dipic)_3]^{3-}$ on Zn_2Al-NO_3-LDHs····· 121
3.5 Intercalation of $[Ce(dipic)_3]^{3-}$ with other LDHs····· 124
3.5.1 Structural characterization of CuZnAl-Ce(dipic)-LDHs····· 124
3.5.1.1 UV spectroscopy····· 124
3.5.1.2 Elemental analysis····· 125
3.5.1.3 XRD analysis····· 127
3.5.1.4 IR spectroscopy····· 129
3.5.1.5 TEM analysis····· 130
3.5.2 Structural characterization of Zn_2Cr-Ce(dipic)-LDHs····· 132
3.5.2.1 XRD analysis····· 132
3.5.2.2 IR spectroscopy····· 133
3.5.2.3 TEM analysis····· 135
3.5.2.4 Adsorption isotherm of $[Ce(dipic)_3]^{3-}$ on Zn_2Cr-Cl-LDHs····· 136
3.5.3 Structural characterization of varied $[Ce(dipic)_3]^{3-}$-LDHs····· 138

3.6 Intercalation of other complexes into LDHs····· 140
3.6.1 Intercalation of $[Ce(DTPA)]^{2-}$ complex····· 140
3.6.1.1 XRD analysis····· 140
3.6.2.2 IR spectroscopy····· 142
3.6.2 Intercalation of $[Eu(dipic)_3]^{3-}$ complex····· 143
3.6.2.1 XRD analysis····· 144
3.6.2.2 IR spectroscopy····· 147
3.6.2.3 Luminescence properties of $[Eu(dipic)_3]^{3-}$-LDHs····· 148
3.7 Thermal behaviors of intercalated LDHs····· 150
3.7.1 Thermal behaviors of $[Ce(dipic)_3]^{3-}$-LDHs····· 150
3.7.1.1 Zn_2Al-Ce(dipic)-LDHs····· 150
3.7.1.1.1 Coupled TG/Mass analysis····· 150
3.7.1.1.2 *In situ* variable temperature XRD analysis····· 154
3.7.1.2 CuZnAl-Ce(dipic)-LDHs····· 156
3.7.1.2.1 Coupled TG/Mass analysis····· 156
3.7.1.2.2 *In situ* variable temperature XRD analysis····· 158
3.7.1.3 Varied $[Ce(dipic)_3]^{3-}$-LDHs····· 161
3.7.2 Thermal behaviors of $[Ce(DTPA)]^{2-}$-LDHs····· 162
3.7.2.1 Coupled TG/Mass analysis····· 162
3.7.2.2 *In situ* variable temperature XRD analysis····· 164
3.7.3 Thermal behaviors of $[Eu(dipic)_3]^{3-}$-LDHs····· 166
3.8 Conclusions····· 168
References····· 170
Chapter 4 Controllable preparation, structural characterization and catalytic properties of cerium–containing CLDHs
4.1 Introduction····· 177
4.2 Preparation of Ce-containing CuZnAl-CLDHs····· 180
4.2.1 Experimental conditions····· 180
4.2.1.1 Co-precipitation method····· 180
4.2.1.2 Ion-exchange method····· 181
4.2.2 Characterization techniques····· 181
4.2.3 Catalytic reaction····· 182
4.3 Structural characterization····· 183
4.3.1 CeX-LDHs and their calcined products····· 183
4.3.1.1 Elemental analysis····· 183
4.3.1.2 XRD analysis····· 184
4.3.1.3 IR spectroscopy····· 187
4.3.1.4 TG-DTA analysis····· 189
4.3.1.5 BET analysis····· 189
4.3.2 CuZnAl-Ce(dipic)-LDHs and their calcined products····· 192
4.3.2.1 XRD analysis····· 192

4.3.2.2 IR spectroscopy····· 193
4.3.2.3 BET analysis····· 194
4.3.2.4 XPS analysis····· 199
4.4 Catalytic properties····· 205
4.4.1 CeX-CLDHs prepared by the co-precipitation method····· 205
4.4.1.1 Catalyst activity and selectivity····· 205
4.4.1.2 Catalyst stability····· 207
4.4.2 CuZnAl-Ce(dipic)-CLDHs prepared by the ion-exchange method····· 209
4.4.2.1 Catalyst activity and selectivity····· 209
4.4.2.2 Catalyst stability····· 214
4.4.3 Comparison in catalytic properties of two Ce-containing CuZnAl-CLDHs prepared by different methods····· 215
4.4.4 Mechanism of oxidation reaction of phenol····· 217
4.5 Conclusions····· 219
References····· 221
Chapter 5 Conclusions····· 229
Acknowledgments····· 234
Publications····· 236

Chapter 1

Introduction

1.1 Layered Double Hydroxides (LDHs)

1.1.1 Structure and composition

Layered double hydroxides (LDHs), anionic clays, are a family of compounds which have attracted considerable attention in recent years [1-4]. The structure of most of these materials corresponds to that of hydrotalcite, a natural magnesium–aluminum hydroxycarbonate, which was discovered in Sweden around 1842 although the first exact formula, $Mg_6Al_2(OH)_{16}CO_3{\cdot}4H_2O$, was not published until 1915 by Manasse [5]. Partial substitution of Al^{3+} for Mg^{2+} in brucite-like layers gives rise to positively charged layers, thus leading to intercalation of charge-balancing anions in the interlayer galleries. The metal cations are coordinated by six oxygen atoms forming $M^{2+}/M^{3+}(OH)_6$ octahedra. These octahedra form two-dimensional sheets via edge sharing and may stack together by hydrogen bonding and other electrostatic interactions between the hydroxyl groups of adjacent sheets and interlayer anions. Stacking of the layers can be accomplished in different ways, of which the two most common give rise to polytypes with rhombohedral (3*R* symmetry) or hexagonal cell (2*H* symmetry); hydrotalcite corresponds to symmetry 3*R*, Fig.1-1, while the 2*H* analogue is known as manasseite [3]. LDHs are characterized [2,4,6-8] by the general formula $[M^{2+}_{1-x}M^{3+}_x(OH)_2][A^{n-}_{x/n}{\cdot}mH_2O]$. The charge density on the layers of the LDH will

clearly depend upon the M^{2+}/M^{3+} ratio. A particular advantage of LDHs, therefore, is that the anion-exchange capacity of the LDH, and hence the number and arrangement of the charge balancing anions in the interlayer galleries, may be controlled by varying the M^{2+}/M^{3+} ratio which usually lies between 2 and 4 [4]. Variable amounts of water molecules are also incorporated in the interlayer galleries. The idealized structure of an LDH with interlayer carbonate anions is shown in Fig. 1-1.

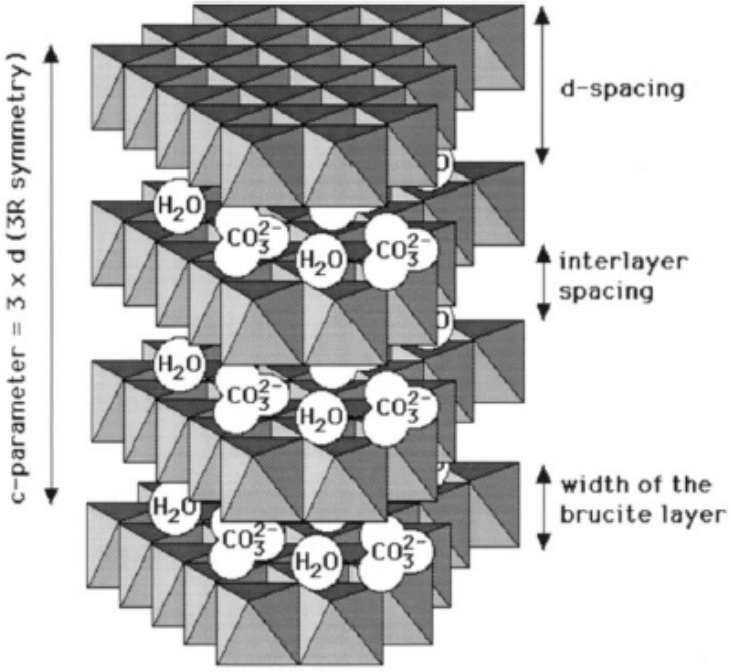

Fig.1-1 Idealized structure of a layered double hydroxide with interlayer carbonate anions (several parameters are defined) [1].

1.1.2 Properties

1.1.2.1 Controllable modulation of chemical composition of the layers

The chemical composition of the layers determines the charge density of the layers, and hence the anion-exchange capacity and supramolecular structure of the LDH. The

brucite-like layers may [9-12] contain a wide range of divalent (M^{2+}) and trivalent cations (M^{3+}). It is often stated [4] that LDH formation is favored when both M^{2+} and M^{3+} ions have an ionic radius close to that of Mg^{2+} (ionic radius = 0.65 Å). All divalent metal ions from Mg^{2+} to Mn^{2+} except Cu^{2+} form binary LDHs. Cu^{2+} only forms ternary LDHs in the presence of other divalent metal cations, which has been ascribed to the influence of the Jahn–Teller distortions prevalent for Cu^{2+} [13,14].

1.1.2.2 Controllable modulation of charge density in the layers

As noted above, the value of the ratio M^{2+}/M^{3+} is limited (between 2 and 4). Attempts to synthesize LDHs with M^{2+}/M^{3+} ratios lower than 2 lead to a high proportion of M^{3+} octahedra in the hydroxide layers, which leads to segregation of an $M(OH)_3$ phase; similarly, at ratios higher than 4 the formation of $M(OH)_2$ is probable. For Mg-Al LDHs, because the ionic radius of Al^{3+} (0.56 Å) is less than that of Mg^{2+} (0.65 Å), substituting Al^{3+} for Mg^{2+} leads to a decrease in the lattice parameter *a*, which corresponds to the mean distance between adjacent cations. Although most of the studies reported in the literatures refer to systems with M^{2+} and M^{3+} cations in the layers, there have been reports of LDHs with M^{2+}/M^{4+} cation combinations [15,16]; the more well studied Li^{+}/Al^{3+} system [17] also has an LDH-type structure.

1.1.2.3 Controllable modulation of nature and orientation of anions in the interlayer galleries

An enormous variety of interlayer anions (A^{n-}) can be incorporated in LDHs. They range from simple inorganic anions, such as CO_3^{2-}, SO_4^{2-}, NO_3^{-}, F^{-}, Cl^{-} or PO_4^{3-}, to organic anions such as dodecylsulfate and terephthalate [18-21], complex anions [22,23],

heteropolyanions such as $V_{10}O_{28}^{6-}$ [24,25] and macroorganic anions [26,27]. The number, size, orientation, and affinity of intercalated anions for the brucite layers affect the properties of LDHs, including their anion exchange capacity, interlamellar spacing, surface area and thermal stability. This allows the preparation of materials having a variety of different applications.

1.1.2.4 Controllable modulation of particle size and distribution

The properties of both LDHs and their calcination products (CLDHs) are strongly linked to the chemical composition and morphology of the LDH. The physicochemical properties of the platelet-like crystallites of the LDH, such as particle size and its distribution, are strongly influenced by the nature and experimental parameters of the synthesis procedure, including mixing and aging times, pH, concentration and temperature. The nucleation rate is related to the concentration and temperature in the initial solutions; the growth rate is affected by aging time, temperature and extent of supersaturation.

1.1.2.5 Basic properties

LDHs themselves are weak solid bases and acquire considerably enhanced basic properties when activated by thermal treatment (calcination) [28,29]. When calcined at the appropriate temperature, LDHs form mixed oxides that show a marked increase in surface area and reactivity compared with the precursor. The basic character of these oxides has been studied most extensively for the MgAl-CO_3^{2-} system and the presence of three different types of basic sites has been demonstrated. Strongly basic O^{2-} sites are present on the surface of the material, medium basic O^- sites are located beside the

hydroxyl groups and the residual OH groups give rise to sites of weak basicity. The formation of active basic sites leads to the observed increase in catalytic reactivity after calcination.

1.1.2.6 Thermal stability

The thermal stability of LDHs is an important consideration for many potential applications. In general, the thermal decomposition of LDHs can be divided into three stages: (I) the removal of physisorbed water at the surface and between the hydroxide layers, which occurs between room temperature and approximately 300 °C; (II) dehydroxylation of the hydroxide layers in the range 300-500 °C and (III) elimination and/or combustion of the interlayer anion. The precise temperature at which each stage starts and finishes depends on many factors, including the identity of M^{2+} and M^{3+}, the M^{2+}/M^{3+} ratio and the nature of the anion. In particular the temperature at which stage III occurs can vary considerably. The difference may be attributed to the strength of the interaction between the anions and the hydroxide layers, the nature of the decomposition process of the anion and the orientation of the anion in the interlayer galleries.

1.1.2.7 Memory effect

An important feature of LDHs is that they can be regenerated from their calcined products, which is often described [4,12] as a ‘memory effect’. When an LDH is calcined at moderate temperatures, the layered structure is lost and an essentially amorphous material is obtained. If this material is allowed to come in contact with aqueous solutions containing anions, the layered structure will be regenerated with concomitant

incorporation of the anions in the interlayer galleries. The calcination temperature range which gives materials for which the regeneration process is possible varies with the nature of the cations. For example, Miyata [12] reported that in the case of an Mg/Al LDH, the mixed magnesium aluminium oxide obtained after heat treatment at 500-800 °C may be reconverted to an LDH. Calcination at higher temperatures however affords spinel phases, which do not regenerate LDHs on treatment with aqueous solutions of anions.

1.1.3 Synthesis methods

There are four main general methods for the preparation of LDHs [12,30]: (I) coprecipitation; (II) anion-exchange of a precursor LDH; (III) rehydration of a calcined LDH precursor and (IV) direct reaction of LDH-carbonate precursors with acids. More non-conventional methods are actually developed in order to control morphology and size of LDHs particles.

1.1.3.1 Coprecipitation

The coprecipitation method for the direct synthesis of LDHs has been developed over a number of years [31,32]. The M^{2+} and M^{3+} hydroxide layers are nucleated and grown from an aqueous solution containing the anion that is to be incorporated into the LDH. Usually, the coprecipitation is performed at constant pH by simultaneously adding metal salt and base solutions. To obtain phase-pure LDHs, the choice of coprecipitation pH value is very important. The optimum value varies depending on the combination of metal cations utilized and the anion present [2,33]. The coprecipitation procedure is followed by crystallization of the product, typically for several hours at a

temperature in the range 65-75 °C.

1.1.3.2 Anion exchange

Anion-exchange is probably the most common method for the preparation of LDHs [34-36]. The affinity of simple inorganic anions for LDHs decreases in the order CO_3^{2-} > SO_4^{2-} >HPO_4^{2-} > F^- > Cl^- > NO_3^-. Thus LDHs containing nitrate or chloride anions are the most suitable precursors for anion-exchange syntheses. In general, the anion-exchange reaction is carried out by dispersing the precursor LDH in an aqueous solution containing an excess of the anion that is to be incorporated. Both the anion and the hydroxide layers must be stable at the pH of exchange.

1.1.3.3 Rehydration of calcined LDH precursors

The so-called memory effect property of LDHs discussed in Section 1.1.2.7 provides an effective synthetic route for inserting inorganic and organic anions into LDHs [37,38]. An advantage of this method is that in principle no other anions are present to compete with the target anion, although in fact the inclusion of carbonate arising from atmospheric CO_2 is often a problem. The ease and extent of reconstruction of the calcined LDH are controlled by the nature of the metal cations as well as the calcination temperature and the coordination properties of the anion [39,40].

1.1.3.4 Reaction of LDH-carbonate precursors with acids

Although the carbonate anion is tenaciously held in the interlayer galleries and does not generally undergo direct anion-exchange, it is possible to replace it by treatment with an appropriate acid, which leads to liberation of carbon dioxide and incorporation of the conjugate base of the acid [41-43]. Clearly control of pH is paramount:

if the pH is too high, carbonate will not be liberated whereas if the pH is too low, dissolution of the layers will occur. For example, Carlino and Hudson [43] reported that reaction of molten sebacic acid with MgAl-CO_3-LDH afforded the corresponding organic-LDH phase, although the exchange was incomplete.

1.1.4 Potential applications

Both LDHs and the products of their calcination find widespread applications in many fields including as catalysts or catalyst supports [44], as pharmaceuticals [27], as polymer additives [45] in environmental cleanup by ion exchange [1] or adsorption process [46,47], as selective chemical nanoreactors [48], in separation and membrane technology [49], and as photoactive materials [50].

1.1.4.1 Heterogeneous catalysis and supported catalysis

The wide variety of different metal cations which can form LDHs (in addition to binary LDHs, ternary or quaternary LDHs containing two or more different M^{2+} and/or M^{3+} cations in the brucite-like layers have also been prepared) make these materials rather suitable for a fine modulation of chemical composition and hence potential catalytic properties [51,52]. Furthermore, as the cations in the layers of the LDH precursors are relatively uniformly dispersed, heterogeneous catalysts obtained after thermal decomposition usually show a high degree of dispersion of the metal sites [1]. The use of microporous and mesoporous molecular sieve materials in catalysis, including LDHs and pillared LDHs, has been recently reviewed [53]. In 1991, Cavani *et al.* reviewed catalytic applications of LDHs in the following areas: 1) Basic catalysis; 2) Reforming of hydrocarbons; 3) Hydrogenation reactions; 4) Oxidation reactions; 5)

Supported catalysis.

It has been reported that catalysts prepared from transition metal-containing LDHs are generally characterized by higher stability and longer lifetimes compared with catalysts prepared by conventional techniques such as impregnation or precipitation [54-57]. For example, Cu/Zn/Al LDH precursors containing different ratios of the metals have been prepared in attempts to obtain an oxide phase for use in catalytic oxidation reactions [58]. Other workers have suggested that modification of LDHs through the addition of other elements, such as rare-earth metals or noble metals, leads to a further improvement in catalytic performance [59,60]. In the last few years, pillared materials obtained from LDH precursors containing anionic metal complexes have been reported to be active in selective adsorption and oxidation catalysis [61,62]. One interesting example involves incorporation of metallophthalocyanine anions into LDHs [63,64], since the macrocyclic complexes can function as biomimetic catalysts for the autoxidation of organic molecules in aqueous solution.

In many examples of LDH-based oxidation catalysts, the active elements are introduced into the interlayer region as heteropolyanions and the brucite-like sheets act only as a catalyst support [65-67].The mixed metal oxides prepared by decomposition of LDHs can also be utilized as a catalyst support. For example, when used as a support for CeO_2 in SOx removal a calcined Mg/Al LDH phase was shown to afford a higher activity than that observed with CeO_2 supported on either Al_2O_3 or MgO.

1.1.4.2 Sorbents

LDHs have attractive adsorbent properties by virtue of their large interlayer

galleries which are accessible to a wide variety of anions and polar molecular species. The main advantages of LDHs over traditional anionic exchange resins are their higher anionic exchange capacities and the fact that LDHs are more resistant to high temperature treatment. LDHs are therefore used as the ion exchanger in some high temperature applications such as treatment of the cooling water in nuclear reactors [68]. The hydrophobic nature and accessibility of the interlayer region of so-called organo-LDHs, synthesized by pre-intercalation of surfactants, makes these materials candidates for the adsorption of other organic molecules. Kopka *et al.* [69] have found that ZnCr-LDHs containing surfactant anions have the ability to take up a large variety of small organic molecules such as ethylene glycol, propane-1,2-diol and glycerol into the interlayer galleries. It should be noted that calcined LDHs may also be used as adsorbents in environmental applications [70]. In addition, the potential application of an LiAl(myrisate)-LDH as a stationary phase in gas chromatography has been reported [71].

1.1.4.3 Functional materials

It has recently been reported that LDHs have potential applications in the formulation of new functional materials, including electronic, optical, pharmaceutical and magnetic materials [4,5]. Most recently, the focus has shifted to the intercalation of biologically active materials, such as porphyrins [72,73], nucleoside phosphates [74,75], drugs [76,77], vitamins [78] and amino acids [19,79]. A wide range of derivatives containing various combinations of cations and anions can be synthesized either directly or by anionic exchange. After intercalation of these functional guests into the LDH host, the resulting hybrid materials have very promising future applications.

1.1.4.4 Decontamination of wastewater

Potential applications of LDHs in environmental cleanup involve removal of both inorganic and organic anionic contaminants from aqueous systems, and thus LDHs have been applied in soil remediation and as filters for water decontamination. Furthermore as noted above, the incorporation of surfactants by anionic exchange of LDHs imparts hydrophobic properties to the original LDHs, and allows LDHs to act as sorbents for non-anionic organic contaminants, as well as anionic species. Many organic contaminants such as phenols, aromatic carboxylic acids, dyes and pesticides have been successfully removed from wastewater. Lakraimi *et al.* [80] reported that Zn-Al LDHs with interlayer Cl^- ions are good adsorbents for removal of 2,4-dichlorophenoxyacetic acid from aqueous solutions, with adsorption occurring via an ion-exchange process. In addition to simple adsorption of organic contaminants, *in situ* degradation is also possible. For example, Shannon *et al.* [81] have recently studied the oxidation of cyclohexene in wastewater over a Zn/Al-LDH containing a supported metallophthalocyanine complex $[CoPcTs]_4^-$ which demonstrated the feasibility of such an approach.

1.1.5 Calcined LDHs (CLDHs)

The calcination of LDHs at moderate temperatures (typically 300 – 600 °C) leads to the formation of metastable mixed oxide phases (CLDHs), which are very poorly crystalline or amorphous [4,7]; a spinel phase, together with the oxide of the divalent metal, is formed at higher temperatures. The properties of the CLDH phases depend on: the cations in the original LDH phase; small differences in LDH preparation, such as the

time or temperature of aging; the calcination conditions (temperature, time, rate of temperature rise and atmosphere); and the presence of impurities (residues from the precipitation step). The structure of the CLDH phases has been described as that of a non-stoichiometric spinel. In general, the CLDH phases are characterized by basicity, paracrystallinity and an ability to reform an LDH phase on exposure to aqueous solutions (see Section 1.1.3.3).

Cu/Zn/Al mixed oxides prepared from Cu/Zn/Al-LDHs have been investigated as catalysts for many reactions. Clausen *et al.* [82] studied Cu/Zn/Al oxides as catalysts for methanol synthesis and concluded that Cu^{2+} was homogeneously distributed in a mixed oxide phase containing the three metal cations and present in a local environment that is different from that in CuO. The decomposition products of Zn/Cr-LDHs not only depend on the calcination temperature but also on the atmosphere in which the treatment is carried because the calcination of Zn/Cr-LDH may be accompanied by concomitant oxidation of Cr^{3+} to Cr^{6+} [83].

CLDHs are useful solid base catalysts that find potential applications in many catalytic processes, for example for the decomposition of nitrous oxides [84,85], hydrogenation [86,87], condensation [88,89] and alkylation [90,91] reactions or wet oxidations [92,93]. They also have pharmaceutical and biological applications, for example porphyrins [94], nucleoside phosphates [75], drug [27,95], amino acids [79]. The adsorption properties of CLDHs are also exploited in many fields, such as the purification of cyclohexanone from by-product organic acids, the insertion of photoactive molecules [50] and the formation of new clay-modified electrodes [96].

1.2 Rare Earth Elements

1.2.1 Electronic structure

Rare earth elements (REEs) consist of the fourteen elements (cerium to lutetium) following lanthanum in the periodic table and arise because of the successive filling of the 4f sub-shell. Because the 4f orbitals are an inner shell they are relatively core-like and do not participate in chemical bonding and as result the chemical properties of the rare earth ions are in general very similar. They all form trivalent cations possessing characteristic $4f^n$ open shell configurations (n=1-14) [97-99] formed by loss of 6s and 5d or 4f electrons. Some REEs also exhibit oxidation states of +2 or +4: Ce^{3+} ($4f^1$), Pr^{3+} ($4f^2$) and Tb^{3+} ($4f^8$) may be oxidized to the corresponding tetravalent cations, whilst Sm^{3+} ($4f^5$), Eu^{3+} ($4f^6$) and Yb^{3+} ($4f^{13}$) can be reduced to divalent cations [100]. Many of the REEs, especially cerium and europium, have extensive applications in catalysis and luminescence. Cerium oxides, especially ceria (CeO_2), are common industrial catalysts used in CO oxidation, ethanol dehydrogenation, ester hydrolysis and hydroxybenzene oxidation [101,102]. By virtue of its spectroscopic properties and structural features europium, especially in the +3 oxidation state, is widely used as a structural and analytical luminescent probe providing information on the spectral and structural properties of organic compounds [103-105].

1.2.2 Properties of cerium and europium

1.2.2.1 Structure and characterization of cerium oxides

As far as organic chemists are concerned, interest in the REEs has long been

centered on a few applications such as oxidation by cerium compounds. Cerium oxides are common catalysts, which exist widely in nature and can also be generated by calcination of cerium hydroxides. CeO_2 has a number of advantageous properties which allow it to be used in many kinds of catalysis:

1) A number of oxygen species including O_2 (adsorbed molecules), O_2^- (superoxide), O_2^{2-} (peroxide) and O^- may be present on the surface of the CeO_2 catalyst. Bielanski *et al.* [106] have reviewed the importance of the different types of oxygen sites in catalysis. In general, O_2^{2-} or O^- ions are considered as the active species. Using electron paramagnetic resonance (EPR) Louis *et al.* [107] studied the formation, stability and other properties of the O_2^- ion on La_2O_3 as a model system. The authors suggested that the surface O_2^- ions are formed by insertion of O_2 into the surface oxygen vacancies formed during vacuum pre-treatment at 650 °C combined with electron donation to the oxygen molecule. Wang *et al.* [108] used temperature programmed reduction to study the role of cerium oxide in $CeO_2/MgAl_2O_4$ catalysts. Three different oxygen species were observed to exist on the surface of these catalysts. The reduction of the lattice oxygen of CeO_2 monolayers was observed to be easier than that of pure CeO_2 and this was ascribed to the interaction with $MgAl_2O_4$ support. Furthermore there was a form of adsorbed oxygen which was reduced at a lower temperature than the lattice oxygen, which was proposed to be O^- ion. An important conclusion was that the lattice oxygen on $CeO_2/MgAl_2O_4$ is very active and has a high recoverability.

2) CeO_2 is an electronic conductor, which allows it to act as a promoter. Palladium, rhodium or platinum added to CeO_2 have been shown to improve the effectiveness of

three-way catalysts in automotive exhaust catalysis. A study of surface segregation of Rh^{3+}, Pd^{2+} and Pt^{2+} ions in cerium dioxide has been performed by Sayle *et al.* [109]. It was shown that these ions segregate, together with oxygen vacancies, on the surface of the CeO_2. This provides a possible explanation of the influence of these metals on the catalytic activity.

3) CeO_2 has a large surface area, which enables it to act as an effective catalyst support.

1.2.2.2 Structure and characterization of cerium complexes

Several types of rare earth complexes have been successfully developed as functional molecular derivatives in the fields of chemistry, biology, medicine and materials science. Examples include luminescent sensors and light converters [110,111], nuclear magnetic resonance (NMR) and magnetic resonance imaging (MRI) probes [112,113] and practical catalysts in organic and biological reactions [114,115].

It has been reported that many inorganic and organic ligands can coordinate with rare earth cations to produce anionic complexes: these include fluoride, phosphate anions and pyridine, ketone and amino acid derivations. The number of ligand donor sites coordinated to a trivalent rare earth ion in a complex may vary between 6 and 12 depending on the size of the cation, with 8 or 9 being common coordination numbers [116]. Due to their Lewis acid character, the trivalent REEs are generally found coordinated with anionic ligands having high electronegativities, the best electron donors being oxygen and nitrogen [117]. It should be also noted that hydroxide anions and water molecules can also be readily coordinated to trivalent REEs [118].

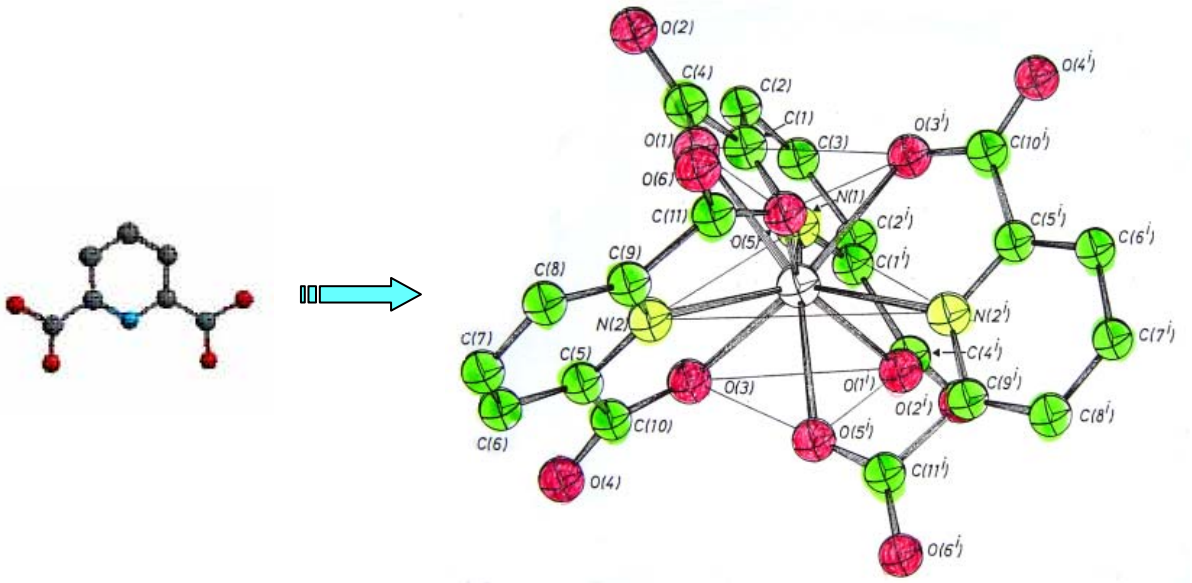

Fig. 1-2 Representation of the molecular structure of $Na_3[Ce(dipic)_3]\cdot 15H_2O$ [119]

The dianion of pyridine-2,6-dicarboxylic acid (H_2dipic) is often used as a tridentate ligand (denoted dipicolinate or dipic^{2-}) in studies of the luminescence of rare earth complexes. Fig. 1-2 shows the molecular structure of triclinic trisodium tris(pyridine-2,6-dicarboxylato)cerium(III) 15-hydrate ($Na_3[Ce(dipic)_3]\cdot 15H_2O$) determined by single crystal X-ray diffraction [119]. The Ce^{3+} ion is surrounded by six carboxylate oxygen atoms and three nitrogen atoms which together form a distorted tri-capped trigonal prism.

Fig. 1-3 shows the molecular structure of a second commonly used ligand, diethylenetriaminepentaacetic acid (DTPA, H_5L) and its complex with Ce^{3+} [120]. In the $Ce(DTPA)^{2-}$ anion, the nine-coordinate Ce^{3+} ion is bound to five carboxylate oxygen atoms, three amino nitrogen atoms and one oxygen atom from a water molecule. The coordination geometry is a distorted capped square antiprism.

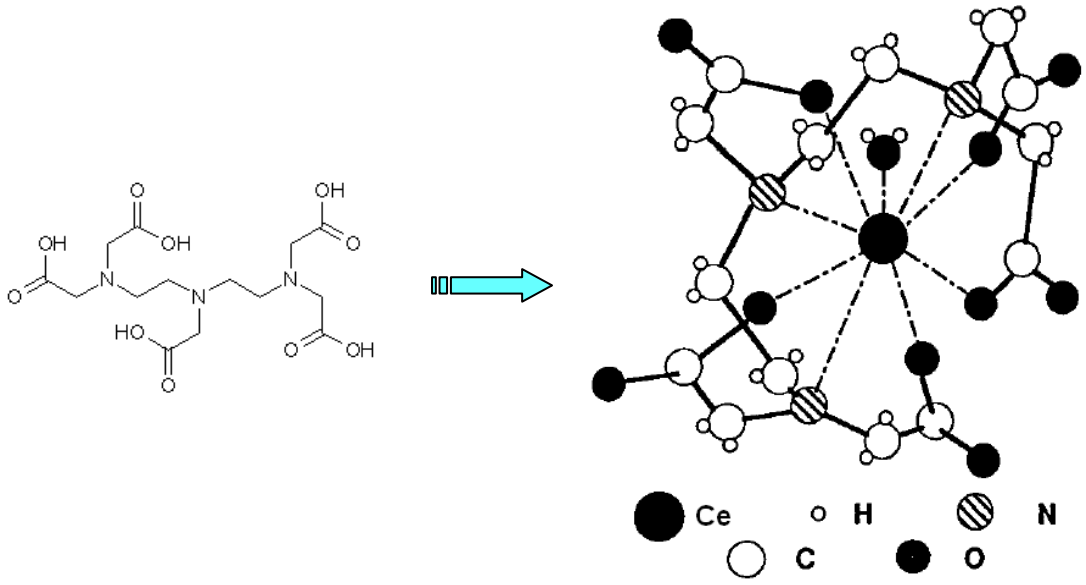

Fig.1-3 Representation of the molecular structure of $Ce(DTPA)^{2-}$ [120].

1.2.2.3 Structure and characterization of europium complexes

Recently, rare earth complexes have attracted considerable attention as materials for use in organic electroluminescent (EL) devices [121,122] as well as for optical microcavity emitters [123] owing to their inherent extremely sharp emission bands and potentially high internal quantum efficiency. The luminescent properties of Eu^{3+} in particular have led to its use in many fields such as tunable lasers, luminescent displays and amplifiers for optical communication [103,104].

The highest luminescence efficiencies are expected in europium complexes having bulky and /or multidentate ligands that limit clustering and can protect the Eu^{3+} ions from direct electron-phonon couplings with high frequency oscillators situated in the first coordination sphere [124]. Several workers have reported that some ligands can enhance the luminescence properties of Eu^{3+} by complex formation. Meng *et al.* [125]

demonstrated the beneficial effect of bi-dentate dibenzoylmethane $(DBM)^-$ groups on the luminescence properties of Eu^{3+} and Alvaro *et al.* [126] have reported the characterization of highly luminescent europium complexes, including those with the dipicolinate ligand, inside zeolites Y and mordenite. Based on these results, in this work, the tris(dipicolinato)europium(III) complex is used as a guest anion for intercalation in LDH hosts. In this complex, the nine-coordinated Eu(III) ion is surrounded by 3 dipicolinato groups, with the coordination sphere being made up of six oxygen atoms from carboxylate groups and three nitrogen atoms from pyridine rings, very similar to to the geometry of the Ce(III) complex shown in Fig. 1-2. Each tris(dipicolinato)europium(III) unit possesses D_3 point group symmetry.

1.2.3 Catalytic applications

1.2.3.1 CeO_2 as catalyst

Rare earth oxides have been widely investigated in catalysis as structural and electronic promoters which can lead to improved activity, selectivity and thermal stability of catalysts [106]. As discussed in Section 1.2.2.1, the most significant of the oxides of rare earth elements in industrial catalysis is certainly CeO_2 due to its numerous properties such as being an oxygen storage compound, enhancing the dispersion of metals and stabilizing the alumina washcoat [127]. Trovarelli [128] has reviewed studies of the different catalytic applications of CeO_2. Specifically, it has potential uses for the removal of soot from diesel engine exhaust [129], for the removal of organics from wastewaters [130], as an additive for combustion catalysts and processes [131] and in fuel cell technology [132].

CeO_2-based $MgAl_2O_4$ spinel catalysts for SOx removal and novel CeO_2-based catalysts for auto-exhaust treatment were first developed during 1984 - 1992 [133-135]. In a magnesium aluminate spinel/MgO solid solution containing CeO_2, the role of the latter as a catalyst was shown to result from its basic/redox character [136]. CeO_2 possesses sufficient oxidation activity to promote oxidation of SO_2 to SO_3 and its basic sites allow the adsorption of SO_2/SO_3 with formation of sulfates [137]. The solid solution of MgO and $MgAl_2O_4$ spinel acts as a catalyst support and has sufficient SO_3 adsorption capacity to facilitate removal of sulfates.

Reconstruction of the outer surfaces during the calcination processes, together with the availability of a low-energy route for the Ce^{4+} to Ce^{3+} reduction, may be an important factor in the high storage capacity of CeO_2 for oxygen. Sayle *et al.* [138,139] investigated the energetics of defects near the interface in the CeO_2/Al_2O_3 system. It was found that oxygen vacancies in a triple CeO_2 layer on Al_2O_3 are more stable than on free CeO_2.

1.2.3.2 CeO_2 as catalyst promoter

Rare earth oxides mixed with other metal oxides are used in many fields, and their presence often enhances the catalytic activity and selectivity of other metals i.e. the rare earth oxide is acting as a promoter. Day *et al.* [140,141] reported that pure rare earth oxides exhibit negligible catalytic activity for the oxidation of alcohols, but they have a good promotion effect on other catalysts. For example, in oxidation reactions of methanol or ethanol to CO_2 and H_2O, the reaction temperature required decreased significantly when using CuO as catalyst and Sm_2O_3 as promoter. Mantzavinos [142] found that addition of

La, Ce, Y or Sm oxides to NiO/Al_2O_3 led to an improvement in the thermal stability and activity, and a decrease in the amount of carbonaceous deposit. Agarwal *et al.* [143] found that CeO_2 promoted hopcalite (a mixture of copper and manganese oxides) has a higher initial activity for hydrocarbon oxidation than a Pt catalyst. Rare earth oxide additives have been widely applied as textural and structural promoters for supported noble metal catalysts.

Cerium oxide addition prevents alumina from sintering at high temperature and improves the dispersion and thermal stability of noble metals [144-146]. In addition, cerium oxide has been added to noble metal catalysts for treatment of automobile exhaust by simultaneous removal of CO, hydrocarbons and NOx using its oxygen storage ability [147,148].

1.2.3.3 Composite catalyst of CuO and CeO_2

Copper oxide is a well known component of catalysts for CO, phenol [149] and alcohol oxidation [150] as well as for NOx [151] and SO_2 [152] reduction. Because they are economic and efficient, these heterogeneous catalysts have been widely studied, but formation of carbonaceous deposits and leaching of copper are difficult to avoid. Several workers [153] have reported that copper oxide based catalysts show similar activities to noble metal catalysts for CO oxidation, as well as butanal and mercaptan oxidation.

Recently CeO_2 has been examined both as a promoter and as a support for oxidation reactions over copper oxide based catalysts. There are many publications in the literature [154,155] concerning the promotion of catalytic activity in such Cu-Ce oxide

systems in oxidation reactions. Park [156] reported that CeO_2 has an effect on the dispersion and crystallinity of the copper species and that cerium addition increases the CO oxidation activity of the copper catalysts. This can be explained by the strong interaction of CeO_2 with crystalline CuO and, subsequently, an enhancement in redox activity of the copper oxide phase. Flytzani-Stephanopoulos and coworkers [131,157,158] reported recently that a Cu-Ce-O composite catalyst shows high activity for CO and CH_4 oxidation and high resistance to water poisoning. They also attributed the enhanced catalytic activity and stability to the strong interaction of copper and cerium oxides. The interaction between the two oxides led to stabilization of reduced copper and an enhancement of copper reducibility, thus leading to a substantial increase in CO oxidation for $CuO/Ce–Al_2O_3$ catalyst. Furthermore, Stanko [159] demonstrated some other advantages of Cu-Ce catalysts: leaching of the active component, copper, was reduced, catalyst stability was improved and the problem of carbonaceous deposit was eliminated because CeO_2 has fewer surface acidic sites.

Synergism of copper and cerium in catalysis

The electronic state of surface copper plays an important role in Cu-containing catalysts for a number of catalytic processes such as deep and selective oxidation and dehydrogenation. Modification of the catalysts by inorganic additives having electron-attracting or electron-donating properties is a promising method of perturbing the electronic state of the copper sites. Pestryakov *et al.* [160] claimed that addition of rare earth oxides had an effect on both the electronic state and redox properties of the surface of supported copper oxide. The electron-attracting nature of CeO_2 produces a

marked change in electronic state and coordination structure of the surface atoms and ions of copper. Moreover, CeO_2 provides oxygen storage capacity and transfer channels.

Liu *et al.* [161] reported that the Cu-Ce-O oxide system was a very active catalyst for CO oxidation which was interpreted in terms of the strong synergism displayed by the copper-cerium oxide system. Stabilization of Cu^+ clusters by cerium oxide, and, in turn, increased amounts of active oxygen on the cerium oxide caused by the presence of copper were invoked to explain the synergism. CO adsorbs strongly on Cu^+ sites and reacts with labile oxygen at the interface of the two materials. A nano-CuO/CeO_2 mixture was used as a model to study the synergism.

Ferrandon *et al.* [162] reported the formation of a Cu-Ce solid solution, despite the fact that the ionic radius of Cu(II) differs significantly from that of Ce(IV), showing that copper can dissolve within the CeO_2 lattice. The promotion by Ce of the Cu-containing samples leads to a reduction in the amount and particle size of $CuAl_2O_4$. The stabilizing effect of Ce on Cu can be ascribed to the interactions between Cu and Ce in the solid solution. In addition, CeO_2 promoted the formation of some reduced copper (Cu^+) in catalysts calcined in air, particularly after one redox cycle. Also, the Cu-Ce interaction brings about a significant increase in oxygen mobility that results in an increase of copper reducibility. These last two effects lead to a substantial enhancement of oxidation reactions.

1.3 Research objectives

1.3.1 Incorporation of REEs into LDHs

The process of incorporation of REEs into LDHs is very complex, and many variables must be taken into account. In general, these variables can be divided into two classes, preparation conditions and the nature of host and guest species. The preparation conditions, including temperature, time, pH and drying environment in the synthesis process, can influence the stability, intercalation orientation and interaction between host layers and anions. In the case of the host and guest, the variables refer to their variety, charge density, decomposition ability, and orientation.

Guest anions: If ligands and their complexes are to be intercalated into LDH hosts, they should be stable in basic or neutral conditions since the structure of the LDH will be destroyed in acid solution. As noted in Section 1,2.2.2, the dipicolinate ($dipic^{2-}$) ligand is often used in studies of the luminescence of rare earth complexes. Although it meets the criterion of being stable under basic conditions, there have been no reports of intercalation of $dipic^{2-}$ or its complexes into LDH hosts. In this Thesis, the ability of $dipic^{2-}$ to facilitate intercalation of rare earth complexes in LDH hosts will be explored and compared with that of $DTPA^{5-}$ (Fig. 1-3) and $EDTA^{4-}$.

Host cations: Zn/Al-LDH is used in the optimization of synthesis conditions in this work because the LDH is stable over a larger range of pH compared with other LDHs. Subsequent studies of the interaction of LDHs containing divalent M^{2+} (Cu^{2+}, Zn^{2+}, Co^{2+}) and trivalent M^{3+} (Al^{3+}, Cr^{3+}) cations with different electronegativities and variable M^{2+}/ M^{3+} ratios with the rare earth complexes allow an investigation of the effect of varying the nature of the layers on the host-guest interaction.

Preparation methods: Coprecipitation and ion-exchange methods are used to introduce rare earth elements (Ce, Eu, Y) in the form of negatively charged complexes (with $DTPA^{5-}$ and $dipic^{2-}$ as ligands) into the interlayer galleries of LDHs. After detailed investigation of the effects of varying the experimental parameters, the optimized synthesis conditions are derived. The new layered materials are calcined to give mixed oxides with the aim of achieving a uniform high degree of dispersion of the different metal cations.

1.3.2 Characterization of REE-containing LDHs

Variables such as the nature of the layers, particle size and its distribution, charge density in the layers, extent of dispersion of the metal elements, interlamellar spacing, pore size and its distribution, location and number of active catalytic centers, are very important. The relationship between structure and preparation conditions is studied in order to control the structure of these new materials.

1.3.3 Discussion of catalytic abilities and mechanism

The physicochemical properties of REE-containing LDHs including the surface area, pore structure, chemical composition and basicity which determine their catalytic abilities, are characterized by different techniques. The catalytic abilities are investigated using the Catalytic Wet Oxidation of phenol as a probe reaction. The reaction mechanism is then discussed. Finally, a comparison between the two types of cerium sites present in the catalysts prepared by coprecipitation and ion-exchange methods is carried out and the differences are rationalized.

The luminescence properties of europium-containing LDHs are also discussed,

focusing on the role of the $dipic^{2-}$ ligands in promoting the luminescence.

1.3.4 Characterization techniques

The LDHs are characterized by a variety of techniques including X-ray diffraction (XRD), thermogravimetric analysis (TG-DTA), transmission electron microscopy (TEM), scanning electron microscopy (SEM), gas adsorption measurements (BET), temperature programmed desorption (TPD), extended X-ray absorption fine structure (EXAFS), X-ray photoelectron spectroscopy (XPS), nuclear magnetic resonance (NMR) and Fourier transform infrared (FT-IR) spectroscopies. Several techniques are often used in combination, in order to provide unambiguous structural information. The most routine methods for structure elucidation are powder XRD, FT-IR, UV, TG-DTA and BET.

XRD

XRD is the most frequently employed technique. A typical diffractogram of an LDH phase consists of sharp basal (00*l*) reflections at low values of 2θ corresponding to successive orders of the basal reflection. In addition, relatively weak non-basal reflections at higher values of 2θ are present. In certain cases, the non-basal reflections are quite broad, which may be attributed to the disordered stacking of the hydroxide layers (This is particularly true if the reflexion is not symmetric). Generally, the patterns are indexed on the basis of a hexagonal unit cell. The interlayer spacing of the LDH is equivalent to 1/n of the parameter *c*, where *n* is the number of layers in the unit cell which depends upon the stacking sequence of the layers. Subtracting the hydroxide layer thickness of approximately 4.8 Å from the interlayer spacing yields the gallery

height, which depends on the size and orientation of the charge balancing anion. The changes in the gallery height are used to confirm the successful intercalation of guest anions. The size, charge and properties of the cations in the host layers determine the unit cell parameter *a*, which is calculated using the relationship $a = 2d_{110}$, where d_{110} is the d spacing of the 110 reflection.

In situ high temperature XRD (HTXRD)

Information about changes in the size and orientation of interlayer anions and the crystalline phase and structure of LDHs during the process of thermal decomposition can be obtained from *in situ* HTXRD patterns. For example, the shift in the (003) reflection indicates the gradual changes in orientation or structure of interlayer guests with increase of temperature, and the loss of this reflection, or the emergence of other reflections, is indicative of decomposition of LDHs giving mixed oxide phases.

FT-IR

IR spectroscopy is not a key diagnostic tool for LDHs, but can be useful to identify the presence of the charge balancing anion in the interlayer galleries between the brucite-like sheets. Furthermore, information about the type of bonds formed by the anions and about their orientation can also be obtained. Several environments of functional groups are sometimes apparent, which adds to the complexity of the FT-IR spectra.

TG-DTA

The thermal properties of LDHs are commonly studied using thermogravimetry (TG) and differential thermal analysis (DTA). The thermal behavior of LDHs depends

on many factors, such as M^{2+}/M^{3+} ratio, type of anions, low temperature treatment (hydration, drying etc.). In certain cases the technique is used in combination with a mass spectrometer, in order to study the nature of the gases evolved during the thermal treatment. TG-DTA analyses also make it possible to demonstrate the presence of impurities or other compounds.

BET

Measurement of nitrogen adsorption/desorption isotherms represents the most widely used method of investigating textural properties of LDH materials, often providing the input data for analytical models for determining surface area, pore volume and pore size distribution information. The pore size distribution is determined using the BJH model on the desorption branch and the surface area is calculated using the BET model. Quantitative evaluation of the information is a crucial aspect of the processes involved in the design and application of materials for adsorption and catalysis. According to the IUPAC definition, calcined LDH materials exhibit a Type IV adsorption-desorption isotherm [163]. At low relative pressures (p_0/p) the adsorption only occurs as a thin layer on the walls - monolayer coverage. Depending on the pore size, an increase is seen at high relative pressures, which corresponds to capillary condensation of N_2 in the mesopores.

XPS

Information about the oxidation state and local coordination geometry of transition metals can be achieved by X-ray photoelectron spectroscopy (XPS), X-ray absorption near edge structure (XANES) and extended X-ray absorption fine structure (EXAFS).

TEM and SEM

Electron microscopy is a powerful tool to visualize the texture and morphology of LDHs. Particle size and dispersion are also apparent from the TEM/SEM images.

Chemical Analysis

Quantitative evaluation of the chemical compositions of intercalated LDHs, CLDH catalysts and filtrate after oxidation reactions can be carried out by inductively coupled plasma emission spectroscopy (ICP) and classical quantitative analysis. The formula of a sample can be calculated from these data, in combination with those from TG-DTA.

1.4 Significance of this work

In recent years, application of CeO_2 for the removal of organic compounds from wastewater through oxidation (catalytic wet oxidation, CWO) has been widely investigated [164]. The aim is the catalytic abatement of organic pollutants present in wastewater: for less toxic compounds, a biological treatment is suitable for final purification but prior catalytic wet oxidation is usually carried out at high oxygen pressure and high temperature in order to oxidize a significant proportion of the organic compounds in the aqueous phase [130]. Attention has been focused on CeO_2 and related compounds because they are highly active towards the oxidation of lower carboxylic acids which are relatively resistant to oxidation by other reagents. They are rapidly becoming key compounds in the degradation of organic pollutants, and may replace commercial homogeneous copper-based catalysts [165]. Novel catalyst materials containing transition metals and cerium oxide should have considerable potential as

catalysts in CWO.

LDHs and REEs have both attracted extensive attention because of their unique structures and properties. The layered structure of LDHs makes it possible for many metal cations or functional anions to be introduced. Incorporation of metal-containing anions in the interlayer galleries or metal cations in the layer provides several opportunities for enhancing the properties of functional materials: in the case of catalysts, it permits incorporation of, at least, a third metal component in the mixed oxides obtained upon thermal decomposition. In the case of other materials, the interlayer galleries provide a sterically constrained environment, thus potentially enhancing the selectivity of reactions. The electronic structure of REEs offers many advantages in the areas of optical, magnetic and catalytic materials. It is, therefore, of interest to prepare hybrid materials based on transition metal LDHs incorporating rare earth ions in order to investigate potential synergies between the two components and the resultant influence on catalytic and luminescent properties. There have been few reports to date of the incorporation of REEs into LDH materials.

1.5 Research aims

1) To prepare a series of novel lanthanide-containing LDHs and investigate the effects of varying experimental parameters in order to optimize the properties of the resulting materials.

2) To synthesize a series of novel catalytic materials by calcination of copper-containing LDH precursors with cerium ions incorporated in either the layers or the interlayer

galleries of the LDH.

3) To investigate the catalytic properties of these materials in the phenol oxidation reaction and carry out detailed mechanistic studies of the synergistic effect between Cu and Ce on the catalytic performance.

4) To synthesize a series of novel luminescent LDH materials containing tris(dipicolinato)europium complex anions in the interlayer galleries.

References:

1. V. Rives, M. A. Ulibarri, Layered double hydroxides (LDH) intercalated with metal coordination compounds and oxometalates, *Coordin. Chem. Rev.*, 1999, 181, 61-120.
2. A. de Roy, C. Forano, K. El Malki, J. P. Besse, in: M.L. Occelli, H.E. Robson (Eds.), Synthesis of Microporous Materials, vol. 2, Expanded Clays and Other Microporous Systems, Van Nostrand Reinhold, New York, 1992, 108-169.
3. F. Trifiro, A. Vaccari, in: J. L. Atwood, J. E. D. Davies, D. D. MacNicol, F. Vogtle, J.-M. Lehn, G. Alberti, T. Bein (Eds.), Comprehensive Supramolecular Chemistry, vol. 7, Solid-State Supramolecular Chemistry: Two- and Three-Dimensional Inorganic Networks, Pergamon, Oxford, 1996, 251-291.
4. F. Cavani, F. Trifiro, A. Vaccari, Hydrotalcite-type anionic clays: preparation, properities and applications, *Catal. Today*, 1991, 11, 173-301.
5. A. I. Khan, D. O'Hare, Intercalation chemistry of layered double hydroxides: recent developments and applications, *J. Mater. Chem.*, 2002, 12, 3191-3198.
6. V. Rives (Ed.), Layered Double Hydroxides: Present and Future, Nova Science Publishers, New York, 2001.
7. V. Rives, Characterization of layered double hydroxides and their decomposition products, *Mater. Chem. Phys.*, 2002, 75(1-3), 19-25.
8. F. Malherbe, C. Forano, J. P. Besse, in: Book of Abstracts of 213*th* ACS National

Meeting, San Francisco, 1997, April 13-17.

9. F. Malherbe, J. P. Besse, Investigating the effects of Guest-Host Interactions on the Properties of Anion-Exchange Mg-Al Hydrotalcites, *J. Solid State Chem.*, 2000, 155(2), 332-341.
10. D. Tichit, N. Das, B. Coq, R. Durand, Preparation of Zr-containing Layered Double Hydroxides and Characterization of the Acido-Basic Properties of Their Mixed Oxides, *Chem. Mater.*, 2002, 14(4), 1530-1538.
11. U. Olsbye, D. Akporiaye, E. Rytter, M. Ronnekleiv, E. Tangstad, On the stability of mixed M^{2+}/M^{3+} oxides, *Appl. Catal. A: Gen.*, 2002, 224(1-2), 39-49.
12. S. P. Newman, W. Jones, Synthesis characterization and application of layered double hydroxides containing organic guests, *New J. Chem.*, 1998, 22(2), 105-115.
13. H. Roussel, V. Briois, E. Elkaim, A. De Roy, J. P. Besse, Cationic Order and Structure of [Zn-Cr-Cl] and [Cu-Cr-Cl] Layered Double Hydroxides: A XRD and EXFS Study, *J. Phys. Chem. B*, 2000, 104(25), 5915-5923.
14. V. Rives, S. Kannan, Layered double hydroxides with the hydrotalcite-type structure containing Cu^{2+}, Ni^{2+} and Al^{2+}, *J. Mater. Chem.*, 2000(10), 10, 489-495.
15. R. M. Taylor, The rapid formation of crystalline double hydroxyl salts and other compounds by controlled hydrolysis, *Clay Miner.*, 1984, 19, 591-603.
16. S. Velu, V. Ramaswamy, A. Ramani, B. M. Chanda, S. Sivasanker, New hydrotalcite-like anionic clays containing Zr^{4+} in the layers, *Chem. Commun.*, 1997, (21), 2107-2108.
17. C. J. Serna, J. L. Rendon, J. E. Iglesias, Crystal-chemical study of layered $[Al_2Li(OH)_6]^{PL}$ X(super-) • nH_2O, *Clays Clay Miner.*, 1982, 30, 180-184.
18. L. Raki, D. G. Rancourt, C. Detellier, Preparation, Characterization, and Moessbauer Spectroscopy of Organic Anion Intercalated Pyroaurite-like Layered Double Hydroxides, *Chem. Mater.*, 1995, 7(1), 221-224.
19. N. T. Whilton, P. J. Vickers, S. Mann, Bioinorganic Clays: synthesis and characterization of amino- and polyamine acid intercalated layered double hydroxides, *J. Mater. Chem.*, 1997, 7(8), 1623-1629.
20. E. Lopez-Salinas, Y. Ono, Intercalation chemistry of a Mg-Al layered double

hydroxides ion-exchanged with complex MCl_4^{2-} (M=Ni Co) ions from organic media, *Microporous Mater.*, 1993, 1(1), 33-42.

21. S. Carlino, The intercalation of carboxylic acids into layered double hydroxides: a critical evaluation and review of the different methods, *Solid State Ionics*, 1997, 98(1-2), 73-84.
22. H. C. B. Hansen, C. B. Koch, Synthesis and properties of hexacyanoferrate interlayered into hydrotalcite: I Hexacyanoferrate(II), *Clays Clay Miner.*, 1994, 42, 170-179.
23. C. P. Kelkar, A. A. Schutz, Ni-, Mg- and Co- containing hydrotalcite-like materials with a sheet-like morphology: synthesis and characterization, *Microporous Mater.*, 1997, 10(4-6) 163-172.
24. E. W. Serwicka, P. Nowak, K. Bahranowski, W. Jones, F. Kooli, Insertion of electrochemically reduced Keggin anions into layered double hydroxides, *J. Mater. Chem.*, 1997, 7(9), 1937-1939.
25. T. Kwon, G. A. Tsigdinos, T. J. Pinnavaia, Pillaring of layered double hydroxides (LDH's) by polyoxometalate anions, *J. Am. Chem. Soc.*, 1988, 110(11), 3653-3654.
26. L. L. Ren, J. He, S. C. Zhang, D. G. Evans, X. Duan, R. Y. Ma, Immobilization of penicillin gacylase in layered double hydroxides pillared by glutamate ions, *J. Mol. Catal.: B-Enzym.*, 2002, 18, 3-11.
27. J. H. Choy, J. S. Jung, J. M. Oh, M. Park, J. Jeong, Y. K. Kang, O. J. Han, Layered double hydroxide as an efficient drug reservoir for folate derivatives, *Biomaterials*, 2004, 25, 3059 - 3064.
28. S. Casenave, H. Martinez, C. Guimon, A. Auroux, V. Hulea, E. Dumitriu, Acid and base properties of MgCuAl mixed oxides, *J. Therm. Anal. Calorim.*, 2003, 72, 191-198.
29. M. Park, C. Lee, E. J. Lee, J. H. Choy, J. E. Kim, J. Choi, Layered double hydroxides as potential solid base for beneficial remediation of endosulfan-contaminated soils, *J. Phys. Chem. Solids*, 2004, 65, 513-516.
30. Y. W. You, Use of layered double hydroxides and their derivatives as absorbents for inorganic and organic pollutants, PhD thesis, Department of Renewable Resources,

the University of Wyoming, 2002.

31. J. Tronto, L. P. Cardoso, J. B. Valim, Studies of the intercalation and “in vitro” liberation of amino acids in magnesium aluminium layered double hydroxides, *Mol. Cryst. Liq. Cryst.*, 2003, 390, 79-89.
32. A. Vaccari, Preparation and catalytic properties of cationic and anionic clays, *Catal. Today*, 1998, 41(3), 53-71.
33. M. Guenane, C. Forano, J. P. Besse, Intercalation of Organic Pillars in [Zn-Al] and [Zn-Cr] Layered Double Hydroxides, *Mater. Sci. Forum*, 1994, 152/153, 343-346.
34. M. Meyn, K. Beneke, G. Lagaly, Anion-exchange reactions of layered double hydroxides, *Inorg. Chem.*, 1990, 29(26), 5201-5206.
35. M. Wei, S. X. Shi, J. Wang, Y. Li, X. Duan, Studies on the intercalation of naproxen into layered double hydroxide and its thermal decomposition by in situ FT-IR and in situ HT-XRD, *J. Solid State Chem.*, 2004, 177, 2534-2541.
36. H. Hao, k. Nagy, Dodecyl sulfate–hydrotalcite nanocomposites for trapping chlorinated organic pollutants in water, *J. Colloid Interf. Sci.*, 2004, 274, 613-624.
37. S. iyata, Physico-chemical properties of synthetic hydrotalcites in relation to composition, *Clays Clay Miner.*, 1980, 28, 50-55.
38. T. Stanimirova, G. Kirov, Cation composition during recrystallization of layered double hydroxides from mixed (Mg, Al) oxides, *Appl. Clay Sci.*, 2003, 22, 295-301.
39. T. Sato, H. Fujita, T. Endo, M. Shimada, A. Tsunashima, Synthesis of hydrotalcite-like compounds and their pyhsico-chemical properties, *React. Solids*, 1988, 5(2-3), 219-228.
40. F. Kooli, V. Rives, M. A. Ulibarri, Vanadate-Pillared Hydrotalcite Containing Transition Metal Cations, *Mater. Sci. Forum*, 1994, 152/153, 375-378.
41. S. Carlino, M. J. Hudson, S. W. Husain, The reaction of mloten phenylphosphonic acid with a layered double hydroxide and its calcined oxide, *Solid State Ionics*, 1996, 84(1-2), 117-129.
42. S. Carlino, M. J. Hudson, Thermal Intercalation of Layered Double Hydroxides: Capric Acid into an Mg-Al LDH, *J. Mater. Chem.*, 1995, 5(9), 1433-1442.
43. S. Carlino, M. J. Hudson, Reaction of molten sebacic acid with a layered

(Mg/Al)double hydroxide, *J. Mater. Chem.*, 1994, 4(1), 99-104.

44. J. Carpentier, J. F. Lemonier, S. Siffert, E. A. Zhilinskaya, A. Aboukais, Characterisation of Mg/Al hydrotalcite with interlayer palladium complex for catalytic oxidation of toluene, *Appl. Catal. A. Gen.*, 2002, 234(1-2), 91-101.
45. F. Leroux, J. P. Besse, Polymer Interleaved Layered Double Hydroxides: A New Emerging Class of Nanocomposites, *Chem. Mater.*, 2001, 13(10), 3507-3515.
46. J. Inacio, C. Taviot-Gueho, C. Forano, J. P. Besse, Adsorption of MCPA pesticide by MgAl- layered double hydroxides, *Appl. Clay Sci.*, 2001, 18(5-6) 255-264.
47. Y. You, H. Zhao, G. F. Vance, Adsorption of dicamba (3,6-dichoro-2-methoxy benzoic acid) in aqueous solution by calcined- layered double hydroxides, *Appl. Clay Sci.*, 2002, 21(5-6), 217-226.
48. V. Prévot, B. Casal, E. Ruiz-Hitzky, Intracrystalline aldylation of benzoate ions into layered double hydroxides, *J. Mater. Chem.*, 2001, 11, 554 - 560.
49. E. Gardner, K. M. Huntoon, T. J. Pinnavaia, Direct Synthesis of Alkonide-Intercalated Derivatives of Hydrotalcite-like Layered Double Hydroxides: Precursors for the Formation of Colloidal Layered Double Hydroxide Suspensions and Transparent Thin Films, *Adv. Mater.*,2001, 13(16), 1263-1266.
50. M. Ogawa, K. Kuroda, Photofunctions of intercalation compounds, *Chem. Rev.*, 1995, 95(2), 399-438.
51. R. Szostak, C. Ingram, in: H. K. Beyer, H. G. Karge, I. Kiricsi, J. B. Nagy (Eds.), Catalysis by Microporous Materials, Elsevier, Amsterdam, Stud. Surface Sci. Catal., 1995, 94, 13-38.
52. T. J. Pinnavaia, M. Chibwe, V. R. L. Constantino, S. K. Yun, Organic chemical conversions catalyzed by intercalated layered double hydroxides (LDHs), *Appl. Clay Sci.*, 1995, 10(1-2), 117-129.
53. M. A. Drezdzon, Synthesis of isopolymetalate-pillared hydrotalcite via organic anion pillared precursors, *Inorg. Chem.*, 1988, 27, 4628-4632.
54. B. M. Choudary, M. L. kantam, B. Bharathi, Superactive Mg-Al-O-t-Bu hydrotalcite for epoxidation of olefins, *Synlett.*, 1998, 1203-1042.
55. B. M. Choudary, K. M. Lakshmi, B. Kavita, Aldol condensation catalysed by novel

Mg-Al-o-Bu- hydrotalcite, *Tetrahed Lett.*, 1998, 39(21), 3555-3558.

56. H. Zhang, R. Qi, D. G. Evans, X. Duan, Synthesis and characterization of a novel nano-scale magneticsolid base catalyst involving a layered double hydroxide supported on a ferrite core, *J. Solid State Chem.*, 2004, 177, 772-780.
57. A. Corma, From Microporous to Mesoporous Molecular Sieve Materials and Their Use in Catalysis, *Chem. Rev.*, 1997, 97(6), 2373-2420.
58. L. H. Zhang, F. Li., D. G. Evans, X. Duan., Structure and surface characteristics of Cu-based composite metal oxides derived from layered double hydroxides, *Mater. Chem. Phys.*, 2004, 87, 402-410.
59. S. Velu, K. Suzuki, Selective production of hydrogen for fuel cells via oxidative steam reforming of methanol over CuZnAl oxide catalysts: effect of substitution of zirconium and cerium on the catalytic performance, *Topics in Catalysis*, 2003, 22(3-4), 235-244.
60. S. Narayanan, K. Krishna, Hydrotalcite-supported palladium catalysts Part II. Preparation, characterization of hydrotalcites and palladium hydrotalcites for CO chemisorption and phenol hydrogenation, *Appl. Catal. A: Gen.*, 2000, 198, 13-21.
61. C. Hu, Q. L. He, Y. H. Zhang, E. B. Wang, T. Okuhara, M. Misono, Synthesis, stability and oxidative activity of polyoxometalates pillared anionic clays ZnAl-SiW_{11} and ZnAl-$SiW_{11}Z$, *Catal. Today*, 1996, 30, 141-146.
62. P. Beaudot, M. E. De Roy, J. P. Besse, Intercalation of noble metal complexes in LDH compounds, *J. Solid State Chem.*, 2004, 177, 2691-2698.
63. L. Ukrainczyk, M. Chibwe, T. J. Pinnavaia, S. A. Boyd, ESR study of Cobalt(II) Tetrakis (N-methyl-4-pyridiniumyl) porphyrin and Cobalt(II) Tetrasulfophthalocyanine Intercalated in Layered Aluminosilicates and a Layered Double Hydroxides, *J. Phys. Chem.*, 1994, 98(10), 2668-2676.
64. K. A. Carrado, J. E. Forman, R. E. Botto, R. E. Winans, Incorporation of phthalocyanines by cationic and anionic clays via ion exchange and direct synthesis, *Chem. Mater.*, 1993, 5(4), 472-478.
65. S. Narayanan, K. Krishna, Hydrotalcite-supported palladium catalysts: Part I: Preparation, characterization of hydrotalcites and palladium on uncalcined

hydrotalcites for CO chemisorption and phenol hydrogenation, *Appl. Catal.*, 1998, 174(1-2), 221-229.

66. M. Chibwe, T. J. Pinnavaia, Stabilization of a cobalt(II) phthalocyanine oxidation catalyst by intercalation in a layered double hydroxide host, *J. Chem. Soc., Chem. Commun.*, 1993(3), 278-280.
67. M. E. Perez-Bernal, R. Ruano-Casero, T. J. Pinnavaia, Catalytic autoxidation of 1-decanethiol by cobalt(II) phthalocyaninetetrasulfonate intercalated in a layered double hydroxide, *Catal. Lett.*, 1991, 11(1), 55-61.
68. S. Miyata, Eur. Patent 152, 010 (1985), to Kyowa Chem. Ind. Co.
69. H. Kopka, K. Beneke, G. Lagaly, Anionic surfactants between double metal hydroxide layers, *J. Colloid Interface Sci.*, 1988, 123(2), 427-436.
70. O. Neil, A. Gary, Goyak, Method for removing color-imparting contaminants from pulp and paper waste streams using a combination of adsorbents[P], US: 5378367, 1995-1-3.
71. M. Jakupca, P. K. Dutta, Thermal and Spectroscopic Analysis of a Fatty Acid-Layered Double Hydroxides and Its Application as a Chromatographic Stationary Phase, *Chem. Mater.*, 1995, 7(5), 989-994.
72. S. Bonnet, C. Forano, A. de Roy, J. P. Besse, Synthesis of Hybrid Organo-Mineral Materials : Anionic Tetraphenylporphyrins in Layered Double Hydroxides, *Chem. Mater.*, 1996, 8(8), 1962-1968.
73. D. S. Robins, P. K. Dutta, Examination of Fatty Acid Exchanged Layered Double Hydroxides as Supports for Photochemical Assemblies, *Langmuir*, 1996, 12(2), 402-408.
74. J. H. Choy, S. Y. Kwak, J. S. Park, Eur. Pat. Appl., EP200,003, 22, 2000.
75. B. Lotsch, F. Millange, R. I. Walton, D. O'Hare, Separation of nucleoside monophosphates using preferential anion exchange intercalation in layered double hydroxides, *Solid State Sci.*, 2001, 3(8), 883-886.
76. V. Ambrogi, G. Fardella, G. Grandolini, L. Perioli, Intercalation compounds of hydrotalcite-like anionic clays with antiinflammatory agents-I. Intercalation and in vitro release of ibuprofen, *Int. J. Pharm.*, 2001, 220(1-2), 23-32.

77. A. I. Khan, L. Lei, A. J. Norquist, D. O'Hare, Intercalation and controlled release of pharmaceutically active compounds from a layered double hydroxides, *Chem. Commun.*, 2001, (22), 2342-2343.

78. J. H. Choy, Y. H. Son, Intercalation of Vitamer into LDH and Their Controlled Release Properties, *Bull. Korean Chem. Soc.*, 2004, 25(1), 122-126. S. H. Hwang, Y. S. Han, J. H. Choy, *Bull. Korean Chem. Soc.*, 2001, 22, 1019.

79. S. Aisawa, S. Takahashi, W. Ogasawara, Y. Umetsu, E. Narita, Direct Intercalation of Amino Acids into Layered Double Hydroxides by coprecipitation, *J. Solid State Chem.*, 2001, 162(1), 52-62.

80. A. Legrouri, M. Lakraimi, A. Barroug, A. De Roy, J. P. Besse, Removal of the herbicide 2,4-dichlorophenoxyacetate from water to zinc-aluminium-chloride layered double hydroxides, *Water Res.*, 2005, 39(15), 3441-3448.

81. I. J. Shannon, T. Maschmeyer, G. Sankar, J. M. Thomas, R. D. Oldroyd, M. Sheehy, D. Madill, A. M. Waller, R. P. Townsend, A new cell for the collection of combined EXAF/XRD data in situ during solid/liquid catalytic reactions, *Catal. Lett.*, 1997, 44(1-2), 23-27.

82. B. S. Clausen, B. Lengeler, B. S. Rasmussen, X-ray absorption spectroscopy study of copper-based methanol catalysts. 1. Calcined state, *J. Phys. Chem.*, 1985, 89(11), 2319-2324.

83. G. Del Piero, M. Di Conca, F. Trifiro, A. Vaccari, in P. Barret, L. C. Dufour (Editors), Reactivity of Solids, Elsevier, Amsterdam, 1985, 1029.

84. R. S. Drago, K. Jurczyk, N. Kob, Catalyzed decomposition of N_2O on metal oxide supports, *Appl. Catal. B: Environ.*, 1997, 13(1), 69-79.

85. H. Dandl, G. Emig, Mechanistric approach for the kinetics of the decomposition of nitrous oxide over calcined hydrotalcites, *Appl. Catal. A: Gen.*, 1998, 168(2), 261-268.

86. F. Medina, R. Dutartre, D. Tichit, B. Coq, N. T. Dung, P. Salagre, J. E. Sueiras, Characterization and activity of hydrotalcite-type catalysts for acetonitrile hydrogenation, *J. Mole. Catal. A: Chem.*, 1997, 119(1-3), 201-212.

87. Y. Z. Chen, C. W. Liaw, I. I. Lee, Selectibe hydrogenation of phenol to

cyclohexanone over palladium supported on calcined Mg/Al hydrotalcite, *Appl. Catal. A: Gen.*, 1999, 177(1), 1-8.

88. E. Dumitriu, V. Julea, C. Chelaru, C. Catrinescu, D. Tichit, R. Durand, Influence of the acid-base properties of solid catalysts derived from hydrotalcite-like compounds on the condensation of formaldehyde and acetaldehyde, *Appl. Catal. A: Gen.*, 1999, 178(2), 145-157.
89. M. A. Aramendy, Y. Aviles, J. A. Benytez, V. Borau, C. Jimenez, J. M. Marinas, J. R. Ruiz, F. J. Urbano, Comparative study of Mg/Al and Mg/Ga layered double hydroxides, *Microporous Mesoporous Mater.*, 1999, 29(3), 319-328.
90. S. Velu, C. S. Swamy, Alkylation of phenol with methanol over magnesium-aluminium calcined hydrotalcites, *Appl. Catal. A: Gen.*, 1994, 119(2), 241-252.
91. S. Velu, C. S. Swamy, Selective, C-alkylation of phenol with methanol over catalysts derived from copper-aluminium hydrotalcite-like compounds, *Appl. Catal. A: Gen.*, 1996, 145(1-2), 141-153.
92. St. G. Christoskova, M. Stoyanova, M. Georgieva, Low-temperature iron-modified cobalt oxide system: Part 2. Catalytic oxidation of phenol in aqueous phase, *Appl. Catal. A: Gen.*, 2001, 208(1-2), 243-249.
93. J. Barrault, C. Bouchoule, K. Echachoui, N. Frini-Srasra, M. Trabelsi, F. Bergaya, Catalytic wet peroxide oxidation (CWPO) of phenol over (Al-Cu) - pillared clays, *Appl. Catal. B: Environ.*, 1998, 15(3-4), 269-274.
94. D. S. Robins, P. K. Dutta, Examination of Fatty Acid Exchanged Layered Double Hydroxides as Supports for Photochemical Assemblies, *Langmuir*, 1996, 12(2), 402-408.
95. M. D. Arco, E. Cebadera, S. Gutierrez, C. Martin, M. J. Montero, V. Rives, J. Rocha, M. A. Sevilla, Mg, Al Layered Double Hydroxides with intercalated Indomethacin: Synthesis, Characterization, and Pharmacological Study, *J Pharm Sci*, 2004, 93, 1649-1658.
96. L. Gaillon, F. Bedioui, J. D. Battioni, Electrochemical characterization of manganese prophyrins fixed onto silica and layered dihydroxide matrices, *J.*

Electroanal. Chem., 1993, 347(1-2), 435-442.

97. N. M. Edelstein, Comparison of the electronic structure of the lanthanides and actinides, *J. Alloys Compd.*, 1995, 223, 197-203.

98. V. Alexander, Design and Synthesis of Macrocyclic Ligands and Their Complexes of Lanthanids and Actinides, *Chem. Rev.*, 1995, 95(2), 273-342.

99. C. Piguet, J. C. G. Bünzli, Mono-and polymetallic lanthanide-containing functional assembilies: a field between tradition and novelty, *Chem. Soc. Rev.*, 1999, 28(6), 347-358.

100. T. Moeller Jr., The chemistry of the lanthanides, in: J. C. Bailar Jr., H. J. Emeleus, R. Nyholm, A. F. Trotman-Dickenson (Eds.), Comprehensive Inorganic Chemistry, Pergamon, Oxford, 1975.

101. C. R. Ronda, T. Justel, H. Nikol, Rare earth phosphors: fundamentals and applications, *J. Alloys Compd.*, 1998, 275-277, 669-676.

102. S. I mamura, T. Yamashita, R. Hamada, Y. Saito, Y. Nakao, N. Tuda, C. Kaito, Strong interaction between rhodium and ceria, *J. Mol. Catal. A: Chem.*, 1998, 129(2-3), 249-256.

103. R. T. Yang, N. Tharappiwattananon, R. Q. Long, Ion-exchanged pillared clays for selective catalytic reduction of NO by ethylene in the presence of oxygen, *Appl. Catal. B: Environ.*, 1998, 19(3-4), 289-304.

104. C. Feldmann, T. Justel, C. R. Ronda, J. Schmidt P, Inorganic Luminescent Materials: 100 Years of Research and Application, *Adv. Funct. Mater.*, 2003, 13(7), 511-516.

105. C. Li, G. Wang, L. Y. Wang, D. G. Evans, X. Duan, Incorporation of rare earth ions in Mg-Al layered double hydroxides: intercalation with an $[Eu(EDTA)]^-$ chelate, *J. Solid State Chem.*, 2004, 177(12), 4569-4575.

106. P. J. Gellings, H. J. M. Bouwmeester, Solid state aspects of oxidation catalysis, *Catal. Today*, 2000, 58, 1-53.

107. C. Louis, T. L. Chang, M. Kermarec, T. LeVan, J. M. Tatibouët, M. Chea, EPR study of the stability and the role of the O^{2-} species on La_2O_3 in the oxidative coupling of methane, *Catal. Today*, 1992, 13(2-3), 283-289.

108. J. A. Wang, L. Chen, C. Li, Roles of cerium oxides and the reducibility and recoverability of the surface oxygen species in the $CeO_2/MgAl_2O_4$ catalysts, *J. Mol. Catal. A: Chem.*, 1999, 139(2-3), 315-323.

109. T. X. T. Sayle, S. C. Parker, C. R. A. Catlow, Surface Segregation of Metal Ions in Cerium Dioxide, *J. Phys. Chem.*, 1994, 98(51), 13625-13630.

110. W. D. Horrocks, J. D. R. Sudnick, Lanthanide ion luminescence probes of the structure of biological macromolecules, *Acc. Chem. Res.*, 1981, 14(12), 384-392.

111. D. Parker, Luminescent lanthanide sensors for pH, pO_2 and selected anions, *Coord. Chem. Rev.*, 2000, 205(1), 109-130.

112. D. Parker, NMR determination of enantiomeric purity, *Chem. Rev.*, 1991, 91(7), 1441-1457.

113. P. Caravan, J. J. Ellison, T. J. McMurry, R. B. Lauffer, Gadolinium(III) Chelates as MRI Contrast Agents: Structure, Dynamics, and Applications, *Chem. Rev.*, 1999, 99(9), 2293-2352.

114. T. Imamoto., Lanthanides in Organic Synthesis, Academic Press, London, 1994.

115. M. Komiyama, N. Takeda, H. Shigekawa, Hydrolysis of DNA and RNA by lanthanide ions: mechanistic studies leading to new applications, *Chem. Commun.*, 1999, 16, 1443-1451.

116. S. P. Sinha, Structure and bonding in highly coordinated lanthanide complexes, *Struct. Bond.*, 1976**,** 25, 69-149.

117. R. G. Pearson, Hard and Soft Acids and Bases, *J. Am. Chem. Soc.*, 1963**,** 85(22), 3533-3539.

118. S. A. Cotton, Encyclopedia of Inorganic Chemistry, Scandium, Yttrium and the Lanthanides: Inorganic Coordination Chemistry, Ed. R. B. King, John Wiley & Sons, Chichester, 1994.

119. J. Albertsson, Structural studies on the rare earth carboxylates, *Acta Chem. Scand.*, 1972, 26(3), 1023-1044.

120. S. Benazeth, J. Purans, M. C. Chalbot, M. K. Nguyen-van-Duong, L. Nicolas, F. Keller, A. Gaudemer, Temperature and pH Dependence XAFS Study of $Gd(DOTA)^-$ and $Gd(DTPA)^{2-}$ Complexes: Solid State and Solution Structures,

Inorg. Chem., 1998, *37*, 3667-3674.

121. M. S. Weaver, D. G. Lidzey, M. A. Pavier, H. Mellor, S. L. Thorpe, D. D. C. Bradley, T. Richardson, T. M. Searle, C. H. Huang, H. Lui, D. Zhou, Organic light-emittingdiodes (LEDS) based on langmuir-Blodgett films containing rare-earth complexes, *Synth. Met.*, 1996, 76(1-3), 91-93.
122. Y. X. Zheng, J. L. Liang, Q. Lin, Y. N. Yu, Q. G. Meng, Y. H. Zhou, S. B. Wang, H. A. Wang, H. J. Zhang, A comparative study on the electroluminescence properties of some terium β-diketonate complexes, *J. Mater. Chem*., 2001, 11(10), 2615-2619.
123. S. Dirr, S. Wiese, H. H. Johannes, D. Ammermann, A. Böhler, W. Grahn, W. Kowalsky, Luminescence enhancement in microcavity organic multilayer structures, *Synth. Met*., 1997, 91(1-3), 53-56.
124. Q. G. Meng, Preparation, Characterization and Luminescence Properties of Organic-Inorganic Hybrids Processed by Wet Impregnation of Mesoporous Silica, PhD thesis, Lab des Materiaux Inorganiques, Universite Blaise Pascal, 2005.
125. Q. G. Meng, P. Boutinaud, A. C. Franville, H. J. Zhang, R. Mahiou, Preparation and characterization of luminescent cubic MCM-48 impregnated with an Eu^{3+} b-diketonate complex, *Microporous and Mesoporous Materials*, 2003, 65, 127-136.
126. M. Alvaro, V. Fornes, S. Garcia, H. Garcia, J. C. Scaiano, Intrazeolite Photochemistry. 20. Characterization of Highly Luminescent Europium Complexes inside Zeolites, *J. Phys. Chem. B*, 1998, 102(44), 8744-8750**.**
127. P. J. Gellings, H. J. M. Bouwmeester, Ion and mixed conducting oxides as catalysts, *Catal. Today*, 1992, 12(1), 1-101.
128. A. Trovarelli, C. de Leitenburg, M. Boaro, G. Dolcetti, The utilization of ceria in industrial catalysis, *Catal, Today*, 1999, 50, 353-367.
129. J. Lahaye, S. Boehm, P. H. Chambrion, P. Ehrburger, Influence of cerium oxide on the formation and oxidation of soot, *Combustion and Flame*, 1996, 104(1-2), 199-207.
130. Y. I. Matatov-Meytal, M. Sheintuch, Catalytic Abatement of Water Pollutants, *Ind. Eng. Chem. Res.*, 1998, 37, 309-326.

131. W. Liu, M. Flytzani-Stephanopoulos, Total Oxidation of Carbon-Monoxide and Methane over Transition Metal Fluorite Oxide Composite Catalysts: II. Catalyst Characterization and Reaction-Kinetics, *J. Catal.*, 1995, 153(2), 317-332.

132. M. Sahibzada, B. C. H. Steele, K. Zheng, R. A. Rudkin, I. S. Metcalfe, Development of solid oxide fuel cells based on a Ce (Gd) O_{2-x} electrolyte film for intermediate temperature operation, *Catal. Today*, 1997, 38(4), 459-466.

133. J. S. Yoo, J. A. Jaecker, US Patent 4 469 589, 1984.

134. M. Ozawa, M. Kimura, A. Isogai, S. Matsumoto, N. Miyoshi, Ger. Offen, DE 3 913 972, 1989.

135. M. G. Sanchez, S. R. Schmidt, M. V. Ernest, US Patent 5 102 850, 1992.

136. A. A. Bhattacharyya, G. M. Woltermann, J. S. Yoo, J. A. Karch, W. E. Cormier, Catalytic SOx abatement: the role of magnesium aluminate spinel in the removal of SOx from fluid catalytic cracking (FCC) flue gas, *Ind. Eng. Chem. Res.*, 1988, 27(8), 1356-1360.

137. M. Waqif, P. Bazin, O. Saur, J. C. Lavalley, G. Blanchard, O. Touret, Study of ceria sulfation, *Appl. Catal. B Environ.*, 1997, 11(2), 193-205.

138. D. C. Sayle, T. X. T. Sayle, S. C. Parker, J. H. Harding, C. R. A. Catlow, The stability of defects in the ceramic interface, MgO/MgO and CeO_2/Al_2O_3, *Surf. Sci.*, 1995, 334(1-3), 170-178.

139. D. C. Sayle, T. X. T. Sayle, S. C. Parker, C. R. A. Catlow, J. H. Harding, Effect of defects on the stability of heteroepitaxial ceramic interfaces studied by computer simulation, *Phys. Rev. B*, 1994, 50(19), 14498-14505.

140. A. R. Day, Catalytic Oxidation of Ethyl Alcohol, *J. Phys. Chem.*, 1931, 35(11), 3272-3279.

141. F. R. Lawdermilk, A. R. Day, A study of vapor phase oxidation of organic compounds using rare earth oxides as catalysts. I. methyl and ethyl alcohols, *J. Am. Chem. Soc.*, 1930, 52, 3535-3545.

142. D. Mantzavinos, Catalytic Wet Oxidation of p- Coumaric Acid: Partial Oxidation Intermediates Reaction Pathways and Catalyst Leaching, *Appl. Cata. B: Environ.*, 1996, 7, 379-396.

143. S. K. Agarwal, J. J. Spivey, J. B. Butt, Deep oxidation of hydrocarbons, *Appl. Catal. A: Gen.*, 1992, 81(1) 239-255.

144. Y.-F. Yu-Yao, J. T. Kummer, Low-concentration supported precious metal catalysts prepared by thermal transport, *J. Catal.*, 1987, 106(1), 307-312.

145. R. Dictor, S. Roberts, Influence of ceria on alumina-supported rhodium: observation of rhodium morphology made using FTIR spectroscopy, *J. Phys. Chem.*, 1989, 93(15), 5846-5850.

146. F. Le Normand, L. Hilaire, K. Kili, G. Krill, G. Maire, Oxidation state of cerium in cerium-based catalysts investigated by spectroscopic probes, *J. Phys. Chem.*, 1988, 92(9), 2561-2568.

147. H. C. Yao, Y.-F. Yu-Yao, Ceria in automotive exhaust catalysts: I. Oxygen storage, *J. Catal.*, 1984, 86(2), 254-265.

148. T. Jin, T. Okuhara, G. J. Mains, J. M. White, Temperature-programmed desorption of carbon monoxide and carbon dioxide from platinum/ceria: an important role for lattice oxygen in carbon monoxide oxidation, *J. Phys. Chem.*, 1987, 91(12), 3310-3315.

149. E. A. James, R. A. James, A. M. Jeffrey, O. T. John, Low Temperature Aqueous Catalytic Oxidation of Phenol, *Chemosphere*, 1997, 34(1), 203-212.

150. H. Rajesh, U.S. Ozkan, Complete oxidation of ethanol, acetaldehyde and ethanol/methanol mixtures over copper oxide and copper-chromium oxide catalysts, *Ind. Eng. Chem. Res.*, 1993, 32(8), 1622-1630.

151. F. Kapteijn, S. Stegenga, N. J. J. Dekker, J. W. Bijsterbosch, J. A. Moulijn, Alternatives to Noble Metal Catalysts for Automotive Exhaust Purification, *Catal. Today*, 1993, 16(2), 273-287.

152. V. N. Goetz, A. Sood, J. R. Kittrell, Catalyst Evaluation for the simultaneous Reduction of Sulfur Dioxide and Nitric Oxide by Carbon Monoxide, Ind. Eng. Chem. Prod. Res. Develop., 1974, 13(2), 110-114.

153. J. T. Kummer, Catalysts for automobile emission control, *Prog. Energy Combust. Sci.*, 1980, 6(2), 177-199.

154. J-dyakonov Alexander, Modification of Transition Metal Catalysts with Rare-

Earth Elements, *Appl. Cata. A: Gen.*, 2000, 192, 235-246.

155. F. Schuth, Oxide Loaded Ordered Mesoporous Oxides for Catalytic Applications, *Microporous and Mesoporous Materials*, 2001, 44/45, 465-476.

156. P. W. Park, J. S. Ledford, The influence of surface structure on the catalytic activity of cerium promoted copper oxide catalysts on alumina: oxidation of carbon monoxide and methane, *Catal. Lett.*, 1998, 50, 41-48.

157. W. Liu, A. F. Sarofim, M. Flytzani-Stephanopoulos, Reduction of sulfur dioxide by carbon monoxide to elemental sulfur over composite oxide catalysts, *Appl. Catal. B Environ.*, 1994, 4(2-3), 167-186.

158. W. Liu, M. Flytzani-Stephanopoulos, Total Oxidation of Carbon Monoxide and Methane over Transition Metal Fluorite Oxide Composite Catalysts: I Catalyst Composition and Activity, *J. Catal.*, 1995, 153(2), 304-316.

159. H. Stanko, Wet Oxidation of Phenol on $Ce_{1-x}Cu_xO_{2-y}$ Catalyst, *J. Catal.*, 1999, 184, 39-48.

160. A. N. Pestryakov, A. A. Davydov, The influence of modifying additions of La and Ce oxides on electronic state of surface atoms and ions of supported copper, *Appl. Surface Sci.*, 1996, 103, 479-483.

161. W. Liu, M. Flytzani-Stephanopoulos, Transition metal-promoted oxidation catalysis by fluorite oxides: A study of CO oxidation over Cu-CeO_2, *Chem. Eng. J.*, 1996, 64, 283-294.

162. M. Ferrandon, B. Ferrand, E. Bjornbom, F. Klingstedt, A. Kalantar Neyestanaki, H. Karhu, I. J. V ayrynen, Copper Oxide–Platinum/Alumina Catalysts for Volatile Organic Compound and Carbon Monoxide Oxidation: Synergetic Effect of Cerium and Lanthanum, *J. Catal.*, 2001, 202**,** 354-66.

163. S. J. Gregg, K. S. W. Sing, Adsorption, Surface Area and Porosity, Academic Press, London, 1982.

164. F. Arena., R. Giovenco, T. Torre, A. Venuto, A. Parmaliana, Activity and resistance to leaching of Cu-based catalysts in the wet oxidation of phenol, *Appl. Catal. B: Environ.*, 2003, 45, 51-62.

165. S. Imamura, M. Nakamura, N. Kawabata, J. Yoshida, S. Ishida, Wet oxidation of

poly (ethylene glycol) catalyzed by manganese-cerium composite oxide, *Ind. Eng. Chem. Prod. Res. Dev.*, 1986, 25(1), 34-37.

Chapter 2

Controllable Preparation and Structural Characterization of Nanosize ZnAl-LDHs

2.1 Introduction

Layered double hydroxides (LDHs) and their calcination products (CLDHs) find widespread applications in many fields, including industrial catalytic processes [1], pharmaceuticals [2], polymer reinforcement [3,4] and environmental clean-up by ion exchange [5] or adsorption processes [6,7]. The properties of the calcined materials are strongly linked to the chemical composition and morphology of their LDH precursors because their high surface area and porosity result mainly from the thermal decomposition of both interlayer anion and host structure, as well as the textural properties of the platelet-like crystallites of the LDH precursor. Because textural properties of solids are strongly influenced by the nature of the synthesis procedures, a wide range of synthetic routes for LDHs have been developed and are currently under investigation.

Although sol-gel processes [8], the urea method [9,10], the reconstruction method [11] or emulsion solution [12] techniques have been reported in the literature, the coprecipitation of inorganic salts at constant neutral or basic pH is still the most common method to synthesize LDHs [13-16]. In this method, LDHs are obtained in batch reactors, using the simultaneous dropwise addition at constant pH of aqueous solutions of an alkali and

mixed M^{II}/M^{III} salts containing the desired interlayer anion, if different from that in the metal salt precursor. The influence of varying the M^{II} and M^{III} salts, the M^{II}/M^{III} ratio and the interlayer anion on the crystallinity and morphological properties of the coprecipitated LDHs have been widely reported in the literature. A few studies have also investigated the effects of varying the thermal treatment [17-20] or solvent composition [21]. The first drawback of this approach is that supersaturation always remains low, except locally in the region of injection points, which does not favor the formation of nanometer-size platelets of LDHs. Additionally, precipitation conditions vary from the beginning to the end of the synthesis. Therefore, differences in crystallinity over time and broad crystallite size distributions are difficult to avoid. Up to now, aging constitutes the most common way to obtain more uniform particle properties. This is the reason why, if the addition procedure lasts a few hours, it is generally followed by a long aging period, from 10 to 80 h and often longer.

In this work, an alternative to the traditional technology has been developed. It consists of a continuous precipitation method under steady-state conditions. Such a technique is known to be the most satisfactory for the preparation of solid catalysts [22] because experimental parameters, such as residence time, pH, concentration and temperature can be simultaneously kept constant over time during the operation. As a result, the supersaturation level and consequently, the structural and textural properties of the solid phase in the exit stream of the reactor do not change with time, which should give constant and narrow LDH particle size distributions. As higher supersaturation levels can be achieved, this method should also lead to smaller particle

sizes and higher specific surface areas which should be advantageous in terms of enhanced catalytic activity. Additionally, continuous precipitation is easier to adapt for large-scale production. Its main drawback however is that it is more difficult to carry out on the laboratory scale than the standard coprecipitation method, as it requires simultaneous control of two inlet feed streams and the effluent.

The aim of this study is therefore to investigate a continuous coprecipitation technique under steady-state conditions and to determine whether it constitutes a viable alternative to the standard coprecipitation technique for the preparation of nanosized LDH particles. Using $Zn_2Al(OH)_6(CO_3)_{0.5}\cdot 2H_2O$ as a model, systematic experiments have been conducted in order to investigate the influence of operating conditions on LDH properties such as chemical composition, crystallinity, particle size and shape.

2.2 Controllable preparation under steady-state conditions

2.2.1 Experimental methods

Experiments have been carried out in a laboratory-scale “vortex” reactor under steady-state conditions (Fig. 2-1), at atmospheric pressure and room temperature (21 °C). The reactor consists of a cylindrical PVC tank without baffles, having a diameter of 64 mm and height of 73 mm and containing 230 ml of solution. Mixing was achieved using a magnetic stirrer that can be adequately replaced by a Rushton turbine placed in the bottom of larger tanks [23] for industrial-scale production. A constant rotation speed of 300 rpm was used for all experiments. The rotation of the mixer without baffles generates a “forced central vortex” of cylindrical-conical form, which is

confined by a liquid volume of annular form, denoted the “free-vortex region”. Such a hydrodynamic mixing avoids the formation of incrustations. Its main drawback is that mixing is not rapid and residence times lower than 5 min are difficult to achieve. The reactants consist of metal cation and alkali solutions that are supplied using two injection points located above the central zone. A pH electrode is placed in the free-vortex region for pH control during operation. Nucleation takes place essentially totally in the forced vortex region around the injection points where supersaturation is high, while the particles can undergo only growth, agglomeration and Ostwald ripening in the free-vortex region where supersaturation is lower. Feed flows are supplied by two variable-speed peristaltic pumps connected to a PC and the rates are controlled independently using the Labworldsoft 2.6 software (*Labworld-online Gmbh*, FRG). While pH and the flow rate of the cation solution are two operating parameters directly chosen by the operator, the flow rate of the alkali solution is adjusted automatically by the software so that the desired pH value is obtained. In this work, pH was maintained at either 7.0 ± 0.2, 9.0 ± 0.2 or 11.0 ± 0.2, while the flow rate of the cation solution was varied in order to achieve residence times between 5 and 15 min.

In the continuous coprecipitation technique, the effluent containing LDH particles, without any long-time aging, is collected continuously through the overflow pipe and stored in a tank, once steady-state conditions have been achieved in the reactor. Both the reactor and the storage tank are maintained in an inert nitrogen atmosphere during the operation in order to minimize the carbonation of the solutions due to the carbon dioxide from the atmosphere when anions other than carbonate are present in the

preparation medium. Solid LDH particles are then separated from the liquid effluent using centrifugation, washed with deionized water and air-dried before storage.

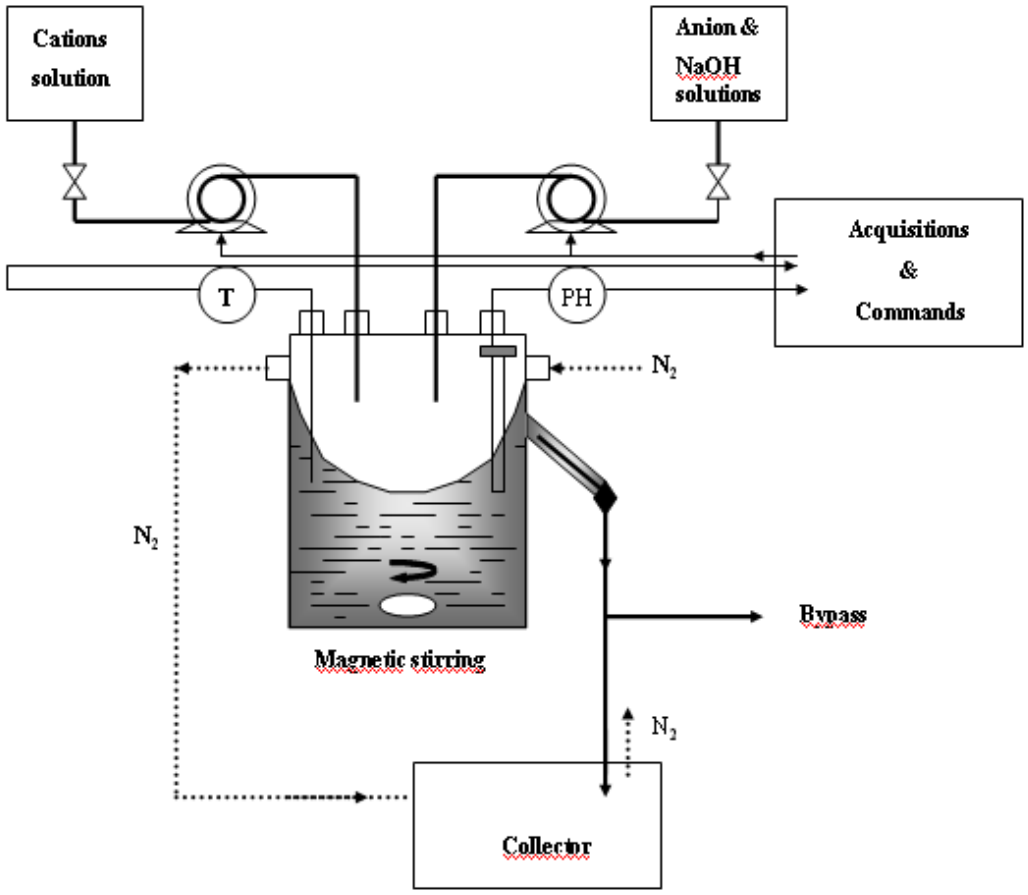

Fig. 2-1 Experimental setup for the continuous coprecipitation of LDH samples under steady-state conditions

2.2.2 Experimental conditions

All the reactants used in this work were purchased from Acros Organics France and used as supplied. For the preparation of the cation solutions, $ZnCl_2$ and $AlCl_3 \cdot 6H_2O$ were dissolved in either deionized water or mixed water-organic solvents including water-ethanol and water-monoethylene glycol (MEG) with different volume ratios from

1:4 to 4:1 for EtOH/H_2O and MEG/H_2O. An aqueous solution of polyethylene glycol (PEG) (40% w/v) was also used as a solvent. Total cation concentration, $[Zn^{2+}] + [Al^{3+}]$, was varied from 3.0 x 10^{-3} to 3.0 x 10^{-1} M with a constant $[Zn^{2+}]/[Al^{3+}]$ ratio equal to 2 in order to form the $Zn_2Al(OH)_6(A^{n-})_{1/n}\cdot mH_2O$ LDH. The alkali solution consists of NaOH and sodium salts of the different anions to be intercalated: carbonate, acetate or benzoate. The NaOH concentration was always equal to the total cation concentration. To favor the anion exchange reaction, intercalation anions were supplied in excess, using a 5:2 molar ratio for $[CO_3^{2-}]/[Al^{3+}]$ and 5:1 for the monovalent organic anions. A set of 28 experiments was carried out with CO_3^{2-} as the interlayer anion. These experiments have been described using a four-term label, as follows: the first term represents the solvent (e.g. “W” for water, “Et40” for a 40:60 EtOH-H_2O mixed solvent and EG80 for a 80:20 MEG-H_2O solvent, “PE40” for the 40% w/v polyethylene glycol aqueous solution), the second one represents the cation concentration (“1” = 3.0 x 10^{-1} M; “2” = 3.0 x 10^{-2} M; “3” = 3.0 x 10^{-3} M), the third one corresponds to the pH value and the last one represents residence time in minutes. For example, the EG80-2-9-5 run was conducted in an 80:20 MEG/H_2O mixture with a total cation concentration of 3 x 10^{-2} M at pH 9 with a residence time of 5 min. Additional experiments, the aim of which was to investigate the influence of varying the intercalation anions, summarized in Table 2-1.

For comparison purposes, a $Zn_2Al(OH)_6(CO_3)_{0.5}\cdot 2H_2O$ LDH was also prepared by the standard coprecipitation technique, using the slow addition of an alkali solution (1.0 M NaOH, 0.5 M Na_2CO_3) with a metal salt solution ($[Zn^{2+}]$ = 0.66 M, $[Al^{3+}]$ = 0.33 M)

at constant pH [13]. The addition was conducted at pH 9 and took nearly 24 hours. The precipitate was aged for 48 hours and recovered using a similar procedure to that described for the continuous coprecipitation technique.

Table 2-1 Additional experiments to investigate the influence of the interlayer anion on the continuous coprecipitation technique

Sample	H_2O (% v/v)	MEG (% v/v)	EtOH (% v/v)	Residence time (min)	pH	Total cation concentration (M)	Intercalation anion concentration
W-2-9-5-Be	100	0	0	5	9	3×10^{-2}	Benzoate (10^{-1} M)
W-2-9-15-Ac	100	0	0	15	9	3×10^{-2}	Acetate (5×10^{-2} M)
W-2-9-10-Ac	100	0	0	10	9	3×10^{-2}	Acetate (10^{-1} M)
EG40-2-9-5-Ac	60	40	0	5	9	3×10^{-2}	Acetate (5×10^{-2} M)
Et40-2-9-5-Ac	60	0	40	5	9	3×10^{-2}	Acetate (5×10^{-2} M)

2.2.3 Characterization techniques

Elemental analysis for C, H and Al, Zn were carried out at the Centre d'Analyses de Vernaison (CNRS, France). The powder X-ray diffraction (XRD) patterns were recorded on a Siemens D501 diffractometer with CuK_α radiation using a scanning rate of 1.2 °/min. The crystallite size of the synthesized LDHs was calculated from the line broadening of the reflections in the XRD patterns according to the Laue-Scherrer equation

$$D = K\lambda/[\Delta\varepsilon_{(2\theta)} \cos\theta] \quad (1)$$

where $\Delta\varepsilon_{(2\theta)}$ is the full width at half maximum, K = 0.94, is a proportionality factor

related to the (00*l*) reflection and D is the crystallite size. The (006) reflection has been used for the determination of the full width at half maximum and the corresponding crystallite size developed along the stacking direction is noted Ø006 in this work. The infrared transmission spectra were obtained on a Perkin-Elmer 2000 FT-IR spectrometer using the KBr technique. The nitrogen adsorption/desorption isotherms were measured on a QuantaChrome ABSORB-1 gas sorption analyzer from Micromeritics after outgassing the samples at 60 °C for 3 h. The pore size distribution was determined using the BJH model on the desorption branch. Scanning electron micrographs were taken on a Cambridge Stereoscanner electron microscope (SEM) at CASIMIR S.A. (France). For Transmission Electron Microscopy (TEM), a droplet of a sample resuspended in a limited volume of ethanol was layered on a Formvar-coated grid (400 Mesh) and air-dried. After deposition, the grids were examined using a Phillips CM 20 electron microscope running at 200 kV. Some samples were analyzed by energy dispersive X-ray spectroscopy (EDX) to check their chemical composition. Selected area electron diffraction (SAED) patterns were also recorded in order to analyze qualitatively the crystallite size and the crystallinity of the samples. Transmission electron micrographs were also used to estimate the average diameter (ØTEM) of the platelets.

2.3 Structural and textural characterization

The common characteristics of the solid phases obtained using the continuous coprecipitation technique will firstly be described and summarized. The objective is to show that most of the operating conditions used with the continuous coprecipitation

technique give rise to fine particles having the characteristic composition and structure of LDH phases. The effects of varying the operating conditions will be detailed, including the influence of total salt concentration, solvent, residence time, pH and intercalation anion. An attempt to explain theoretically the experimental results will be proposed. Finally, the properties of the resulting LDH compounds will be compared with those of a material obtained using the standard coprecipitation method.

2.3.1 Common characteristics

2.3.1.1 Elemental analysis

ICP elemental analysis shows that all the solid phases synthesized using the continuous coprecipitation technique contain no residual Cl^- anions from the metallic salts and that they have a Zn^{2+}/Al^{3+} molar ratio close to 2, which is consistent with the ideal LDH formula $Zn_2Al(OH)_6(A^{n-})_{1/n}\cdot mH_2O$ (A = carbonate, acetate or benzoate). Table 2-2 illustrates this for some typical samples with carbonate as the interlayer anion. It is however noteworthy that, for all of the samples, the C/Al molar ratio is higher than the expected value, 0.5. This excess of carbon is not caused by intercalation of organic anions coming from the preparation medium because both FTIR and XRD measurements indicated that they did not intercalate (Figures 2-3 and 2-5). One possibility may be residual organic solvent or CO_3^{2-} ions adsorbed on external surfaces of the LDHs. EDX microanalysis measurements performed on five points for each sample show small disparities in the values of Zn^{2+}/Al^{3+} molar ratio, but on the whole, they are in good agreement with those obtained by ICP for all the experiments.

Table 2-2 Compositional analysis, crystallite size estimations using TEM and XRD patterns and surface areas based on nitrogen adsorption of some samples prepared using the continuous coprecipitation technique

Sample	Zn/Al molar ratio (ICP)	C/Al molar ratio (ICP)	Ø006 (nm)	Ø TEM (nm)	Spec. surface area (m^2/g)
W-2-9-5	1.94	0.62	45.5	130	21.7
W-2-9-15	1.93	0.78	53.5	160	38.7
W-3-9-5	2.03	0.79	43.9	170	29.8
W-3-9-15	2.00	0.71	56.2	200	16.7
EG40-2-9-15	2.09	1.18	57.1	100	61.9
EG80-2-9-15	1.91	0.78	31.1	80	51.6
EG80-3-9-5	1.93	0.64	21.4	95	18.1
EG80-3-9-15	1.93	0.66	31.5	110	23.6
PE40-2-9-15	1.96	0.97	26.5	65	59.7

2.3.1.2 TEM analysis

Transmission electron micrographs confirm that most samples clearly exhibit the characteristic LDH platelet structure with a uniform size (ØTEM), from 80 to 200 nm, and an ill-defined shape (Fig. 2-2). This is also consistent with the XRD patterns that exhibit the characteristic peaks of crystalline Zn/Al-CO_3-LDH phases. These patterns have been indexed using a hexagonal cell with rhombohedral symmetry (R-3m) where the *a* parameter represents the average intermetallic distance calculated from the position of the (110) reflection and the *c* parameter corresponds to 3 times the basal spacing (003). Similarly, the selected area electron diffraction (SAED) patterns display ring-patterns which match well with the hexagonal structure of polycrystalline LDHs (Fig. 2-2), even if in comparison, only a few of the theoretical interplanar distances can

be found in the electron diffraction patterns. From ØTEM (measured from TEM micrographs) and Ø006 (Table 2-2) calculated from the Laue-Scherrer law, it is clear that the operating conditions, such as solvent nature, total cation concentration and residence time affect LDH properties.

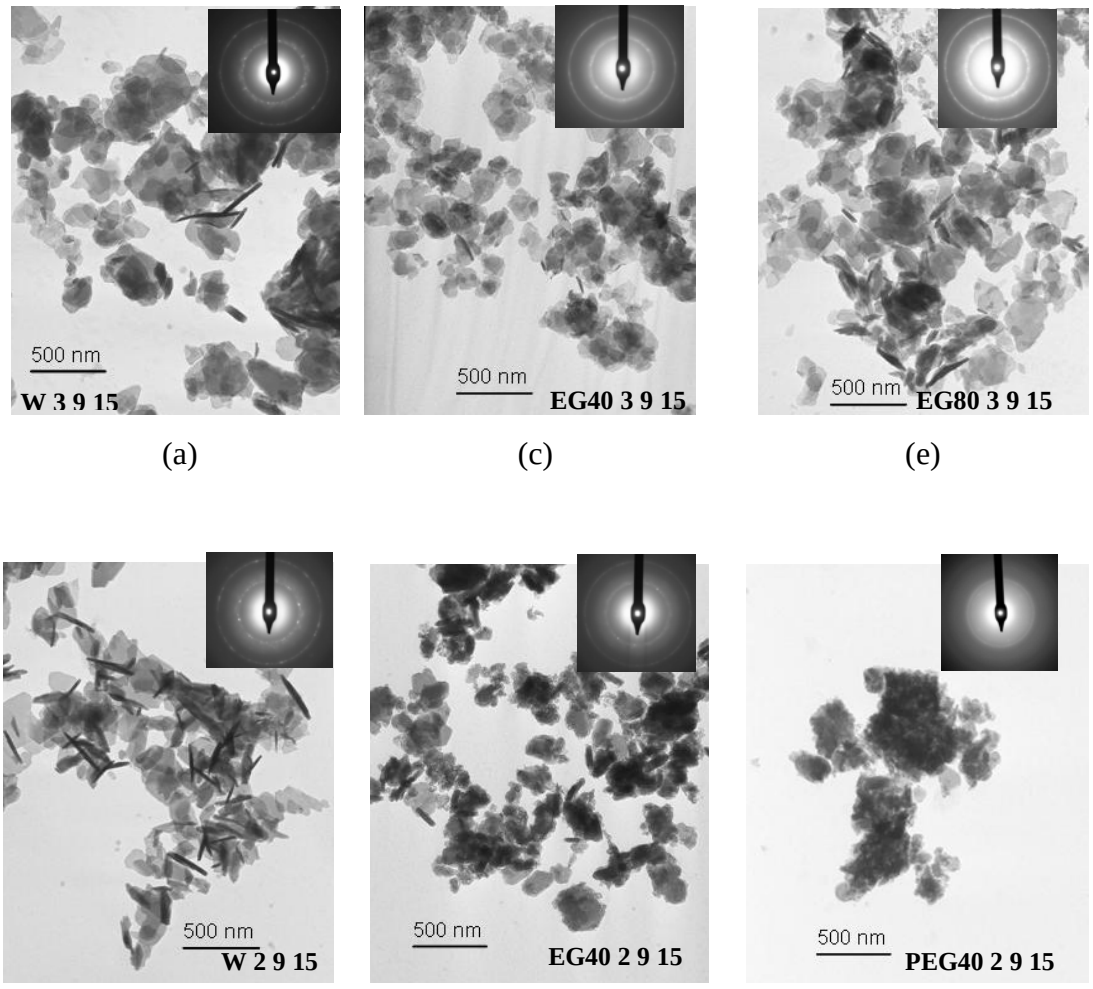

Fig. 2-2 TEM micrographs of LDH samples prepared at different cation concentrations in different solvents: (a) W-3-9-15, (b) W-2-9-15, (c) EG-40-3-9-15, (d) EG40-2-9-15, (e) EG80-3-9-15, (f) PEG40-2-9-15. The insets are the corresponding SAED patterns.

2.3.1.3 FT-IR spectroscopy

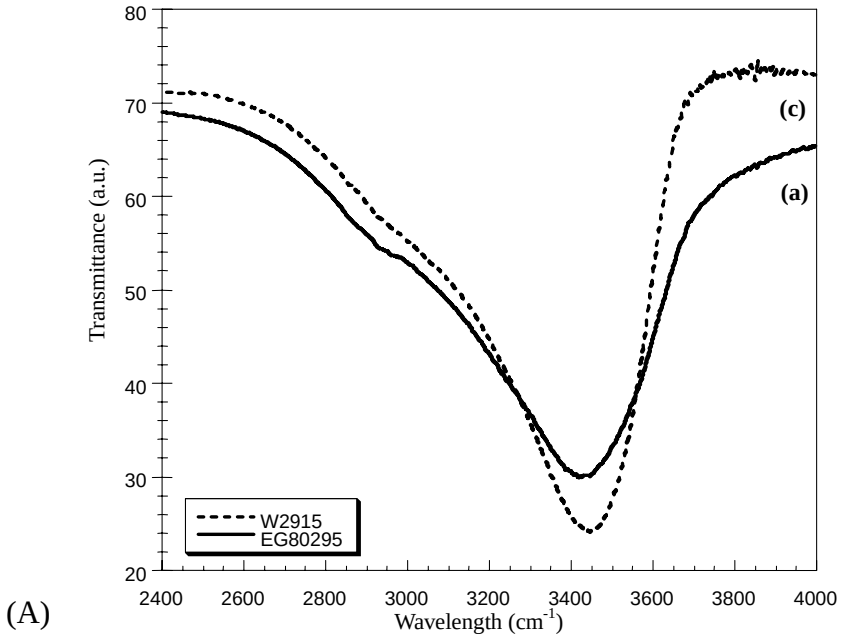

(A)

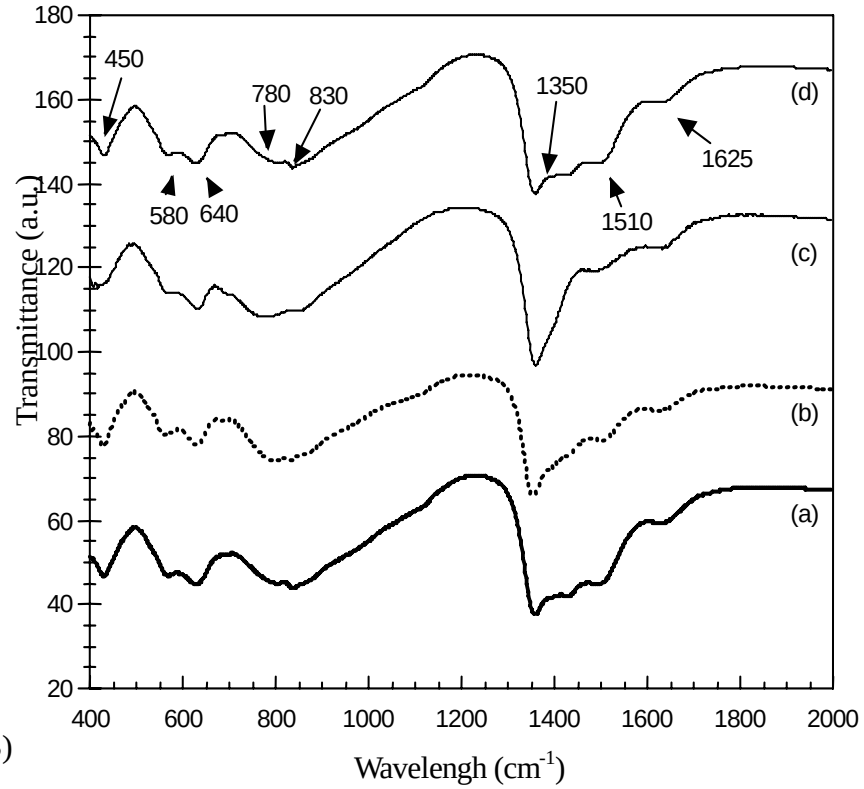

(B)

Fig. 2-3 FT-IR spectra of LDH samples, at higher (A) and lower (B) wavenumbers: (a) EG80-2-9-15, (b) EG40-2-9-15, (c) W-2-9-15, (d) PE40-2-9-15

Fig. 2-3 shows a series of FT-IR spectra of LDH compounds prepared under different conditions. The bands in the range 400 - 900 cm^{-1} provide evidence that the characteristic LDH network has been formed. The absorption band at 450 cm^{-1} is due to the O-M-O deformation mode, while those at 580 and 780 cm^{-1} correspond to M-O stretching vibrations [24,25]. The strong band observed at 1350 cm^{-1} can be assigned to the υ_3 vibration of the interlayer carbonate anions [25,26]. The band at 1625 cm^{-1} corresponds to the H-O-H deformation mode of intercalated water molecules and the weaker band at 640 cm^{-1} to the bending vibration mode of hydroxyl groups. It is noteworthy that for some samples, extra bands are observed around 1510 cm^{-1}, which can be ascribed to adsorbed CO_3^{2-} species. Conversely, there are no absorption bands of residual or intercalated organic solvent such as EtOH, MEG or PEG (Fig. 2-3 (A)), suggesting that the solvents can be removed easily by the washing procedure employed. These results suggest that the high values of C/Al molar ratio reported in Table 2-2 are due mainly to CO_2 adsorption on the basic surface sites of the LDH during air-drying or final storage.

2.3.1.4 BET analysis

In a preliminary study of the textural properties of the LDH materials the specific surface area of the samples as measured by BET was found to never exceed 62 m^2/g, although much higher values would be expected in view of the very low particle sizes. This is due to the sample pretreatment process used in BET analysis (degassing for 3 h at 60 °C). Indeed, in order not to further modify the textural properties of the samples

we decided to use such relatively mild conditions which may explain why the surface areas of our LDHs are substantially lower than those observed for most LDH materials.

2.3.2 Effect of varying experimental conditions

2.3.2.1 Effect of varying total salt concentration

Fig. 2-4 presents the powder X-ray diffraction patterns of samples prepared in water with total salt concentrations of 3.0×10^{-1}, 3.0×10^{-2} and 3.0×10^{-3} M. For W-1-9-10, it is worthy of note that the solid is rather amorphous and that it does not correspond to a pure LDH phase, as additional peaks can be observed. Further analysis suggests that it is composed of a mixture of LDH phases and zinc and aluminum hydroxides. This is also confirmed by IR spectra. Conversely, for lower total cation concentrations, LDH phases can be clearly identified by their XRD patterns. These display very little difference between 3.0×10^{-3} M (W-3-9-15) and 3.0×10^{-2} M (W-2-9-15), which shows that the particles have nearly the same size. This is in agreement with Ø006 values for W-2-9-5, W-3-9-5, W-2-9-15, and W-3-9-15 in Table 2-2. Furthermore, the salt concentration effect on particle shape and size is illustrated in Fig. 2-2 for LDHs obtained in pure water for 3.0×10^{-2} M (W-2-9-15) and 3×10^{-3} M (W-3-9-15), respectively. Transmission electron micrographs and SAED patterns confirm that the particle size decreases with increasing concentration, although this effect remains slight in pure water. However, this trend appears more clearly in MEG/H_2O mixed solvents. Only 3.0×10^{-2} and 3.0×10^{-3} M salt concentrations have been studied in this case because of the relatively low solubility of metallic salts in the water-organic solvent mixtures. XRD patterns are qualitatively similar to those observed

in pure water for the same salt concentrations. SAED patterns (EG40-3-9-15 and EG40-2-9-15 in Fig. 2-2) and ØTEM and Ø006 values (EG80-3-9-15 and EG80-2-9-15 in Table 2-2) confirm that particle size and crystallinity both decrease when the salt concentration is increased. This effect seems more pronounced in MEG/H_2O solutions, as is clearly shown by the variation of specific surface area with salt concentration given in Table 2-2. Specific surface areas are indeed always higher for a salt concentration of 3.0 x 10^{-2} M than for 3.0 x 10^{-3} M in MEG/H_2O mixtures and they are approximately halved when the salt concentration is reduced by a factor of 10.

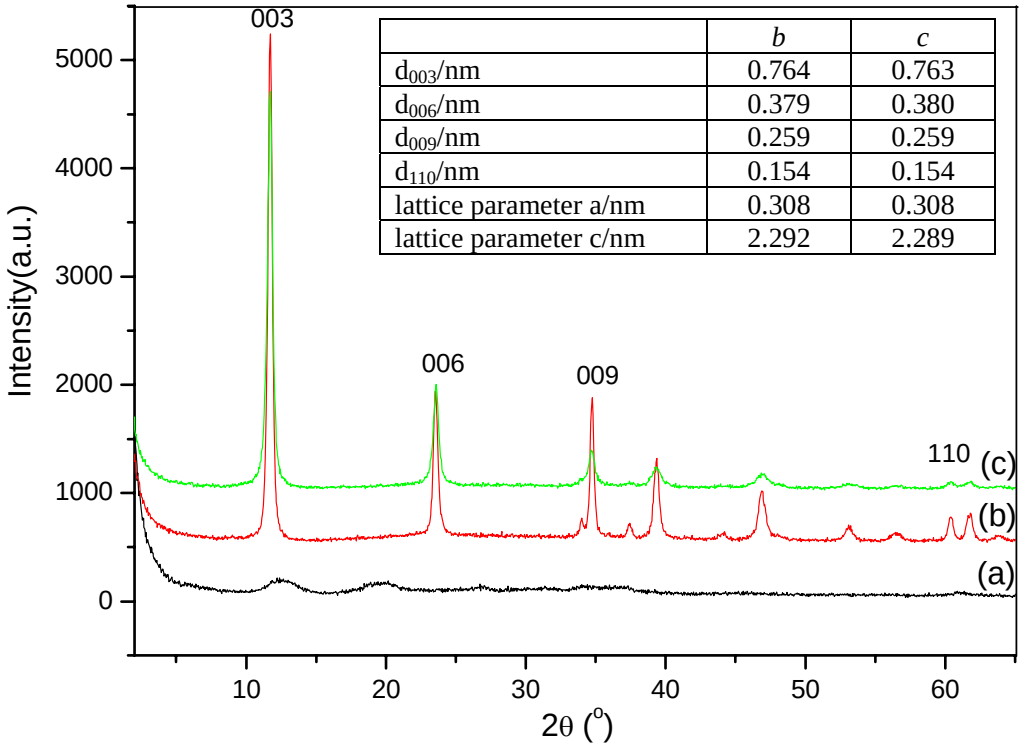

	b	*c*
d_{003}/nm	0.764	0.763
d_{006}/nm	0.379	0.380
d_{009}/nm	0.259	0.259
d_{110}/nm	0.154	0.154
lattice parameter a/nm	0.308	0.308
lattice parameter c/nm	2.292	2.289

Fig. 2-4 XRD patterns of samples prepared at different cation concentrations: (a) W-1-9-10, (b) W-2-9-15, (c) W-3-9-15

2.3.2.2 Effect of varying solvent

Solvent effect is obvious through comparison of data for W-2-9-15, EG40-2-9-15 and PEG40-2-9-15 in Fig. 2-2. The TEM micrographs show clearly that samples with small crystallite sizes are more easily prepared in water-organic solvent mixtures and especially in PEG solution. This trend is confirmed by SAED patterns. For samples prepared in water, diffraction rings are discontinuous and consist of rather sharp spots, which indicates that the particles are relatively well crystallized. Conversely, for samples prepared in the PEG solution (PE40-2-9-15), the SAED pattern consists of broad diffuse rings, typical of very small particles.

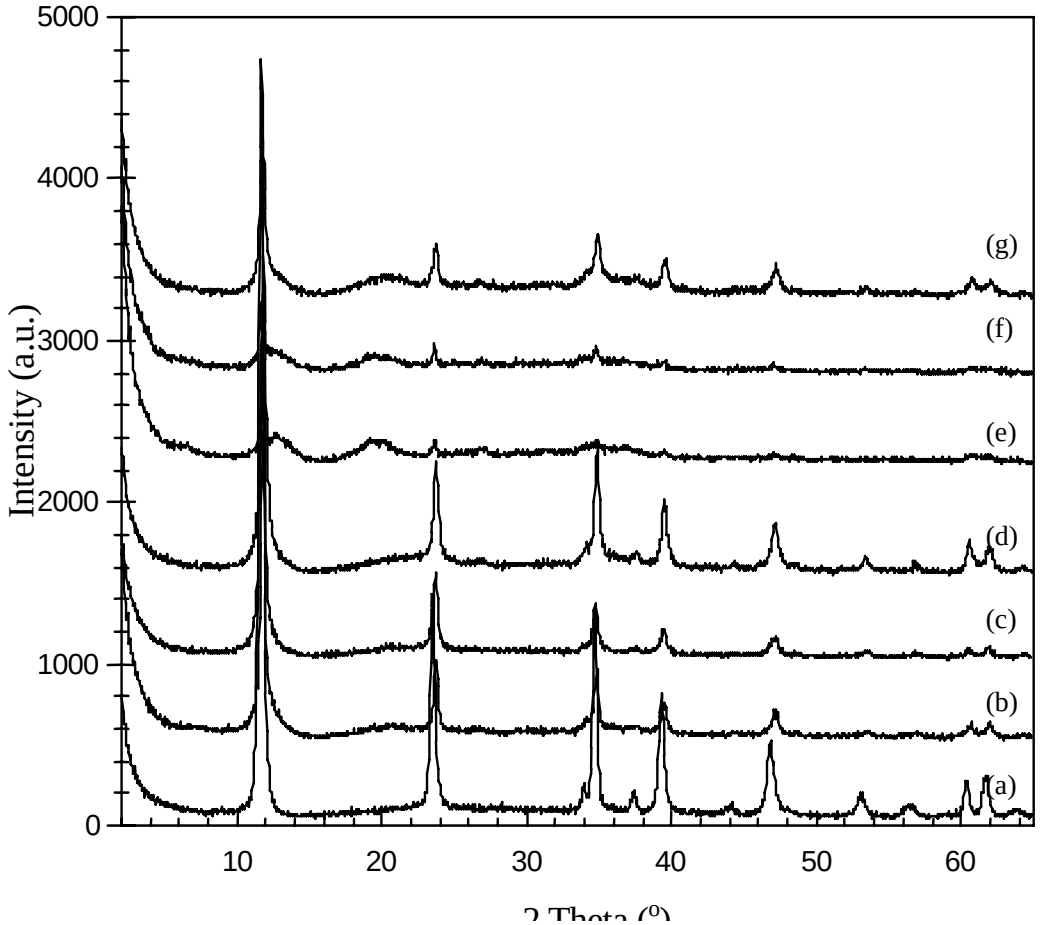

Fig. 2-5 XRD patterns of samples obtained in different solvents: (a) W-2-9-15, (b) EG40-2-9-15, (c) EG60-2-9-15, (d) EG80-2-9-15, (e) Et40-2-9-15, (f) Et60-2-9-15, (g) PE40-2-9-15

The effect of preparation medium can also be observed from the XRD patterns in Fig. 2-5, illustrating the role of the solvent by a comparison between pure water, EtOH/H_2O, MEG/H_2O mixed solvents and PEG aqueous solution. All the syntheses conducted in EtOH/H_2O mixtures produced amorphous samples when the salt concentration was 3.0 x 10^{-2} M, except in the presence of acetate anions. This particular result will be commented on later. The solid phases obtained in EtOH/H_2O mixtures show the same XRD patterns as those obtained for W-1-9-10 (Fig. 2-4), and correspond to a mixture of the ZnAl-CO_3 LDH with zinc and aluminum hydroxides. For PE40-2-9-15, one must mention that slight quantities of such impurities can be seen in the XRD patterns, although the LDH phase is predominant (Fig. 2-5). TEM micrographs confirm that particles obtained in PEG solutions have the platelet structure of LDH phases (Fig. 2-2).

In comparison to pure water, ØTEM (Table 2-2) shows a slight decrease in crystallite size in a 40:60 MEG/H_2O solvent, while ØTEM and Ø006 (Table 2-2) confirm that this decrease is more significant in the 80:20 MEG/H_2O solvent mixture. The TEM micrographs for LDHs obtained in pure water, 40:60 MEG/H_2O and 80:20 MEG/H_2O as solvents illustrate the influence of the preparation medium on the shape and level of agglomeration of the particles (Fig. 2-2). It is noteworthy that in 80:20 MEG/H_2O mixtures, the particles are more uniform, regular and easier to disperse in comparison with those obtained in the 40:60 MEG/H_2O solution and pure water. It appears that precipitation conditions with one of the solvents as the major phase (80%

or 100%) favors a higher homogeneity of particle size and a better crystallization than when a highly heterogeneous medium is used (40/60 for instance) (see Fig. 2-5 (a), (b), (c) and (d)). The samples prepared in the PEG solution and in the 80:20 MEG/H_2O have the smallest particle size according to Ø006. However, the SAED pattern of PE40-2-9-15, consisting of broader diffuse rings (Fig. 2-2), and its ØTEM value tend to suggest that the experimental conditions for PE40-2-9-15 give the smallest particle sizes (Table 2-2).

The changes in crystallinity and pore structure have also been confirmed using nitrogen adsorption measurements. In Table 2-2, a series of specific surface area values is reported. It shows an increase in specific surface area of the samples from 20 - 40 m^2/g in the case of pure water as solvent to 50 - 60 m^2/g in MEG/H_2O mixtures and PEG aqueous solutions. This variation is clearly related to the changes in crystallinity and particle size distribution that affect the pore structure of the samples. BET adsorption and pore size distribution curves of EG80-2-9-15 and PE40-2-9-15 show that pore distribution is narrower and the average pore diameter is centered around 30 - 40 Å for PE40-2-9-15, while there is a bimodal pore size distribution for EG80-2-9-15. This result is in accordance with the fact that more uniform and more amorphous materials are obtained in PEG aqueous solutions.

2.3.2.3 Effect of varying residence time

Two typical residence times have been systematically tested, 5 min and 15 min, while other values, such as 10 min, have been studied for a few samples in order to check the evolution of LDH properties as a function of residence time. Both the platelet

size and the coherence of the platelet organization increase gradually with residence time in water. Fig. 2-2 confirms the evolution of platelet size with residence time, both in deionized water and MEG/H_2O mixtures, which is also shown by the values of Ø006 and ØTEM in Table 2-2. These data clearly show that the effect of varying residence time is more pronounced in MEG/H_2O solvents than in pure water. Decreasing the residence time and increasing the amount of organic component in the mixed solvents also have a similar effect on crystallinity. Rather amorphous particles are observed for EG80-3-9-5, while crystallinity increases both with residence time and water fraction in the solvent. However, it is obvious that the effect of residence time is quantitatively less significant than that of solvent or salt concentration. This is shown, for example, by the slight variation of the specific surface area in Table 2-2 with residence time.

2.3.2.4 Effect of varying pH

XRD patterns of samples prepared at different pH values are shown in Fig. 2-6. They show that LDH phases are not obtained at pH 7.0, while similar results are observed at pH 9.0 and 11.0 when total cation concentration is 3.0×10^{-2} M. It should be noted that Zn_2Al-CO_3 LDHs particles are readily prepared using standard coprecipitation methods at pH values as low as 7.0. But in such conditions, long aging periods are generally used and thermodynamically stable solids are then obtained. In steady-state conditions, with short contact times such as 5 to 15 min, we must presume that the kinetic product is first prepared at pH 7.0 and is not allowed to transform to an LDH. Compositional analysis, FT-IR spectra and XRD patterns confirm that W-2-11-10 and W-2-9-15 have nearly the same characteristics, for example Ø006 values around 55

nm. The only difference between them is apparent from Fig. 2-6 where the presence of less organized platelets in the SEM micrographs for W-2-11-10 probably denotes more rapid kinetics when the pH is 11.0.

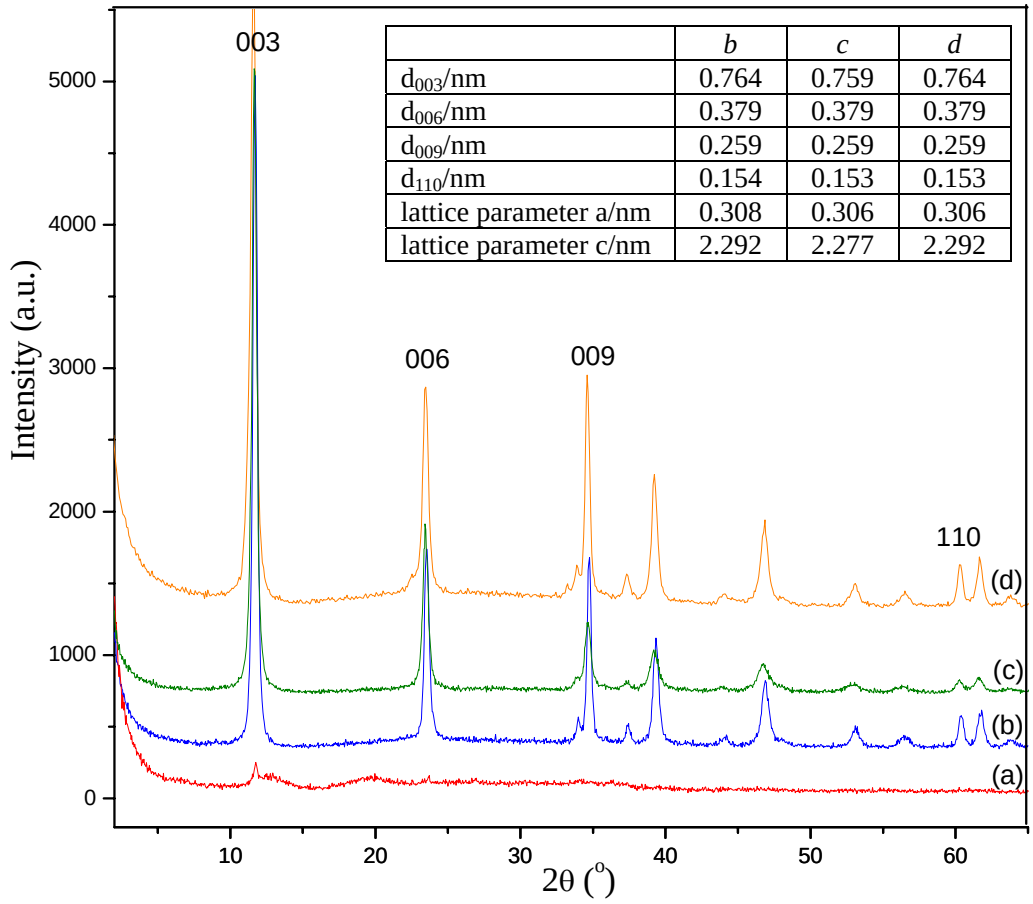

	b	*c*	*d*
d_{003}/nm	0.764	0.759	0.764
d_{006}/nm	0.379	0.379	0.379
d_{009}/nm	0.259	0.259	0.259
d_{110}/nm	0.154	0.153	0.153
lattice parameter a/nm	0.308	0.306	0.306
lattice parameter c/nm	2.292	2.277	2.292

Fig. 2-6 XRD patterns of LDH samples prepared at different pH values: (a) W-2-7-10, (b) W-2-9-15, (c) W-2-11-10, (d) standard method (pH 9)

2.3.2.5 Effect of varying the anions present in preparation medium

Some additional experiments were carried out using acetate or benzoate in place of carbonate. XRD data and FTIR spectra have confirmed that the organic anions are intercalated in the resulting LDH phases as reported in Table 2-1. The organic anions

appear to give smaller crystallites in pure water than carbonate-based LDHs, as Ø006 is around 27 nm for W-2-9-5-Be and 23 nm for W-2-9-10-Ac, while Ø006 is 45 nm and 53 nm for W-2-9-5 and W-2-9-15, respectively (Table 2-2). A similar result has been obtained in 40:60 MEG/H_2O mixtures for which Ø006 decreases from 57 nm in EG40-2-9-15 to 28 nm in EG40-2-9-5-Ac. Although any attempt to prepare LDH phases in EtOH/H_2O mixtures using a 3.0 x 10^{-2} M total salt concentration was unsuccessful, unexpectedly only the presence of acetate anions in conditions similar to those for carbonate anions seems to permit the precipitation of LDH phases (sample Et40-2-9-5-Ac). This confirms that the anion plays an active role in the mechanism of LDH formation.

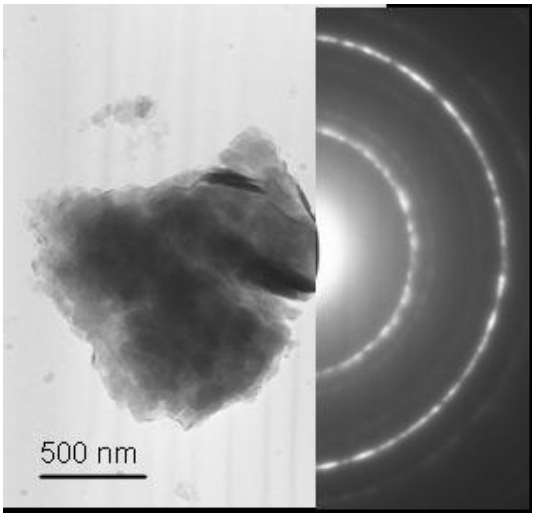

Fig. 2-7 TEM micrograph and SAED pattern of LDH sample EG40-2-9-5-Ac prepared in the presence of acetate anions

Moreover, acetate addition to 40:60 MEG/H_2O mixtures gives rise to the formation of LDH particles with a much more pronounced agglomeration level and a

higher degree of crystallinity (Fig. 2-7). Similar trends have been observed in the SEM micrographs, especially for EG40-2-9-5-Ac and Et40-2-9-5-Ac. As a result, it can be concluded that the acetate and benzoate anions favor the synthesis of smaller crystallites, but form bigger particles due to the large amount of agglomeration and present finally a higher degree of crystallinity than carbonate-based LDHs.

2.4 Thermal behaviors of the materials prepared under steady-state conditions

2.4.1 *In situ* variable temperature XRD analysis

Fig. 2-8 shows *in situ* HT-XRD patterns in the range from room temperature to 1000 ^{o}C of samples obtained in different solvents. Sample EG40-2-9-15 and PEG40-2-9-15 were prepared using 40:60 EG/H_2O and 40:60 PEG/H_2O mixtures as solvents, respectively. They show similar changes in structure and interlayer spacing. With increasing temperature up to 150 ^{o}C, the position of the **(**003**)** reflection shifts to higher angle indicating a decrease in interlayer spacing, associated with the elimination of physisorbed and interlayer water and loss of hydrogen bonding without collapse of the layered structure. At higher temperatures in the range 150-550 °C, the (003) reflection disappears and amorphous phases appear, indicative of dehydroxylation of the layers as well as decomposition of the interlayer carbonate anions. Above 550 °C, the characteristic peaks of mixed metal oxides are apparent and at around 800 °C a mixture of spinel $ZnAl_2O_4$ and ZnO phases evolves [27].

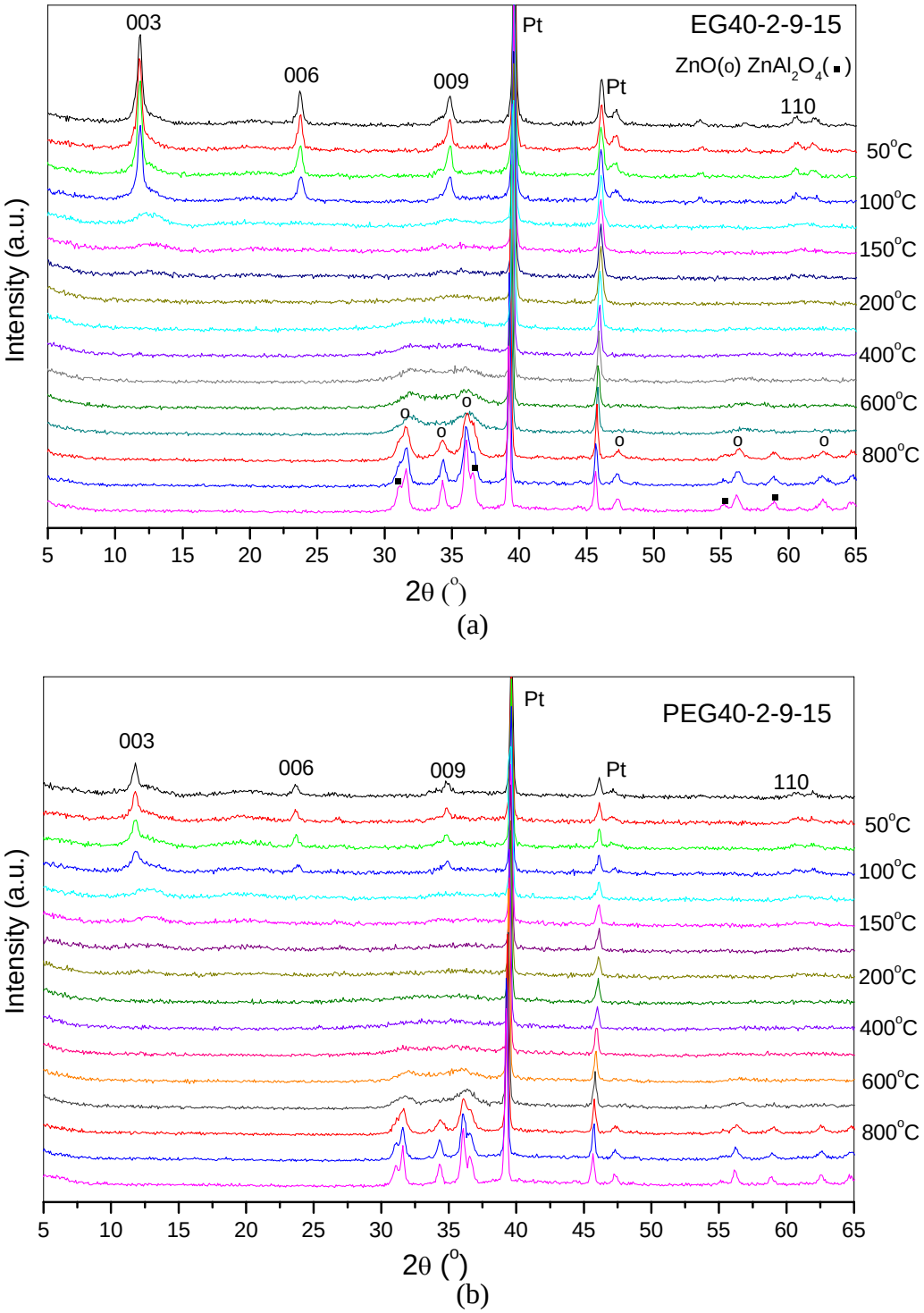

Fig. 2-8 *In situ* HT - XRD patterns of samples obtained in different solvents: (a) EG40-2-9-15, (b) PEG40-2-9-15

At room temperature, the intensities of the (00*l*) characteristic reflections of sample PEG40-2-9-15 are weaker than those of sample EG40-2-9-15. The poor crystallinity of sample PEG40-2-9-15 indicates that the PEG solvent gives rise to materials with small particle size. However, the two samples display the similar reflection intensities when they are calcined at higher temperature, which suggests that these mixed metal oxide phases have similar particle size and textural character under these conditions. This demonstrates that at higher temperatures the pore structure was eliminated completely by sintering, and LDH precursors with poor crystallinity and small particle size also generate crystalline $ZnAl_2O_4$ spinel phases which are similar to those obtained from other better crystalline LDH precursors. Therefore, the surface area and porosity of mixed metal oxides could be controlled by using the textural character of LDH precursors only calcined in the range 150-550 °C [28].

2.4.2 TG analysis

All of samples prepared under steady-state conditions have similar TG profiles, as illustrated for W-2-9-15 in Fig. 2-9(a), though they were synthesized under different experimental conditions. This suggests they have almost identical stoichiometries. As for LDHs prepared by conventional routes [28-30], in each case the weight loss occurs in three steps. The first one, up to *ca.* 200 ^{o}C, is a result of removal of water physisorbed on the external surface of the crystallites as well as water intercalated in the interlayers, corresponding to *ca.* 26% of the total weight of the sample. The second weight loss, corresponding to *ca.* 18 % of the total sample weight, was complete at *ca.* 400 ^{o}C, and can be attributed to dehydroxylation of the layers as well as elimination of CO_2 arising

from decomposition of the interlayer CO_3^{2-} ions. The less weight loss above 400 °C amounted to only *ca.* 6% of the total sample weight, and is usually ascribed to the removal of strongly held hydroxyl and CO_3^{2-} groups [31-33]. The results are consistent with these obtained by *In situ* HT - XRD.

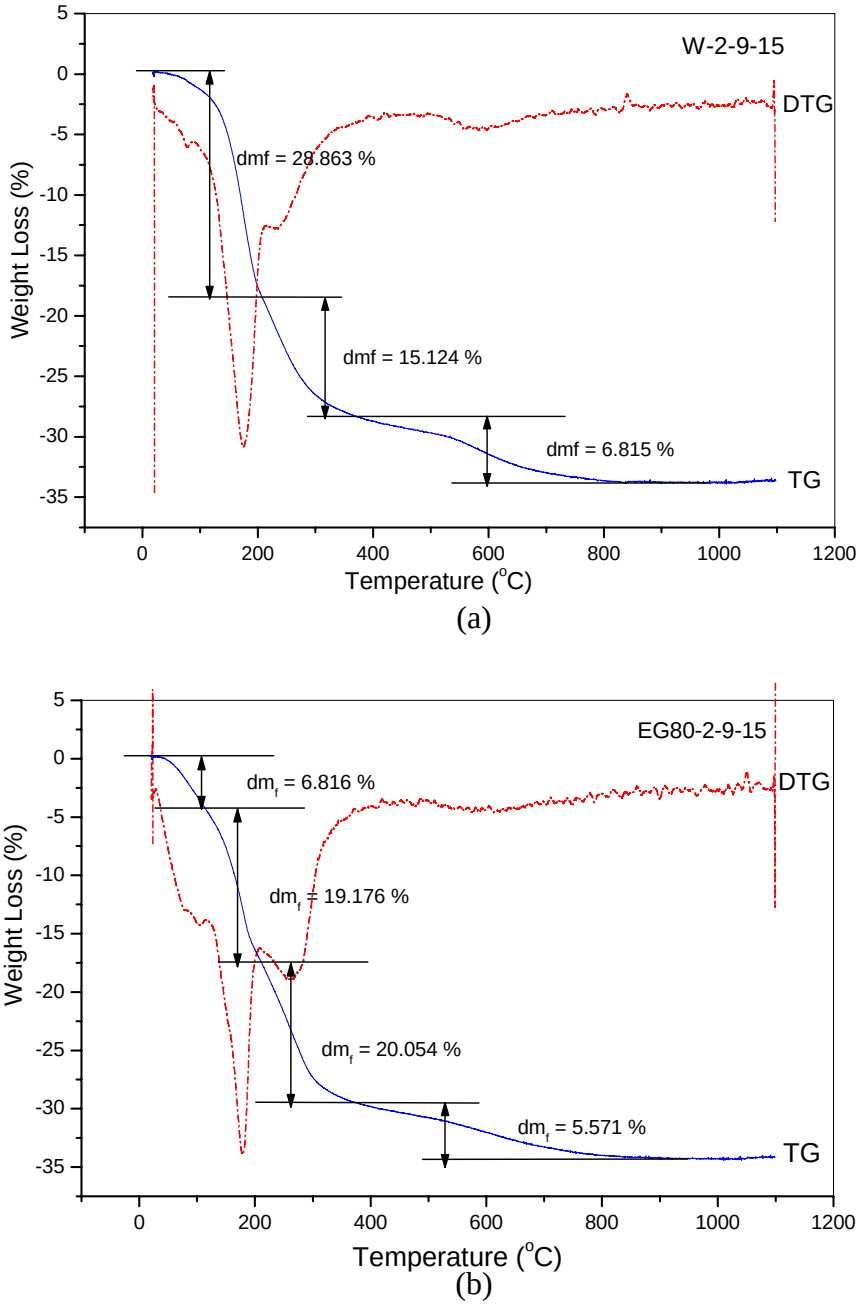

Fig. 2-9 TG curves of samples obtained in different solvents: (a) W-2-9-15, (b) EG80-2-9-15

There are only slight differences between the TG profiles for W-2-9-15 (Fig. 2-9(a)) and EG80-2-9-15 (Fig. 2-9(b)), essentially corresponding to the smaller particle size of the latter sample. The peaks recorded at 100 - 200 ^{o}C in the DTG curve (b), related to the loss of two kinds of water molecules, more clearly consist of two peaks. This may indicate an increase in the amount of physisorbed water molecules as a consequence of a decrease in the crystallinity of LDH sample. In addition, the peak intensity in the DTG curve (b) in the range 200 - 400 ^{o}C corresponding to the second weight loss, is higher due mainly to more CO_2 adsorption on these basic surface sites of EG80-2-9-15 with a bigger specific surface area during air-drying or final storage. This is in agreement with the results from ICP and FT-IR spectroscopy.

2.5 Discussion and comparison with the standard preparation method

2.5.1 Theoretical analysis of the new preparation method

Supersaturation constitutes the thermodynamic driving force for all precipitation and crystallization processes. It is usually defined as the difference ("absolute supersaturation") or the ratio ("supersaturation ratio") between the concentration and the solubility of a chemical compound. Using the reaction quotient (Q_R) concept [34], the classical expression of the chemical potential (μ) as a function of molar fractions x_i and activity coefficients γ_i can be written as follows:

$$\mu = \mu_0 + RT \cdot \sum_i \log x_i \gamma_i = \mu_0 + RT \cdot \log Q_R = RT \cdot \log Q_R / K_S$$

where K_S is the solubility constant. By introducing the supersaturation ratio (S), one

obtains therefore:

$$S = Q_R / K_S \quad \text{and} \quad \mu = RT \cdot \log S$$

In the classical coprecipitation technique, the dropwise addition of the alkaline solution is used to achieve $Q_R > K_S$ ($S > 1$), but the cation consumption decreases in the vessel during precipitation, which correspond to a decrease in S and Q_R over time. As a result, Q_R tends to K_S during precipitation and the properties of crystals formed by chemical reaction may change over time. Conversely, in steady-state method, the simultaneous addition of the cation and the alkali solutions ensures a better control on supersaturation level: the supersaturation ratio is constant over time and S can be adjusted precisely using the flow rates of the reactant feeds. In both cases, supersaturation governs the kinetics of crystallite nucleation and growth, but it may also affect the mechanisms of nucleation and growth. While these mechanisms have been widely described in the literature for simple precipitation processes, the more complex field of coprecipitation remains relatively unexplored, although one can assume that the general rules of simple precipitation can be applied. The quantification of these phenomena for coprecipitation remains a problem to be tackled in the future however. As a rule of thumb, one can assume [35-37] that nucleation rate, r_N, is related to supersaturation, S, as follows:

$$r_N = A \exp[-B/(\log S)^2] \qquad (2)$$

while the growth rate G, is expressed as

$$G = C.S^n \qquad (3)$$

where A, B, C are constant parameters and $1 < n < 2$ when $S > 1$. From these equations,

it can be concluded that low supersaturation favors growth and Ostwald ripening, thus leading to large crystallites and rather well-crystallized compounds, whereas high supersaturation favors nucleation and agglomeration, producing small crystallites and more amorphous materials [38,39]. This explains and justifies the influence of varying the solvent and the total salt concentration described above for a fixed Zn^{2+}/Al^{3+} ratio. Supersaturation increases with total salt concentration, which corresponds to smaller crystallites exhibiting a more pronounced level of agglomeration and larger specific surface areas. Similarly, supersaturation increases in water-organic mixed solvents due to the lower solubility of metallic salts in such mixtures, which also leads to similar effects on crystallite size and crystallinity. This trend is however limited to a total salt concentration of 3.0×10^{-1} M in pure water, as the precipitation of aluminum and zinc hydroxides begins to compete with that of LDH compounds. This is confirmed in $EtOH/H_2O$ mixtures at a lower salt concentration, 3.0×10^{-2} M, probably corresponding to a similar supersaturation level. While precipitation of LDH phases is difficult in $EtOH/H_2O$ mixtures, it is easy in MEG/H_2O mixed solvents and, to a lesser extent, in PEG aqueous solutions, which indicates that the effect of solvent is not limited to a change in supersaturation. Increasing MEG content induces an increase in viscosity and in PEG solutions it is even higher. Viscosity affects mixing, which acts on the local supersaturation and seems to favor the precipitation of compounds requiring a lower supersaturation level (i.e. the LDH phase) as long as mixing is sufficiently good. Additionally, viscosity is known to have a strongly negative effect on growth rate, as it decreases ion diffusivity near the surface of already formed crystallites. This explains

why residence time has a greater impact in viscous solvents. As nucleation seems to be rapid, residence time affects only particle size by controlling growth, especially in the free vortex zone where supersaturation is low. In pure water, growth is so rapid that the differences in crystallite size remains small when the residence time increases from 5 and 15 minutes, which is not the case in viscous media, such as 80:20 MEG/H_2O and PEG solutions. If chloride is exchanged easily by carbonate, acetate or benzoate anions, the influence of the intercalation anion is probably the most difficult to interpret. Acetate anions have been found to favor LDH phases over simple hydroxides in EtOH/H_2O mixtures. This could be due to the complexing properties of acetate, which may interact with the metallic cations in solution since this in accordance with the high degree of agglomeration observed in this case. It is also clear that the intercalation reaction cannot be considered independently from the formation of the pillared LDH structure in the continuous coprecipitation technique. This is a very important point that highlights another difference between the conventional and our novel LDH synthesis technique. In the former case, the interlayer anion is usually added along with the alkali solution, and as a result its concentration changes with time in the reactor and the kinetics of the LDH formation and intercalation reaction may differ. For example, the Zn/Al-Cl-LDH could be formed in the initial period when there is a large excess of chloride in solution and transform gradually into the Zn/Al-CO_3-LDH when the amount of CO_3^{2-} in the reactor is sufficiently high. This is not the case in the continuous technique for which the ratio between the anion of the metallic salts (here, Cl^-) and the intercalation anion is constant over time. So, LDH formation and intercalation reaction

occur simultaneously, which reinforces the role of the interlayer anion. It is therefore possible that the intercalation reaction could slow down the whole process of LDH precipitation, which would explain why smaller particles are obtained with acetate and benzoate.

2.5.2 Comparison with the standard preparation method

From the preceding results, it is clear that the continuous coprecipitation method under steady-state conditions constitutes a versatile tool for producing nanometer-platelet Zn/Al-CO_3-LDH structures in water or organic-water mixed solvents, such as MEG/H_2O or PEG aqueous solutions when the total cation concentration is 3.0 x 10^{-2} M or lower. Comparison with samples obtained using the traditional method in pure water with a long aging period shows that batch synthesis provides large platelets (Ø006 ≈ 80 nm) with a high degree of crystallinity and a low specific surface area, only 6.01 m^2/g. TEM confirms the change in particle size and shows that these platelets can be more difficult to disperse than those obtained using the continuous method. To obtain the same quantity of LDH compounds in reactors of similar volumes using either the continuous (total salt concentration: 3.0 x 10^{-2} M) or the batch process (total salt concentration: 1.0 M), the preparation time can be decreased from 10 - 70 to 3 - 9 h in pure water. The benefit is even higher in MEG/H_2O mixtures or PEG aqueous solutions because of the lower solubility of metallic salts in these media, which has a particularly adverse affect in the case of the standard method. Additionally, the new procedure has the advantage of keeping constant simultaneously all the experimental parameters, such as residence time, pH and supersaturation, thus allowing a better control over LDH

phase properties, such as particle size and crystallinity. As this method can be easily adapted for large-scale production, it appears therefore to be a promising alternative to the traditional technology for the manufacture of nanometer-size crystallized LDHs.

2.6 Conclusion

1. In this Chapter, it has been shown that nanometer-size standard LDH materials characterized by narrow size distributions and uniform platelet configurations can be easily synthesized using a novel continuous coprecipitation technique under steady-state conditions.

2. The effects of varying preparation conditions on the structural and textural properties of LDHs have been studied in detail, using Zn_2Al-CO_3-LDH as an example. Of the different parameters investigated, the total metallic cation concentration and the use of mixed water-organic solvents have been shown to have the most significant influence on LDH properties. These effects have been explained primarily through changes in supersaturation, but the role of the viscosity of the preparation medium has also been highlighted. A total salt concentration of 3.0×10^{-2} M has been shown to be optimal, either in pure water or mixed solvents based on MEG and PEG, for the production of large quantities of small LDH particles. To a lesser extent, residence time can also be used to adjust the properties of the LDH materials, as it has been shown to affect mainly particle growth. The role of the interlayer anion has also been noted, although this remains difficult to interpret.

3. The steady-state technique offers two main advantages over the standard

coprecipitation route. First, it eliminates an aging step, which reduces the preparation time considerably, but it also enables a better control over LDH characteristics, such as the size and shape of the platelets, their agglomeration level and their specific surface area. Secondly, it should be relatively easy to scale-up for future application in large-scale production.

References:

1. J. Carpentier, J. F. Lemonier, S. Siffert, E. A. Zhilinskaya, A. Aboukais, Characterisation of Mg/Al hydrotalcite with interlayer palladium complex for catalytic oxidation of toluene, *Appl. Catal. A. Gen.*, 2002, 234(1-2), 91-101.
2. A. I. Khan, L. Lei, A. J. Norquist, D. O'Hare, Intercalation and controlled release of pharmaceutically active compounds from a layered double hydroxides, *Chem. Commun.*, 2001, (22), 2342-2343.
3. T. J. Pinnavaia, G. W. Beall, in: Polymer-Clay Nanocomposites, Wiley, West Sussex, 2000.
4. F. Leroux, J. P. Besse, Polymer Interleaved Layered Double Hydroxides: A New Emerging Class of Nanocomposites, *Chem. Mater.*, 2001, 13(10), 3507-3515.
5. V. Rives, M. A. Ulibarri, Layered double hydroxides (LDH) intercalated with metal coordination compounds and oxometalates, *Coordin. Chem. Rev.*, 1999, 181(1), 61-120.
6. J. Inacio, C. Taviot-Gueho, C. Forano, J. P. Besse, Adsorption of MCPA pesticide by MgAl- layered double hydroxides, *Appl. Clay Sci.*, 2001, 18(5-6), 255-264.
7. Y. You, H. Zhao, G. F. Vance, Adsorption of dicamba (3,6-dichoro-2-methoxy benzoic acid) in aqueous solution by calcined- layered double hydroxides, *Appl. Clay Sci.*, 2002, 21(5-6), 217-226.

8. T. Lopez, P. Bosh, E. Ramos, R. Gomez, O. Novaro, D. Acosta, F. Figueras, Synthesis and Characterization of Sol-Gel Hydrotalcites: Structure and Texture, *Langmuir*, 1996, 12(1), 189-192.
9. M. Ogawa, H. Kaiho, Homogeneous Precipitation of Uniform Hydrotalcite Particles, *Langmuir*, 2002, 18(11), 4240-4242.
10. M. Adachi-Pagano, C. Forano, J. P. Besse, Synthesis of Al-rich hydrotalcite-like compounds by using the urea hydrolysis reaction-control of size and morphology, *J. Mater. Chem.*, 2003, 13(8), 1988-1993.
11. F. Kooli, C. Depège, A. Ennaqadi, A. de Roy, J. P. Besse, Rehydration of Zn-Al layered double hydroxides, *Clays Clay Miner.*, 1997, 45, 92-98.
12. J. He, B. Li, D. G. Evans, X. Duan, Synthesis of layered double hydroxides in an emulsion solution, *Colloids Surf. A: Physicochem. Eng. Aspects*, 1999, 251(1-3) 191-196.
13. A. de Roy, C. Forano, J. P. Bess, in Layered Double Hydroxides: Present and Future, V. Rives (Ed.), chapter 1, Nova Science Publishers, New York, USA, 2001.
14. F. Cavani, F. Trifiro, A. Vaccari, Hydrotalcite-type anionic clays: preparation, properities and applications, *Catal. Today*, 1991, 11, 173-301.
15. A. de Roy, C. Forano, K. El Malki, J. P. Besse, in: M. L. Occelli, H. E. Robson (Eds.), Synthesis of Microporous Materials, vol. 2, Expanded Clays and Other Microporous Systems, Van Nostrand Reinhold, New York, 1992, 108-169.
16. J. W. Boclair, P.S. Braterman, Layered Double Hydroxides Stability. 1. Relative Stabilities of Layered Double Hydroxides and Their Simple Counterparts, *Chem. Mater.*, 1999, 11(2) 298-302.
17. F. Basile, G. Fornasari, M. Gazzano, A. Vaccari, Synthesis and thermal evolution of hydrotalcite-type compounds containing noble metals, *Appl. Clay Sci.*, 2000, 16(3-4), 185-200.
18. F. M. Labajos, V. Rives, M. A. Ulibarri, Effect of hydrothermal and thermal treatments on the physicochemical properties of Mg-Al hydrotalcite-like materials, *J. Mater. Sci.*, 1992, 27(6), 1546-1552.

19. S. Möhmel, I. Kurzawski, D. Müller, W. Geßner, The Influence of a Hydrothermal Treatment using Microwave Heating on the Crystallinity of Layered Double Hydroxides, *Cryst. Res. Tech.*, 2002, 37(4), 359-369.
20. Y. Zhao, F. Li, R. Zhang, D. G. Evans, X. Duan, Preparation of Layered Double Hydroxide Nanomaterials with a Uniform Crystallite Size Using a New Method Involving Separate Nucleation and Aging steps, *Chem. Mater.*, 2002, 14(10), 4286-4291.
21. F. Malherbe, C. Forano, J. P. Besse, Use of organic media to modify the surface and porosity properties of hydrotalcite-like compounds, *Microporous Mater.*, 1997, 10(1-3), 67-84.
22. Ph. Courty, Ch. Marcilly, in: Preparation of Catalysts III, G. Poncelet, P. Grange, P. A. Jacobs (Eds.), Elsevier Science Publishers, Amsterdam, The Netherlands, 1983, 485.
23. N. Bénet, H. Muhr, E. Plasari, J. M. Rousseaux, New technologies for the precipitation of solid particles with controlled properties, *Powder Technol.*, 2002, 128(2-3), 93-98.
24. I. Lagadic, A. Leaustic, R. Clement, Intercalation of polyethers into the MPS_3 (M=Mn, Cd) host lattice, *J. Chem. Soc., Chem. Commun.*, 1992, (19), 1396-1398.
25. F. Li., L. H. Zhang, D. G. Evans, X. Duan. Structure and surface chemistry of manganese-doped copper-based mixed metal oxides derived from layered double hydroxides, *Colloids Surf. A: Physicochem. Eng. Aspects*, 2004, 244, 169-177.
26. J. T. Kloprogge, R. L. Frost, Fourier Transform Infrared and Raman Spectroscopic Study of the Local Structure of Mg-, Ni-, and Co- Hydrotalcites, *J. Solid State Chem.*, 1999, 146(2), 506-515.
27. V. Rives, in Layered Double Hydroxides: Present and Future, V. Rives (Ed.), chapter 4, Nova Science Publishers, New York, USA, 2001.
28. J. M. Fernandez, C. Barriga, M. A. Ulibarri, F. M. Labajos, V. Rives, New Hydrotalcite-like Compounds Containing Yttrium, *Chem. Mater.*, 1997, 9, 312-318
29. T. Sato, H. Fujita, T. Endo, M. Shimada, Synthesis of hydrotalcite-like compounds and their physico-chemical properties, *React. Solids*, 1988, 5(2-3), 219-228.

30. S. Miyata, Anion-exchange properties of hydrotalcite-like compounds, *Clays Clay Miner.*, 1983, 31, 305-311.
31. G. W. Brindley, S. Kikkawa, Thermal behaviour of hydrotalcite and of anion-exchange forms of hydrotalcite, *Clays Clay Miner.*, 1980, 28, 87-91.
32. M. J. Hernandez, M. A. Ulibarri, J. L Rendon, C. J. Serna, Thermal stability of Ni, Al double hydroxides with various interlayer anions, *Thermochim. Acta*, 1984, 81, 311-318.
33. J. M. Fernandez, C. Barriga, M. A. Ulibarri, F. M. Labajos, V. Rives, Preparation and thermal stability of manganese-containing hydrotalcite: $[Mg_{0.75}Mn^{II}_{0.04}Mn^{III}_{0.21}(OH)_2](CO_3)_{0.11}\cdot nH_2O$, *J. Mater. Chem.*, 1994, 4(7), 1117-1121.
34. P. Atkins, J. de Julia, Atkins's Physical Chemistry (7th Ed.), Oxford Press, 2001.
35. A. S. Myerson (Ed.), in: Handbook of Industrial Crystallisation, 2nd Ed., Butterworth-Heinemann, Woburn, MA, USA, 2002.
36. O. Söhnel, J. Garside, in: Precipitation: Basic Principles and Industrial Applications, Butterworth-Heinemann, Oxford, UK, 1992.
37. A. G. Jones, in: Crystallisation Process Systems, Butterworth-Heinemann, London, UK, 2002.
38. A. Mersmann, Crystallization and precipitation, *Chem. Eng. Process.*, 1999, 38(4-6), 345-353.
39. J. Franke, A. Mersmann, The influence of the operational conditions on the precipitation process, *Chem. Eng. Sci.*, 1995, 50(11), 1737-1753.

Chapter 3

Controllable preparation and structural characterization of LDHs with rare earth complexes intercalated in the interlayer galleries

3.1 Introduction

3.1.1 General introduction

Key features of the intercalation chemistry of layered double hydroxides (LDHs) and the properties of rare earth compounds were reviewed in Chapter 1. The work described in this Chapter involves the intercalation of some anionic rare earth complexes into the interlayer galleries in LDHs. Many organic ligands can coordinate with rare earth elements to produce anionic complexes [1,2]. Taking into account that the ligands and their complexes should be stable under basic and neutral conditions if they were to be intercalated into LDH hosts, a literature search was carried out which identified 2,6 pyridinedicarboxylic acid (H_2dipic), oxalic acid, diethylenetriaminepentaacetic acid (DTPA) and diethylenetriaminepenta methylenephosphonic acid (DTPMPA) as potential ligands. Of these, H_2dipic was chosen because it has often been used as a ligand to coordinate with rare earth elements in luminescence studies [3,4] and complexation of rare earth ions by the dipic^{2-} ligand has been shown to offer considerable advantages in terms of enhanced luminescence efficiency [5]. Our work dealt with intercalation of the tris(dipicolinato)cerium(III)

complex $[Ce(C_7H_3NO_4)_3]^{3-}$ into LDHs, especially ZnAl-NO_3-LDH, and the method was subsequently extended to the corresponding europium(III) complex which should have better luminescent properties. Some comparative studies with a cerium(III) complex of DTPA were also reported.

3.1.2 Intercalation chemistry of LDHs

As described in Chapter 1, the intercalation chemistry of LDH hosts is very extensive. A wide variety of anions can be incorporated into the interlayer region of these hosts using a range of methods: direct synthesis, ion exchange, swelling with a large organic anion, which is subsequently displaced by the target anion, or reconstruction of the layered structure when contacting a calcined precursor with solutions of anions [6-8].

LDH materials containing intercalated metallo-organic species, including oxalate complexes, cyano-complexes, phthalocyanines, and porphyrins, have been prepared. These hybrid materials have potential applications as catalytic, photoactive, or electroactive materials. LDHs containing metal complexes of chelate ligands, mainly nitrilotriacetate (NTA) and EDTA (ethylenediaminetetraacetate), have also been prepared, either directly by intercalation of the metal complex or indirectly by forming the metal complex *in situ* between the host layers following pre-intercalation of the ligand [9,10]. Although such materials involving rare earth chelate complexes would be of interest because of their potential applications in optoelectronic devices [11-15], there have only been very few reports of such materials, which are reviewed here.

Li et al. [16] reported that the reaction of an MgAl-NO_3-LDH with a four-fold

excess of Na[Eu(EDTA)] gave a layered material in which the interlayer anions comprised not only the chelate complex $[Eu(EDTA)]^-$ but also CO_3^{2-}. The gallery height of the Eu-containing LDH was 9.0 Å; considering the maximal dimension (9-10 Å) of $[M(EDTA)]^-$, it was concluded that the chelate anion was oriented with this maximal dimension being perpendicular to the host layers. Geometrical considerations were used to show that the high positive charge density on the layers cannot be balanced by intercalation of the chelate complex alone, because its charge density is too low. Co-intercalation of carbonate ions, which have a much higher charge density, is therefore observed. After calcination, the presence of an $Al_2Eu_4O_9$ phase together with the absence of an Eu_2O_3 phase was taken to indicate that europium was well dispersed in the resulting metal oxide matrix and, hence, presumably also in the LDH precursor itself.

Gago *et al.* [6] studied the immobilization of rare earth ions (Eu^{3+}, Gd^{3+}) in a ZnAl-LDH pillared by 2,2'-bipyridine-5,5'-dicarboxylate (BDC) anions via the formation of intercalated complexes. It was shown that the BDC anions are arranged with their longest dimension nearly perpendicular to the host layers. Subsequent photoluminescence results for the Eu-containing LDH showed that there was only one type of Eu^{3+} binding site and the presence of free BDC ligands could be observed in the emission spectra. The material showed the incorporation of about two europium cations for every three BDC anions. On the basis of the results obtained a structural model was proposed involving a 6-coordinate Eu^{3+} ion with one bidentate bipyridyl ligand and four water molecules. The low coordination number compared with that of most Eu^{3+}

complexes (8- or 9-coordination) may be due to the fact that the europium ions were confined within a constrained environment.

In an alternative approach, Zhuravleva *et al.* [17] have shown that $[Ln(pic)_4]^-$ (Ln = Tb(III), Eu(III); pic = picolinate) complexes react with calcined LDHs to give LDHs containing anionic complexes derived from hydrolysis of the $[Ln(pic)_4]^-$ precursor under the basic conditions employed.

In addition to these few reports of rare earth chelate complexes intercalated in LDHs, related studies with transition metal complexes are also relevant. Tarasov and O'Hare [18] reported that an LiAl-LDH which had been pre-intercalated with $EDTA^{4-}$ was able to take up transition metal ions (Co^{2+}, Ni^{2+}, and Cu^{2+}) from aqueous solutions to form intercalated chelate $[M(EDTA)]^{2-}$ complexes. The details of the reaction depend on the nature of the anion present in solution along with the transition metal cations. Co-intercalation of either Cl^- or NO_3^- anions was observed and the products were multiphase materials. It was also shown that direct ion exchange of LiAl-LDH with $[M(EDTA)]^{2-}$ complexes was possible, in which case co-intercalation of other anions can be ignored. Such solid-state chelating agents that are able to immobilize metal ions in solid matrixes may potentially be of interest for the removal of contamination in wastewater.

Tsyganok *et al.* [19] reported a nickel-containing MgAl-LDH in which nickel was introduced via pre-complexation with the $EDTA^{4-}$ ligand followed by incorporation of the resultant chelate $[Ni(EDTA)]^{2-}$ anion into the LDH host by co-precipitation, anion exchange, or through the reconstruction reaction. It should be noted that the purity of

the product phases varied according to the preparation method. An impurity MgAl-CO_3-LDH phase, formed by absorption of CO_2 from the air, was always observed with the latter two methods. The corresponding LDH-derived Ni-Mg-Al mixed oxides obtained by calcination demonstrated high and stable catalytic activity in methane reforming with carbon dioxide to give synthesis gas at 800 °C. It was shown that the state of the supported nickel and the extent of coke deposition are significantly influenced by the method of catalyst preparation.

Carrado *et al.* found that copper and nickel nitrilotriacetate ($[Cu(nta)]^-$ and $[Ni(nta)]^-$) complexes could be intercalated into a Zn-Cr-LDH [20,21]. In the case of $[Cu(nta)]^-$, a mixture of products with basal spacings of approximately 14.2 and 12.0 Å were formed at ambient temperature. At 60 ^oC however, only the product with the lower basal spacing was observed. In contrast, for the Ni complex the phase with basal spacing of 14.2 Å was the sole product at 25 ^oC and the formation of the product with the lower basal spacing was observed only at temperatures of about 100 ^oC. These differences were explained in terms of the complexes being arranged in a tilted (12.0 Å phase) or vertical arrangement (14.2 Å phase) in the interlayer region. The tilted orientation is energetically favored owing to the greater host–guest interactions (i.e. more hydrogen bonding) but this orientation cannot be achieved at low temperatures.

3.2 Controllable preparation of rare earth complexes and REE -containing intercalated LDHs

3.2.1 Experimental conditions

A common problem with all the methods used to prepare LDHs with anions other than carbonate is contamination with carbonate anions from adsorption of CO_2 in air; these are readily incorporated and tenaciously held in the interlayer galleries. Consequently, decarbonated and deionized water is used and exposure of the material to the atmosphere is kept to a minimum.

3.2.1.1 Synthesis of LDH precursors

The LDH precursors were prepared by a co-precipitation method at controlled pH as described in the literature [22].

Mixed salt solutions containing M^{2+} and M^{3+} ions (M^{2+} = Zn^{2+}, Ni^{2+}, Co^{2+}, Cu^{2+}; M^{3+} =Al^{3+}, Cr^{3+}) as their nitrate salts in molar ratios [$M^{2+}_xM^{3+}$] (x = 2, 3, 4, or 5) were added dropwise to water in a flask at room temperature, the solution being maintained at pH 7 or 9 by simultaneous addition of aqueous NaOH. Once the addition was complete, the mixture was stirred at 60 ^oC for 24 h. All the procedures were conducted under a nitrogen atmosphere. The products were separated by centrifugation, washed, and dried in air at room temperature. $M^{2+}_xM^{3+}$-NO_3-LDH phases are denoted Zn_2Al, Zn_3Al, Zn_4Al, Zn_5Al, Ni_2Al, Co_2Al, and CuZnAl-LDH respectively. In addition, mixtures of Zn^{2+} and Cr^{3+} as chloride salts were used to prepare Zn_2Cr-LDH at pH 5.5 following the same method.

3.2.1.2 Synthesis of rare earth complexes

The synthesis of $[REE(dipic)_3]^{3-}$ (REE = Ce or Eu) and $[Ce(DTPA)]^{2-}$ complex anions was carried out according to methods described in the literature for closely

related complexes [2,23-29].

$[REE(dipic)_3]^{3-}$ complex anion: An aqueous solution of disodium dipicolinate was obtained by stirring a mixture of pyridine-2,6-dicarboxylic acid (H_2dipic) (1.5 mmol in 50 ml of water) and NaOH (3 mmol in 25 ml of water). A solution of the REE(III) nitrate salt (REE(III) = Ce^{3+} or Eu^{3+}) (0.5 mmol) in water (15 ml) was added slowly to the disodium dipicolinate solution until the molar ratio reached REE^{3+}/$dipic^{2-}$ = 1:3. The pH values of the resulting solutions were near 7. The solution contains the tris(dipicolinato)REE(III) complex anions $[REE(dipic)_3]^{3-}$, denoted below as REE(dipic). Slow evaporation at 60 °C gave prismatic crystals of $Na_3[REE(C_7H_3NO_4)]\cdot xH_2O$ (x was generally ~15).

$[Ce(DTPA)]^{2-}$ complex anion: Diethylenetriaminepentaacetic acid (DTPA, H_5L) (1.2 mmol) was dissolved in water (120 ml) and 0.2 M NaOH solution was added until the pH reached 7. A solution of $Ce(NO_3)_3\cdot 6H_2O$ (1.2 mmol) in water (10 ml) was added slowly to the above DTPA solution to give a molar ratio Ce^{3+}/$DTPA^{5-}$ = 1:1, while maintaining the solution at pH 7 by addition of further NaOH. The resulting solution contained the $[Ce(DTPA)]^{2-}$ complex anion, denoted Ce(DTPA) below.

3.2.1.3 Synthesis of REE-containing LDHs

Anion exchange method:

Synthesis of $[REE(dipic)_3]^{3-}$-LDHs: Aqueous solutions of tris(dipicolinato)REE(III) complexes with different concentrations were kept under nitrogen before reactions. $M^{2+}{}_xM^{3+}$-NO_3-LDHs (M^{2+} = Zn^{2+}, Ni^{2+}, Co^{2+} or Cu^{2+}; M^{3+} =Al^{3+} or Cr^{3+}; x represents

the molar ratio of M^{2+}/M^{3+}). Powders were first dispersed in deionized water for 24 h and then added to the $[REE(dipic)_3]^{3-}$ solutions (with $[REE(dipic)_3]^{3-}/M^{3+}$=3:1, 1:1 or 1:3). The resulting suspensions were vigorously stirred for 24 h under an N_2 atmosphere at different temperatures (room temperature, 60 °C or 120 °C in autoclave). Finally, the products were separated by three repeated washing/centrifugation cycles and dried in air. The samples are denoted $M^{2+}_xM^{3+}$-REE(dipic)-LDH. For comparison purposes, Zn_2Al-dipic-LDH without any REE was prepared by the same ion exchange method using $dipic^{2-}$ to replace $[REE(dipic)_3]^{3-}$. The $dipic^{2-}$ solution was mixed with the Zn_2Al-NO_3-LDH precursor in the molar ratio $dipic^{2-}/Al^{3+}$=2:1.

In addition, Zn_2Al-DDS-LDH (DDS = dodecyl sulfate) [30] and Zn_2Al-Cl-LDH were used as alternative precursors in ion exchange reactions with $[Ce(dipic)_3]^{3-}$ solutions following the above procedure.

Synthesis of $[Ce(DTPA)]^{2-}$-LDHs: The ion exchange process was the same as before. A $[Ce(DTPA)]^{2-}$ solution purged with N_2 and Zn_2Al-NO_3-LDH pre-dispersed in water for 24 h were mixed in different molar ratios $[Ce(DTPA)]^{2-}/Al^{3+}$=2:1, 1:5, or 1:10 for 24 h at room temperature under an N_2 atmosphere. The resulting product, denoted Zn_2Al-Ce(DTPA)-LDH, was collected after washing and drying. Similarly, Zn_2Al-DTPA-LDH without any rare earth ion was prepared by the same ion exchange method, using $DTPA^{5-}$ instead of $[Ce(DTPA)]^{2-}$.

Samples prepared under the different conditions are listed in Table 3-1.

Table 3-1. Different experimental conditions employed for the ion-exchange method

Sample	Precursor	$[Ce(dipic)_3]^{3-}$	Ce/Al	T/ °C
Zn_2Al-Ce(dipic)-LDH	Zn_2Al-NO_3-LDH	0.006M	1/1	25
Zn_2Al-Ce(dipic)-auto-LDH	Zn_2Al-NO_3-LDH	0.006M	1/1	120
Zn_3Al-Ce(dipic)-LDH	Zn_3Al-NO_3-LDH	0.004M	1/1	25
Zn_4Al-Ce(dipic)-LDH	Zn_4Al-NO_3-LDH	0.004M	1/1	25
Zn_5Al-Ce(dipic)-LDH	Zn_5Al-NO_3-LDH	0.004M	1/1	25
Zn_2Al-Ce(dipic)-Cl-LDH	Zn_2Al-Cl-LDH	0.006M	1/1	25
Zn_2Al-Ce(dipic)-DDS-LDH	Zn_2Al-DDS-LDH		1/1	25
Zn_2Al-dipic-LDH	Zn_2Al-NO_3-LDH	0.024M $dipic^{2-}$	$dipic^{2-}$/ Al=1/1	25
Zn_2Al-dipic-auto-LDH	Zn_2Al-NO_3-LDH	0.024M $dipic^{2-}$	$dipic^{2-}$/ Al=2/1	120
Ni_2Al-Ce(dipic)-LDH	Ni_2Al-NO_3-LDH	0.004M	1/1	25
Co_2Al-Ce(dipic)-LDH	Co_2Al-NO_3-LDH	0.004M	1/1	25
Zn_2Cr-Ce(dipic)-LDH	Zn_2Cr-Cl-LDH	0.004M	1/1	25
CuZnAl-Ce(dipic)-LDH	CuZnAl-NO_3-LDH	0.006M	1/1	25
CuZnAl-Ce(dipic)-3/1-LDH	CuZnAl-NO_3-LDH	0.006M	3/1	25
CuZnAl-Ce(dipic)-1/3-LDH	CuZnAl-NO_3-LDH	0.006M	1/3	25
CuZnAl-Ce(dipic)-1/6-LDH	CuZnAl-NO_3-LDH	0.006M	1/6	25
Zn_2Al-Eu(dipic)-LDH	Zn_2Al-NO_3-LDH	0.006M	1/1	25
Zn_2Cr-Eu(dipic)-LDH	Zn_2Cr-Cl-LDH	0.006M	1/1	25
Zn_2Al-Ce(DTPA)-LDH	Zn_2Al-NO_3-LDH	0.0005M	2/1	25

Co-precipitation method:

A mixed salt solution containing $Zn(NO_3)_2{\cdot}6H_2O$ and $Al(NO_3)_3{\cdot}9H_2O$ in the molar ratio 2:1 was added dropwise to a $[Ce(dipic)_3]^{3-}$ solution previously purged under N_2 for 24 h, maintaining pH 7 or 9 by simultaneous addition of NaOH. The suspension was aged at 60 ^oC for 24 h with stirring, washed in deionized water until the pH of the washings reached 7, and finally dried at room temperature. Experimental conditions used for different samples are listed in Table 3-2.

Table 3-2. Different experimental conditions employed for the co-precipitation method

Sample	Conditions	
	pH	$[Ce(dipic)_3]^{3-}/Al^{3+}$
Zn_2Al-co-LDH	7	1/1
Zn_2Al-co-1/3-LDH	7	1/3
Zn_2Al-co-9-LDH	9	1/1
Zn_2Al-co-dipic-LDH	7	$dipic^{2-}/Al^{3+}$=1/1

3.2.1.4 Adsorption experiments

The adsorption isotherm for $[Ce(dipic)_3]^{3-}$ and Zn_2Al-NO_3-LDH was determined at 23 ^oC under a nitrogen atmosphere with magnetic stirring, using the batch reaction procedure already published [31] with fixed mass of LDH (50 mg) and total solution volume (25 ml). To reduce effect of contamination by CO_3^{2-}, $[Ce(dipic)_3]^{3-}$ solutions were purged with N_2 for 24 h before the LDH powders were added. The adsorption experiments were carried out by varying the initial $[Ce(dipic)_3]^{3-}$ concentrations (from 0.25 to 6 mmol/l). After a contact time of 48 h, the suspensions were centrifuged. The initial concentrations of $[Ce(dipic)_3]^{3-}$ and those in the supernatants were analyzed by UV spectroscopy; the absorbance wavelength used was 271 nm. The amount of $[Ce(dipic)_3]^{3-}$ adsorbed by the LDH (Q) was determined from the difference between the initial (C_i) and equilibrium concentrations (C_e) of the $[Ce(dipic)_3]^{3-}$ solutions and expressed per gram of LDH adsorbent: $Q=(C_i-C_e)*V/m$, where V = 25 ml and m = 50 mg. The adsorption isotherms were obtained by plotting the amount of $[Ce(dipic)_3]^{3-}$ adsorbed (Q) versus the adsorbate concentration (C_e) in the equilibrium solution.

In addition, the adsorption isotherm of $[Ce(dipic)_3]^{3-}$ on Zn_2Cr-Cl-LDH was determined under the same conditions.

3.2.2 Characterization techniques

Room temperature X-ray powder diffraction (PXRD) data were collected on a Siemens D500 diffractometer using Cu Kα radiation. The samples as unoriented powders, were scanned from 2 to 70° in steps of 0.08° with a count time of 4 s at each point. *In situ* variable temperature XRD patterns were recorded using an X' Pert Pro Philips diffractometer equipped with a HTK16 Anton Paar chamber and with a PSD-50m Braum detector.

Infrared transmission spectra were recorded on a Perkin-Elmer 2000 FT spectrometer at a resolution of 2 cm^{-1} by averaging 15 scans in the 400-4000 cm^{-1} region, using the KBr technique.

UV-visible spectra were recorded on a Perkin-Elmer lambda 2S spectrometer.

Thermogravimetric analysis (TGA) was performed on a SETARAM thermogravimetric analyser. Samples with mass of about 10.0 mg were heated in air at a heating rate of 5 °C min^{-1} to a maximum of 1100 °C.

Elemental analysis for metal ions was carried out using a Shimadzu ICPS-7500 inductively coupled plasma emission spectrometer (ICP-ES). Solutions were prepared by dissolving the samples in dilute nitric acid.

Surface areas and pore volumes were determined from N_2 adsorption-desorption measurements on a Quantachrome Autosorb-1C-VP system using the BET equation for surface area. Prior to the measurements, the samples were outgassed at 200 ^oC under vacuum for 2 h.

Transmission electron microscopy (TEM) was performed using a Hitachi H-800 electron microscope. The accelerating voltage applied was 100 kV.

The photoluminescence spectra were recorded using an experimental setup described by Meng [32]. Continuous fluorescence emission and excitation spectra were recorded by using a monochromatized 450 W xenon lamp as the excitation source. The emitted light was focused at the entrance slit of a Jobin Yvon HR1000 monochromator and detected with a R1104 Hamamatsu PMT followed by a 162 PAR boxcar integrator and a data acquisition card (Keithley SA).

3.3 Structural characterization of the $[Ce(dipic)_3]^{3-}$ complex

3.3.1 Crystal structure

Crystal structures of $[REE(dipic)_3]^{3-}$ complexes have been well established in terms of the coordination geometry, coordination number and bond distances [23,24,33]. In 1972, Albertsson [23] described the crystal and molecular structure of $Na_3[Ce(dipic)_3]\cdot 15H_2O$ from three-dimensional X-ray intensity data collected with the Weissenberg multi-film technique. The reported unit cell parameters were a = 10.377(14) Å, b = 11.067(14) Å, c = 18.003(22) Å, α =1 07.60(5)°, β = 90.72(7)°, and γ = 110.38(12)°. The anion is mononuclear with the cerium ion being coordinated to six carboxylate oxygen atoms and three nitrogen atoms which form a slightly distorted tri-capped trigonal prism (illustrated in Fig. 1-2). The maximum dimension of the $[Ce(dipic)_3]^{3-}$ complex is estimated to be about 9 Å.

In this work, a $[Ce(dipic)_3]^{3-}$ complex salt was prepared following the method

described by Albertsson and usually stored in the mother liquor. However, slow evaporation at room temperature gave product crystals and the molecular formula and structure of the complex were determined from the combination of ICP, IR, UV and TG data.

3.3.2 Composition and structural analysis

3.3.2.1 NaOH titration analysis

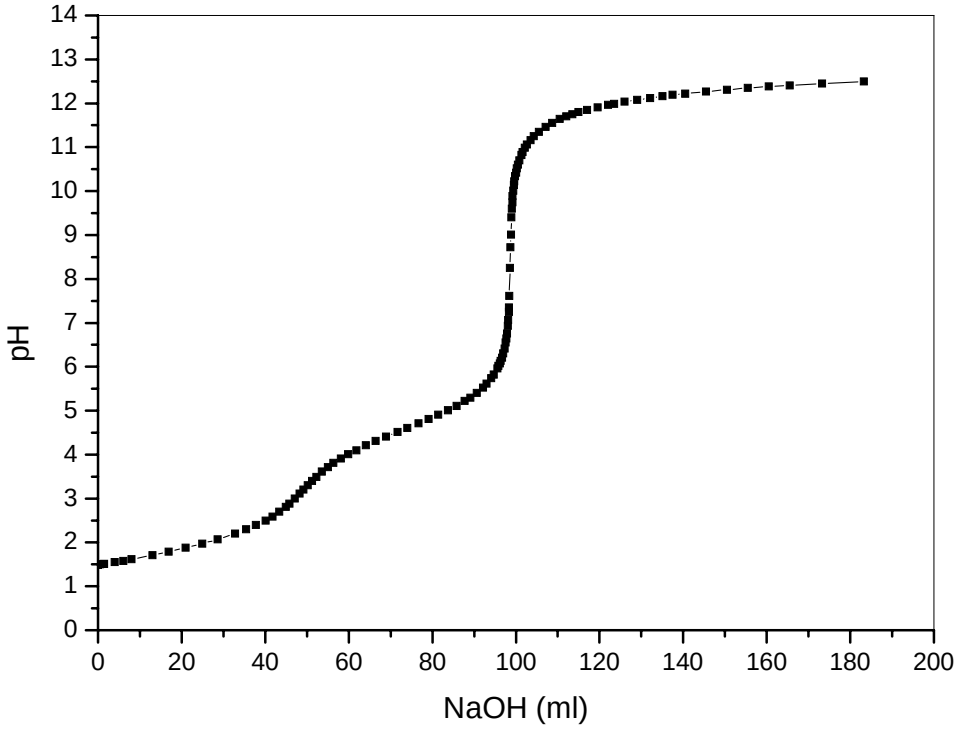

Fig. 3-1 Titration curve of NaOH against H_2dipic

It has been reported in many literature [23,34,35] that dipic^{2-} ligands could form a variety of complexes with Ce^{3+} generally including $Na_3[Ce(dipic)_3]$, Ce(dipic)(Hdipic) and $Ce_2(dipic)_3$. Therefore, it is necessary to confirm the composition of the product and determine the metal-ligand coordination mode. The experiment involving NaOH

titration into H_2dipic was quite important in terms of choosing synthesis conditions which would ensure a complete ionization of H_2dipic into dipic^{2-}. Fig. 3-1 shows the variation of pH when aqueous 0.04 M NaOH was added dropwise to a H_2dipic solution (100ml, 0.02M). The titration curve was divided into 3 steps: below pH 4, the pH value increased slowly with the addition of NaOH, corresponding mainly to the first ionization of H_2dipic to yield Hdipic$^-$ at pH 4-6.5. The second stage was due to the second ionization of Hdipic$^-$ to generate dipic^{2-}; when the pH value reached 6.5, there was an obvious increase from 6.5 to 12 with the addition of few drops of NaOH, which demonstrated that H_2dipic had been completely transformed into dipic^{2-}. Thus if reactions were carried out at pH 7 or above, the presence of Ce(dipic)(Hdipic) complex could be excluded.

3.3.2.2 UV spectroscopy

As shown in Fig. 3-2, the UV absorption spectra of the free dipic^{2-} ligand (b) and its complex (c) were different, which demonstrated that a change of the coordination environment of ligands, consistent with the formation of complexes. Free trivalent rare earth cations generally have a broad characteristic UV absorption band at around 250 nm, as observed at 252 nm for Ce^{3+} in the spectrum of $Ce(NO_3)_3$ solution shown in Fig. 3-2 (a). In the spectrum of the final complex solution, shown in Fig. 3-2(c), the typical UV absorption band of free Ce^{3+} was absent, suggesting that Ce^{3+} was coordinated with the ligands. Moreover, the absorption band of dipic^{2-} (Fig. 3-2(b)) was shifted and split into 2 peaks after the introduction of Ce^{3+}, and two new absorption bands appeared at 273 nm and 279 nm. This suggested that the environment of dipic^{2-} was different, which

could be explained by the presence of bonds between Ce^{3+} and oxygen or nitrogen atoms.

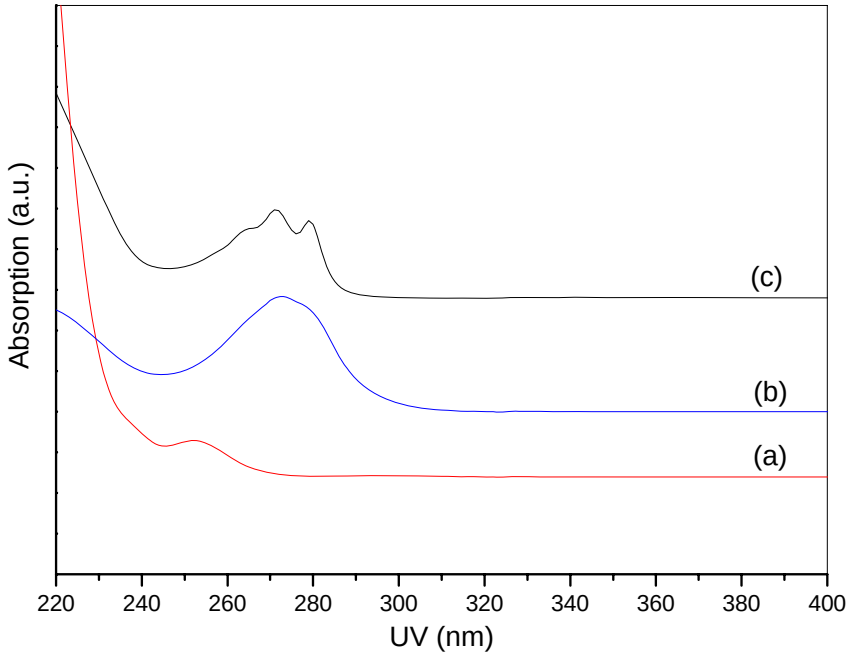

Fig. 3-2 UV spectra of $Ce(NO_3)_3$ (a), H_2dipic (b) and $[Ce(dipic)_3]^{3-}$ complex (c) solutions

3.3.2.3 IR spectroscopy

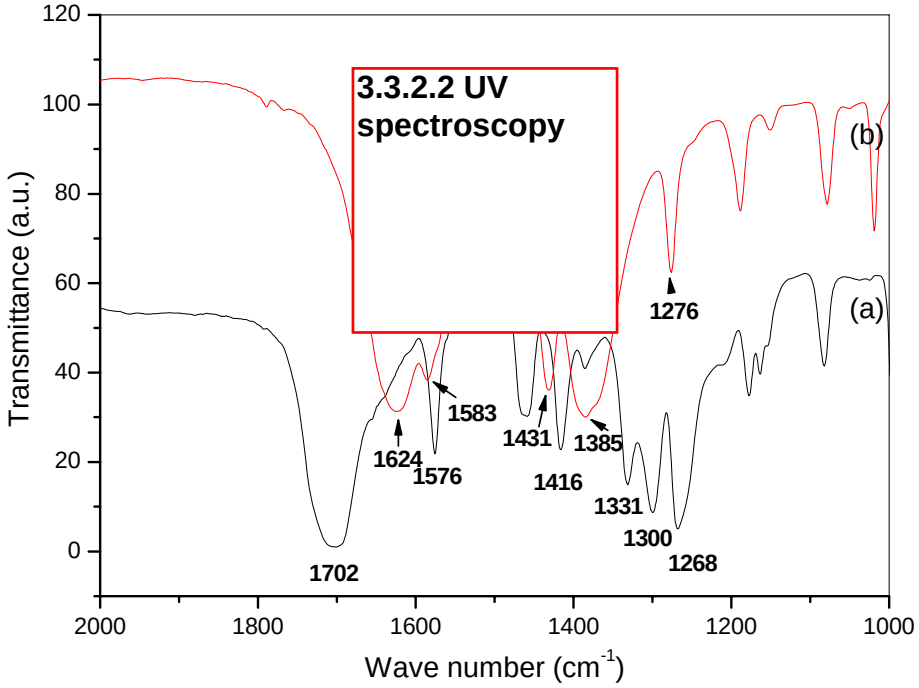

Fig. 3-3 IR spectra of H_2dipic (a) and $Na_3[Ce(dipic)_3]$ complex (b)

More information concerning the ligand to Ce^{3+} bonding in the complex may be obtained from the IR absorption spectra (Fig. 3-3). The two IR spectra had some similar peaks arising from the basic skeletal modes of the pyridine ring. This more interesting region was from 1200 to 1800 cm^{-1}, which provided information about the metal-ligand association. The assignments given here were based on those published by Dexpert-Ghys [25]. The spectrum of $[Ce(dipic)_3]^{3-}$ complex showed bands at about 1624 and 1385 cm^{-1} assignable to the asymmetric and symmetric stretching vibrations of the carboxylate group, respectively. These bands were red and blue shifted respectively with respect to the free ligand H_2dipic, where ν_{as}(OCO) and ν_s(OCO) were located at 1702 and (1331, 1300) cm^{-1}. This indicated that coordinate bonds were formed between Ce^{3+} and O donors from the carboxylate groups. The remaining bands around 1583, 1431 and 1276 cm^{-1} may be assigned to the vibrations of the skeletal modes of the pyridine ring. These vibrations were significantly shifted after the formation of $[Ce(dipic)_3]^{3-}$ complex with respect to H_2dipic, where these peaks were observed at 1576, 1416 and 1268 cm^{-1}, which indicated that the nitrogen atom from the ligand also participated in the metal-ligand coordination. In the IR spectrum of $Ce_2(dipic)_3$ complex reported by Brzyska [34], the vibration peaks of the aromatic backbone were almost unchanged after the formation of the complex because the nitrogen atom did not take part in coordination to the metal. The significant differences between the spectrum of $Ce_2(dipic)_3$ and that of the complex prepared here confirmed that the latter was $[Ce(dipic)_3]^{3-}$.

3.3.2.4 Elemental analysis

The molar ratios of all kinds of elements in the product were usually used as a direct evidence to confirm the structure. The elemental analysis showed that the actual Na/Ce/C/N molar ratio in the powder obtained by evaporation at room temperature was 5.70/1/21.03/5.77. It could be explained that the product was a mixture of two parts, 1 $Na_3[Ce(C_7O_4NH_3)_3]$ (Na/Ce/C/N=3.00/1/21.03/3.00) and 2.7 $NaNO_3$ which was inevitable to be left after evaporation. The elemental analysis result supports the proposed composition of the $Na_3[Ce(dipic)_3]$ complex.

Therefore, on the basis of the above results, it was concluded that the anions used for the intercalation reactions in the complex solutions has the same structure shown in Fig. 1-2.

3.3.2.5 TG-DTA analysis

The TGA/DTG and DTA curves for the sample $Na_3[Ce(dipic)_3]\cdot xH_2O$ in a temperature range from ambient to 1100 °C are shown in Fig. 3-4 and they are similar to those described in the literature [24]. The first weight-loss stage from 25 °C to 120 °C could be attributed to the liberation of adsorbed water molecules; the second step from 120 °C to 220 °C arose from the loss of intercalated water molecules; the decomposition and combustion of organic anions was responsible for the main weight-loss, from 330 to 540 °C; in the high temperature region the fourth weight-loss stage was due to the formation of metal oxides. *In situ* HT-XRD pattern analysis explained the last weight-loss stage: some new phases due to crystallized metal oxides were present at more than 825 °C, consistent with the TG result. It should be noted that the weight-loss

stage corresponding to the loss of organic parts showed 3 exothermic peaks at about 390, 410 and 460 °C, respectively. The dehydration and decomposition of the complex anions were connected with small exothermic effects at 390 and 410°C, whereas the combustion showed a strong exothermic effect at 460 °C. But the quantitative conclusions were difficult to be concluded because of the mixture of two compounds - $Na_3[Ce(C_7O_4NH_3)_3]$ and $NaNO_3$. The thermal behavior was changed obviously once the complex was incorporated into LDH interlayers, which would be discussed in chapter 3.4.2.

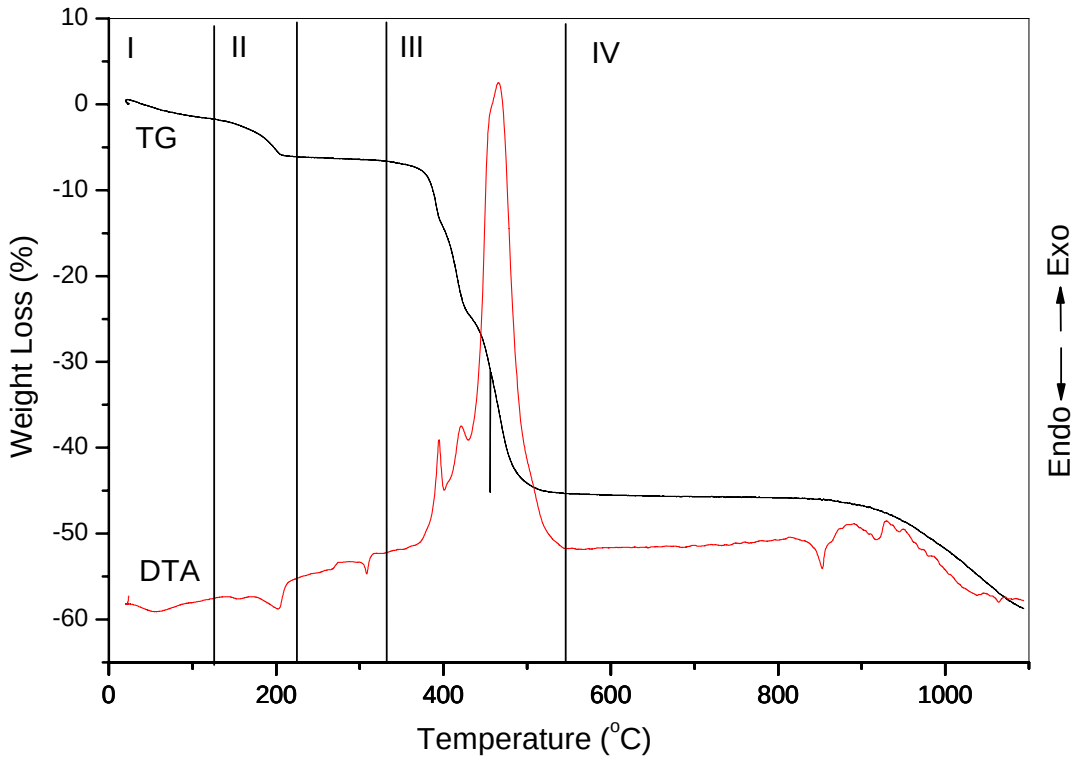

Fig. 3-4 TG, DTG and DTA curves for $Na_3[Ce(dipic)_3]\cdot xH_2O$

3.4 Attempted intercalation of $[Ce(dipic)_3]^{3-}$ into ZnAl-LDHs

3.4.1 Co-precipitation method

3.4.1.1 Structure characterization

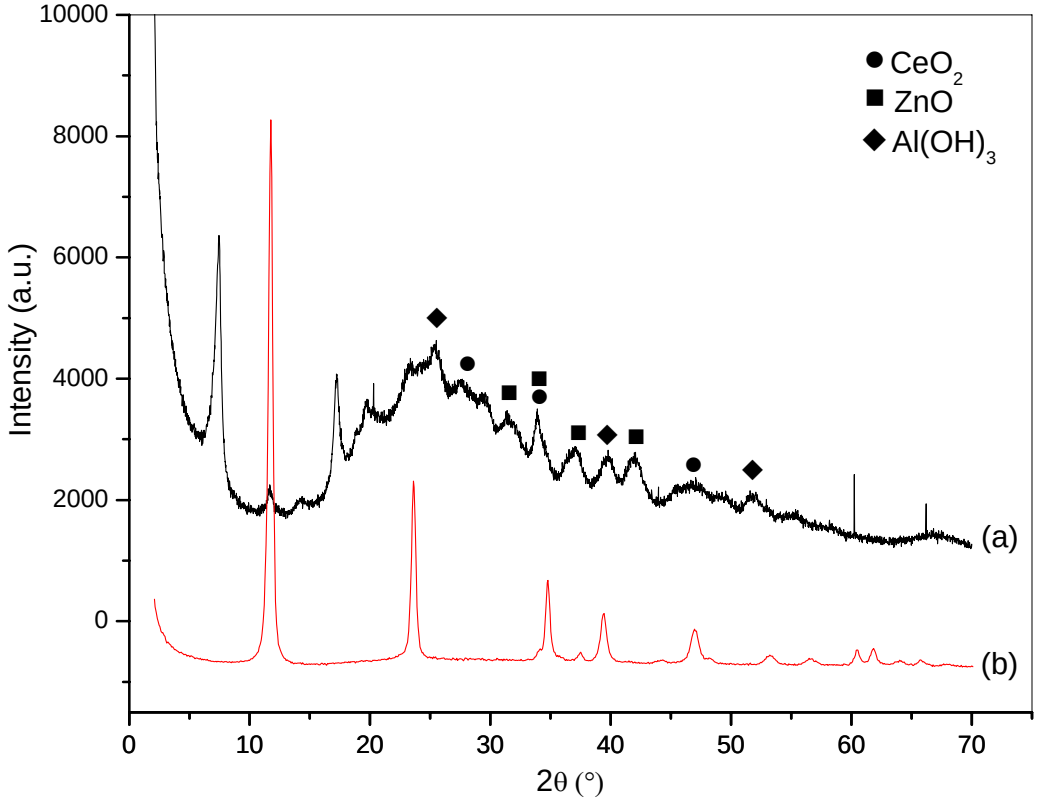

Fig. 3-5 XRD patterns of Zn_2Al-co-LDH sample (a) and Zn_2Al-CO_3-LDH (b)

All of the samples prepared by the co-precipitation method displayed very similar properties so that the sample Zn_2Al-co-LDH (see Table 3-2) was selected as a representative example to characterize.

Fig. 3-5 shows the XRD pattern of the sample Zn_2Al-co-LDH. It was seen that although two diffraction peaks at low angles were consistent with an expanded LDH phase, other characteristic diffractions of the LDH structure, particularly the (110) peak, were absent. It suggested the absence of a great quantity of expected intercalated LDHs.

Moreover, the XRD pattern indicated the presence of a small quantity of Zn_2Al-CO_3-LDH phase, arising from the contamination with CO_2, CeO_2, ZnO and $Al(OH)_3$, recognised using these weak and tanglesome peaks marked in the Figure, and other unidentified impure phases. This demonstrated that the attempted intercalation of $[Ce(dipic)_3]^{3-}$ into LDHs by the co-precipitation method was unsuccesful and the reasons for this would be briefly discussed in the following section.

3.4.1.2 Discussion

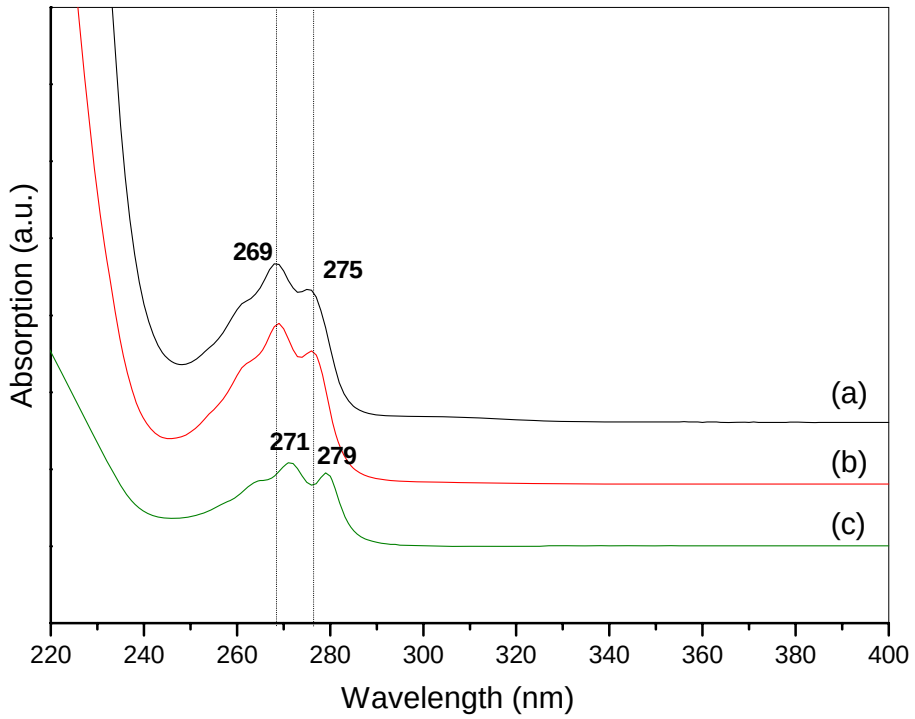

Fig. 3-6 UV adsorption spectra of the supernatant solutions from the preparation of samples Zn_2Al-co-1/3-LDH (a) and Zn_2Al-co-9-LDH (b) and $[Ce(dipic)_3]^{3-}$ precursor (c)

Fig. 3-6 (a) and (b) show the UV absorption spectra of the supernatant solutions when Zn_2Al-co-1/3-LDH and Zn_2Al-co-9-LDH were prepared by the co-precipitation

method. Two UV spectra were very similar but significantly differed from the spectrum of the precursor $[Ce(dipic)_3]^{3-}$ shown in Fig. 3-6 (c). Because the position and shape of UV absorption bands were effected by the chemical environment of organic $dipic^{2-}$ ligands, the shift of UV peaks indicated that the coordination environment of $dipic^{2-}$ ligands was changed after the co-precipitation process.

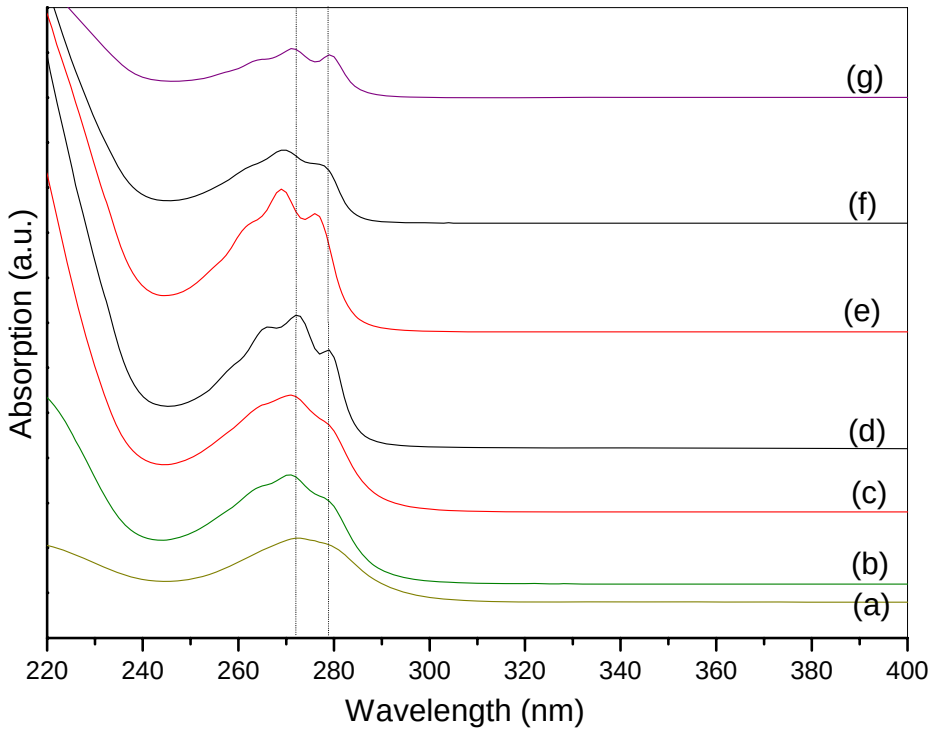

Fig. 3-7 UV spectra of H_2dipic (a), $H_2dipic/NaOH$ (b), $H_2dipic/Al(NO_3)_3$-NaOH (c), $Na_3[Ce(dipic)_3]/Al(NO_3)_3$ (d), $H_2dipic/Zn(NO_3)_2$-NaOH (e), $Na_3[Ce(dipic)_3]/Zn(NO_3)_2$ (f) and $Na_3[Ce(dipic)_3]$ (g)

To further study the reason why the intercalation of $[Ce(dipic)_3]^{3-}$ into the LDH host by the co-precipitation method was unsuccessful, a series of solutions were prepared and their UV spectra recorded as shown in Fig. 3-7. After two solutions were

mixed, the third solution was added in order to study the changes in metal-ligand coordination. For example, H_2dipic/$Zn(NO_3)_2$-NaOH represented the addition of a third solution (NaOH) to a mixture of H_2dipic and $Zn(NO_3)_2$. From the series of UV spectra in Fig. 3-7, the following conclusion could be drawn. The UV absorption bands of H_2dipic/$Zn(NO_3)_2$-NaOH (e) were shifted significantly in comparison with those of H_2dipic/NaOH (b), which suggested the formation of a Zn-dipic complex. Even in $Na_3[Ce(dipic)_3]/Zn(NO_3)_2$ (f), the UV absorption bands were located in the same positions as for H_2dipic/$Zn(NO_3)_2$-NaOH (e), and differed from those in precursor $Na_3[Ce(dipic)_3]$ (g), which indicated that $Na_3[Ce(dipic)_3]/Zn(NO_3)_2$ (f) and H_2dipic/$Zn(NO_3)_2$-NaOH (e) solutions had the similar chemical environment of $dipic^{2-}$ ligands and so they contained the same Zn-dipic complexes. Furthermore, the same complex was present in the supernatant solutions of samples Zn_2Al-co-1/3-LDH (Fig. 3-6 (a)) and Zn_2Al-co-9-LDH (Fig. 3-6 (b)). In contrast, the UV absorption bands of $Na_3[Ce(dipic)_3]/Al(NO_3)_3$ (d) were identical to those of precursor $Na_3[Ce(dipic)_3]$ (g), which suggested Al-dipic coordination was weaker than Ce-dipic so that the presence of Al^{3+} did not destroy the structure of $[Ce(dipic)_3]^{3-}$ complexes. It has been reported [36] that transition metals were eluted before lanthanides from an iminodiacetate chelating resin when using $dipic^{2-}$ as the eluant, which also pointed to the larger stability constants of transition metal-dipic complexes than those containing lanthanides.

It could therefore be concluded that the strong affinity between Zn^{2+} and $dipic^{2-}$ led to the breakdown of the $[Ce(dipic)_3]^{3-}$ complex during the coprecipitation process, holding back the generation of intercalated LDH phases. This also explained the

presence of CeO_2 and $Al(OH)_3$ phases (see Fig. 3-6) because the formation of the Zn-dipic complexes generated free Ce and excess Al which were precipitated on addition of the alkali solutions.

3.4.2 Ion-exchange method

3.4.2.1 Structural characterization

3.4.2.1.1 Elemental analysis

The Zn, Al, Ce, C and N contents of Zn_2Al-Ce(dipic)-LDH and Zn_2Al-dipic-LDH were determined. For Zn_2Al-Ce(dipic)-LDH, elemental analysis indicated that experimental C/Ce and N/Ce atomic ratios were larger than expected values (27.5 and 4.1 instead of 21.0 and 3.0, respectively). The deficiency of Ce^{3+} was explained by a partial decomposition of the $[Ce(dipic)_3]^{3-}$ complex into $dipic^{2-}$ and Ce^{3+} during the exchange process. However, the C/N ratio (6.8) still remained near the theoretical value for $dipic^{2-}$ ligand (7.0). According to the TGA analysis, the molar number of water molecules per intercalated products was 2.91. The calculated formula was $Zn_2Al(OH)_6[Ce(dipic)_3]_{0.15}(dipic)_{0.14}(CO_3)_{0.12}(NO_3)_{0.04}\cdot 2.91H_2O$. It was shown that one half of $[Ce(dipic)_3]^{3-}$ anions were intercalated directly into interlayers, and the others were decomposed into $dipic^{2-}$ ligands which were also intercalated. For Zn_2Al-dipic-LDH, the calculated formula was $Zn_2Al(OH)_6(C_7O_4NH_3)_{0.36}(CO_3)_{0.13}(NO_3)_{0.03}\cdot 2.24H_2O$, indicating that the $dipic^{2-}$ anions were responsible for balancing 72% of the positive charges on the layers and the remaining positive charges were compensated by the unavoidable contamination - CO_3^{2-} species.

3.4.2.1.2 XRD analysis

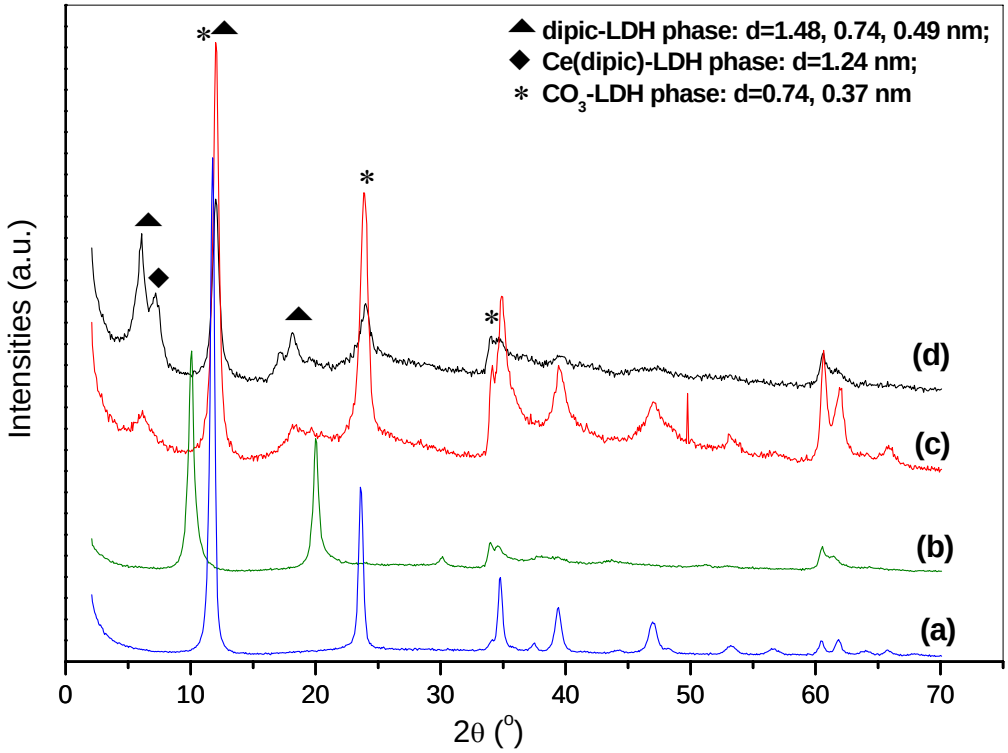

Fig. 3-8 XRD patterns for Zn_2Al-CO_3-LDH (a), Zn_2Al-NO_3-LDH (b), Zn_2Al-dipic-LDH (c) and Zn_2Al-Ce(dipic)-LDH (d)

The X-ray diffraction pattern of the product of reaction of $[Ce(dipic)_3]^{3-}$ with a Zn_2Al-NO_3-LDH precursor, shown in Fig. 3-8 (d), suggests that a mixture of LDH phases is present. The (00*l*) diffraction line series of the products are shifted to lower angle compared with the precursor indicating an increase in basal spacing and the characteristic (110) diffraction peak is also observed. In order to confirm the intercalation of $dipic^{2-}$ anion, we performed the direct exchange reaction with the free ligands. The diffraction pattern of the product, which has an interlayer spacing of 1.48 nm, is shown in Fig.3-8 (c). The X-ray diffraction pattern of the product of reaction of

$[Ce(dipic)_3]^{3-}$ with a Zn_2Al-NO_3-LDH precursor (Fig.3-8 (d)) is consistent with the presence of a small amount of the same Zn_2Al-dipic-LDH phase, while the second phase with basal spacing of 1.24 nm can be identified as the Zn_2Al-LDH phase intercalated by $[Ce(dipic)_3]^{3-}$. This experimental value of the gallery height (0.76 nm) is lower than the diameter of 0.9 nm reported for $[Ce(dipic)_3]^{3-}$ in the publication [23], suggesting that the anion adopts a tilted orientation in the interlayer galleries [37,38]. The presence of some LDH containing intercalated $dipic^{2-}$ is consistent with the lability of the $[Ce(dipic)_3]^{3-}$ complex. It should be noted that a third LDH phase with a basal spacing of 0.74 nm is also present. This is the characteristic value for a carbonate-containing LDH, indicating that even under tightly controlled conditions, contamination by carbonate is difficult to avoid totally [39] because the driving force of the ion-exchange reaction by CO_3^{2-} is larger than that of $[Ce(dipic)_3]^{3-}$ or $dipic^{2-}$ in the solutions. In the XRD pattern of the intercalated product calcined at 1100 °C, the presence of CeO_2 along with ZnO and $ZnAl_2O_4$ confirmed the successful incorporation of cerium into the LDH structure.

3.4.2.1.3 IR spectroscopy

The FTIR absorption spectrum of Zn_2Al-Ce(dipic)-LDH shown in Fig. 3-9 (b) is consistent with the formation of a cerium complex-containing LDH network. The typical bands in the low frequency region (400 - 900 cm^{-1}) [40] can be assigned to the O-M-O deformation mode at 431 cm^{-1}, and M-O stretching vibrations at 555 and 766 cm^{-1}. Comparison of the spectra of $Na_3[Ce(dipic)_3]$ (c) and Zn_2Al-Ce(dipic)-LDH (b) showed a good coincidence of the majority of the characteristic bands in the region

1000 - 1800 cm^{-1}. The most intense absorption bands at about 1623 and 1383 cm^{-1} can be assigned to the asymmetric and symmetric stretching vibrations of the carboxylate group, respectively. The bands at 1590, 1437 and 1278 cm^{-1} may be assigned to the vibrations of the skeletal modes of the pyridine ring. It should be pointed out that the strong broad band observed around 1380 cm^{-1} also involves a contribution from other interlayer species (nitrate anions, carbonate anions) and as well as the symmetric vibration of the carboxylate groups. Both free and coordinated $dipic^{2-}$ ligands display very similar IR features and are difficult to differentiate.

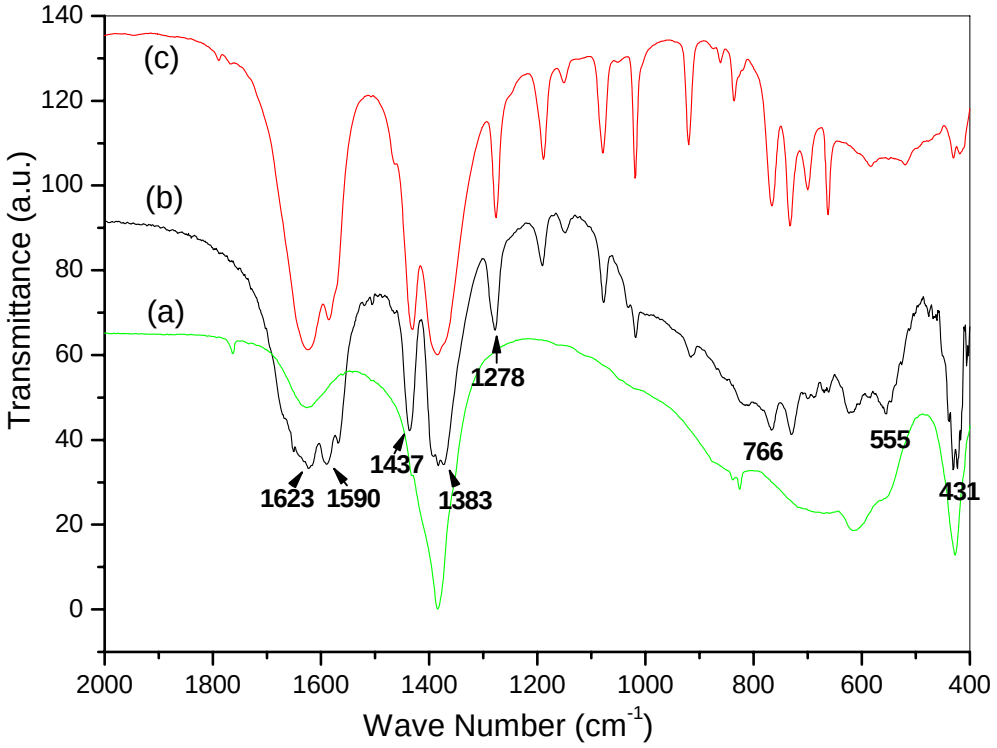

Fig. 3-9 FTIR spectra of Zn_2Al-NO_3-LDH precursor (a), Zn_2Al-Ce(dipic)-LDH (b) and $Na_3[Ce(dipic)_3]$ complex (c)

3.4.2.1.4 UV spectroscopy

The UV absorption spectra for the supernatant liquids remaining after the ion-exchange reactions are shown in Fig. 3-10. For a variety of $[Ce(dipic)_3]^{3-}$/CuZnAl-LDH molar ratios, the UV absorption bands of the ligand species were identical to those of the $[Ce(dipic)_3]^{3-}$ precursor. This demonstrates that once Zn^{2+} cations were incorporated into LDH layers in advance, they could not coordinate with $dipic^{2-}$ ligands and promote the decomposition of $[Ce(dipic)_3]^{3-}$ anions. Thus the ion-exchange method is superior to the coprecipitation one.

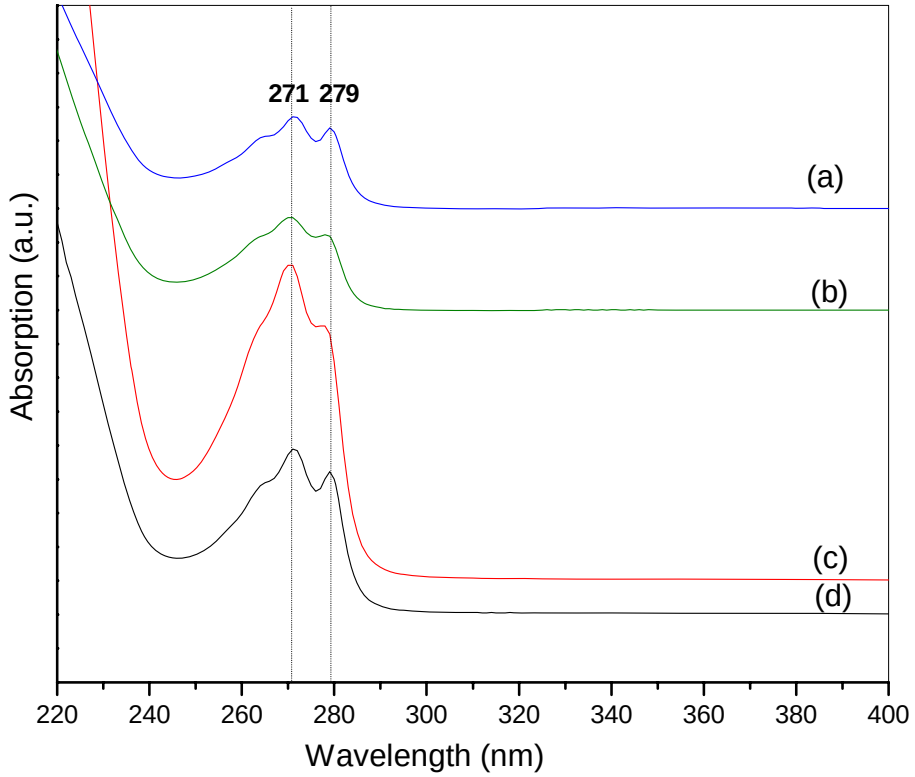

Fig. 3-10 UV absorption spectra of $[Ce(dipic)_3]^{3-}$ complex (a) and the supernatant solutions of some products with different $[Ce(dipic)_3]^{3-}$/ZnAl-LDH ratios: Zn_2Al-Ce(dipic)-1/3-LDH (b), Zn_2Al-Ce(dipic)-1/1-LDH (c), Zn_2Al-Ce(dipic)-1/6-LDH (d)

Moreover, the solid state diffuse reflectance UV spectra of

$[Ce(dipic)_3]^{3-}$-Zn_2Al-LDH materials were also recorded, and they were identical to that of $Na_3[Ce(dipic)_3]$ complex. This confirms that the complex anion has been successfully incorporated in the LDH host.

3.4.2.1.5 Back-exchange experiments

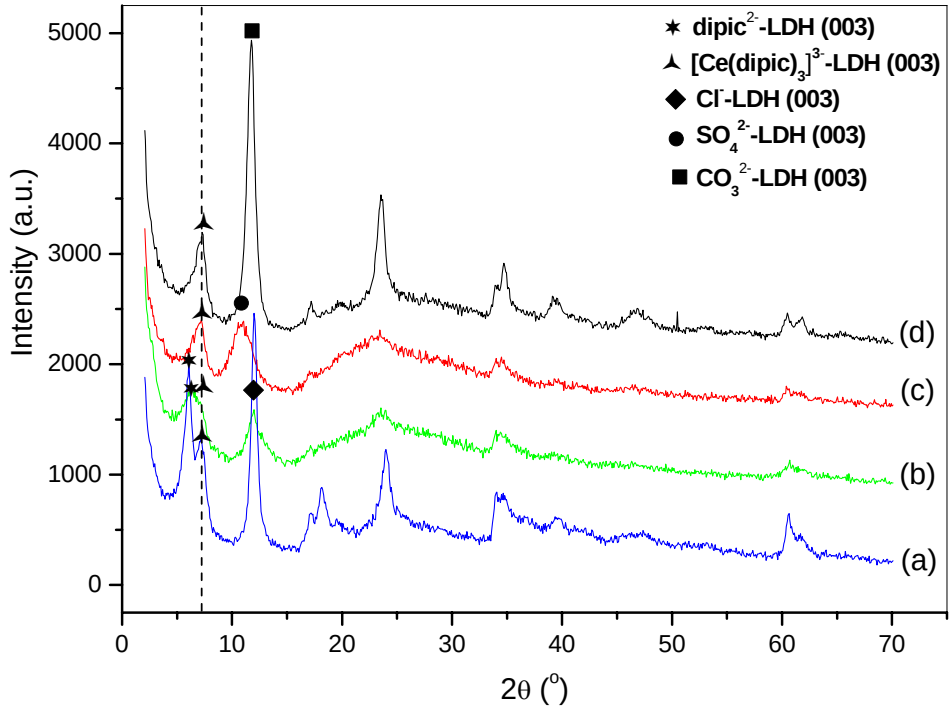

Fig. 3-11 XRD patterns of the samples prepared by the back-exchange method: Zn_2Al-Ce(dipic)-LDH precursor(a), and products after exchange with Cl^- (b), SO_4^{2-} (c) and CO_3^{2-} (d) (The signs in figures represent the (003) reflections of different LDH phases)

The sample Zn_2Al-Ce(dipic)-LDHs were back exchanged with some inorganic anions having the affinities for LDHs which vary in the order $Cl^- < SO_4^{2-} < CO_3^{2-}$ [41,42]. After the back exchange, the XRD and IR spectra of products are shown in Fig. 3-11 and Fig. 3-12, respectively. In XRD patterns, it was shown that the first reflection of (00*l*) peaks at d = 1.48 nm which corresponds to the LDH phase with interlayer $dipic^{2-}$

anions became reduced in intensity after exchange with Cl^-, and disappeared after exchange with SO_4^{2-} and CO_3^{2}. And the characteristic (003) reflections of the LDH phases containing Cl^-, SO_4^{2-} and CO_3^{2-} anions [41,42] were observed at d = 0.76, 0.89 and 0.76 nm, respectively. However, most noteworthy is that the (003) reflection of the second LDH phase at d = 1.24 nm which arises from the LDH with interlayer $[Ce(dipic)_3]^{3-}$ anions remained after the back exchange reactions with three inorganic anions (see the marked line in Fig. 3-11). This suggests that although $dipic^{2-}$ is readily replaced by the inorganic anions, the $[Ce(dipic)_3]^{3-}$ anion is more strongly held and is not displaced even by CO_3^{2-} anion which is known to have a strong affinity for LDHs.

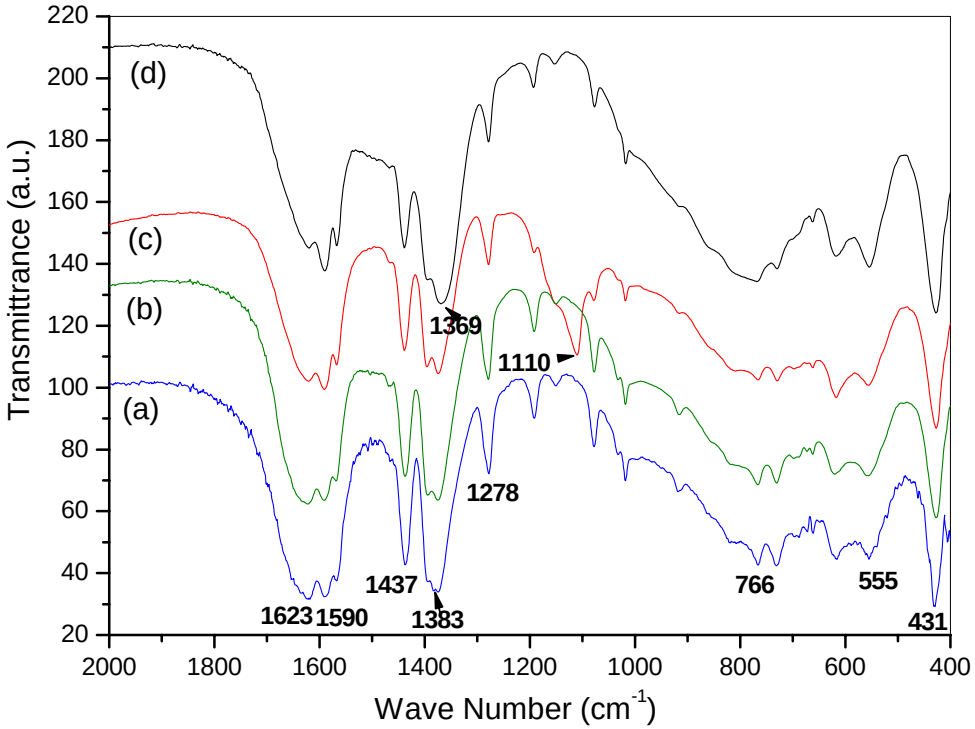

Fig. 3-12 IR spectra of samples prepared by the back-exchange method: the precursor Zn_2Al-Ce(dipic)-LDH (a), and after exchange with Cl^- (b), SO_4^{2-} (c) or CO_3^{2-} (d)

In IR spectra (Fig. 3-12) of the LDH materials obtained by the exchange reactions

of Zn_2Al-Ce(dipic)-LDH with the inorganic anions, the characteristic bands of the carboxylate group (1623, 1383 cm^{-1}) and pyridine ring (1590, 1437, 1278 cm^{-1}) are still present, but their intensity is reduced compared with that in the precursor. This is consistent with the loss of $dipic^{2-}$ but the retention of $[Ce(dipic)_3]^{3-}$ in the LDH galleries. The strong and broad IR band centred at around 1383 cm^{-1} is reserved but the centre of this peak shifts in different exchange products, especially to 1369 cm^{-1} in Fig. 3-12 (d). It is related to the overlap of the vibration bands of CO_3^{2-}, NO_3^- and OCO^- at this region, and so it is difficult to distinguish these groups. In Fig. 3-12 (c) however, the IR vibration of SO_4^{2-} at 1110 cm^{-1} is obvious, which confirms the replacement of intercalated anions by SO_4^{2-}.

3.4.2.2 Effect of varying the experimental conditions

The effects on the intercalation process of varying some parameters such as reaction temperature/pressure, reaction time, initial concentration and identity of LDH precursor were investigated.

3.4.2.2.1 Effect of precursor

The LDH precursor containing intercalated dodecyl sulfate (DDS) was prepared following the method described by Prévot *et al.* [30]. The XRD pattern of the resulting Zn_2Al-DDS-LDH is illustrated in Fig. 3-13(a) and features both a series of (00*l*) reflections and the (110) reflection, characteristic of LDHs. The interlayer spacing of Zn_2Al-DDS-LDH is 2.60 nm. After the exchange with $[Ce(dipic)_3]^{3-}$ anion under the same condition as for the Zn_2Al-NO_3-LDH precursor above, the interlayer spacing of Zn_2Al-Ce(dipic)-DDS-LDH decreased to 1.22 nm (b), suggesting that the interlayer

DDS anions had been completely replaced by $[Ce(dipic)_3]^{3-}$ by this ion-exchange reaction. Interestingly, no evidence for the intercalation of $dipic^{2-}$ ligands was observed suggesting that the pre-expansion of LDH structure with DDS favors the intercalation of large complex anions rather than their decomposition. Similarly, Zn_2Al-Ce(dipic)-Cl-LDH was prepared by an anion-exchange reaction of Zn_2Al-Cl-LDH precursor with $[Ce(dipic)_3]^{3-}$. However, for the resulting Zn_2Al-Ce(dipic)-Cl-LDH (c), the XRD pattern was similar to that of Zn_2Al-Ce(dipic)-NO_3-LDH (d) but the chloride precursor favors a bigger amount of LDH phase with intercalated $[Ce(dipic)_3]^{3-}$ and a smaller amount of LDH phase with intercalated $dipic^{2-}$. The interlayer anions in LDH precursors have an effect on the composition of final exchange products [42]. The IR analysis is consistent with the conclusions obtained from XRD data.

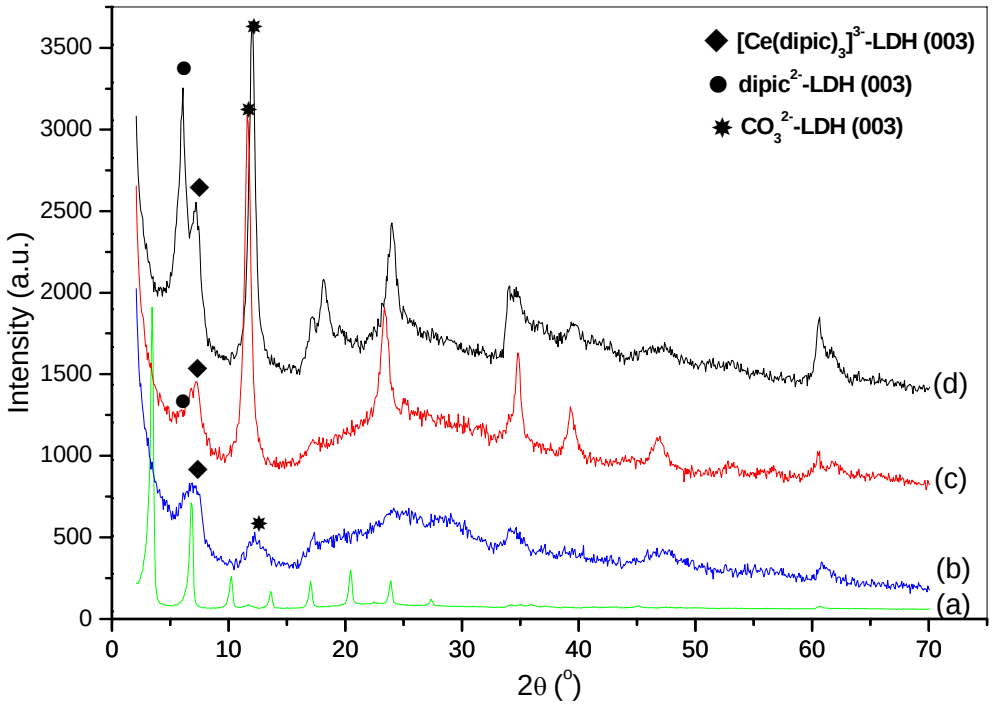

Fig. 3-13 XRD patterns of Zn_2Al-DDS-LDH precursor (a) and the ion-exchange products from

different LDH precursors with $[Ce(dipic)_3]^{3-}$: Zn_2Al-Ce(dipic)-DDS-LDH (b), Zn_2Al-Ce(dipic)-Cl-LDH (c) and Zn_2Al-Ce(dipic)-NO_3-LDH (d)

(The signs mark the (003) reflections of different LDH phases)

3.4.2.2.2 Effect of temperature/pressure

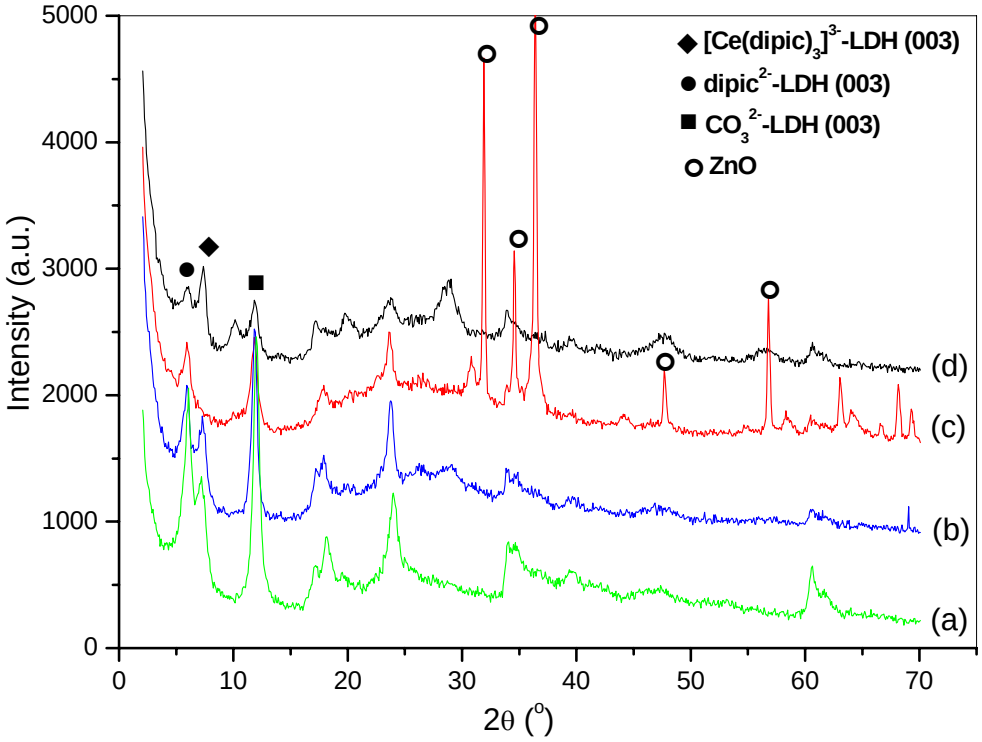

Fig. 3-14 XRD patterns of Zn_2Al-Ce(dipic)-LDH (a), Zn_2Al-Ce(dipic)-LDH+H_2O-auto (b), Zn_2Al-dipic-auto-LDH (c) and Zn_2Al-Ce(dipic)-auto-LDH (d)

The XRD patterns of intercalated samples prepared in an autoclave at 120 °C or at room temperature/pressure were different, as shown in Fig. 3-14. In the pattern (b) of pre-formed Zn_2Al-Ce(dipic)-LDH suspended in water and then treated in an autoclave, the positions and intensities of all the diffraction peaks were unchanged compared with

the pattern (a) of Zn_2Al-Ce(dipic)-LDH, which indicates that the material has considerable structural stability. When it was attempted to prepare Zn_2Al-dipic-LDH or Zn_2Al-Ce(dipic)-LDH under autoclave conditions however, impurity phases were invariably present. For Zn_2Al-dipic-auto-LDH (c), the characteristic reflections of ZnO phase were very obvious and for Zn_2Al-Ce(dipic)-auto-LDH (d), many unidentified weak peaks were observed. It may be explained that the high temperature/pressure environment promotes the interaction between $dipic^{2-}$ ligands and Zn^{2+} cations, which influences the structure and composition of LDH materials and leads to the presence of impurity phases. It should be noted that in the pattern (d) of Zn_2Al-Ce(dipic)-auto-LDH, the relative diffraction intensity of $[Ce(dipic)_3]^{3-}$-LDH phase (d = 1.24 nm) and $dipic^{2-}$-LDH phase (d = 1.48 nm) was different from that in Zn_2Al-Ce(dipic)-LDH (a). Under autoclave conditions, $dipic^{2-}$ ligands generated from the decomposition of parts of interlayer $[Ce(dipic)_3]^{3-}$ complexes give priority to the formation of Zn-dipic complexes, rather than the direct intercalation into interlayer galleries as is observed under ambient pressure. Furthermore, the autoclave restricts the exposure of the mixture to CO_2 from air in the reaction process so that a smaller amount of CO_3^{2-}-LDH phase was observed.

The comparison of TGA and DTA curves of Zn_2Al-Cedipic-auto-LDH (b) with Zn_2Al-Cedipic-LDH (a) prepared under different Temperature/Pressure conditions, as shown in Fig. 3-15, displayed the product composition. Both had similar thermal behaviours and 4 weight-loss stages, but the whole loss amount of Zn_2Al-Cedipic-auto-LDH (b) was reduced because the quantity of intercalated LDH

structures decreased. The second stage which presented the loss of structural water was smaller, suggesting the high T/P conditions decreased interlayer water molecules. The third stage which showed the dehydroxylation of OH groups and removal of CO_3^{2-} anions were shifted to high temperature (the endothermic peak from 255 to 272 ^oC), which resulted from the dehydration of metal hydroxids. The forth stage which presented the removal of intercalated organic anions was shifted to low temperature (the exothermic peak from 367 to 359 ^oC), which may be explained by the irregular stacking of LDHs and metal oxides leading to the unorderly arrangement of layers and the easy loss of interlayer anions. In a word, the high T/P conditions resulted in the presence of many complicated phases.

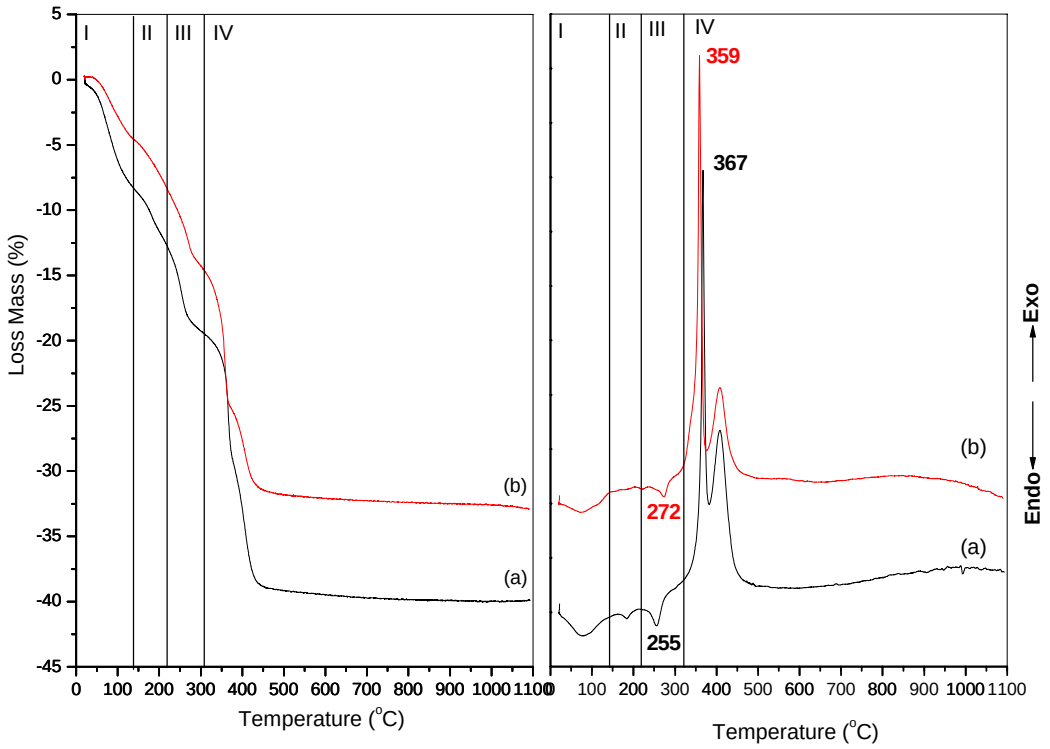

Fig. 3-15 TGA and DTA curves of Zn_2Al-Ce(dipic)-LDH (a) and Zn_2Al-Ce(dipic)-auto-LDH (b)

3.4.2.2.3 Effect of charge density in the layers

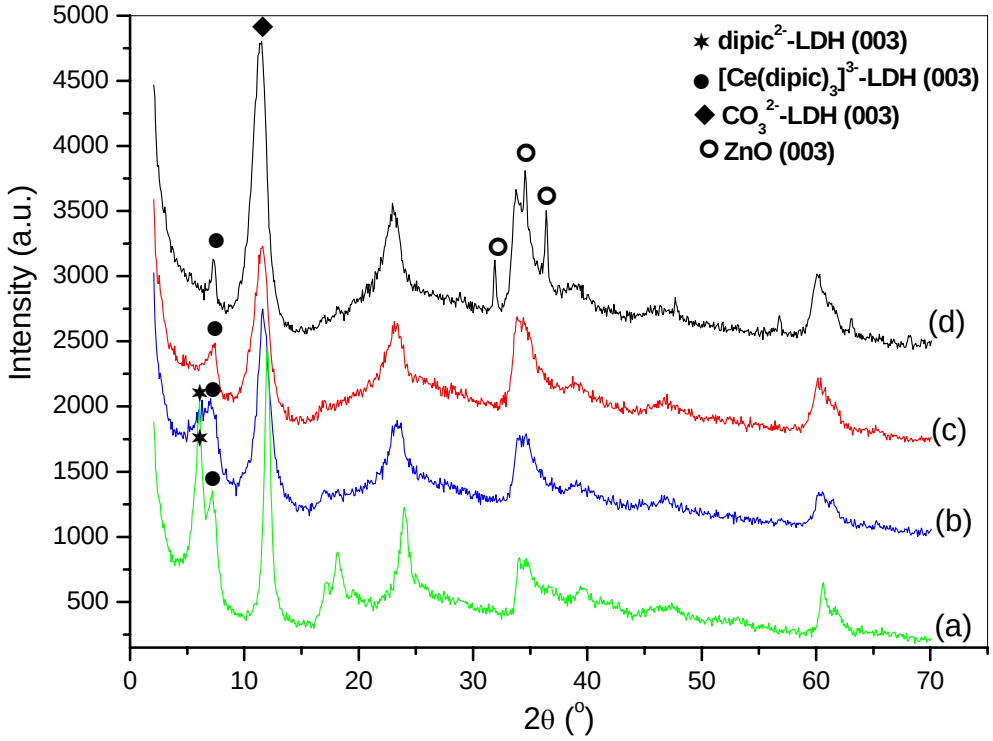

Fig. 3-16 XRD patterns of Zn_xAl-Ce(dipic)-LDHs with different Zn^{2+}/Al^{3+} ratios: x = 2/1 (a), 3/1 (b), 4/1 (c) and 5/1 (d) (The signs mark the (003) reflections of different LDH phases)

The charge density of the LDH layers is related to the value of the M^{2+}/M^{3+} ratio. Zn_xAl-NO_3-LDH precursors with Zn^{2+}/Al^{3+} ratios of 2/1, 3/1, 4/1 and 5/1 corresponding to decreasing charge density of LDH layers, were used as host materials for the intercalation of $[Ce(dipic)_3]^{3-}$ complexes. The XRD patterns of a series of samples are illustrated in Fig. 3-16. The characteristic (110) and (113) reflections at 2θ values between 60 and 62° were clearly observed, indicating the retention of the layer structure. A CO_3^{2-}-LDH phase was present in all samples. In the case of the 2/1 sample, the $[Ce(dipic)_3]^{3-}$-LDH phase (d = 1.24 nm) and $dipic^{2-}$-LDH phase (d = 1.48 nm) were

obtained as discussed above. With increasing Zn/Al ratios, the reflections from the LDH phase containing interlayer $[Ce(dipic)_3]^{3-}$ anions were unchanged but the reflections from the LDH phase with interlayer $dipic^{2-}$ anions were reduced gradually in intensity. Until the 5/1 sample, only the $[Ce(dipic)_3]^{3-}$-LDH phase was observed with no $dipic^{2-}$-LDH phase. The impurity phase giving reflections at $2\theta = 31.9°$, 34.5° and 36.5° in Fig. 3-16 (d) could be identified as ZnO, arising from excess zinc nitrate in the precursor. A correlation was found to exist between the Zn^{2+}/Al^{3+} molar ratio and the composition and property of the material obtained after the exchange reaction with $[Ce(dipic)_3]^{3-}$. With increasing Zn^{2+}/Al^{3+} ratio, the charge density of the layers decreased, which reduced the electrostatic interaction between positively charged layers and negatively charged interlayer anions [39]. Therefore, the quantity of intercalated $[Ce(dipic)_3]^{3-}$ decreased, the complex anions with a stronger driving force were preferentially incorporated, and their decomposition was inhibited.

The IR spectra of the $[Ce(dipic)_3]^{3-}$ intercalated LDHs with different Zn^{2+}/Al^{3+} ratios are shown in Fig. 3-17. In each case the characteristic bands of the host lattice and interlayer anions, as described above, are observed. The bands around 1590, 1437 and 1278 cm^{-1} may be assigned to the skeletal modes of the pyridine ring and their intensities are clearly reduced with increasing Zn^{2+}/Al^{3+} ratio. The absorption band of the 2/1 sample at 1623 cm^{-1}, due to the asymmetric stretching vibration of the carboxylate group is shifted to 1643 cm^{-1} in the 5/1 sample. This shift to higher wave number indicates that the interaction between the layers and interlayer anions becomes weaker, consistent with the decrease in the charge density of the layers. The position of

the symmetric stretching vibration of the carboxylate group at around 1380 cm^{-1} has no obvious change, which was explained by three superposed vibrations of nitrate, carbonate and complex anions.

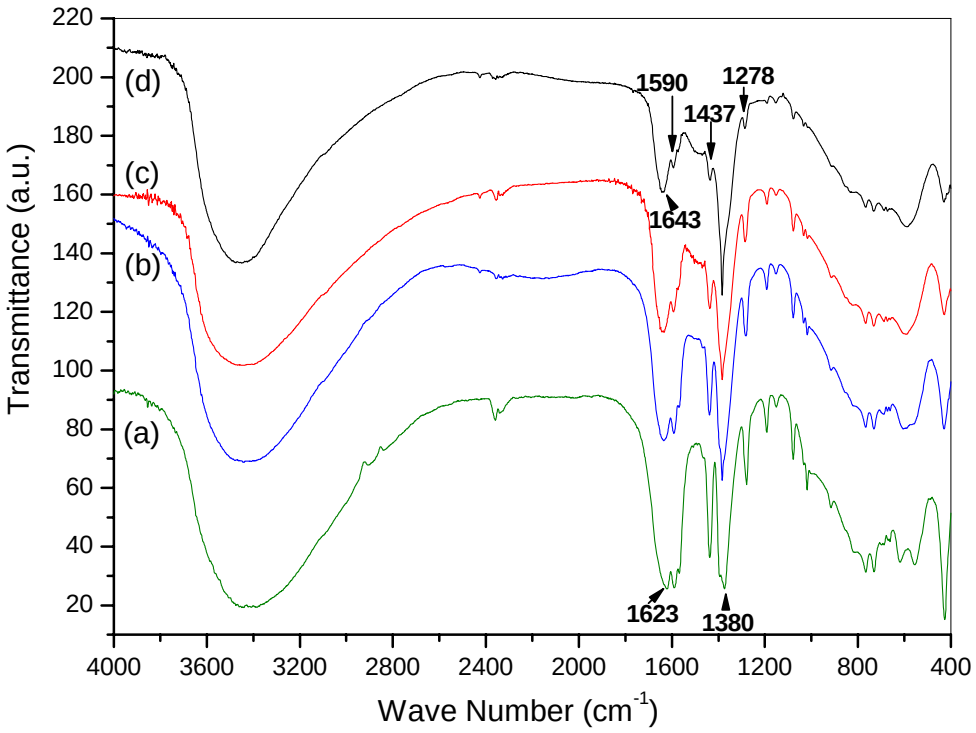

Fig. 3-17 IR spectra of Zn_xAl-Ce(dipic)-LDHs with different Zn^{2+}/Al^{3+} ratios: x = 2/1 (a), 3/1 (b), 4/1 (c) and 5/1 (d)

Table 3-3 Zn/Al/Ce molar ratios of intercalated samples

sample	expected ratio	actual ratio
Zn_2Al-NO_3-LDH	Zn_2Al	$Zn_{2.01}Al$
Zn_2Al-Ce(dipic)-LDH	$Zn_2AlCe_{0.33}$	$Zn_{1.94}AlCe_{0.15}$
Zn_3Al-Ce(dipic)-LDH	$Zn_3AlCe_{0.33}$	$Zn_{2.61}AlCe_{0.27}$
Zn_4Al-Ce(dipic)-LDH	$Zn_4AlCe_{0.33}$	$Zn_{3.42}AlCe_{0.19}$
Zn_5Al-Cedipic-LDH	$Zn_5AlCe_{0.33}$	$Zn_{4.03}AlCe_{0.09}$

The elemental analysis results for a series of samples with different Zn^{2+}/Al^{3+} are listed in Table 3-3. It is shown that Zn/Al ratios are relatively close to the expected ones, but the discrepancy between actual Ce/Al ratios and expected ones increases with increasing Zn/Al ratios. For the 2/1 sample, Ce/Al ratio is 0.15, lower than the theoretical value of 0.33, which was due to the decomposition of $[Ce(dipic)_3]^{3-}$ into $dipic^{2-}$ as observed in the XRD analysis. For other samples, Ce/Al ratios are lower than the expected one and they decrease gradually, especially 0.09 in the 5/1 sample. For these samples with higher Zn/Al ratios, the main reason for inhibiting the intercalation of $[Ce(dipic)_3]^{3-}$ anions was the decrease of the charge density of the layers rather than the decomposition of the complexes. And then the driving force of the ion-exchange reaction was reduced as the interaction between layers cations and interlayer anions decreased, so that it became more difficult for intercalation of the complex cations into LDH interlayers. The quantity of $[Ce(dipic)_3]^{3-}$-LDH phase was reduced gradually, in agreement with the XRD and IR analysis.

3.4.2.2.4 Effect of reagent concentration

To study the effect of initial $[Ce(dipic)_3]^{3-}$ concentration on the ion-exchange process with Zn_2Al-NO_3-LDH, some experiments were carried out under the same conditions except for varying the initial concentration of $[Ce(dipic)_3]^{3-}$ and added LDH masses with a fixed ratio of Ce/Al = 1:1. Fig. 3-18 shows the exchange ratios for various initial concentrations. The vertical axis is exchange ratio which was calculated from Qe/Qs, where Qs is the ideal saturation amount of complex per unit weight of the LDH (conversion 100%, Qs=(1/3)/358*1000 = 0.9311 mmol/g, where (1/3) is the ideal

molar amount of $[Ce(dipic)_3]^{3-}$ complex per unit hybrid and 358 is the unit molar mass of the Zn_2Al-LDH precursor, expressed by the formula $[Zn_2Al(OH)_6](NO_3)\cdot 2H_2O$) and Qe is the actual amount of complex per unit weight of the LDH. Exchange ratio represents the percentage of this maximum that the ion exchange process reaches. With the increase in reagent concentration, the exchange ratio increased up to 40% because the high concentration could restrict the effect of CO_3^{2-} contamination and favor the intercalation of the complex anions. The curve showed a maximum value at around 5 mmol/l under this experimental condition. At this point, it seemed that the diffusion step and the exchange step reached a balance. If the experimental conditions are further optimized, the exchange rate may be accurately controlled until 100%.

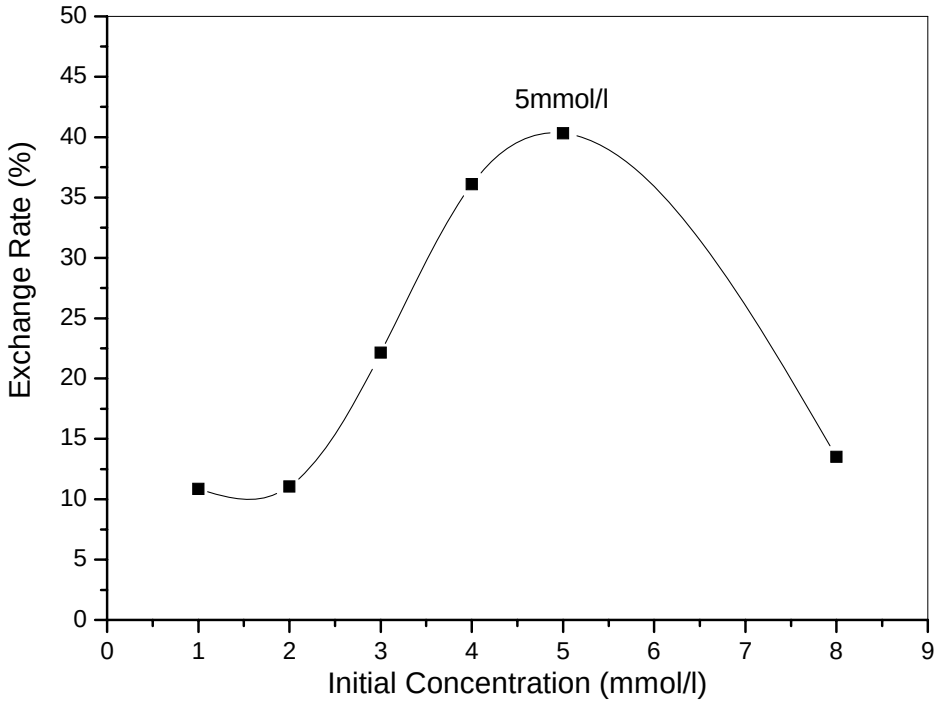

Fig. 3-18 The variation of ion-exchange rate of Zn_2Al-NO_3-LDH and $[Ce(dipic)_3]^{3-}$ with different initial concentrations

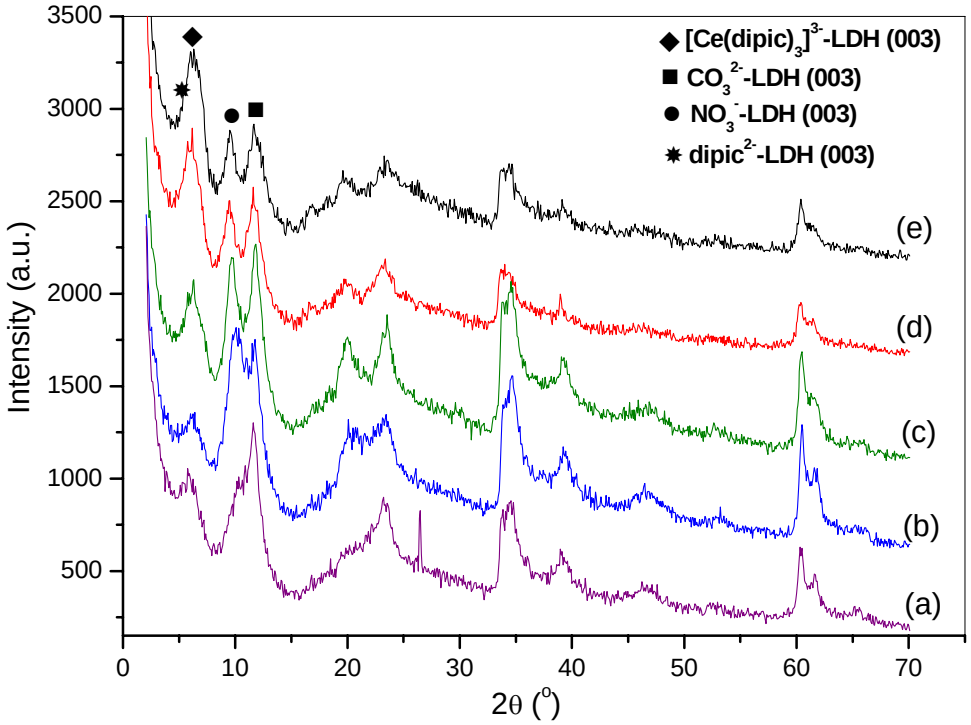

Fig. 3-19 XRD patterns of Zn_2Al-Ce(dipic)-LDH samples prepared with different initial $[Ce(dipic)_3]^{3-}$ concentrations: 1 mmol/l (a), 2 mmol/l (b), 3 mmol/l (c), 4 mmol/l(d), and 5 mmol/l(e) (The signs mark the (003) reflections of different LDH phases)

XRD patterns of Zn_2Al-Ce(dipic)-LDH samples prepared with different initial $[Ce(dipic)_3]^{3-}$ concentrations at a fixed Ce/Al ratio showed that the composition changes with concentration. In Fig. 3-19, it was seen that when the reagent concentration increased from 1 mmol/l to 5 mmol/l, the intensities of reflection peaks of varied LDH phases took on different trends: those of $[Ce(dipic)_3]^{3-}$-LDH phase were enhanced but NO_3^--LDH and CO_3^{2-}-LDH phases were reduced gradually. These $dipic^{2-}$-LDH reflections were always very weak, due to the ion-exchange conditions. This confirms that a high $[Ce(dipic)_3]^{3-}$ concentration favored intercalation of the complex anions and inhibited formation of the contaminant phases.

After studying the influence of varying the experimental conditions, these

optimized parameters for the preparation of $[Ce(dipic)_3]^{3-}$ intercalated LDH materials were: a ratio M^{2+}/M^{3+} = 2, a $[Ce(dipic)_3]^{3-}$ concentration around 5 mmol/l and an exchange period around 10 h at room temperature/pressure.

3.4.2.3 Adsorption isotherm of $[Ce(dipic)_3]^{3-}$ on Zn_2Al-NO_3-LDH

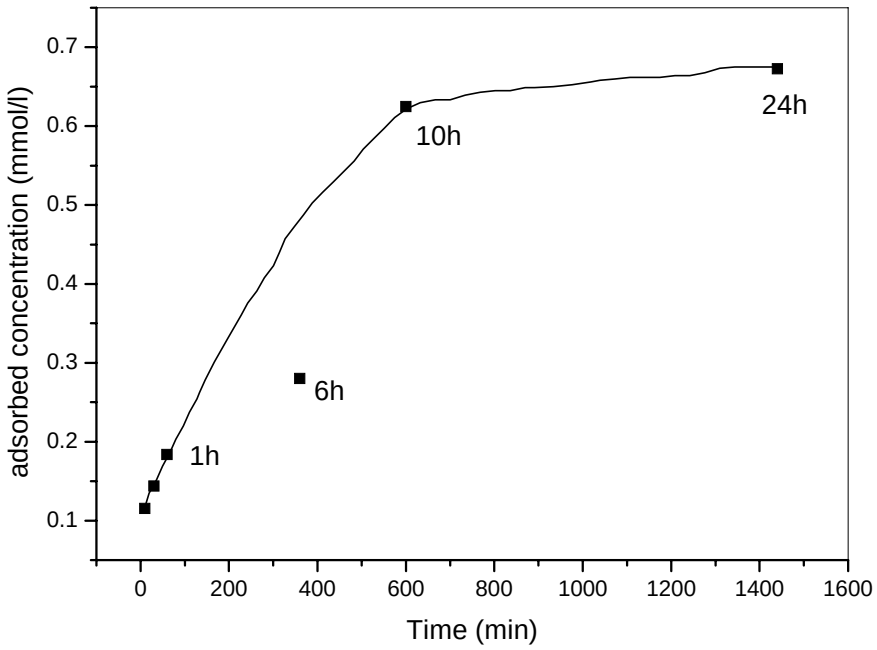

Fig. 3-20 Kinetic curve for the exchange reaction of $[Ce(dipic)_3]^{3-}$ with Zn_2Al-NO_3-LDH

Before carrying out adsorption experiments, the kinetics of the exchange reaction of $[Ce(dipic)_3]^{3-}$ with the Zn_2Al-NO_3-LDH phase was investigated using UV spectroscopy (at 271 nm), as shown in Fig. 3-20. As monitored by the variation in $[Ce(dipic)_3]^{3-}$ absorbance in solution, the amounts of $[Ce(dipic)_3]^{3-}$ adsorbed increased over a 10 h period, thereafter reaching equilibrium. To ensure an equilibrium state was reached, a contact time of 45 h was employed in our adsorption experiments.

Fig. 3-21 shows the adsorption isotherm for $[Ce(dipic)_3]^{3-}$ on Zn_2Al-NO_3-LDH. The results suggest that the adsorption proceeds in two steps: saturation of the external

sites takes place up to 0.35 mmol/g and is followed by an interlayer exchange process occurring at high equilibrium concentrations from 0.35 to 0.55 mmol/g [31]. The first part of the adsorption isotherm can be clearly identified as an L-type isotherm, which implies that the adsorption sites are independently distributed on the surface of the layers. The adsorption isotherm reaches a plateau at an intermediate equilibrium concentration (Ce). At higher Ce, Qe increases again, and the isotherm tends towards an S-type for Ce > 0.8 mmol/L. This suggests that the adsorption process involves different mechanisms. At first, the Ce-containing complex is adsorbed onto the external surface of LDHs through hydrogen bonding and other electrostatic forces. The initially adsorbed species may modify the surface characteristics of LDHs from hydrophilic to hydrophobic. Subsequently, the hydrophobic interactions between complex molecules may increase the adsorption. For higher values of Ce > 0.8 mmol/L, an interlayer anion exchange process with complex anions on LDHs may occur [43]. Several models have been developed to describe adsorption phenomena. Here, the adsorption data were in good accord with the Langmuir equation at lower Ce (< 0.8 mmol/L): Ce/Qe = Ce/Qm + 1/(Qm Ke), where Qe is the amount of complex per unit weight of the LDH, Ce the equilibrium concentration of the adsorbate, Qm the maximum amount of adsorbate that could be adsorbed in a monolayer (adsorption capacity, mmol/g), and Ke is the Langmuir constant related to the energy of adsorption. The fit based on the Langumir adsorption model is displayed in the inset of Fig. 3-21: Ce/Qe = 0.3527 + 2.3575Ce (R = 0.98). This confirms a surface adsorption process is occurring at lower Ce. Qm as calculated from this model is 0.42 mmol/L, which should be the maximum uptake.

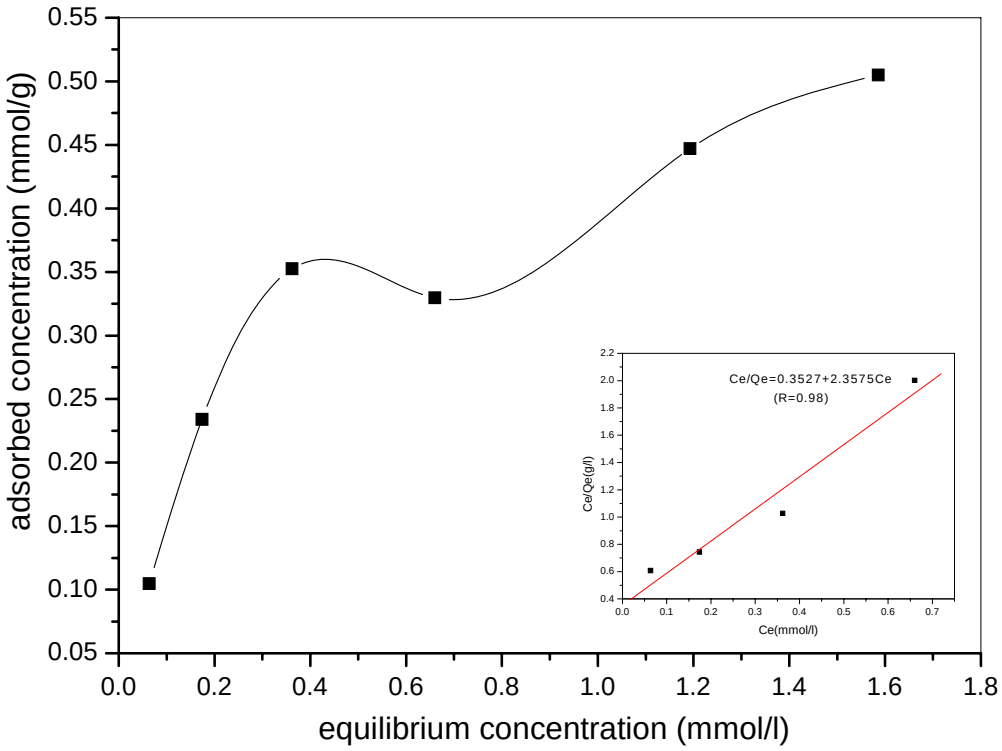

Fig. 3-21 $[Ce(dipic)_3]^{3-}$ adsorption isotherm on Zn_2Al-NO_3-LDH precursors; insert graph: the fit based on the Langumir adsorption model

To further study the interaction mechanism, the XRD patterns and IR spectra of the materials after adsorption were measured. At higher equilibrium concentration values, X-ray diffraction analysis showed a shift of the interlayer spacing to a higher value consistent with the formation of the Zn_2Al-LDH containing the Ce complex. The decrease in the intensity of the d(003) peak of the Zn_2Al-NO_3-LDH phase was simultaneously observed, confirming the topotactic anion exchange in the LDH structure of part of the nitrate by the complex anions. FTIR spectroscopy data are consistent with these conclusions. Thus, the adsorption of $[Ce(dipic)_3]^{3-}$ on Zn_2Al-LDH may generally occur through two processes: external surface adsorption (I, Ce < 0.8mmol/L) and interlayer anion exchange (II, Ce > 0.8mmol/L).

3.5 Intercalation of $[Ce(dipic)_3]^{3-}$ with other LDHs

3.5.1 Structural characterization of CuZnAl-Ce(dipic)-LDHs

3.5.1.1 UV spectroscopy

It was important to study if Cu^{2+} free or fixed in LDH framework would react with $[Ce(dipic)_3]^{3-}$ complex before the preparation of CuZnAl-Cedipic-LDHs. UV spectra of a series of the supernatants including the sample after ion-exchange (Fig. 3-22 (c)) with $[Ce(dipic)_3]^{3-}$, Cu^{2+} + $[Ce(dipic)_3]^{3-}$ (d), and Cu^{2+} + $dipic^{2-}$ (a) were measured to investigate the changes of coordination environment of $dipic^{2-}$ ligands, as shown in Fig. 3-22.

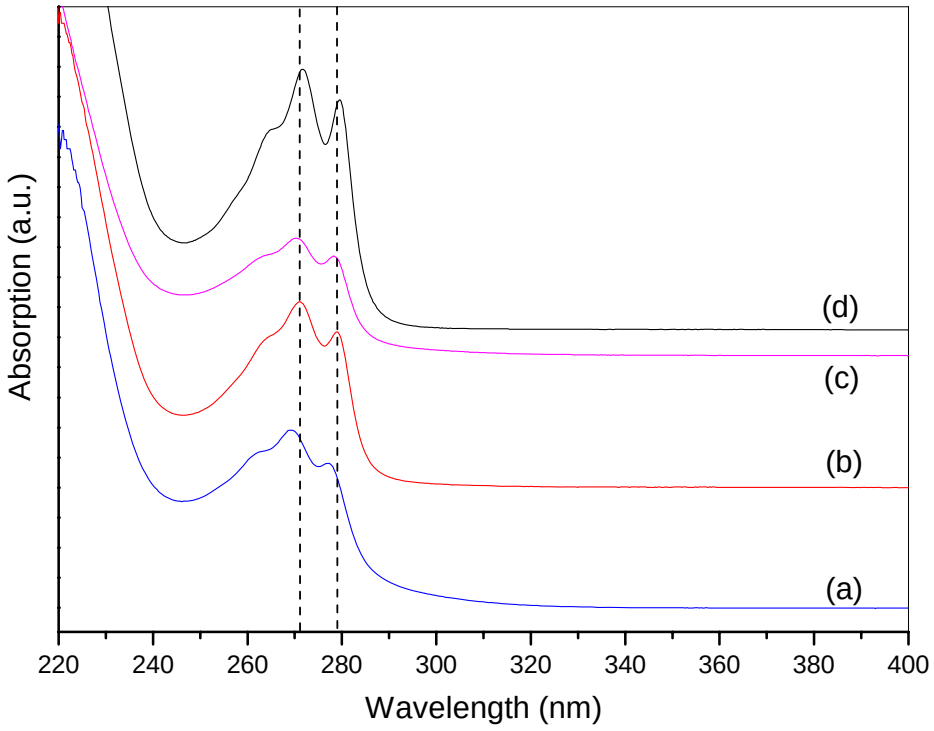

Fig. 3-22 UV absorption spectra of the supernatants of samples: Cu^{2+} + $dipic^{2-}$ (a), after ion-exchange reaction (b), Cu^{2+} + $[Ce(dipic)_3]^{3-}$ (c) and $[Ce(dipic)_3]^{3-}$ (d).

Comparison with these of initial $[Ce(dipic)_3]^{3-}$ (d), UV adsorption bands of free

Cu^{2+} + $[Ce(dipic)_3]^{3-}$ solution (c) were also located at 271 and 279 nm, and had no shifts. But these of Cu^{2+} + $dipic^{2-}$ solution (a) obviously shifted to 269 and 276 nm. It suggested that in the former solution (c), $dipic^{2-}$ ligands in $[Ce(dipic)_3]^{3-}$ complex were still coordinated with cerium like before and Cu^{2+} anions co-existed stably with Ce-dipic complex; however, the shift in the latter solution (a) may be caused by Cu-dipic complex being formed, in which the coordination environment of $dipic^{2-}$ ligands was different. Therefore, the ion-exchange method was appropriate to prepare CuZnAl-Ce(dipic)-LDHs but the co-precipitation method should be ignored because of the presence of Zn-dipic complex to destroy $[Ce(dipic)_3]^{3-}$ structure as the above discussion. It was obvious that the UV spectrum of the supernatant prepared in ion-exchange method (b) was the same as that of Ce-dipic complex precursor (d). In this chapter, CuZnAl-Cedipic-LDHs were synthesized according to the ion-exchange reaction between CuZnAl-NO_3-LDH and $[Ce(dipic)_3]^{3-}$.

3.5.1.2 Elemental analysis

Table 3-4 Cu/Zn/Al/Ce molar ratios for intercalated samples

sample	expected ratio	actual ratio
CuZnAl-LDH	CuZnAl	$Cu_{0.99}Zn_{1.04}Al$
CuZnAl-Ce(dipic)-3/1-LDH （Ce/A l= 3:1）	$CuZnAlCe_{0.33}$	$Cu_{0.83}Zn_{0.90}AlCe_{0.61}$
CuZnAl-Ce(dipic)-LDH （Ce/Al = 1:1）	$CuZnAlCe_{0.33}$	$Cu_{0.89}Zn_{0.82}AlCe_{0.27}$
CuZnAl-Ce(dipic)-1/3-LDH （Ce/Al = 1:3）	$CuZnAlCe_{0.33}$	$Cu_{0.86}Zn_{0.98}AlCe_{0.32}$
CuZnAl-Ce(dipic)-1/6-LDH （Ce/Al = 1:6）	$CuZnAlCe_{0.17}$	$Cu_{0.99}Zn_{0.74}AlCe_{0.17}$

Table 3-4 lists the actual Cu/Zn/Al/Ce molar ratios in CuZnAl-Ce(dipic)-LDH samples prepared by the ion-exchange reactions between CuZnAl-NO_3-LDH and $[Ce(dipic)_3]^{3-}$, from an excess (3/1) to a deficiency (1/6). The Cu/Zn/Al ratios in the products were found to be in the range (0.99-0.83)/(0.98-0.74)/1, close to the values 0.99/1.04/1 in the LDH precursor. The actual Ce/Al ratio values in samples were related to initial contents of $[Ce(dipic)_3]^{3-}$ anions but they were quite consistent to the expected ones which suggested that $[Ce(dipic)_3]^{3-}$ anions could be intercalated into the layers. In this ion-exchange process, the decomposition of $[Ce(dipic)_3]^{3-}$ and contamination of CO_2 were reduced, which was approved in the following XRD and IR analysis. For $[Ce(dipic)_3]^{3-}$/CuZnAl-NO_3-LDH = 3/1, the anionic content was in excess of the stoichiometric value for an ion-exchange reaction, suggesting that the remainder were physically adsorbed on the LDH surface. The anions were strongly adsorbed on the surface since they could not be completely removed by extensive washing. For the other products, the observed Ce/Al ratios were in good agreement with the stoichiometric value. For $[Ce(dipic)_3]^{3-}$/CuZnAl-NO_3-LDH=1/1 and 1/3, the anionic contents were sufficient to completely replace the initial NO_3^- anions. Washing removed any excess physisorbed complexes. A small quantity of CO_3^{2-} anions was also intercalated into the interlayer galleries. For $[Ce(dipic)_3]^{3-}$/CuZnAl-NO_3-LDH = 1/6, the Ce/Al ratio in CuZnAl-Ce(dipic)-1/6-LDH was 0.17/1 which suggested that all of the complexes were intercalated into the LDH structure. The remaining positive charge was balanced by residua NO_3^- and contaminant CO_3^{2-}. Thus it can be concluded that $[Ce(dipic)_3]^{3-}$/CuZnAl-LDH = 1/1 is the appropriate experimental condition to ensure

the complete intercalation of $[Ce(dipic)_3]^{3-}$ anions.

3.5.1.3 XRD analysis

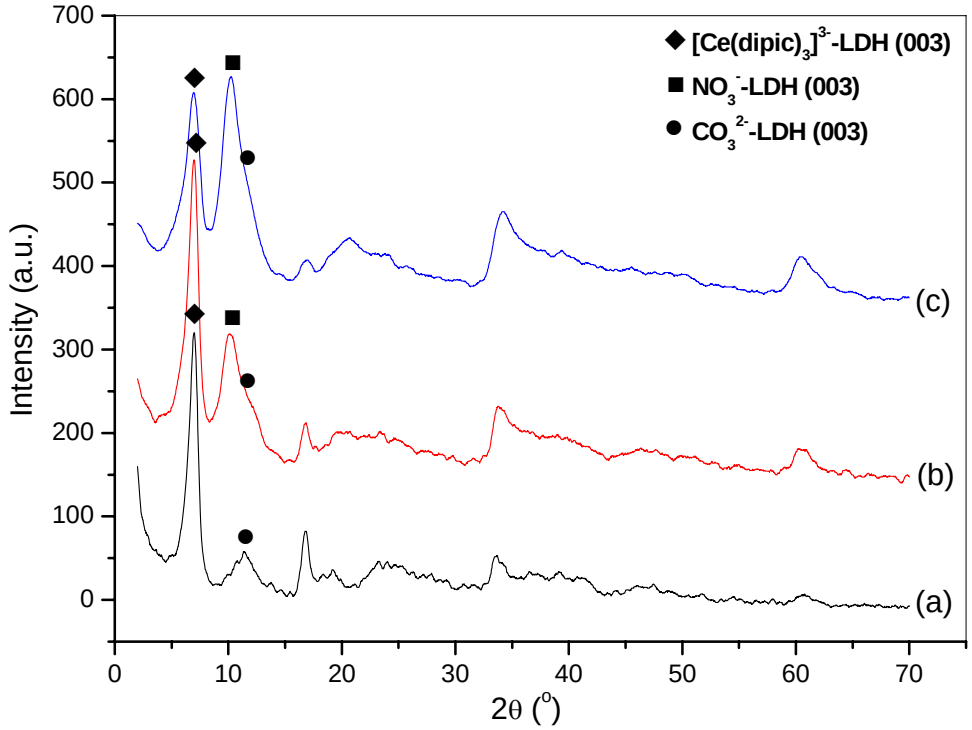

Fig. 3-23 XRD patterns of CuZnAl-Ce(dipic)-LDHs prepared with different $[Ce(dipic)_3]^{3-}$/CuZnAl-NO_3-LDH ratios: 1/1 (a), 1/3 (b), and 1/6 (c)

(The signs mark the (003) reflections of different LDH phases)

Fig. 3-23 displays the XRD patterns of CuZnAl-Ce(dipic)-LDHs prepared using different $[Ce(dipic)_3]^{3-}$/CuZnAl-LDH molar ratios. All of patterns showed the obvious diffraction at d = 1.28 nm, which represented the characteristic (003) reflection of intercalated $[Ce(dipic)_3]^{3-}$-LDH phase, as well as the characteristic (110) reflection. In comparison with the XRD pattern of Zn_2Al-Ce(dipic)-LDH (Fig. 3-8), the intensities of characteristic reflection peaks of $dipic^{2-}$-LDH phase at d = 1.48, 0.74 and 0.47 nm were reduced, suggesting the decomposition of $[Ce(dipic)_3]^{3-}$ anions occured to a lesser

extent. Furthermore the reflection intensity of the CO_3^{2-}-LDH phase decreased. This may be attributed to the change of electrostatic interaction between layer metal cations and interlayer anions because of the addition of Cu^{2+} in host layers.

With decreasing $[Ce(dipic)_3]^{3-}$/CuZnAl-NO_3-LDH ratios from 1/1 to 1/6, the intensities of the (003) diffraction peaks of intercalated products were gradually reduced. For $[Ce(dipic)_3]^{3-}$/CuZnAl-NO_3-LDH = 1/1, the amount of $[Ce(dipic)_3]^{3-}$ anions was in excess of the anion-exchange capacity. The (003) diffraction peak of $[Ce(dipic)_3]^{3-}$-LDH phase at d = 1.28 nm and that of CO_3^{2-}-LDH phase at d = 0.75 nm were present in the XRD pattern (Fig. 3-23 (a)). Although this ion-exchange reaction proceeded completely in theory, the presence of CO_3^{2-} from air could not be avoided. For $[Ce(dipic)_3]^{3-}$/CuZnAl-NO_3-LDH = 1/3, the amount of $[Ce(dipic)_3]^{3-}$ was stoichiometric. Because of the resistance in the diffusion and exchange steps, a fraction of the anions could participate in the reaction. Thus the diffraction peak of NO_3^--LDH phase at d = 0.88 nm was still observed in the pattern (b), in addition to two LDH phases. For $[Ce(dipic)_3]^{3-}$/CuZnAl-NO3-LDH =1/6, the amount of $[Ce(dipic)_3]^{3-}$ was scarce. The diffraction intensity of organic anions containing LDH decreased, accompanying with the obvious diffraction of residual NO_3^- anions. So the interlayer anions included objective $[Ce(dipic)_3]^{3-}$, initial NO_3^- and contamination CO_3^{2-}.

After CuZnAl-Ce(dipic)-LDH was calcined at 1100 °C, it yielded a mixture of metal oxides and spinels, whose diffraction peaks are shown in Fig. 3-24. In the calcination mixture, CuO, ZnO and $CuAl_2O_4$, $ZnAl_2O_4$ spinel phases were derived from layer cations in the LDH precursor and CeO_2 phase from interlayer $[Ce(dipic)_3]^{3-}$

complexes. Due to the nature of cerium, $CeAlO_3$ spinel phase was absent. But the presence of cerium oxide phase confirms the incorporation of Ce into the LDH structure.

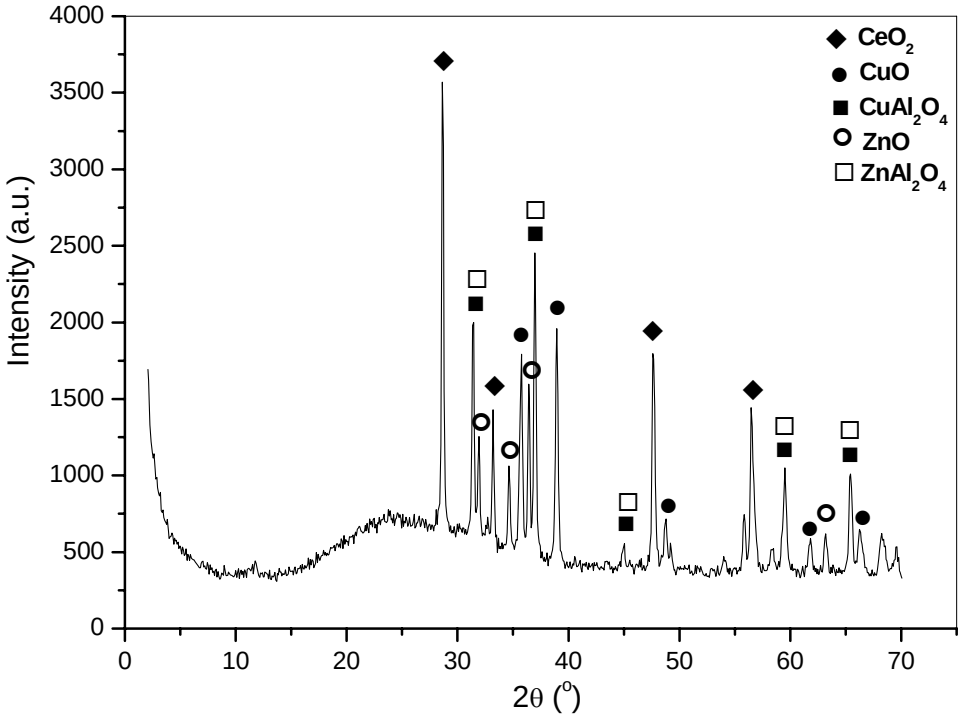

Fig. 3-24 XRD pattern of CuZnAl-Ce(dipic)-LDH calcined at 1100 °C

3.5.1.4 IR spectroscopy

Fig. 3-25 illustrates the IR spectra of samples prepared using different $[Ce(dipic)_3]^{3-}$/CuZnAl-NO_3-LDH ratios. The IR spectra of the samples with Ce/Al=1/1 (a) and 1/3 (b) were similar to the corresponding spectra for ZnAl-Ce(dipic)-LDH (Fig. 3-9). The presence of intense adsorption bands at about 1624 and 1384 cm^{-1} assignable to asymmetric and symmetric stretching vibrations of carboxylate group and these bands at around 1591, 1436, 1279 and 1191cm^{-1} assigned to vibrations of the remaining skeletal modes of pyridine ring indicated the intercalation of $[Ce(dipic)_3]^{3-}$ into

CuZnAl-NO_3-LDH. The bands observed in the low-frequency region corresponded to lattice vibration modes of LDH structure and could be attributed to cation-oxygen (M-O) vibrations at around 766cm^{-1}, 662cm^{-1} and O-M-O vibrations at around 431cm^{-1}. In the IR spectrum for the sample with Ce/Al=1/6 (c), besides the above bands of organic component and LDH lattice structure, the presence of residual NO_3^- vibrations was suggested by the increasing intensity of the band centered at 1384 cm^{-1}, which was the superposition of the symmetric carboxylate stretch and the ν_3 vibration of residual NO_3^-.

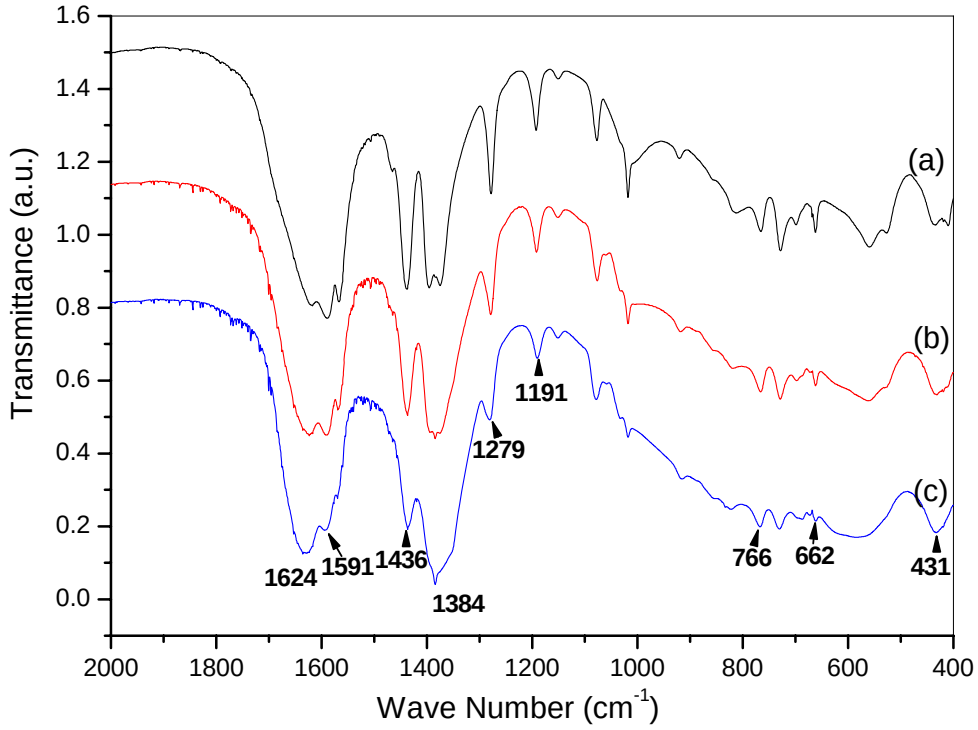

Fig. 3-25 IR spectra of CuZnAl-Ce(dipic)-LDHs prepared using different $[Ce(dipic)_3]^{3-}$/CuZnAl-NO_3-LDH ratios: 1/1 (a), 1/3 (b), and 1/6 (c)

3.5.1.5 TEM analysis

TEM was employed in order to study the particle shape and size of

CuZnAl-Ce(dipic)-LDH and the product resulting after calcination at 500 °C for 6 h. TEM micrographs are illustrated in Fig. 3-26. The crystallites of CuZnAl-Ce(dipic)-LDH have a hexagonal platelet morphology. The diameter of the particles is about 45 nm and with a narrow distribution. After calcination, fibrous particles are observed with a lower crystallinity and the hexagonal particles have a nodular appearance, probably related to the oxides being formed [44].

(a)

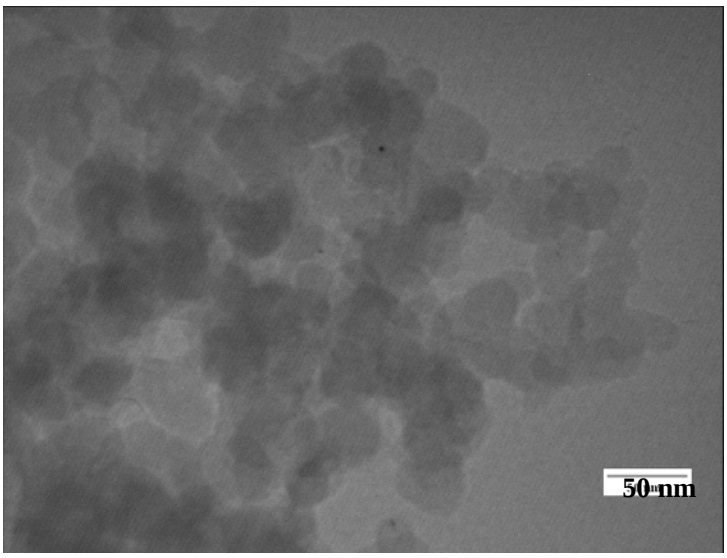

(b)

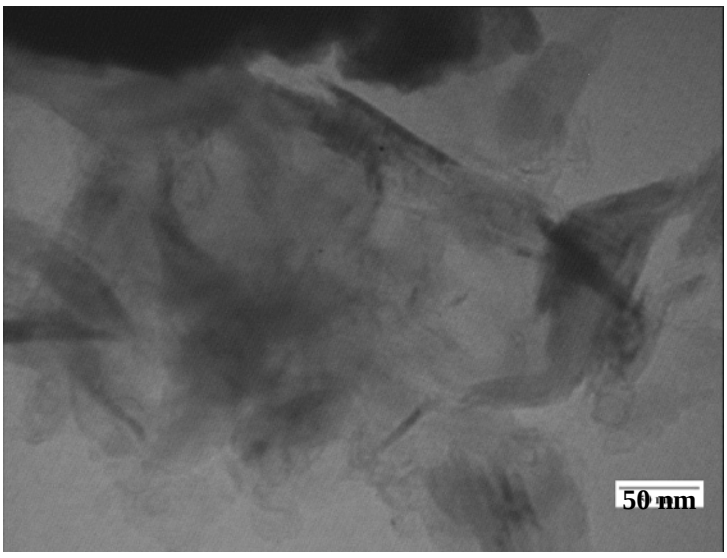

Fig. 3-26 TEM micrographs of CuZnAl-Ce(dipic)-LDH(a) and its calcined product(b)(500 °C,6 h)

3.5.2 Structural characterization of Zn_2Cr-Ce(dipic)-LDH

3.5.2.1 XRD analysis

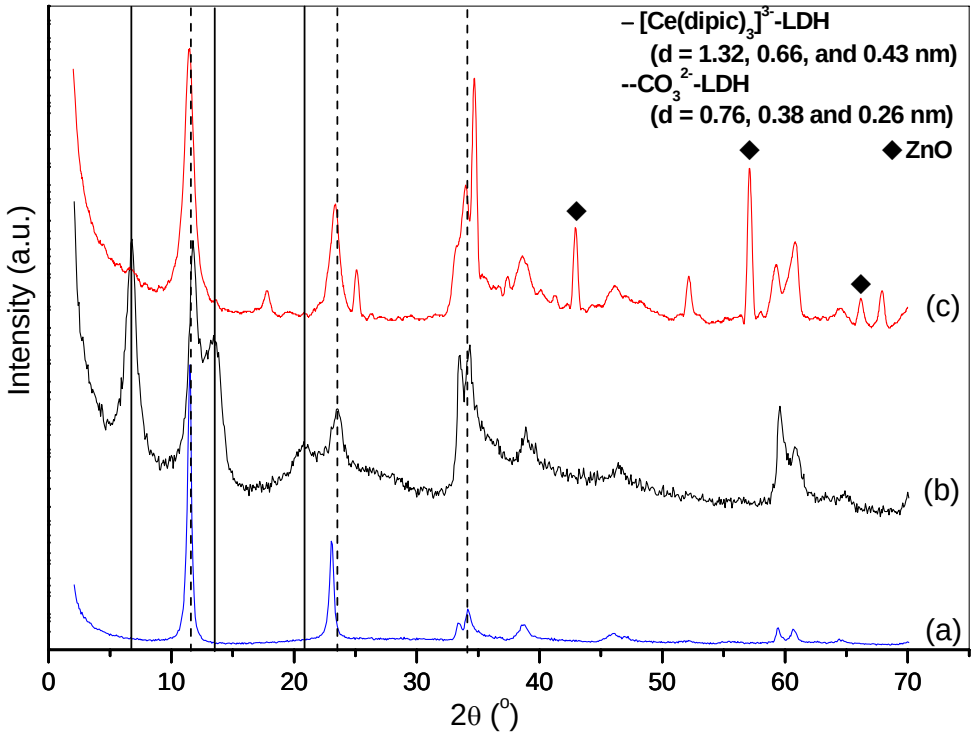

Fig. 3-27 XRD patterns of the precursor Zn_2Cr-NO_3-LDH (a), sample Zn_2Cr-Ce(dipic)-LDH (b), and back exchange product of the sample with CO_3^{2-} (c)

Fig. 3-27 illustrates the XRD patterns of Zn_2Cr-Ce(dipic)-LDH (b) and the corresponding Zn_2Cr-NO_3-LDH precursor (a). The position and spacing of (00*l*) reflections at d = 1.32, 0.66, and 0.43 nm as well as the characteristic (110) peak confirmed that the intercalation of $[Ce(dipic)_3]^{3-}$ into Zn_2Cr-NO_3-LDH took place. Considering that the layer thickness is 0.48 nm, the basal spacing of 1.32 nm corresponds to a gallery height of 0.84 nm, suggesting the $[Ce(dipic)_3]^{3-}$ anions are

arranged with their longest dimension nearly perpendicular to the host layers. The absence of characteristic diffractions of dipic^{2-}-LDH phase indicated that the decomposition of [Ce(dipic)$_3$]$^{3-}$ was inhibited. However, the presence of a series of (00*l*) diffraction lines of CO_3^{2-}-LDH phase at d = 0.76, 0.38 and 0.26 nm indicated that the intercalation of CO_3^{2-} anions accompanied the formation of [Ce(dipic)$_3$]$^{3-}$-LDH phase. After a back-exchange reaction of Zn_2Cr-Ce(dipic)-LDH with excess CO_3^{2-} anions, the characteristic diffraction peaks of [Ce(dipic)$_3$]$^{3-}$-LDH phase essentially disappeared, suggesting interlayer [Ce(dipic)$_3$]$^{3-}$ anions were exchanged by CO_3^{2-} anions. In addition to CO_3^{2-}-LDH phase, ZnO phase was also formed corresponding to the possible dissolution of the layers. The observed difference in structure and composition between Zn_2Cr-Ce(dipic)-LDH and Zn_2Al-Ce(dipic)-LDH resulted from the varied interaction between layer metal cations and interlayer complex anions. The interaction in Zn_2Cr-Ce(dipic)-LDH was weaker due to the replace of Al^{3+} by Cr^{3+}, so that the decomposition of [Ce(dipic)$_3$]$^{3-}$ was inhibited and the basal spacing was enlarged.

3.5.2.2 IR spectroscopy

The FTIR absorption spectrum of Zn_2Cr-Ce(dipic)-LDH in Fig. 3-28 (a) was in a good agreement with X-ray data, indicating the formation of the Ce-containing LDH network with typical bands in the low frequency region (400 - 900 cm^{-1}). The intercalated organic complexes caused a series of narrow and intense bands in 1000-1800 cm^{-1} (marked in Fig 3-28): the bands assigned to vibrations of skeletal modes of the pyridine ring were remained; the band observed at around 1387 cm^{-1} was the vibration superposition of interlayer carbonate anions and carboxylate groups so that

it shifted to high frequency compared with only CO_3^{2-}. The slight difference from the corresponding spectrum of Zn_2Al-Ce(dipic)-LDH (Fig. 3-9) suggested the changes in structure and composition, consistent with the XRD analysis. After the exchange reaction with CO_3^{2-} anions, the weak bands of vibrations of carboxylate groups and pyridine rings indicated a small quantity of $[Ce(dipic)_3]^{3-}$ anions residual or physically adsorbed. The intense band due to the asymmetric stretching of CO_3^{2-} ions at 1358 cm^{-1} and the bands corresponding to lattice vibration modes in the low-frequency region proved the presence of a great quantity of CO_3^{2-}-LDH phase. This successful back exchange suggests that Zn_2Cr-Cedipic-LDH consists of pure LDH phases.

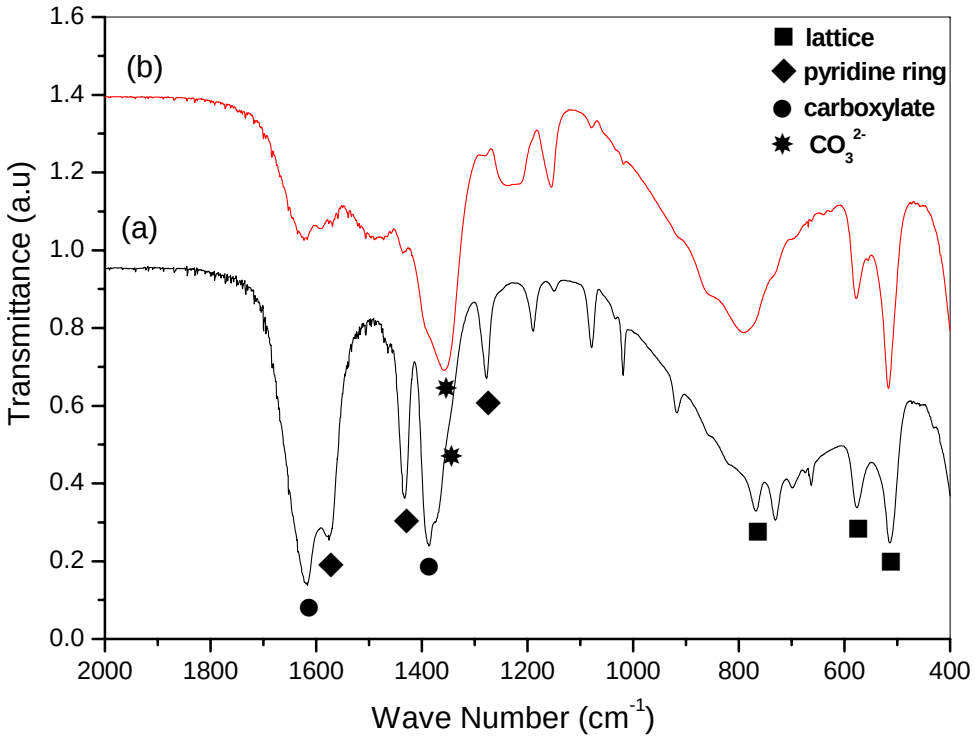

Fig. 3-28 IR spectra of Zn_2Cr-Ce(dipic)-LDH (a) and the back-exchange product with CO_3^{2-} (b)

Table 3-5 Summary of selected IR data and assignments for Zn_2Cr-Ce(dipic)-LDH

carboxylate group	υ-COO_{assym}	υ-COO_{sym}	υ_3-CO_3^{2-}	
	1616	1387	1358	
pyridine ring	-CN	-CN	υ-CN	υ-CN
	1576	1433	1277	1110
lattice	υ-MO	υ-MO	δ-OMO	
	767	576	514	

3.5.2.3 TEM analysis

TEM was employed in order to study the morphology and particle size of Zn_2Cr-Ce(dipic)-LDH and the product after calcinations at 500 °C for 6 h, as shown in Fig. 3-29. The TEM micrographs confirmed that most of Zn_2Cr-Ce(dipic)-LDH particles had the characteristic LDH platelet structure with a relatively uniform size of ~90 nm. Although there was some nodular appearance, overall the general morphology of the LDH particles was mostly retained. After calcination, aggregates of very small particles were observed, with a lower crystallinity. In addition, it was obvious that many small shadows were uniformly distributed on the surface of the calcined material. These shadows were probably supported cerium oxides with the higher density of electron cloud.

(a)

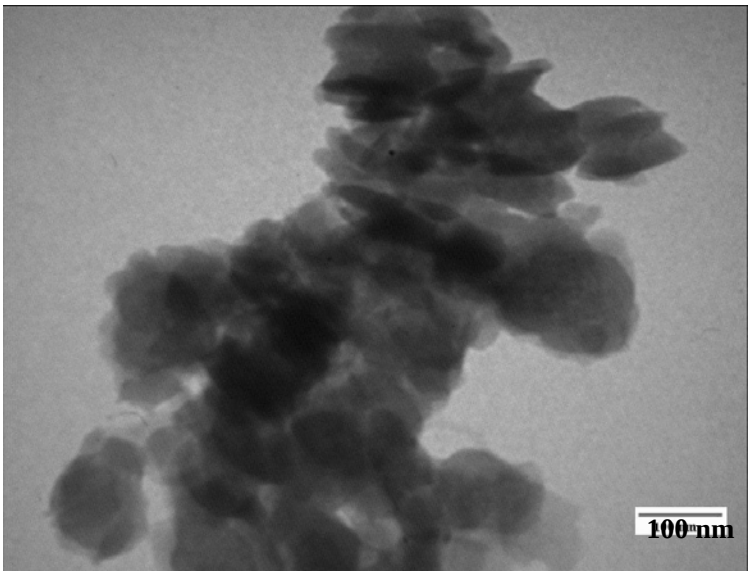

(b)

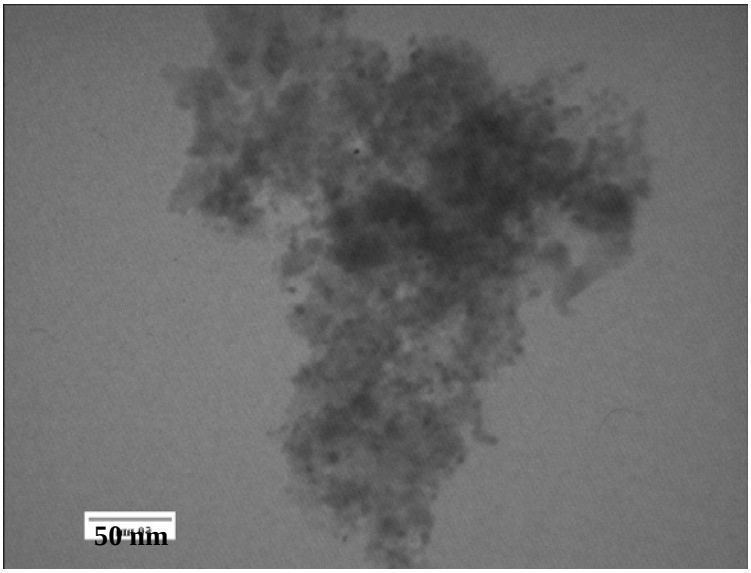

Fig. 3-29 TEM micrograph images of Zn_2Cr-Ce(dipic)-LDH (a) and its calcined product (b) (500 °C for 6 h)

3.5.2.4 Adsorption isotherm of $[Ce(dipic)_3]^{3-}$ on Zn_2Cr-Cl-LDH

The adsorption isotherm of $[Ce(dipic)_3]^{3-}$ on Zn_2Cr-Cl-LDH was investigated using UV spectroscopy (at 271 nm), as shown in Fig. 3-30. The results suggested that the adsorption proceeded in two steps: saturation of the external sites took place up to 0.28 mmol/g and was followed by an interlayer exchange process occurring at high

equilibrium concentrations from 0.28 to 0.48 mmol/g which seemed to be the maximum uptake. The first part of the adsorption isotherm was considered as an L-type isotherm. The adsorption isotherm reached a plateau at intermediate equilibrium concentration (Ce). The fit based on the Langumir adsorption model is displayed in the inset of Fig. 3-30: Ce/Qe = 1.6058 + 2.7298Ce (R = 0.98). This indicates a surface adsorption process is occurring at lower values of Ce. At higher values of Ce, the adsorbed concentration (Qe) increased again and finally reached a second plateau. The adsorption in this stage proceeded via an anion-exchange mechanism. The experimental maximal Qe was 0.48 mmol/g, lower than the ideal value of 0.9355 mmol/g.

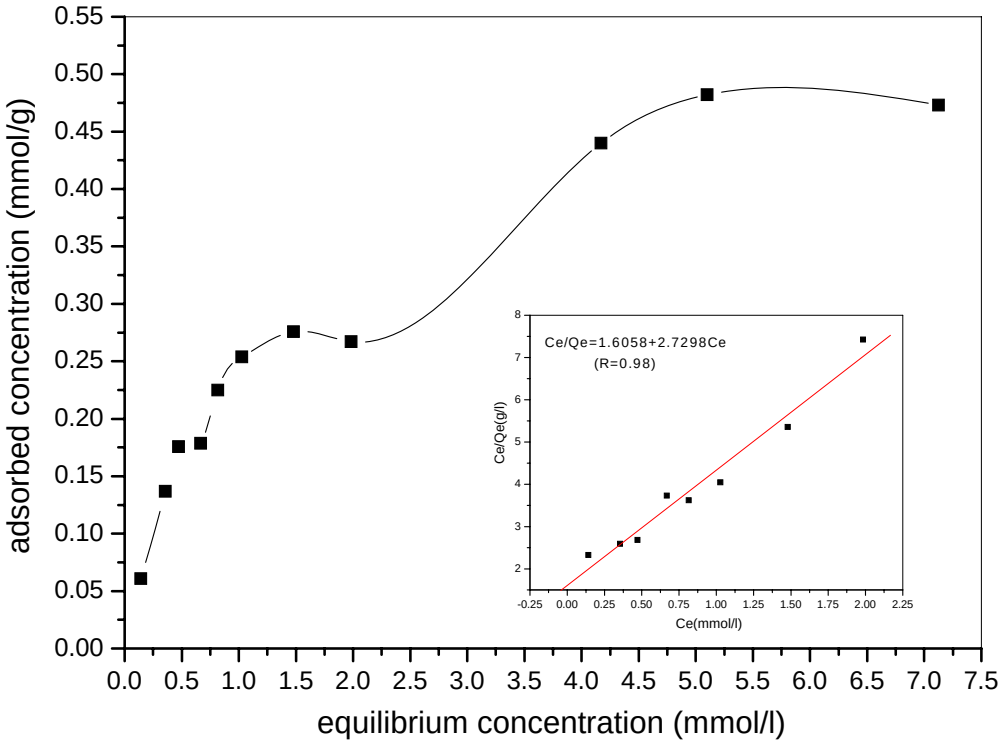

Fig. 3-30 $[Ce(dipic)_3]^{3-}$ adsorption isotherm on Zn_2Cr-Cl-LDH precursor, insert graph: the fit based on the Langumir adsorption model

At higher equilibrium concentration values XRD showed a shift in the interlayer spacing to a higher value, consistent with the formation of a $[Ce(dipic)_3]^{3-}$-containing Zn_2Cr-LDH. The decrease in the intensity of the (003) diffraction peak of Zn_2Cr-Cl-LDH was simultaneously observed, confirming the topotactic anion exchange of parts of interlayer chloride anions by larger $[Ce(dipic)_3]^{3-}$ complexes in the LDH structure.

3.5.3 Structural characterization of varied $[Ce(dipic)_3]^{3-}$-LDHs

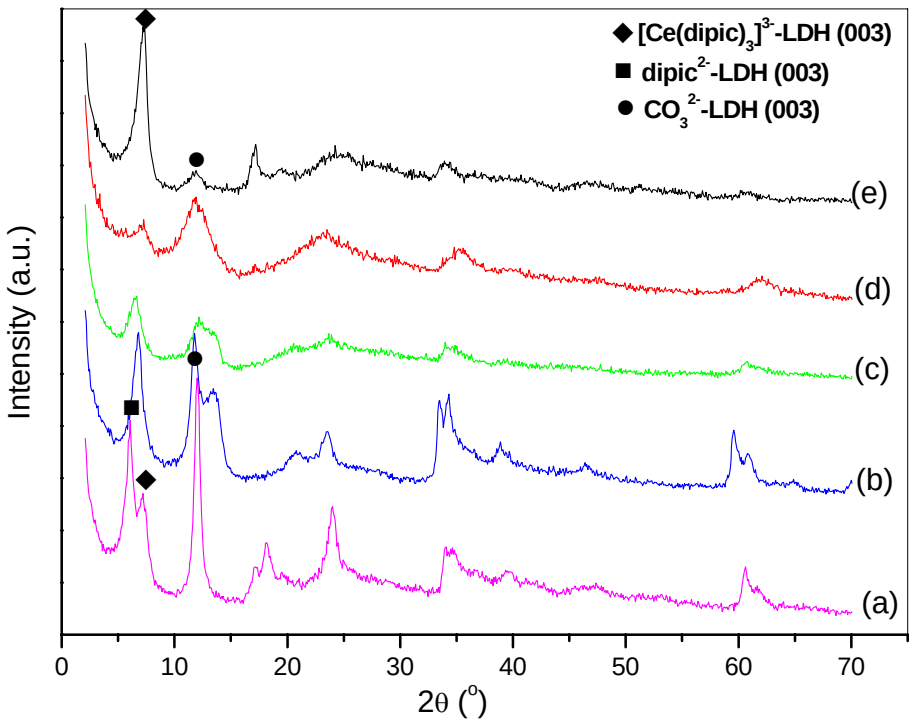

Fig. 3-31 XRD patterns of $[Ce(dipic)_3]^{3-}$-LDHs with different metal elements in the host layers: Zn_2Al-Ce(dipic)-LDH (a); Zn_2Cr-Ce(dipic)-LDH (b); Co_2Al-Ce(dipic)-LDH (c); Ni_2Al-Ce(dipic)-LDH (d); CuZnAl-Ce(dipic)-LDH (e)

(The signs mark the (003) reflections of different LDH phases)

Table 3-6 Basal spacings of some M^{2+}_2Al-Ce(dipic)-LDHs

No.	Sample	d(003)/nm
(a)	Zn_2Al-Ce(dipic)-LDH	1.24
(b)	Zn_2Cr-Ce(dipic)-LDH	1.32
(c)	Co_2Al-Ce(dipic)-LDH	1.37
(d)	Ni_2Al-Ce(dipic)-LDH	1.23
(e)	CuZnAl-Ce(dipic)-LDH	1.23

In order to investigate the anion-exchange ability of LDH precursors with $[Ce(dipic)_3]^{3-}$ complexes, we extended the intercalation study to varied M^{2+}-M^{3+} systems (M^{2+} = Zn^{2+}, Cu^{2+}, Ni^{2+}, Co^{2+}; M^{3+} = Al^{3+}, Cr^{3+}). Fig. 3-31 and Table 3-6 give some details concerning the XRD patterns of varied $[Ce(dipic)_3]^{3-}$-containing LDH materials with different layer compositions. The basal spacing values of $[Ce(dipic)_3]^{3-}$-LDH phases in these samples show a significant variation with layer metal elements and vary from 1.23 nm to 1.37 nm. They were related to the interaction strength between layer cations and interlayer anions. In the XRD patterns, except for Zn_2Al-Ce(dipic)-LDH discussed in the above chapter, other LDH materials had no diffraction peaks at d = 1.48, 0.74 and 0.49 nm assignable to $dipic^{2-}$-LDH phase, indicating that the partial decomposition of $[Ce(dipic)_3]^{3-}$ into Ce^{3+} and $dipic^{2-}$ ions did not occur. So the nature of layer metal cations had an effect on the product composition. Moreover, the diffraction peaks at d = 0.76, 0.38 and 0.26 nm assignable to CO_3^{2-}-LDH phase were present in all of the spectra, due to the unavoidable contamination from air. Our results demonstrate that it is possible to control the chemical compositions and properties of mixed metal oxide systems derived from the calcined LDHs via the

intercalation of Ce containing complexes into different LDH hosts. This leads us to envisage the preparation of a rich variety of oxide catalysts.

3.6 Intercalation of other complexes into LDHs

3.6.1 Intercalation of $[Ce(DTPA)]^{2-}$ complex

Diethylenetriamine-N,N,N',N'',N''-pentaacetic acid (H_5dtpa) forms stable metal complexes with a variety of metal ions [45]. The logarithms of the stability constants for chelation with REEs are similar and big [46]. Some reporters [26] investigated REE-DTPA compounds containing La, Ce, Gd, etc. In particular, many investigations had been carried out on the Gd complex with H_5dtpa since it was a strong paramagnetic compound [47-49]. The $[Ce(DTPA)]^{2-}$ complex was prepared according to the method described by Kato [26] and the composition was confirmed in this chapter. UV absorption bands of the $[Ce(DTPA)]^{2-}$ complex are present at 296 and 269 nm whereas the free $DTPA^{5-}$ ligand does not show any UV absorption band. The Ce-DTPA complex subsequently reacted with the Zn_2Al-NO_3-LDH precursor following the same procedure as for intercalation of the $[Ce(dipic)_3]^{3-}$ complex ($[Ce(DTPA)]^{2-}$/Zn_2Al-NO_3-LDH = 2/1).

3.6.1.1 XRD analysis

Fig. 3-32 shows the XRD patterns of precursor Zn_2Al-NO_3-LDH, products Zn_2Al-DTPA-LDH and Zn_2Al-Ce(DTPA)-LDHs. The basal (003) reflection and two further harmonics for Zn_2Al-Ce(DTPA)-LDH (Fig. 3-32 (c)) indicated a basal spacing of 1.46 nm, and shifted to low 2θ angles compared with the precursor (Fig. 3-32 (a)).

Although the positions of the (00*l*) reflections were essentially identical to those of Zn_2Al-DTPA-LDH (Fig. 3-32 (b)) at d = 14.7, 7.3, 4.9 nm, as found by others in some LDH systems [6], the relative intensities of the peaks showed significant differences. The first-order peak was weaker than the second-order peak for Zn_2Al-Ce(DTPA)-LDH, whereas the opposite was observed for Zn_2Al-DTPA-LDH. This difference can be attributed to a marked increase in the electron density at the midpoint of the interlayer galleries in the former material due to the presence of the rare earth ions [6,50,51]. After calcination at 1100 °C, the XRD pattern of Zn_2Al-Ce(DTPA)-LDH displayed the reflections assigned to ZnO, CeO_2 and $ZnAl_2O_4$ spinel. The presence of cerium oxides confirms the incorporation of Ce into the LDH structure, as we expected.

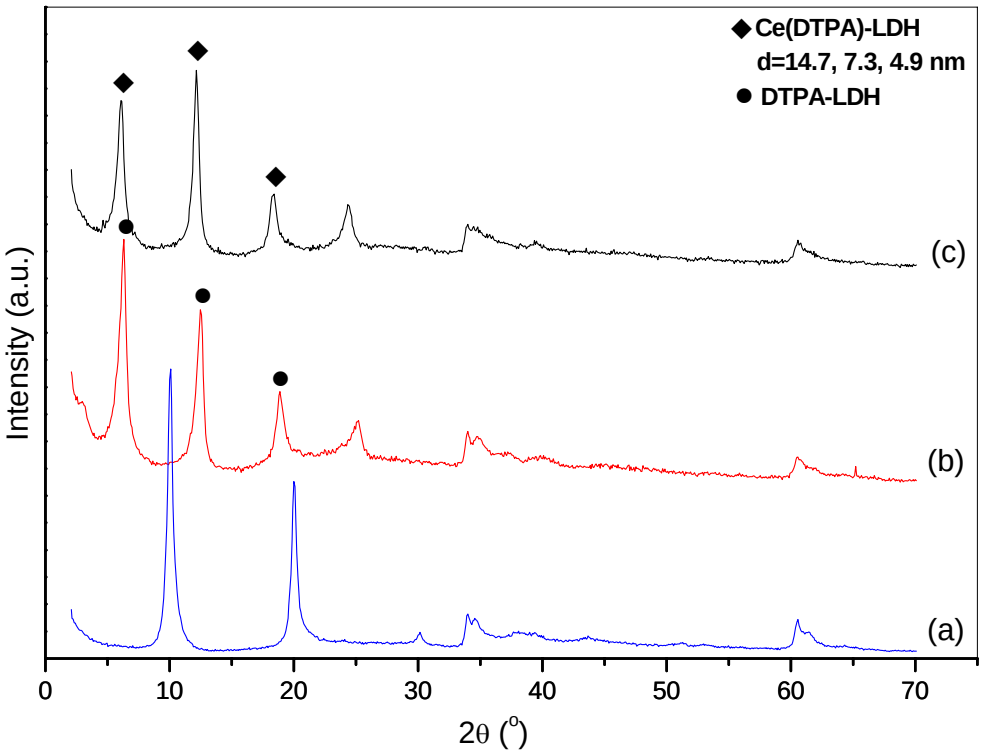

Fig. 3-32 XRD patterns of Zn_2Al-NO_3-LDH(a), Zn_2Al-DTPA-LDH(b), Zn_2Al-Ce(DTPA)-LDH(c)

3.6.2.2 IR spectroscopy

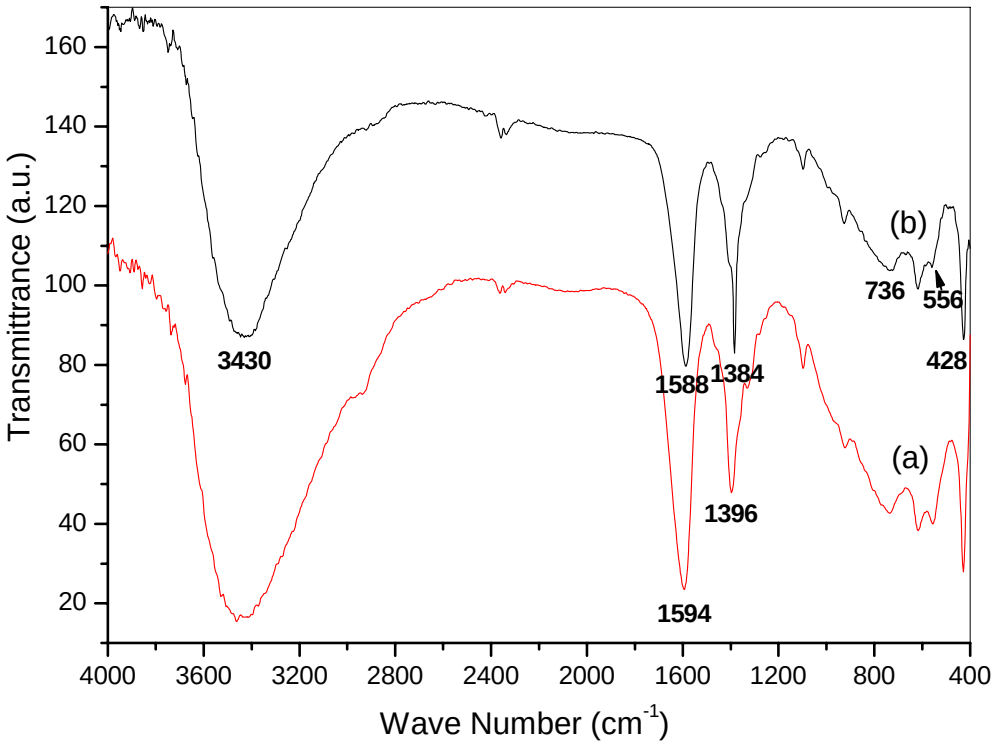

Fig. 3-33 IR spectra of Zn_2Al-DTPA-LDH (a) and Zn_2Al-Ce(DTPA)-LDH (b)

These intercalated LDH materials were also characterized by IR spectroscopy, as shown in Fig. 3-33. The IR bands of Zn_2Al-Ce(DTPA)-LDH were not significantly different from those of Zn_2Al-DTPA-LDH. In the range 3600 - 3200 cm^{-1}, the IR spectrum of Zn_2Al-Ce(DTPA)-LDH was dominated by a broad band at about 3430 cm^{-1}, attributed to the O-H stretch of weakly hydrogen-bonded water molecules and layer hydroxyl groups. In the region between 1800 and 1000 cm^{-1}, the characteristic vibrations of the organic anions were observed. The intense, broad band at 1588 cm^{-1} could be assigned to the antisymmetric stretch of COO^-. The other intense band at 1384 cm^{-1} could be assigned as the symmetric stretch of COO^-. For the sample

Zn_2Al-DTPA-LDH, the COO^- vibrations were shifted to 1594 cm^{-1} and 1396 cm^{-1} respectively, and their relative intensity changed. These differences provide tentative evidence of Ce-DTPA interaction [6,18]. Below 1000 cm^{-1}, no significant changes were observed. Two bands at about 736 and 556 cm^{-1} were due to a metal-oxygen vibration (M-O). Another peak at about 428 cm^{-1} could be attributed to an (M-O-M) vibration.

3.6.2 Intercalation of $[Eu(dipic)_3]^{3-}$ complex

The optical properties of rare earth complexes have been studied extensively owing to their unique absorption and fluorescence [24,52]. Among rare earth ions, trivalent europium offers the versatility in the fluorescence property in conjunction with the structural configuration [53,54], because of its nondegeneracy in the emitting $^5D_0$ state. Many reporters investigated the $[Eu(dipic)_3]^{3-}$ complex [55-57] because dipicolinate, as ligand, could form a very stable bond with Eu^{3+}. The crystalline structure of $[Eu(dipic)_3]^{3-}$ had been well established in terms of the coordination geometry, coordination number and bond distance [23,33].

Although europium and organic ligands readily form complexes, generally speaking these complexes have poor optical, thermal, and chemical stability. In order to alleviate these drawbacks, the incorporation of rare earth organic complexes into inorganic materials has attracted considerable attention [25,58]. Meng *et al.* [32] demonstrated the beneficial effect of impregnation of $Eu(DBM)_3 \cdot 2H_2O$ (DBM = dibenzoylmethane) in MCM-48 on the luminescence properties of Eu^{3+}, and Alvaro *et al.* [14] reported the characterization of highly luminescent europium complexes, including those with dipicolinate ligands, inside zeolites Y and mordenite. The nature of

the chemical environment may affect the optical properties of these europium complexes and be a key factor in controlling the lasing conditions and other properties. Therefore, the optical properties could be used as a useful probe to investigate the structural and binding dynamics of complexes.

Due to the special layered structure, LDHs had been used as carrier to prepare metallo-organic species containing materials for catalytic, photoactive and electroactive fields. The structure of LDHs allows the introduction of Eu-containing complex anions into the interlayer galleries using an ion-exchange synthesis technique. This method affords monophase nanostructured LDH materials in which Eu-complex is linked to LDH layers by attractive electrostatic forces and dispersed homogeneously. So far, concerning LDH materials, the incorporation of $[Eu(EDTA)]^-$ and $[Eu(pic)_4]^-$ (pic=picolinate) complexes into Mg-Al LDHs and $[Eu(BDC)]^{2-}$ (BDC=2,2'-bipyridine-5,5'-dicarboxylate) complex into Zn-Al LDHs had been studied [6,16,17].

In this chapter, the $[Eu(dipic)_3]^{3-}$ complex and its intercalation products Zn_2M-Eu(dipic)-LDHs (M=Al or Cr) were prepared according to the ion-exchange method described above for $[Ce(dipic)_3]^{3-}$-containing materials. Their structures were determined and the luminescence properties discussed.

3.6.2.1 XRD analysis

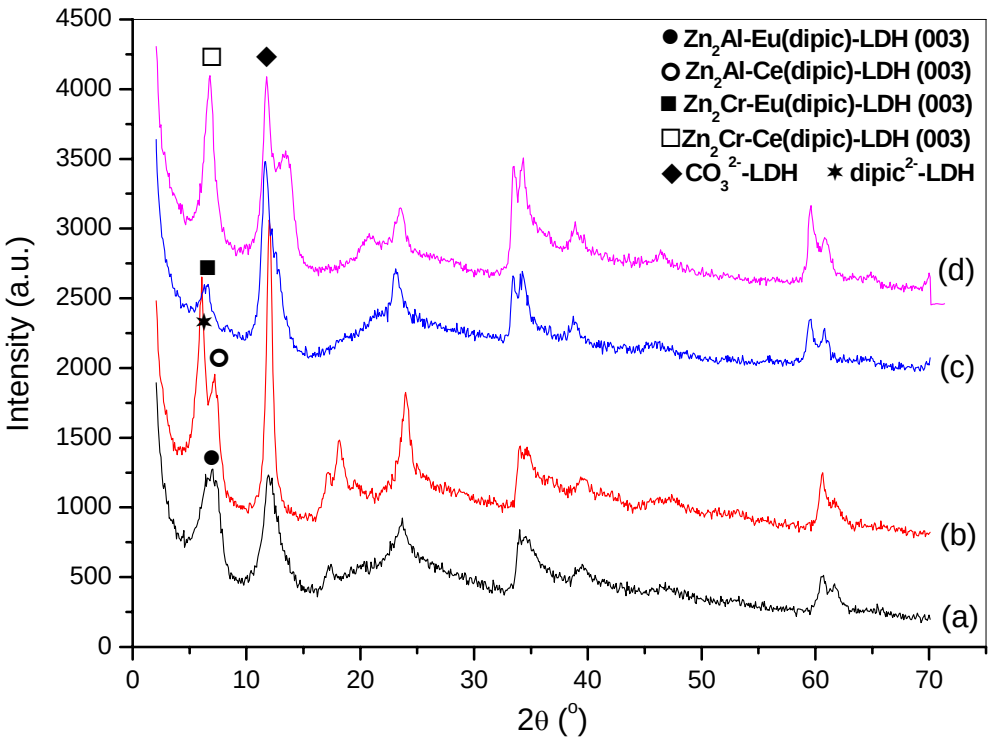

Fig. 3-34 XRD patterns of $[M(dipic)_3]^{3-}$ (M = Eu, Ce) intercalation products: Zn_2Al-Eu(dipic)-LDH (a), Zn_2Al-Ce(dipic)-LDH (b) and Zn_2Cr-Eu(dipic)-LDH (c), and Zn_2Cr-Ce(dipic)-LDH (d)

(The signs mark the (003) reflections of different LDH phases)

In the XRD pattern of Zn_2Al-Eu(dipic)-LDH illustrated in Fig. 3-34 (a), it showed that the basal (003) reflection shifted to lower 2θ angle value compared with that of the Zn_2Al-NO_3-LDH precursor, and the interlayer spacing increased from 0.88 nm to 1.24 nm after intercalation of the complex anion. The same basal spacing was observed for $[Ce(dipic)_3]^{3-}$ and $[Eu(dipic)_3]^{3-}$ complexes intercalated in the Zn_2Al-LDH host. Moreover, the characteristic (110) reflection of an LDH structure was clearly observed. The (00*l*) diffraction series of CO_3^{2-}-LDH phase were present, suggesting the product also consisted of mixed LDH phases. It was noteworthy that the low intensity of the diffraction peak at d = 1.48 nm assigned to $dipic^{2-}$-LDH demonstrated that the

decomposition ability of $[Eu(dipic)_3]^{3-}$ anions was less than $[Ce(dipic)_3]^{3-}$ during the exchange reaction. The better stability of $[Eu(dipic)_3]^{3-}$ can be attributed to the stronger interaction between the central ion and $dipic^{2-}$ ligands, associated with the smaller size and higher charge density of Eu^{3+} compared with Ce^{3+}. For the purpose of comparison, Zn_2Cr-Eu(dipic)-LDH was also prepared and the interlayer spacing was 1.34 nm, close to the value for $[Ce(dipic)_3]^{3-}$ intercalated in the same host (1.32 nm).

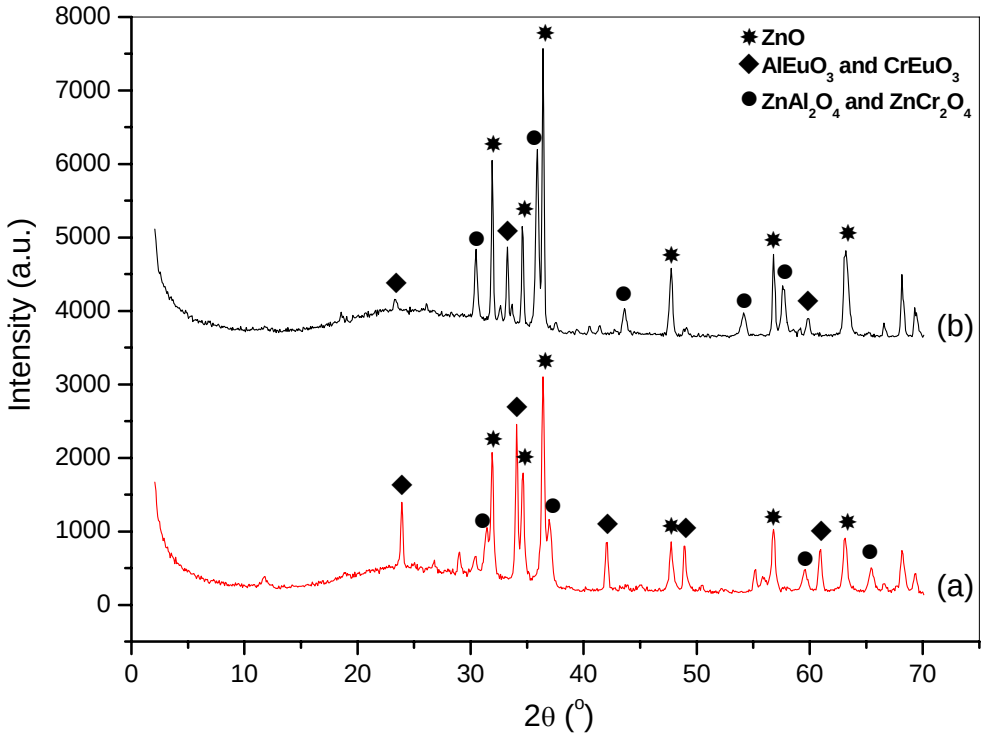

Fig.3-35 XRD patterns of calcined Zn_2Al-Eu(dipic)-LDH(a) and Zn_2Cr-Eu(dipic)-LDH(b) at 1100°C

Fig. 3-35 shows the XRD patterns of two $[Eu(dipic)_3]^{3-}$-LDHs after calcination at 1100 °C, where all of the reflections could be assigned to a mixture of metal oxides and spinels. The calcined Zn_2Al-Eu(dipic)-LDH consisted of ZnO, $ZnAl_2O_4$, and $Al_2Eu_4O_9$ and for the calcined Zn_2Cr-Eu(dipic)-LDH, a mixture of ZnO, $ZnCr_2O_4$, and $Cr_2Eu_4O_9$

was present. It indicated that europium was well dispersed in the Zn-Al or Zn-Cr oxide matrixes since no Eu_2O_3 was formed, which may be caused by the uniform distribution of $[Eu(dipic)_3]^{3-}$ complexes located in the interlayer galleries [16].

3.6.2.2 IR spectroscopy

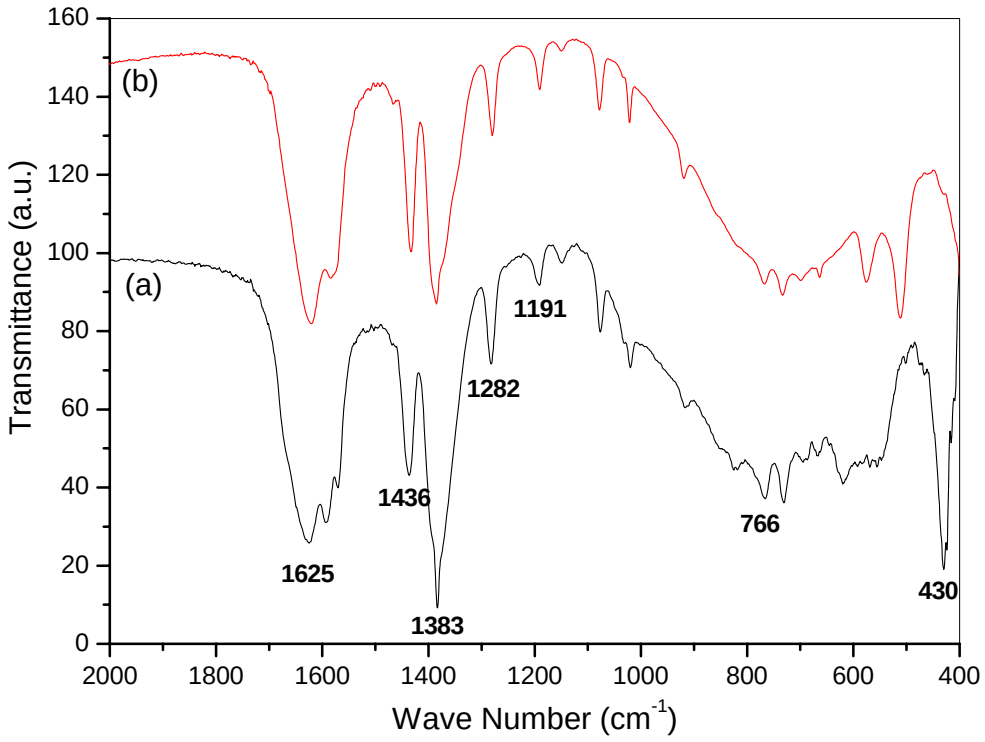

Fig. 3-36 IR spectra of Zn_2Al-Eu(dipic)-LDH (a) and Zn_2Cr-Eu(dipic)-LDH (b)

Fig. 3-36 shows the IR spectra of two LDH hosts intercalated with $[Eu(dipic)_3]^{3-}$. The positions of IR absorption bands of Zn_2Al-Eu(dipic)-LDH (Fig. 3-36 (a)) were very similar to those of Zn_2Al-Ce(dipic)-LDH (see Fig. 3-9): O-H stretching bands of metal-hydroxyl groups and hydrogen bonded interlayer water molecules were observed in a broad band centered at 3446 cm^{-1}; asymmetric and symmetric stretching vibrations of the carboxylate groups occured at 1625 and 1383 cm^{-1} respectively; vibrations of

skeletal modes of the pyridine ring were observed at 1436, 1282 and 1191 cm^{-1}; and lattice vibration modes of the LDH structure at 766 and 430 cm^{-1}. The IR spectra was consistent with the formation of a $[Eu(dipic)_3]^{3-}$-containing Zn_2Al-LDH material. For Zn_2Cr-Eu(dipic)-LDH (Fig. 3-36 (b)), absorption bands in the region 1800-1000 cm^{-1} were similar to those of Zn_2Al-Eu(dipic)-LDH, although the carboxylate vibrations shifted slightly to lower wave numbers, related to a variation in strength of the electrostatic interaction between different layers and interlayer complexes; in the low frequency region, M-O bond vibrations shifted to lower frequencies according to the presence of more heavy metal cations in the layers.

3.6.2.3 Luminescence properties of $[Eu(dipic)_3]^{3-}$-LDHs

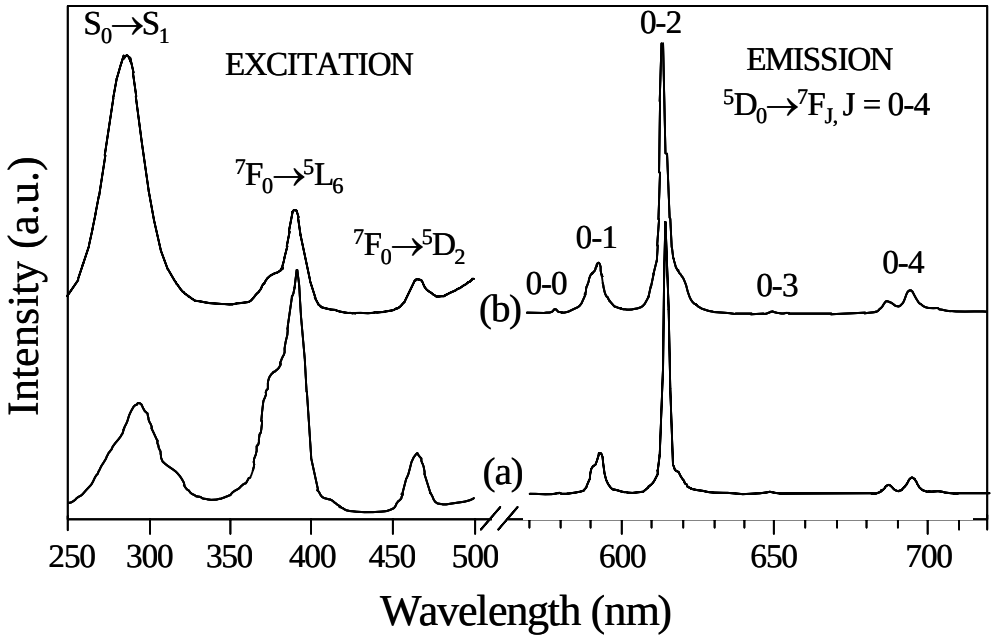

Fig. 3-37 Photoluminescence spectra of $Na_3[Eu(dipic)_3]$ complex (a) and product Zn_2Al-Eu(dipic)-LDH (b) at room temperature (λ_{em} = 613 nm and λ_{exc} = 300 nm)

Typical room temperature steady state excitation and emission spectra of $Na_3[Eu(dipic)_3]$ (a) and the corresponding Zn_2Al-Eu(dipic)-LDH (b) are depicted in Fig. 3-37. The emission spectra showed structureless transitions between the metastable $^5D_0$ level and the ^7F_J Stark components with J = 0-4, dominated by the red hypersentitive $^5D_0 - {}^7F_2$ transition. Despite the apparent similarity of the emission profiles in both samples, it should be noted that the intensity ratio between the $^5D_0 - {}^7F_2$ electric and $^5D_0 - {}^7F_1$ magnetic dipole transitions was slightly lower in the LDH material than in the complex (5.2 and 6.3 respectively), while the $^5D_0 - {}^7F_0$ line was stronger in the LDH material. This behaviour confirmed that the nine-fold coordinated site of the rare earth in the Eu(III)-trisdipicolinate complex had no center of inversion in both cases [23] but also suggested that slight changes had occurred in the chemical environment surrounding Eu^{3+} after incorporation of the complex in the LDH host. The latter argument was further confirmed by the excitation spectra. In the spectral range explored, the spectra consisted of three main transition peaks, at 464 nm, 389 nm (plus a shoulder at 375 nm) and a band whose position depended on the sample (292 nm in the pure complex and 284 nm in the Eu-containing LDH). The two first bands are due to the intra-ionic transitions $^7F_0 - {}^5D_2$ and $^7F_0 - {}^5L_6$ of Eu(III), while the third band can be ascribed to transitions from the ground state S_0 to the first excited state $S_1(\pi, \pi^*)$ of the dipicolinate ligand. In this latter case, the red Eu(III) luminescence was induced by energy transfer from the dipicolinate ligand levels. The hypsochromic shift of $\cong$ 965 cm^{-1} observed for the $S_0 - S_1$ transition going from the pure $Na_3[Eu(dipic)_3]$ complex to the Zn_2Al-Eu(dipic)-LDH is ascribed to a smaller size of the conjugated π electron

system of the dipicolinate ligand and reveals the lower polarizability of the chemical environment surrounding the Eu(III) complex after intercalation. Similar behaviour has been observed previously for Eu(III)-β diketonates incorporated in mesoporous silica and was interpreted in term of a host-guest interaction [32]. In addition, the blue shift of the ligand levels may also contribute to the enhancement of the efficiency of the energy transfer to the Eu(III) levels, as argued for instance by M. Latva [59], thus explaining the much stronger contribution of the S_0-S_1 band relative to the Eu(III) bands in the excitation spectra. In summary, the analysis of the photoluminescence spectra confirmed the incorporation of the $[Eu(dipic)_3]^{3-}$ complex into the LDH and suggested that both the structural integrity and luminescence characteristics of the complex were retained after intercalation.

3.7 Thermal behaviors of intercalated LDHs

3.7.1 Thermal behaviors of $[Ce(dipic)_3]^{3-}$-LDHs

3.7.1.1 Zn_2Al-Ce(dipic)-LDH

3.7.1.1.1 Coupled TG/Mass analysis

The features of the thermal decomposition process for LDH materials depend on the nature of layer cations, the nature of interlayer anions, and the experimental conditions during heating [59-61]. Four steps are generally observed in the thermal evolution of LDHs: the desorption of physisorbed water, the elimination of interlayer structural water, the dehydroxylation of brucite-like sheets, and the decomposition of interlayer anions [39,50].

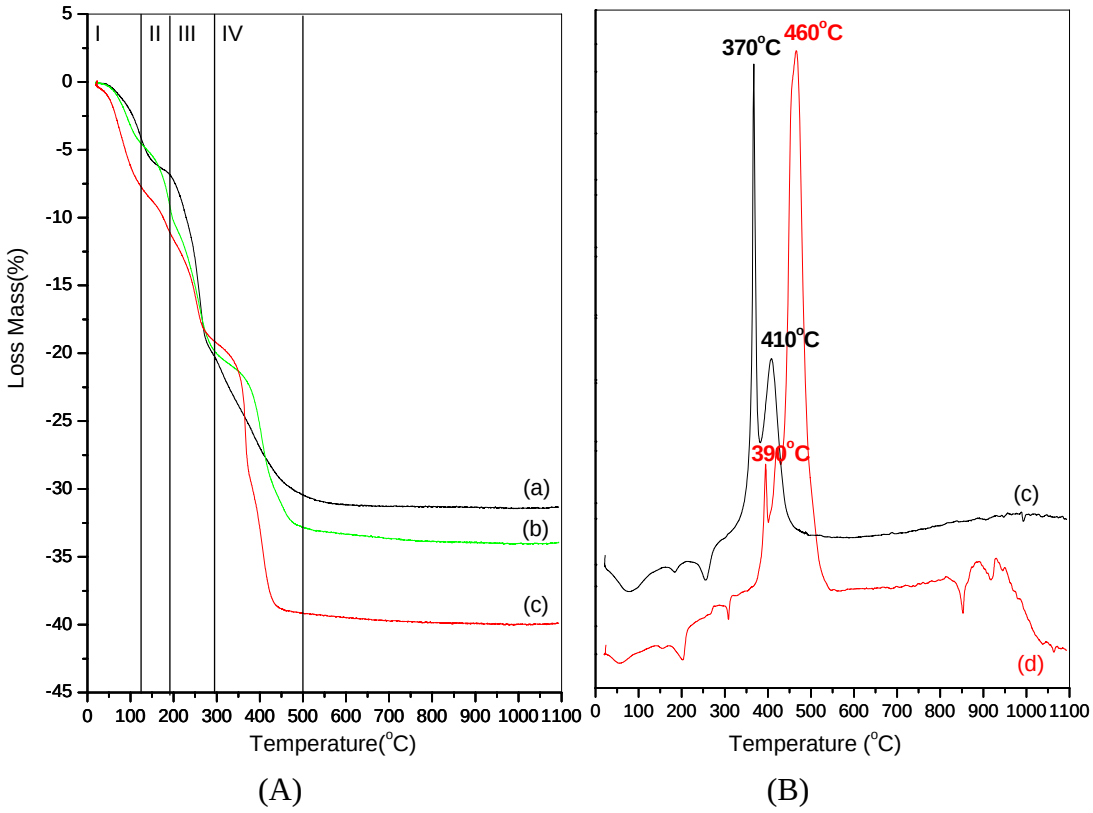

Fig. 3-38 TGA (A) and DTA (B) curves of Zn_2Al-NO_3-LDH (a), Zn_2Al-dipic-LDH (b) Zn_2Al-Ce(dipic)-LDH (c), and $Na_3[Ce(dipic)_3]$ (d)

Table 3-7 Temperature ranges (°C) in weight-loss regions of Zn_2Al-NO_3-LDH (a), Zn_2Al-dipic-LDH (b) Zn_2Al-Ce(dipic)-LDH (c), and $Na_3[Ce(dipic)_3]$ (d)

NO.	sample	I (°C)	II (°C)	III (°C)	IV (°C)
(a)	Zn_2Al-NO_3-LDH	25-80	80-170	170-290	
(b)	Zn_2Al-dipic-LDH	25-140	140-210	210-320	320-500
(c)	Zn_2Al-Ce(dipic)-LDH	25-140	140-200	200-310	310-380,380-460
(d)	$Na_3[Ce(dipic)_3]$	25-120	120-220	220-330	330-540

For the NO_3-LDH precursor, as shown in Fig. 3-38 (a), the first (30 - 80 °C) and second (80 - 170 °C) weight-loss stages can be attributed to the removal of physisorbed

water and water from the interlayer galleries respectively. A major mass loss was observed between 170 and 290 ^{o}C with a strong endothermic effect at 270 ^{o}C, resulting from dehydroxylation of brucite-like layers and decomposition of intercalated NO_3^- anions [38]. The weight-loss stages of the intercalated Zn_2Al-dipic-LDH (Fig. 3-38 (b)) and Zn_2Al-Ce(dipic)-LDH (Fig. 3-38 (c)) were different from those of the precursor but they also could be divided into four parts. The first reduction in mass between 25 and 140 °C was due to the loss of surface adsorbed water. The second event (140 - 210 °C) can be attributed to the elimination of interlayer structural water. The weight-loss for Zn_2Al-dipic-LDH during this stage was larger than that for Zn_2Al-Ce(dipic)-LDH, which suggests that more water molecules are present in the Zn_2Al-dipic-LDH structure. Some differences in thermal behavior can be observed in the third stage between 200 and 320 °C. The large and broad weight loss for the Zn_2Al-NO_3-LDH precursor was not observed for Zn_2Al-Ce(dipic)-LDH, consistent with the original NO_3^- ions being replaced by the $[Ce(dipic)_3]^{3-}$ and $dipic^{2-}$ anions, which do not decompose in this region [38]. Thus only dehydroxylation of LDH layers and removal of CO_3^{2-} impurities occurs in this region. The fourth weight-loss stage was in the region 320-500 °C, associated with the presence of $[Ce(dipic)_3]^{3-}$ and $dipic^{2-}$ anions. In this region, Zn_2Al-Ce(dipic)-LDH showed two weight-loss steps at 310 - 380, 380 - 460 ^{o}C, corresponding to the decomposition and combustion of $[Ce(dipic)_3]^{3-}$ and $dipic^{2-}$ anions in the interlayer galleries, while Zn_2Al-dipic-LDH displayed a single step located mainly at the higher temperature range, due to the combustion of ligands. TGA results were consistent with the foregoing XRD analysis. In the DTA curve of

Zn_2Al-Ce(dipic)-LDH, it showed two exothermic peaks (370 ^oC, 410 ^oC), so that the decomposition and combustion temperature of $[Ce(dipic)_3]^{3-}$ complexes in intercalated products is lower than that observed in $Na_3[Ce(dipic)_3]$ precursor (Fig. 3-38 (d), 460 ^oC). This probably resulted from the perturbation of the carboxylate groups coordinated to Ce^{3+}, which was induced by the interaction between the LDH layers and the ligands in the complex [16]. It confirms further that $[Ce(dipic)_3]^{3-}$ is really intercalated between the layers of Zn_2Al-Ce(dipic)-LDH.

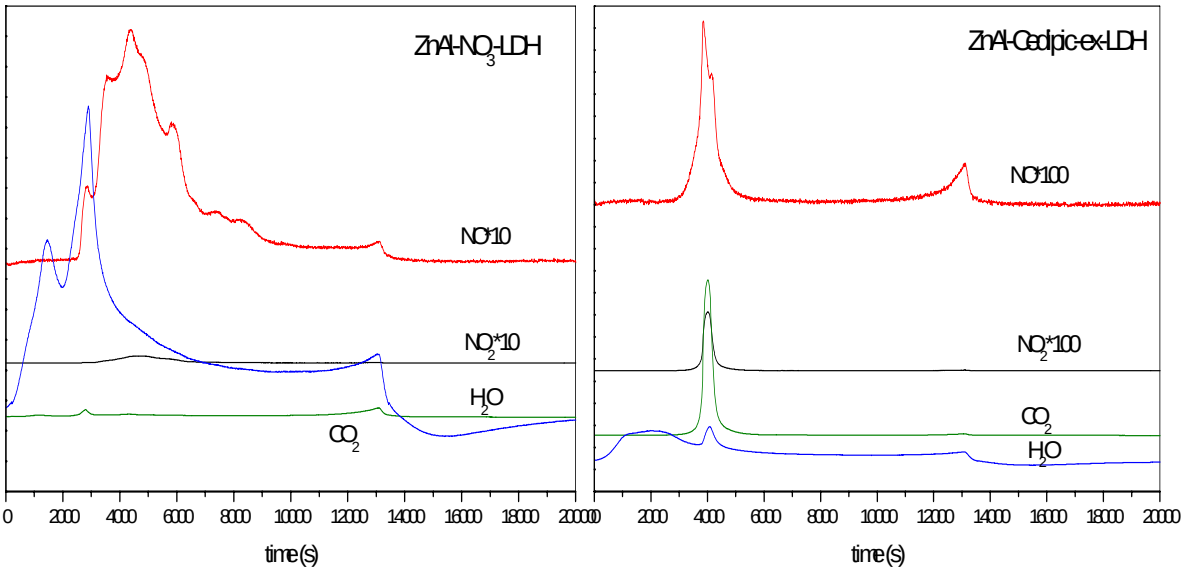

Fig. 3-39 TG-Mass spectra of Zn_2Al-NO_3-LDH (a) and Zn_2Al-Ce(dipic)-LDH (b)

The composition of the gases evolved during thermal decomposition of Zn_2Al-Ce(dipic)-LDH sample and Zn_2Al-NO_3-LDH precursor were measured using coupled TG-mass spectrometry and the results are shown in Fig. 3-39. For the precursor, only water and nitrogen oxides were observed. It can be clearly seen that water

molecules were removed in two steps. For sample Zn_2Al-Ce(dipic)-LDH, in the low temperature region, a continuous elimination of water corresponding to the removal of physisorbed and structural water and then the dehydroxylation of layers was observed. In the high temperature region, the simultaneous loss of H_2O, CO_2 and NO_2 (NO) arising from the decomposition and combustion of interlayer $[Ce(dipic)_3]^{3-}$ and $dipic^{2-}$ anions was observed.

3.7.1.1.2 *In situ* variable temperature XRD analysis

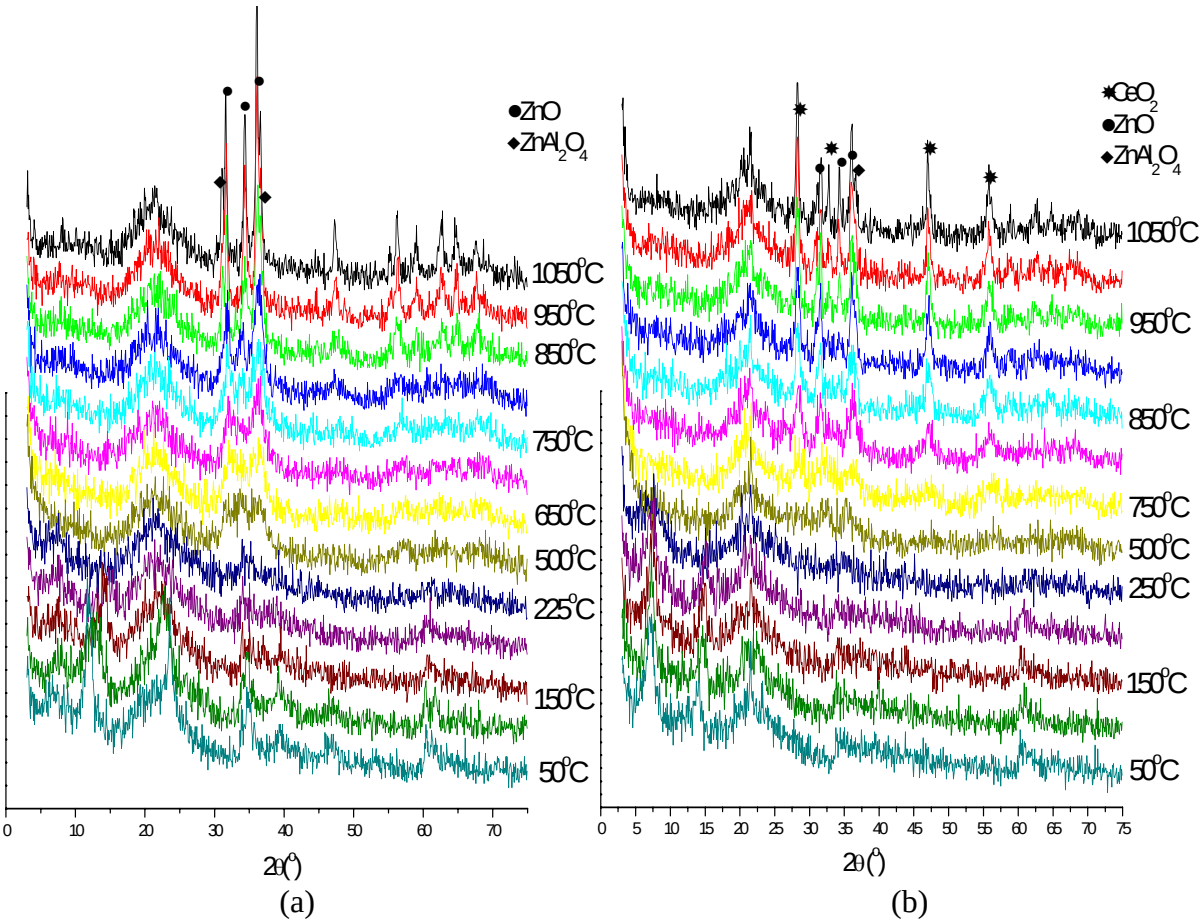

Fig. 3-40 *In situ* variable temperature XRD patterns of Zn_2Al-dipic-LDH (a) and Zn_2Al-Ce(dipic)-LDH (b)

Table 3-8 Temperature ranges (^{o}C) in *in situ* variable temperature XRD patterns of Zn_2Al-dipic-LDH and Zn_2Al-Ce(dipic)-LDH

composition	Zn_2Al-dipic-LDH	Zn_2Al-Ce(dipic)-LDH
LDHs (removal of physisorbed water)	25-150 °C	25-150 °C
collapse LDHs (loss of interlayer water)	150-225 °C	150-250°C
disordered metal oxides (ZnO)	225-650 °C	250-750 °C
crystallized metal oxides (ZnO)	650-850 °C	750-950 °C
ZnO, $ZnAl_2O_4$, CeO_2	850 °C above	950 °C above

The *in situ* variable temperature XRD patterns of Zn_2Al-Ce(dipic)-LDH are shown in Fig. 3-40 (b) and the temperature ranges listed in Table 3-8. In the region 25 to 150 °C, only slight intensity decreases were observed, but no positional shifts of the peaks. This indicated that only physisorbed water was removed in this temperature range, leaving the basic structure completely intact. At higher temperatures (150 - 250 °C), a gradual decrease in the basal spacing was observed, which can be explained by the loss of interlayer water molecules. At higher temperatures, the characteristic peaks of the LDH disappeared almost completely, leaving amorphous materials. Close to 750 °C crystallization of highly disordered ZnO was observed. Finally, well-crystallized ZnO was formed, together with $ZnAl_2O_4$ spinel and CeO_2, when the solid was calcined at 950 °C or above [50]. Zn_2Al-dipic-LDH (Fig. 3-40 (a)) showed a series of similar XRD patterns, but there were some differences in thermal stabilities of two materials. For Zn_2Al-dipic-LDH, crystallization of disordered ZnO began from 650 °C and crystalline ZnO and spinel were observed at 850 °C. This indicated that the presence of cerium in the calcined products increased the crystallization temperature of

metal oxides, which may be useful in catalysis. It was possible that the uniform dispersion of cerium cations increased the separation degree of other metal cations, leading to the decreased sintering during calcination.

3.7.1.2 CuZnAl-Ce(dipic)-LDH

3.7.1.2.1 Coupled TG/Mass analysis

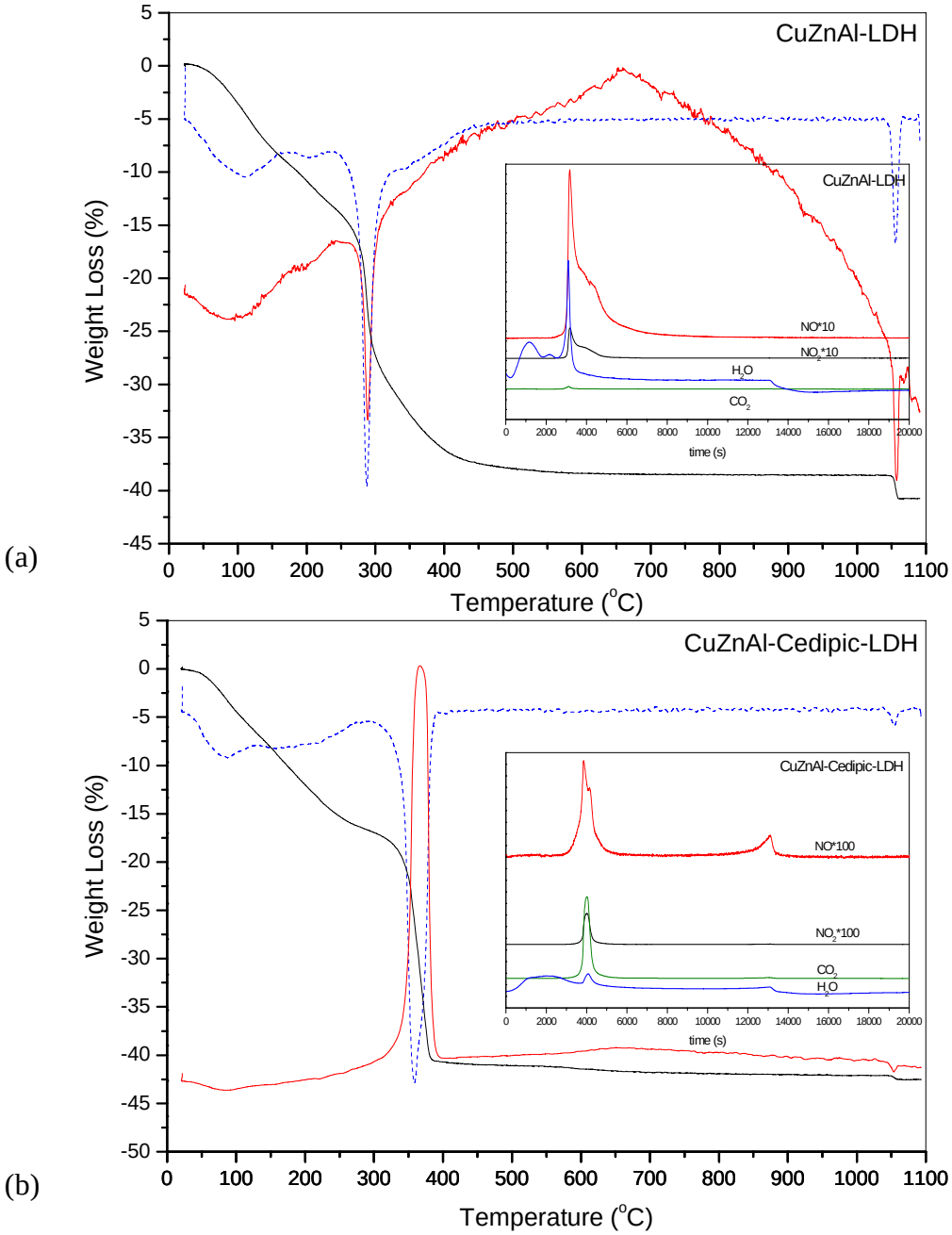

Fig. 3-41 TG/Mass spectra for CuZnAl-NO_3-LDH (a) and CuZnAl-Ce(dipic)-LDH (b)

The TG, DTG and DTA curves of the CuZnAl-NO_3-LDH precursor are shown in Fig. 3-41 (a). The removal of two kinds of water from the interlayer galleries resulted in the first and second weight-loss stage at 25-170 ^oC. The third stage at 170-240 °C corresponds to partial dehydroxylation of the layers as shown by the H_2O^+ signal in the mass spectrum. The majority of the layer dehydroxylation and nitrate decomposition was responsible for the fourth weight loss stage in the range from 240 to 320 °C. At about 285 °C, the mass spectra show strong peaks due to H_2O^+ and NO^+/NO_2^+ with a corresponding large endothermic effect in the DTA curve. During thermal decomposition, no mass signal due CO_2^+ was observed. The weight-loss stages of the intercalated product CuZnAl-Ce(dipic)-LDH are shown in Fig. 3-41 (b). The first and second reduction in mass between 25 °C and 190 °C was due to the loss of surface adsorbed and interlayer structural water. The DTA curve showed a small and broad endothermic effect. Some differences in thermal behavior from the precursor were observed in the third stage between 190 and 290 °C. For CuZnAl-LDH, a major mass loss was observed here, but after intercalation of $[Ce(dipic)_3]^{3-}$ anions, the weight-loss magnitude in this temperature range was reduced because only the dehydroxylation of the LDH layers occurred. The fourth weight-loss stage was in the region 290 - 400 °C, which can be attributed to decomposition and combustion of $[Ce(dipic)_3]^{3-}$ anions and dehydroxylation of a few residual M-OH groups, accompanied by a strong exothermic effect in the DTA at 370 °C. The single exothermic peak of CuZnAl-Ce(dipic)-LDH in this high temperature region suggested the presence of one $[Ce(dipic)_3]^{3-}$-LDH phase. In contrast, as shown in Fig. 3-38, two exothermic peaks are observed in this region for

Zn_2Al-Ce(dipic)-LDH, corresponding to the coexistence of $[Ce(dipic)_3]^{3-}$-LDH and $dipic^{2-}$-LDH phases. Moreover, the decomposition temperature of $[Ce(dipic)_3]^{3-}$ in intercalated products was lower than in the complex salts (460 °C). This may be explained by the perturbation of the carboxylate groups coordinated to Ce^{3+} induced by the interaction with LDH layers. Alternatively, the structure of $Na_3[Ce(dipic)_3]\cdot xH_2O$ salts consists of a strong hydrogen-bonded network of hydrated cations and anions and it is lost when the complex anions are dispersed in the interlayer galleries. It also may be another reason for the greater thermal stability of the precursor complex [16].

The mass spectra traces for H_2O^+ (m/z=18), CO_2^+ (m/z=44), NO^+ (m/z=30) and NO_2^+ (m/z=46) during thermal decomposition of CuZnAl-Ce(dipic)-LDH are displayed in the inset of Fig. 3-41. (The signal intensities of NO^+ and NO_2^+ are magnified 100 times). In the trace for H_2O^+, a broad and continuous signal was present in the regions 25 - 190 °C and 190 - 290 °C, which can be attributed to the water removal and layer dehydroxylation, respectively; a strong signal was also observed in the high temperature region at 320 - 390 °C. Peaks due to CO_2^+, NO^+ and NO_2^+ were observed in the same temperature range, which results from the combustion of interlayer organic moieties.

3.7.1.2.2 *In situ* variable temperature XRD analysis

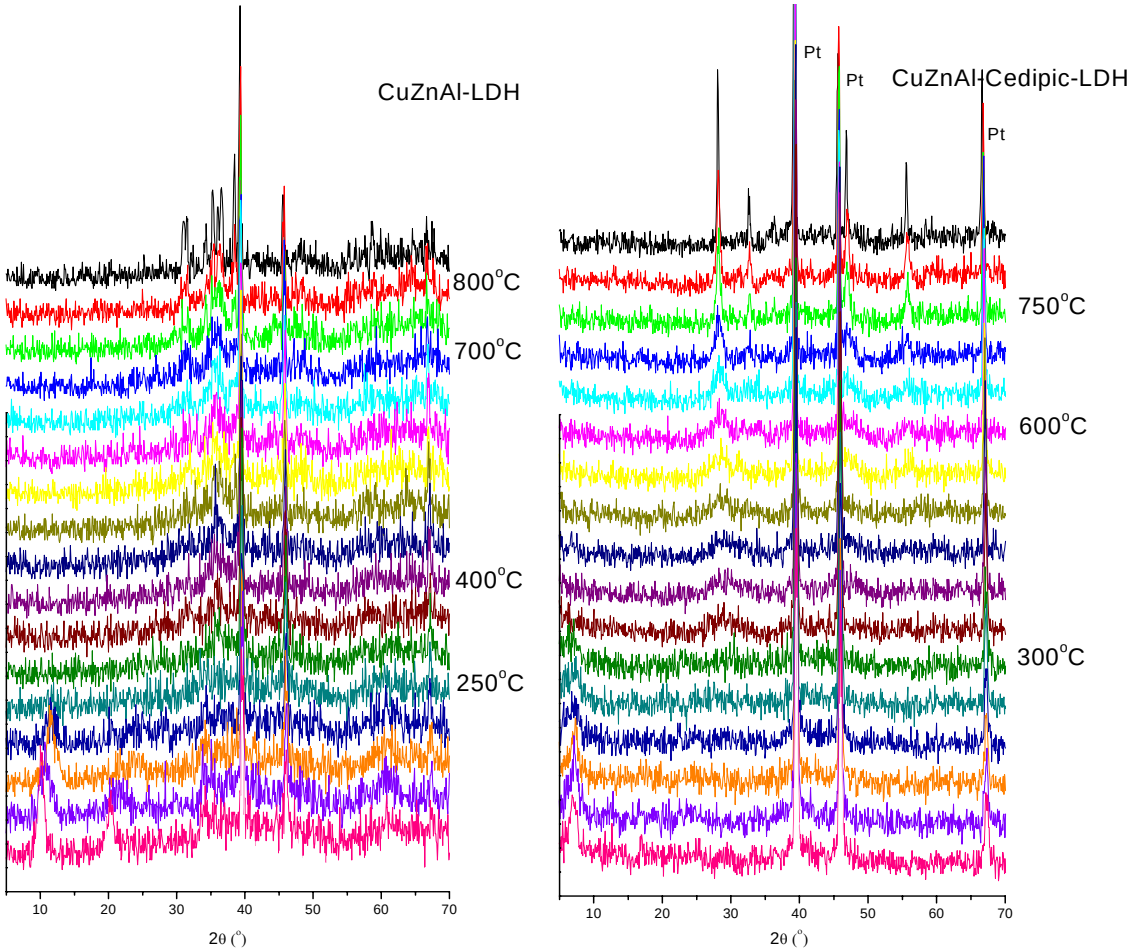

Fig. 3-42 *In situ* variable temperature XRD patterns of precursor CuZnAl-NO_3-LDH (a) and CuZnAl-Ce(dipic)-LDH intercalated sample(b)

Table 3-9 Temperature ranges in *in situ* variable temperature XRD patterns of CuZnAl-NO_3-LDH (a) and CuZnAl-Ce(dipic)-LDH (b)

composition	CuZnAl-NO_3-LDH	CuZnAl-Ce(dipic)-LDH
collapse LDHs (loss of water)	25-250 °C	25-300°C
disordered metal oxides (ZnO, CuO)	250-400 °C	300-600 °C
crystallized metal oxides (ZnO, CuO)	400-700 °C	600-800 °C
ZnO, CuO, $ZnAl_2O_4$, $CuAl_2O_4$,CeO_2	700 °C above	800 °C above

Fig. 3-42 shows *in situ* variable temperature XRD patterns of CuZnAl-Ce(dipic)-LDH product (b) and CuZnAl-NO_3-LDH precursor (a), in which the temperatures of thermal treatment increase from room temperature up to 1100 ^oC. In both cases, with temperature increasing, the (003) reflection initially shifted to higher angle indicating a decrease in interlayer spacing, which can be attributed to the removal of interlayer water. The loss of hydrogen bonding network results in a decrease in the tactic order of guest anions [39,50], which leads to a decrease in crystallinity which is reflected in the reduced intensity of (003) reflection. At higher temperatures, the (003) reflection disappeared and amorphous phases were present, as a result of dehydroxylation of the layers as well as decomposition of the interlayer guest anions. With a further increase in calcination temperature, characteristic peaks appeared indicating that the material consisted of a mixture of spinels and metal oxide phases. As shown in Table 3-9, for CuZnAl-Ce(dipic)-LDH, the characteristic peaks of LDH structure disappeared completely at 300 °C; close to 600 °C the crystallization of highly disordered metal oxides were observed; at 800 °C, well crystallized oxides were formed, together with spinel phases and CeO_2. The chemical composition of the sample after calcination at 1100 °C had been indicated in Fig. 3-24. For CuZnAl-NO_3-LDH, complete collapse of the brucite-like layers occured at 250 °C, crystallization of disordered metal oxides began from 400 °C, and crystallized oxides and spinels were observed at 700 °C. It is clear that the presence of cerium increases the temperature of formation of $CuAl_2O_4$ spinel and enhances the thermal stability of CuO phase, which may be favorable from the point of view of catalysis. It may be caused by the formation

of Cu-Ce solid solution which inhibits the presence of spinel phase [62].

3.7.1.3 Varied $[Ce(dipic)_3]^{3-}$-LDHs

Table 3-10 Temperature ranges (^oC) in weight-loss regions for other $M^{2+}{}_2Al$-Ce(dipic)-LDH

sample	I (^oC)	II (^oC)	III (^oC)	IV (^oC)
Zn_2Al-Ce(dipic)-LDH	25-140	140-200	200-310	310-380,380-460
Zn_2Cr-Ce(dipic)-LDH	25-150	150-200	200-340	340-410
CuZnAl-Ce(dipic)-LDH	25-130	130-190	190-290	290-400

Table 3-10 lists the temperature ranges of weight-loss regions in TG curves for $[Ce(dipic)_3]^{3-}$-LDH materials with different layer cations. The thermal behaviors of these intercalated products were consistent with that of common LDH structure as far as the stage attributed to dehydration was concerned. The temperatures at which dehydroxylation of the layers and decomposition of the interlayer anions occurred were related to chemical composition of the layers, which was confirmed in Table 3-10. In particular, the temperature of dehydroxylation of the layers in Zn_2Cr-Ce(dipic)-LDH was higher than that in other intercalated LDHs, but was close to that in Zn_2Cr-NO_3-LDH precursor. The temperatures of decomposition and combustion of the $[Ce(dipic)_3]^{3-}$ anions in three intercalated LDHs showed some slight differences corresponding to the varied interactions between different layer cations and the complexes. Moreover, it could be found that the weight-loss stage at more than 420 °C was only observed for Zn_2Al-Ce(dipic)-LDH, due to the combustion of interlayer $dipic^{2-}$ anions. This suggests that the decomposition of $[Ce(dipic)_3]^{3-}$ anions into $dipic^{2-}$ and

Ce^{3+} (Ce^{4+}) only occur in the case of Zn_2Al-Ce(dipic)-LDH, which is related to the stronger interaction between layers and interlayer anions in this intercalated product.

3.7.2 Thermal behaviors of $[Ce(DTPA)]^{2-}$-LDHs

3.7.2.1 Coupled TG/Mass analysis

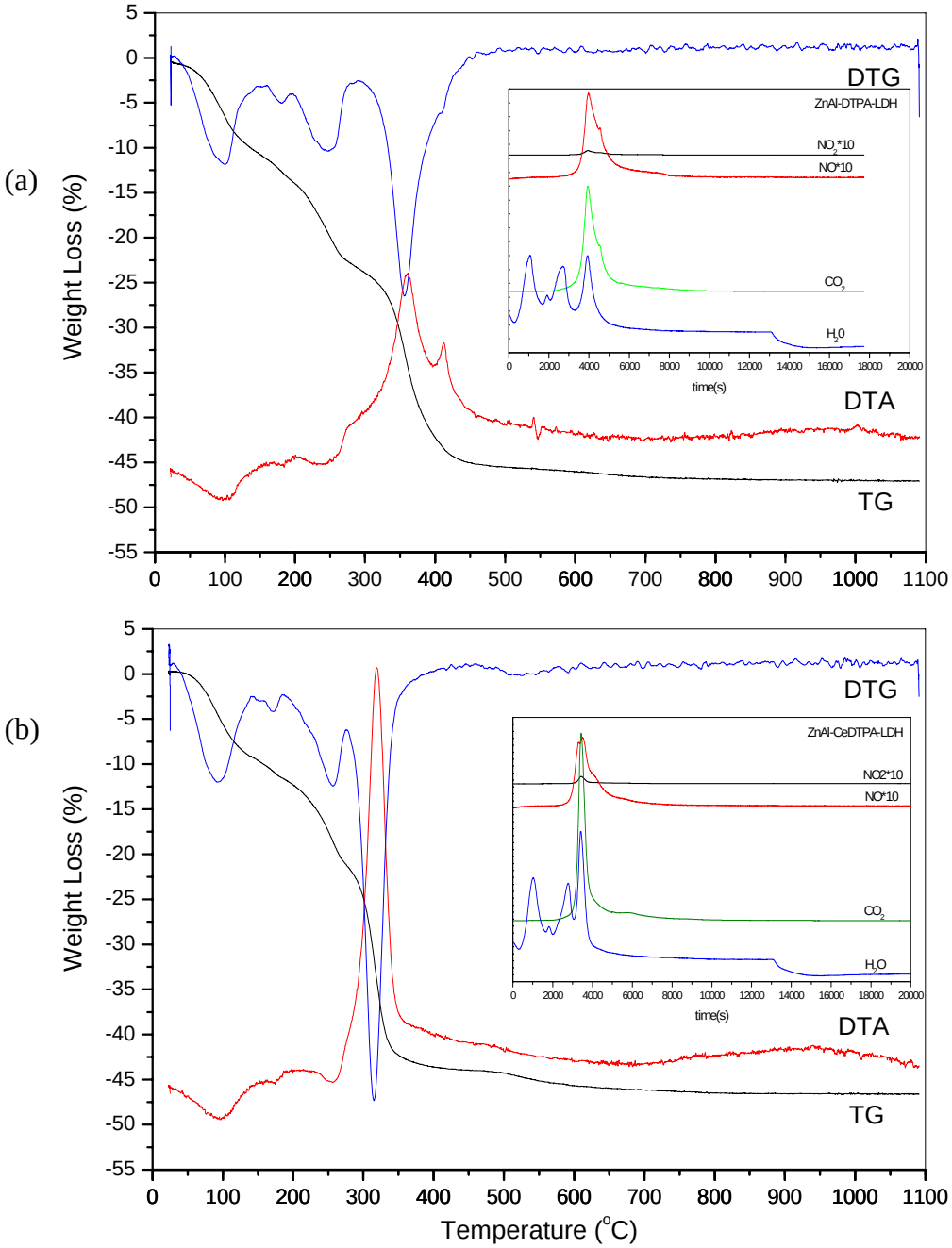

Fig. 3-43 TG/Mass spectra of Zn_2Al-DTPA-LDH(a) and Zn_2Al-Ce(DTPA)-LDH(b)

Table 3-11 Temperature ranges (^{o}C) in weight-loss regions of Zn_2Al-DTPA-LDH (a) and Zn_2Al-Ce(DTPA)-LDH (b)

NO.	sample	I (^{o}C)	II (^{o}C)	III (^{o}C)	IV (^{o}C)
(a)	Zn_2Al-DTPA-LDH	25-155	155-200	200-290	290-470
(b)	Zn_2Al-Ce(DTPA)-LDH	25-155	155-190	190-275	275-385

Fig. 3-43 shows the thermal decomposition behavior of Zn_2Al-DTPA-LDH and Zn_2Al-Ce(DTPA)-LDH. In both cases, the weight-loss can be divided into 4 stages, although they occur in different temperature ranges. For Zn_2Al-Ce(DTPA)-LDH (Fig. 3-43 (b)), the first reduction in mass between 25 and 155 °C and the second event between 155 and 190 °C were due to the loss of surface adsorbed and interlayer structural water, respectively. The DTA curve showed two small broad endothermic effects. The third weight-loss stage in the region 190 - 275 °C accompanying with an small endothermic effect, can be attributed to dehydroxylation of the brucite-like layers. The corresponding temperature was shifted to a lower value for Zn_2Al-DTPA-LDH (Fig. 3-43 (a)), which indicated that the intercalation of a complex into interlayer spaces could influence the properties of not only the guest but also the host [6]. The main difference in thermal behavior between two samples was found in the fourth stage, which resulted from decomposition and combustion of the organic anions and dehydroxylation of a few residual M-OH groups. For Zn_2Al-Ce(DTPA)-LDH, this process occurred at 275 - 385 °C accompanying with a strong exothermic effect at 320 °C. For Zn_2Al-DTPA-LDH, the weight-loss stage appeared at a higher temperature range 290 - 470 °C and 2 exothermic peaks were observed at 360 °C and 410 °C,

respectively. It may be explained by the different interactions between the layers and carboxylate groups located in 2 kinds of chemical environments in the structure of $DTPA^{5-}$ ligand, while for a $[Ce(DTPA)]^{2-}$ complex, the coordination with central Ce ions seemed to reduce the difference so that only a exothermic effect was observed in this weight-loss stage of Zn_2Al-Ce(DTPA)-LDH. Moreover, the coordination decreased the interaction between layers and carboxylate groups, which resulted in the lower combustion temperature of interlayer $[Ce(DTPA)]^{2-}$ complexes than that of $DTPA^{5-}$ ligands.

The mass spectra of H_2O^+ (m/z = 18), CO_2^+ (m/z = 44), NO^+ (m/z = 30) and NO_2^+ (m/z = 46) are displayed in the inset of Fig. 3-43 (the signal intensities of NO^+ and NO_2^+ are magnified 10 times). The mass spectrum trace for H_2O^+ consisted of four signals, which was in great agreement with the TG analysis. At higher temperatures, strong signals from H_2O^+, CO_2^+, NO^+ and NO_2^+ were observed simultaneously, due to combustion of interlayer organic anions.

3.7.2.2 *In situ* variable temperature XRD analysis

Table 3-12 Temperature ranges in *in situ* variable temperature XRD patterns of Zn_2Al-DTPA-LDH and Zn_2Al-Ce(DTPA)-LDH

composition	Zn_2Al-DTPA-LDH	Zn_2Al-Ce(DTPA)-LDH
collapse LDHs (loss of water)	25-250 °C	25-225°C
disordered metal oxides (ZnO, CuO)	250-600 °C	225-650 °C
crystallized metal oxides (ZnO, CuO)	600-750 °C	650-800 °C
ZnO, CuO, $ZnAl_2O_4$, $CuAl_2O_4$,CeO_2	750 °C above	800 °C above

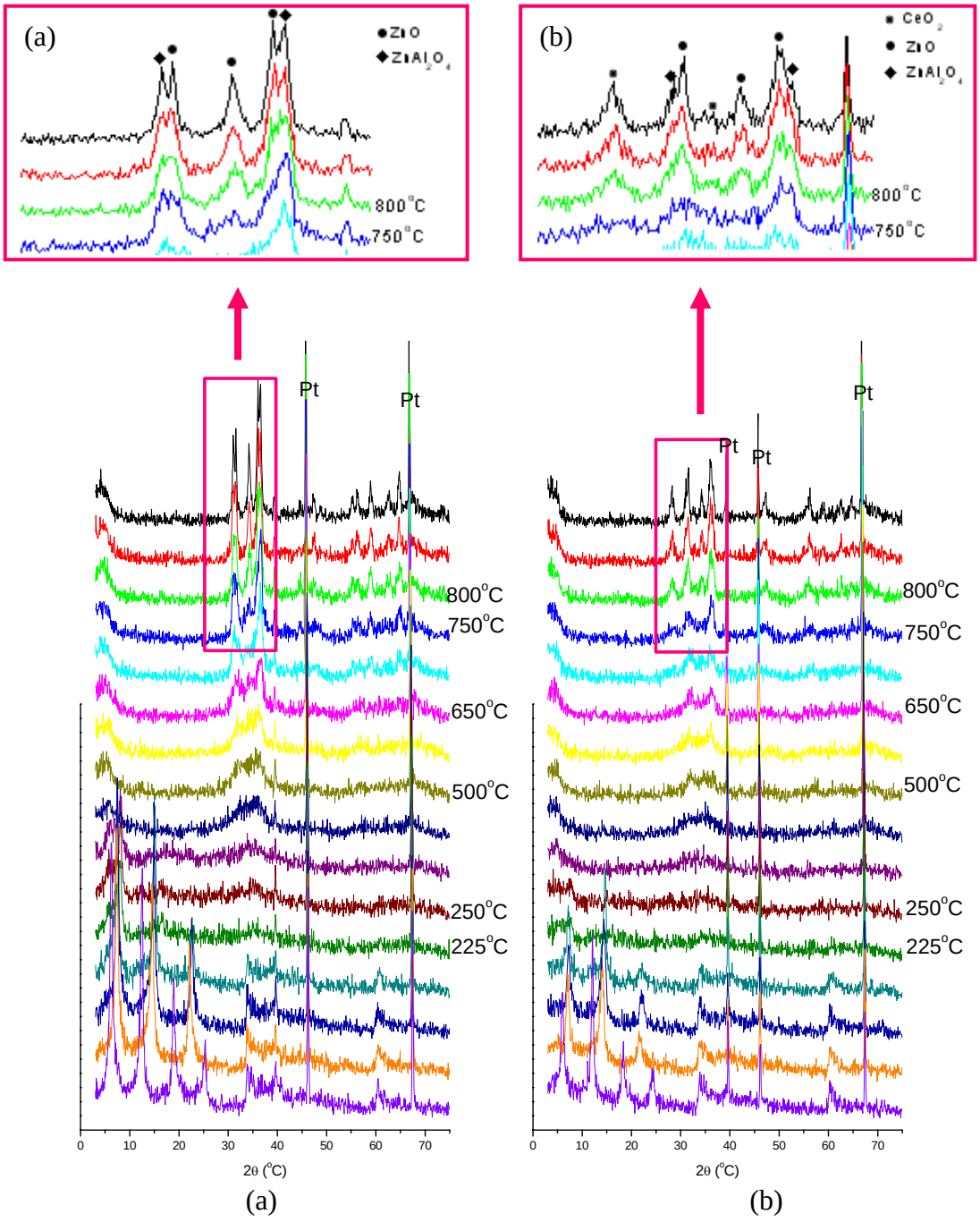

Fig. 3-44 *In situ* variable temperature XRD patterns of Zn_2Al-DTPA-LDH (a) and Zn_2Al-Ce(DTPA)-LDH (b)

Fig. 3-44 shows the *in situ* variable temperature XRD patterns of Zn_2Al-DTPA-LDH (a) and Zn_2Al-Ce(DTPA)-LDH (b), in which the temperature of

thermal treatment is increased from room temperature to 900 ^{o}C. For Zn_2Al-Ce(DTPA)-LDH, the (003) reflection shifted to higher angle with increase of temperature up to 225 °C, corresponding to a decrease in interlayer spacing, which was due to the dehydration process. When the temperature was further increased, the characteristic LDH reflections disappeared, leaving amorphous materials. Close to 650°C crystallization of highly disordered ZnO was observed. At 800 °C or above, well crystallized ZnO was formed, together with $ZnAl_2O_4$ spinel and CeO_2, as indicated in the magnified figure (b). For Zn_2Al-DTPA-LDH however, the characteristic peaks of the LDH structure disappeared completely at 250 °C, the crystallization of disordered ZnO began from 600 °C and crystallized ZnO and spinel were observed at 750 °C. The presence of cerium led to an increase in the temperature of formation of crystalline metal oxides and spinels (as shown in Table 3-12), and a decrease in the quantity of $ZnAl_2O_4$ relative to ZnO at 900 °C, which was in good agreement with the results obtained for the $[Ce(dipic)_3]^{3-}$ complex discussed above. This indicated the incorporation of cerium into Zn_2Al-LDHs using $[Ce(DTPA)]^{2-}$ resulted in a uniform distribution of rare earth element cations within the oxide matrix.

3.7.3 Thermal behaviors of $[Eu(dipic)_3]^{3-}$-LDHs

Table 3-10 lists the temperature ranges in four weight-loss regions of sample Zn_2Al-Eu(dipic)-LDH and Zn_2Cr-Eu(dipic)-LDH. It was seen that three weight loss stages below 320 ^{o}C of Zn_2Al-Ce(dipic)-LDH and Zn_2Al-Eu(dipic)-LDH corresponding to dehydration and dehydroxylation were similar. The fourth weight-loss stage occurred in two steps as discussed above (see Section 3.7.1.1.1), but

the combustion temperature of $[Eu(dipic)_3]^{3-}$-LDH at 430 - 500 ^oC was higher than that of $[Ce(dipic)_3]^{3-}$-LDH at 310 - 380 ^oC, and the decomposition of $dipic^{2-}$-LDH (co-product) mainly occurred at 380 - 430 ^oC. In the DTA curves, the strong exothermic effect due to combustion of $[Eu(dipic)_3]^{3-}$ showed at 450 ^oC, and that in Zn_2Al-Ce(dipic)-LDH displayed at 370 ^oC. Moreover, the strong exothermic effects for Zn_2Cr-Eu(dipic)-LDH and Zn_2Cr-Ce(dipic)-LDH were located at 390 and 370 ^oC, respectively. The temperature of decomposition and combustion of organic segments in $[Eu(dipic)_3]^{3-}$-LDHs was higher than that in $[Ce(dipic)_3]^{3-}$-LDHs, which arose from the difference in thermal stability of two complexes. The coordination between central Eu^{3+} ion and $dipic^{2-}$ ligands is stronger due to the smaller size and higher charge density of Eu^{3+}, so that the thermal stability of $[Eu(dipic)_3]^{3-}$ complex is higher. For intercalated Zn_2Cr-LDH materials, their thermal behaviors took on a similar trend like Zn_2Al-LDHs though the temperature ranges in weight loss regions were different because of the varied layer cations. Especially, the fourth weight loss stage only included a single step. It indicated that the varied interaction between host layers and guest complexes influenced the intercalation process and product structure.

Table 3-10 Temperature ranges (^oC) in weight-loss regions for products Zn_2Al-Eu(dipic)-LDH and Zn_2Cr-Eu(dipic)-LDH

sample	I (^oC)	II (^oC)	III (^oC)	IV (^oC)
Zn_2Al-Ce(dipic)-LDH	25-140	140-200	200-310	310-380,380-460
Zn_2Al-Eu(dipic)-LDH	25-145	145-200	200-320	320-430,430-500
Zn_2Cr-Ce(dipic)-LDH	25-150	150-200	200-340	340-410
Zn_2Cr-Eu(dipic)-LDH	25-150	150-200	200-350	350-450

3.8 Conclusions

1. Ce-containing LDH phases were prepared by an anion exchange process involving $[Ce(dipic)_3]^{3-}$ complex anions and a LDH precursor containing interlayer nitrate anions: the product was mixed with some carbonate-containing LDH. The products were characterized by a variety of physicochemical techniques, which demonstrated the intercalation of $[Ce(dipic)_3]^{3-}$ anions in the layered structure of the host. The interlayer spacing of Zn_2Al-LDH with intercalated $[Ce(dipic)_3]^{3-}$ was 1.24 nm, with a tilted orientation of the complex in the interlayer galleries. For some host matrix compositions, the $[Ce(dipic)_3]^{3-}$ underwent partial decomposition into $dipic^{2-}$ during the intercalation process resulting in the formation of $dipic^{2-}$-intercalated LDH phases as co-product.

2. After studying the influence of varying key synthesis parameters, the experimental conditions were optimized: the best results were obtained with a ratio $M^{2+}/M^{3+} = 2$, a $[Ce(dipic)_3]^{3-}$ concentration around 5 mmol/l and an exchange period around 10 h at room temperature.

3. Attempted syntheses of the materials by co-precipitation methods were unsuccessful because a strong interaction between Zn^{2+} and $dipic^{2-}$ leads to decomposition of the $[Ce(dipic)_3]^{3-}$ complexes.

4. Using the optimized experimental conditions, $[Ce(dipic)_3]^{3-}$-containing LDHs with different layer compositions were prepared, and the varied interactions between the different host layers and the complexes leads to changes in interlayer spacing and exchange capacities.

5. A series of Ce-containing CuZnAl-LDHs was also synthesized using the ion

exchange method and the catalytic abilities of their calcination products were evaluated as described in Chapter 4. For these materials, the decomposition of $[Ce(dipic)_3]^{3-}$ complexes during intercalation and co-intercalation of CO_3^{2-} were less observed than for the other LDH hosts.

6. The adsorption of $[Ce(dipic)_3]^{3-}$ complexes onto LDHs was found to proceed in two steps: saturation of the external sites was followed by an interlayer process occurring at high equilibrium concentrations. The adsorption isotherm was in good agreement with the Langmuir adsorption model at lower equilibrium concentrations. The adsorption capacity on Zn_2Al-LDH was better than on Zn_2Cr-LDH.

7. Another Ce containing complex, $[Ce(DTPA)]^{2-}$, was also employed to prepare a Ce-containing LDH. The product had a well crystallized LDH structure. Its thermal behavior demonstrated the advantages of the presence of cerium in metal oxides.

8. Eu-containing LDHs were prepared by an anion exchange process with $[Eu(dipic)_3]^{3-}$ anions and characterized. The results confirmed the intercalation of $[Eu(dipic)_3]^{3-}$ complexes into LDH hosts. The luminescence properties of the Eu(III)-containing products were investigated. The new luminescent materials improved thermal stability and luminescence properties with respect to a simple $[Eu(dipic)_3]^{3-}$ complex, and Eu^{3+} could be used as structural probe to obtain details of the interaction between the complex and the layered host. The structural information about host-guest interactions deduced using this technique can reasonably be transposed to $[Ce(dipic)_3]^{3-}$-LDHs, considering the similarity between the structures of the two rare earth complexes [4].

9. The thermal behavior of the Ce-containing LDH materials has been analyzed in terms

of dehydration and dehydroxylation of the layers at low temperatures, while the intercalated species were decomposed at higher temperatures. The presence of cerium influenced the thermal stability of the LDHs. The uniform distribution of cerium oxides in the calcination products increased the temperature at which spinels were formed. This enhanced thermal stability of intermediate metal oxide phases may be advantageous from the point of view of catalysis.

Reference

1. C. Sanchez, B. Lebeau, F. Chaput, J. P. Boilot, Optical Properties of Functional Hybrid Organic-Inorganic Nanocomposites, *Adv. Mater.*, 2003, 15(23), 1969-1994.
2. G. R. Choppin, P. A. Baisden, S. A. Khan, Nuclear magnetic resonance studies of diamagnetic metal-diethylenetriaminepentaacetate complexes, *Inorg. Chem.*, 1979, 18(5), 1330-1332.
3. A. Fernandes, J. Jaud, J. Dexpert-Ghys, C. Brouca-Cabarrecq, Study of new lanthanide complexes of 2,6-pyridinedicarboxylate: synthesis, crystal structure of Ln(Hdipic)(dipic) with Ln = Eu, Gd, Tb, Dy, Ho, Er, Yb, luminescence properties of Eu(Hdipic)(dipic), *Polyhedron*, 2001, 20(18), 2385-2391.
4. M. Latva, H. Takalo, V. M. Mukkala, C. Matachescu, J. C. Rodriguez-Ubis, J. Kankare, Correlation between the lowest triplet state energy level of the ligand and lanthanide (III) luminescence quantum yield, *J. Lumin.*, 1997, 75(2), 149-169.
5. A. C. Franville, R. Mahiou, D. Zambon, J. C. Cousseins, Molecular design of luminescent organic-inorganic hybrid materials activated by europium (III) ions, *Solid State Sci.*, 2001, 3(1-2), 211-222.
6. S. Gago, M. Pillinger, R. A. S. Ferreira, L. D. Carlos, T. M. Santos, I. S. Gonsalves, Immobilization of Lanthanide Ions in a Pillared Layered Double Hydroxide, *Chem. Mater.*, 2005, 17, 5803-5809.

7. S. P. Newman, W. Jones, Synthesis characterization and application of layered double hydroxides containing organic guests, *New J. Chem.*, 1998, 22(2), 105-115.
8. V. Rives, M. A. Ulibarri, Layered double hydroxides (LDH) intercalated with metal coordination compounds and oxometalates, *Coord. Chem. Rev.*, 1999, 181(1), 61-120.
9. A. I. Tsyganok, K. Suzuki, S. Hamakawa, K. Takehira, T. Hayakawa, Alternative Approach to Incorporation of Nickel into Layered Structure of Mg-Al Double Hydroxides: Intercalation with [Ni(edta)$^{2-}$] species, *Chem. Lett.*, 2001, 30(1), 24.
10. M. Kaneyoshi, W. Jones, Formation of Mg-Al layered double hydroxides intercalated with nitrilotriacetate anions, *J. Mater. Chem.*, 1999, 9, 805-812.
11. J. Rocha, L. D. Carlos, Mircroporous materials containing lanthanide metals, *Curr. Opin. Solid State Mater. Sci.*, 2003, 7(3), 199-205.
12. D. Sendor, U. Kynast, Efficient Red-Emitting Hybrid Materials Based on Zeolites, *Adv. Mater.*, 2002, 14(21), 1570-1574.
13. H. R. Li, J. Lin, H. J. Zhang, L. S. Fu, Q. G. Meng, S. B. Wang, Preparation and Luminescence Properties of Hybrid Materials Containing Europium(III) Complexes Covalently Bonded to a silica Matrix, *Chem. Mater.*, 2002, 14(9), 3651-3655.
14. M. Alvaro, V. Fornes, S. Garca,; H. Garcia, J. C. Scaiano, Intrazeolite Photochemistry. 20. Characterization of Highly Luminescent Europium Complexes inside Zeloites, *J. Phys. Chem. B*, 1998, 102(44), 8744-8750.
15. E. Brunet, M. J. de la Mata, O. Juanes, J. C.Rodriguez-Ubis, Sensitized Luminescence of Lanthanides within the Walls of Polyethylenoxa-Pillared γ-zirconium Phosphate, *Chem. Mater.*, 2004, 16(8), 1517-1522.
16. C. Li, G. Wang, D. G. Evans, X. Duan, Incorporation of rare-earth ions in Mg.Al layered double hydroxides: intercalation with an [Eu(EDTA)]$^{-}$ chelate, *J. Solid State Chem.*, 2004, 177, 4569-4575.
17. N. G. Zhuravleva, A. A. Eliseev, A. V. Lukashin, U. Kynast, Y. D. Tretyakov, Luminescent Materials Based on Tb- and Eu- Containing Layered Double Hydroxides, *Dokl. Chem.*, 2004, 396(1-3), 87-91
18. K. A. Tarasov, D. O'Hare, Solid-State Chelation of Metal Ions by

Ethylenediaminetetraacetate Intercalated in a Layered Double Hydroxide, *Inorg. Chem.*, 2003, 42(6), 1919-1927.

19. A. I. Tsyganok, T. Tsunoda, S. Hamakawa, K. Suzuki, K. Takehira, T. Hayakawa, Dry reforming of methane over catalysts derived from nickel-containing Mg-Al layered double hydroxides, *J. Catal.*, 2003, 213, 191-203.
20. A. I. Khan, D. O'Hare, Intercalation chemistry of layered double hydroxides: recent developments and applications, *J. Mater. Chem.*, 2002, 12, 3191-3198.
21. N. H. Gutmann, L. Spiccia, T. W. Turney, Complexation of Cu(II) and Ni(II) by nitrilotriacetate intercalated in Zn-Cr layered double hydroxides, *J. Mater. Chem.*, 2000, 10(5), 1219-1224.
22. S. Miyata, Anion-exchange properties of hydrotalcite-like compounds, *Clays Clay Miner.*, 1983, 31, 305-311.
23. J. Albertsson, Structural studies on the rare earth carboxylates, *Acta Chem. Scand.*, 1972, 26(3), 1023-1044.
24. J. G. Kim , S. K. Yoon , Y. Sohn , J. G. Kang, Luminescence and crystal field parameters of the $Na_3[Eu(DPA)_3]\cdot 12H_2O$ complex in a single crystalline state, *J. Alloys Comp.*, 1998, 274, 1-9.
25. J. Dexpert-Ghys, C. Picard, A. Taurines, Complexes of Rare Earths and Dipicolinato Ions Encapsulated in X- and Y-zeolites: Luminescence Properties, *J. Inclusion Phenomena Macrocyclic Chem.*, 2001, 39, 261-267.
26. H. Kato, Y. Kanazawa, M, Okumura, A, Taninaka, T. Yokawa, H. Shinohara, Lanthanoid Endohedral Metallofullerenols for MRI Contrast Agents, *J. Am. Chem. Soc.*, 2003, 125, 4391-4397.
27. S. Benazeth, J. Purans, M. C. Chalbot, M. K. Nguyen-van-Duong, L. Nicolas, F. Keller, A. Gaudemer, Temperature and pH Dependence XAFS Study of $Gd(DOTA)^-$ and $Gd(DTPA)^{2-}$ Complexes: Solid State and Solution Structures, *Inorg. Chem.*, 1998, 37, 3667-3674.
28. M. Kodama, T. Koike, A. B. Mahatma, E. Kimura, Thermodynamic and Kinetic Studies of Lanthanide Complexes of 1,4,7,10,13 -Pentaazacyclopentadecane-N,N',N'',N''',N''''-pentaacetic Acid and

1,4,7,10,13,16-Hexaazacyclooctadecane-*N,N', N", N"', N"", N'""*-hexaacetic Acid, *Inorg. Chem.*, 1991, 30, 1270-1273.

29. N. Sakagami, Y. Yamada, T. Konno, K. Okamoto, Crystal structures and stereochemical properties of lanthanide(III) complexes with ethylenediamine - *N,N,N',N'* - tetraacetate, *Inorg. Chim. Acta*, 1999. 288, 7-16.
30. V. Prevot, C. Forano, J. P. Besse, F. Abraham, Syntheses and Thermal and Chemical Behaviors of Tartrate and Succinate Intercalated Zn_3Al and Zn_2Cr Layered Double Hydroxides, *Inorg. Chem.*, 1998, 37, 4293-4301.
31. J. Inacio, C. Taviot-Gueho, C. Forano, J. P. Besse, Adsorption of MCPA pesticide by MgAl-layered double hydroxides, *Appl. Clay Sci.*, 2001, 18, 255-264.
32. Q. G. Meng, P. Boutinaud, A. C. Franville, H. J. Zhang, R. Mahiou, Preparation and characterization of luminescent cubic MCM-48 impregnated with an Eu^{3+} b-diketonate complex, *Microporous Mesoporous Mater.*, 2003, 65, 127-136.
33. J. Albertsson, Structural Studies on the Rare Earth Carboxylates, *Acta Chem. Scand.*, 1970, 24, 1213-1229.
34. W. Brzyska, W. Oiga, Preparation and properties of rare earth element complexes with pyridine-2,6-dicarboxylic acid, *Thermochimica Acta*, 1994, 247, 329-339.
35. P. A. Brayshaw, J. C. G. Bunzli, P. Froidevaux, J. M. Harrowfield, Y. Kim, A. N. Sobolevt, Synthetic, Structural, and Spectroscopic Studies on Solids Containing Tris(dipico1inato) Rare Earth Anions and Transition or Main Group Metal Cations, *Inorg. Chem.*, 1995, 34, 2068-2076.
36. J. Cobb, P. Warwick, R. C. Carpenter, R. T. Morrison, Determination of strontium-90 in water and urine samples using ion chromatography, *the Analyst*, 1994, 119(8), 1759-1764.
37. C. Barriga, W. Jones, P. Malet, V. Rives, M. A. Ulibarri, Synthesis and Characterization of Polyoxovanadate-Pillared Zn-Al Layered Double Hydroxides: An X-ray Absorption and Diffraction Study, *Inorg. Chem.*, 1998, 37, 1812-1820.
38. C. W. Hu, Q. L. He, Y. H. Zhang, E. B. Wang, T. Okuhara, M. Misono, Synthesis, stability and oxidative activity of polyoxometalates pillared anionic clays ZnAl-SiW_{11} and ZnAl-$SiW_{11}Z$, *Catal. Today*, 1996, 30, 141-146.

39. H. Nijs, A. Clearfield, E. F. Vansant, The intercalation of phenylphosphonic acid in layered double hydroxides, *Microporous Mesoporous Mater.*, 1998, 23, 97-108.

40. J. T. Kloprogge, R. L. Frost, Infrared and Raman Spectroscopic Studies of Layered Double Hydroxides in Layered Double Hydroxides: Present and Future, chapter 5, V. Rives (Eds), NOVA, New York, 2001.

41. F. Cavani, F. Trifiro, A. Vaccari, Hydrotalcite-type anionic clays: preparation, properities and applications, *Catal. Today*, 1991, 11, 173-301.

42. L. H. Zhang, J. Zhu, X. R. Jiang, D. G. Evans, F. Li, Influence of nature of precursors on the formation and structure of Cu-Ni-Cr mixed oxides from layered double hydroxides, *J. Phys. Chem. Solids*, 2006, (in press).

43. F. Li, X. Duan, Study on adsorption of glyphosate (N-phosphonomethyl glycine) pesticide on MgAl-layered double hydroxides in aqueous solution, *J. Hazardous Mater. B*, 2005, 125, 89-95.

44. J. Rocha, Solid-State NMR and EPR Studies of Hydrotalcities in Layered Double Hydroxides: Present and Future, chapter 6, V. Rives (eds), NOVA, New York, 2001.

45. Y. Inomata, T. Sunakawa, F. S. Howell, The syntheses of lanthanide metal complexes with diethylenetriamine-N,N,N',N'',N''-pentaacetic acid and the comparison of their crystal structures, *J. Mole. Struc.*, 2003, 648, 81-88.

46. T. Moeller, Periodicity and the Lanthanides and Actinides, *J. Chem. Educ.*, 1970, 47, 417-430.

47. P. Caravan, J. J. McMurry, R. B. Lauffer, Gadolinium(III) chelates as MRI Contrast Agents : Structure, Dynamics, and Applications, *Chem. Rev.*, 1999, 99(9), 2293.

48. S. Aime, M. Botta, M. Fasano, S. G. Crich, E. Terreno, ^{1}H and ^{17}O-NMR relaxometric investigations of paramagnetic contrast agents for MRI. Clues for higher relaxivities, *Coord. Chem. Rev.*, 1999, 185, 321-333.

49. A. E. Merbach, E. Toth (Eds.), The Chemistry of Contrast Agents in Medical Resonance Imaging, Wiley, Chichester, 2001.

50. P. Beaudot, M. E. de Roy, J. P. Besse, Intercalation of noble metal complexes in LDH compounds, *J. Solid State Chem.*, 2004, 177, 2691-2698.

51. P. Beaudot, M. E. de Roy, J. P. Besse, Preparation and Characterizatiion of

Intercalation Compounds of Layered Double Hydroxides with metallic Oxalato Complexes, *Chem. Mater.*, 2004, 16(5), 935-945.

52. W. T. Carnall, K. A. Gschneidner, L. R. Erying (Eds), Handbook on the Physics and Chemistry of Rare Earths, North-Holland, Amsterdam, New York and Oxford, 1979, 3, Chapter 24.
53. J. C. G. Bunzli, B. Klein, G. O. Pradervand, P. Porcher, Spectroscopic properties, electronic levels, and crystal field parameters of pentakis (nitrado) europate(III) ions, *Inorg. Chem.*, 1983, 22 (25), 3763-3768.
54. J. Holsa, Simulation of crystal field effect in monoclinic rare earth oxyhydroxides doped with trivalent europium, *J. Phys. Chem.*, 1990, 94(12), 4835-4838.
55. G. M. Murray, R. V. Sarrio, J. R. Peterson, The effects of hydration on the luminescence spectra of trisodium tris(2,6-pyridinedicarboxylato) europium(III) compounds, *Inorg. Chim. Acta*, 1990, 176(2) 233-240.
56. N. A. Stump, L. L. Pesterfield, G. K. Schweitzer, J. R. Peterson, A high-resolution Spectral Study of $Li_3Eu(2,6\text{-pyridinedicarboxylato})_3$, *J. Alloys Comp.*, 1992, 180, 141-149.
57. T. A. Hopkins, J. P. Bolender, D. H. Metcalf, F. S. Richardson, Polarized Opitical Spectra, Transition Line Strengths, and the Electronic Energy-Level Structure of $Eu(dpa)_3^{3-}$ Complexes in Single Crystals of Hexagonal $Na_3[Yb_{0.95}(dpa)_3]\cdot NaClO_4\cdot 10H_2O$, *Inorg. Chem.*, 1996, 35(18), 5347-5355.
58. L. J. Bian, X. F. Qian, J. Yin, Z. K. Zhu, Q.H. Lu, Preparation and luminescence properties of the $PMMA/SiO_2/EuL_3\cdot 2H_2O$ hybrids by a sol-gel method, *Mate. Sci. Engin. B*, 2003, 100, 53-58.
59. F. Li., L. H. Zhang, D. G. Evans, X. Duan. Structure and surface chemistry of manganese-doped copper-based mixed metal oxides derived from layered double hydroxides, *Colloids Surfaces A: Physicochem. Eng. Aspects*, 2004, 244, 169-177.
60. N. T. Whilton, P. J. Vickers, S. Mann, Bioinorganic clays: Synthesis and characterization of amino- and polyanimo acid intercalated layered double hydroxides, *J. Mater. Chem.*, 1997, 7(8), 1623-1630.
61. F. M. Cabello, D. Tichit, B. Coq, A. Vaccari, N. T. Dung, Hydrogenation of

Acetonitrile on Nicker-Based Catalysts Prepared from Hydrdotalcite-like Precursors, *J. Catal.*, 1999, 167(1), 142-152.

62. S. Velu, K. Suzuki, Selective production of hydrogen for fuel cells via oxidative steam reforming of methanol over CuZnAl oxide catalysts: effect of substitution of zirconium and cerium on the catalytic performance, *Topic Catal.*, 2003, 22(3-4), 235-244.

Chapter 4

Controllable preparation, structural characterization and catalytic properties of cerium–containing CLDHs

4.1 Introduction

Phenol and its derivatives represent an important class of environmental water pollutants that have been included on the EPA (Environmental Protection Agency) priority pollutants list since 1976 [1]. Phenolic compounds occur in wastewaters from the petrochemical, pharmaceutical, plastics, pesticide and many other industries. As these compounds have high toxicity and a carcinogenic character, they cause considerable damage and threat to the ecosystem in water resources and to human health. Effective and economic treatment processes that will completely mineralize all of the toxic species present in the water stream without leaving behind any hazardous residues are in great demand. Several studies have been performed recently of the catalytic wet oxidation (CWO) of phenolic compounds [2-4]. The key issue in the process of CWO of phenol is the catalyst, which must have high mechanical strength and chemical stability, actively participate in the oxidation reactions, be stable in water and facilitate complete oxidation to carbon dioxide. The commonly used catalysts can be divided into 3 series: noble metals, transition metals and rare earth metals. Noble metal catalysts are often expensive, and whilst copper catalysts are effective they dissolve at high temperature and pressure. Rare earth catalysts on their own have lower catalytic activity than the other two series, but when used in combination with copper catalysts the drawbacks of

the latter, concerning the leaching of copper and carbonisation, are reported to be mitigated because of the synergy between copper and rare earth ions [5,6].

Copper oxide is a well-known component of catalysts for many processes including CO [7-11], hydrocarbon [8,12], and alcohol oxidation [13,14] as well as for NOx [15-17] and SO_2 [17] reduction. Copper oxide based catalysts have been considered as suitable substitutes for noble metal catalysts in catalytic wet oxidations [18-21] due to their high catalytic activity. Cu-containing LDH materials have been investigated widely in this area. A particularly interesting aspect is the use of calcined LDHs, obtained after a controlled thermal treatment generally at around 500 °C, as catalysts [22-26]. At these temperatures LDHs lose their layer structure and form highly active composite metal oxides with high thermal stability, high surface area, and good metal dispersion which are all very important attributes for a potential catalyst.

Cerium oxide has been examined both as a promoter [27] and as a support [28] for oxidation reactions over copper oxide based catalysts. Recently a Cu-Ce-O catalyst was developed and used in several gas-phase pollutant abatement processes [14-17] such as treatment of automobile exhaust gases (three-way catalyst, TWC), low temperature oxidation of carbon monoxide (air purification), and total oxidation of hydrocarbons (especially methane). The authors suggested that the addition of CeO_2 enhances the redox behavior of the copper ion, increases dispersion of the copper species, provides surface oxygen, and improves the oxygen storage capacity of the catalyst. According to the work of Jernigan and Somorjai [29] the apparent activation energy increases with increasing copper oxidation state from Cu, to Cu_2O, to CuO. Liu and

Flytzani-Stephanopoulos [30] reported that the presence of CeO_2 enhanced the oxidation of CO over CuO catalysts and they attributed these results to the presence of small, dispersed Cu^+ clusters stabilized by interaction with CeO_2 [31]. They proposed a model, where copper clusters provide surface sites for CO adsorption and the CeO_2 provides the oxygen source, which is then transferred to CO. This type of catalyst looks promising for use in the CWO of organic pollutants in water [32].

The objective of this research is to introduce rare earth elements into CuZnAl-LDH materials in the hope of generating a similar synergy between the copper and rare earth components. Two methods are attempted: the first involves direct incorporation of the rare earth ions inside the host layers by direct co-precipitation and the other second involves intercalation of anionic rare earth complexes into the interlamellar region by ion-exchange. The latter ion-exchange method was described in Chapter 3 using $[REE(dipic)_3]^{3-}$ (REE = Ce or Eu) and $[Ce(DTPA)]^{2-}$ complex anions as examples. There have been very few reports of the incorporation of rare earths in LDHs by the co-precipitation method; this may reflect the large ionic radii and coordination number (typically 8 or 9) of rare earth ions. The introduction of Y^{3+}, Gd^{3+}, Eu^{3+} or La^{3+} into the MgAl-LDH structure has been reported [33,77,78] but the amounts of rare earth incorporated were small. In the work described in this Chapter, we report on some attempts to prepare of new LDH materials containing Cu, Zn, Al, and Ce as the rare earth. A co-precipitation method is employed and the influences of varying the reaction conditions are studied. Some of the resulting Ce-containing materials are calcined under different conditions. The physicochemical properties of the calcined products are

characterized, and the calcined LDHs investigated as catalysts in the CWO process with aqueous phenol solution. The origin of the synergistic effect between Cu and Ce as dopant is also investigated in more detail.

4.2 Preparation of Ce-containing CuZnAl-CLDHs

4.2.1 Experimental conditions

4.2.1.1 Co-precipitation method

The standard co-precipitation method involving a traditional titration process was employed [34]. The molar ratio of the salts ($Cu(NO_3)_2 \cdot 3H_2O$, $Zn(NO_3)_2 \cdot 6H_2O$, $Al(NO_3)_3 \cdot 9H_2O$ and $Ce(NO_3)_3 \cdot 6H_2O$) was 1:1:1:x (x=0, 0.05, 0.10, 0.15 or 0.20). Solution A: Cu(II), Zn(II), Al(III) and Ce(III) nitrates were dissolved in 50 mL of deionized water to give a total metal ion concentration of 1.2 M. Solution B: NaOH and Na_2CO_3 were dissolved in 100 mL of deionized water. The concentration of the base was related to that of metal ions in solution A, as follows: $[CO_3^{2-}]=2[M^{3+}]$, $[OH^-]=2(2[M^{2+}]+3[M^{3+}])$. The samples were synthesized by simultaneous addition of solutions A and B to a stirred reaction vessel at such a rate that the pH was held constant at pH 10. The resulting stirred suspension was aged at 60 ^oC for 24 h, washed by five dispersion and centrifugation cycles in deionized water, and finally dried at 60 ^oC for 24 h. The preparation process was carried out under N_2 atmosphere, but oxidation may occur during the washing and drying step. Samples with ratios of Ce to Al were 0.05:1, 0.10:1, 0.15:1, and 0.20:1 were marked as sample CeX-LDH (where X represented the Ce/Al ratio in percentage terms). Mixed metal oxides were obtained by thermal

decomposition of above precursors at 500 ^{o}C in air for 3 h, and denoted as CeX-CLDH.

4.2.1.2 Ion-exchange method

The ion-exchange method for preparation of $[Ce(dipic)_3]^{3-}$-CuZnAl-LDHs was described in Chapter 3. Mixed metal oxides were obtained by calcination at 300 °C, 500 °C or 700 °C in air for 3 h or 6 h. The resulting samples are denoted using a five-term label, as follows: the first term represents the metal elements in the LDH precursor; the second one represents Ce (if Ce was absent, this term was omitted); the third and fourth ones correspond to the temperature and time of thermal decomposition; the last one corresponds to the $[Ce(dipic)_3]^{3-}$/CuZnAl-LDH molar ratio (if the ratio was 1/1, this term was omitted). For example, CuZnAl-Ce-500-6h-1/6 represents a $[Ce(dipic)_3]^{3-}$-containing CuZnAl-LDH with Ce/Al = 1/6, calcined at 500 °C for 6 h.

4.2.2 Characterization techniques

The powder X-ray diffraction (XRD) patterns were recorded on a *Shimadzu XRD-6000* diffractometer under the following conditions: 40 kV, 30 mA, Cu K_α radiation (λ = 0.15418 nm). The samples were step-scanned in steps of 0.04° (2θ) in the range from 3° to 70° using a count time of 10 s/step. Fourier transform infrared spectra (FT-IR) were obtained on a *Bruker Vector22* Fourier transform spectrometer in the range 4000 to 400 cm^{-1} using the KBr pellet technique. Elemental analysis was performed using a *Shimadzu ICPS-7500* inductively coupled plasma emission spectrometer (ICP-ES) to determine the contents of metallic ions in solid products and filtrate liquors and an *Elemental Vario EL* instrument to determine C, H, N content of solid products. Thermogravimetric analysis (TGA-DTG) was carried out on a *PCT-1A*

thermal analysis system produced locally. Samples of around 10.0 mg were heated at a rate 10 ^{o}C/min up to 700 ^{o}C in air. The low-temperature nitrogen adsorption-desorption experiments were carried out using a *Quantachrome Autosorb-1C-VP* system. Prior to the measurements, samples were outgassed at 200 ^{o}C under vacuum for 3 h. Specific surface area was calculated from the adsorption branch according to the BET method. The pore size distribution was determined using the BJH model on the desorption branch. The X-ray Photoelectron spectra were obtained with a *Thermo ESCALAB 250* spectrometer (Al Kα, 200 W). The intensity of each peak was estimated by integration after smoothing and subtracting an L-shaped background. The experimental curve was fitted with a program that made use of a combination of Gaussian-Lorentzian lines.

4.2.3 Catalytic reaction

The phenol oxidation reaction was used as a probe reaction to examine the catalytic properties of the calcined products. Hydrogen peroxide solution (30% (w/v), 0.2 ml) was added rapidly to a magnetically stirred aqueous phenol solution (20 ml, 100 mg/L) containing the catalyst (0.04 g) in a conical flask (50 ml). The reaction was carried out at room temperature and pressure for 1 h with vigorous agitation, and after removal of the heterogeneous catalyst by filtration the liquid was then injected into an HPLC (*Shimadzu LC-10AT*). The initial and final concentrations of phenol as well as those of its oxidation products - catechol (CTC), hydroquinone (HQ) and hydroxyhydroquinone (HHQ) were measured. Aliquots of 5 μl were injected into a reverse-phase C-18 column, with a mixture of 30% methanol and 70% redistilled water as the mobile phase at a total flow rate of 0.8 ml/min. The absorbance at 280 nm was

used to measure the distributions of products.

4.3 Structural characterization

4.3.1 CeX-LDHs and their calcined products

4.3.1.1 Elemental analysis

Table 4-1 Formulae of products prepared under different conditions calculated on the basis of results from elemental analysis and TG-DTA

Sample	Condition	formula
Ce10-LDH	As-synthesised	$[Cu_{1.06}Zn_{1.02}Al(OH)_{6.04}](CO_3)_{0.56}\cdot 2.46H_2O\cdot 0.11CeO$
Ce10-CLDH	Calcined	$Cu_{1.07}Zn_{0.98}AlO_{3.01}(OH)_{1.08}\cdot 0.08CeO_2$
Ce10-LDH-R	Restored	$[Cu_{1.07}Zn_{0.94}Al(OH)_{5.92}](CO_3)_{0.55}\cdot xH_2O\cdot 0.09CeO_2$
Ce20-CLDH	Calcined	$Cu_{1.06}Zn_{0.99}AlO_{3.01}(OH)_{1.08}\cdot 0.08CeO_2$
Ce20-LDH-R	Restored	$[Cu_{1.04}Zn_{0.94}Al(OH)_{5.88}](CO_3)_{0.54}\cdot xH_2O\cdot 0.07CeO_2$

The formulae in Table 4-1 were calculated according to the results obtained by elemental analysis and TG. The Cu/Zn/Al ratio values were in the range (1.07-1.04)/(1.02-0.94)/1, in agreement with the value in the precursor solution (1/1/1), but the experimental Ce/Al ratio results varied with the amount of Ce^{3+} in the salt solution: For sample Ce10-LDH the ratio was 0.11, close to the value in the precursor solution (0.10), whereas for sample Ce20 was it less than the value in the precursor solution (0.20), which indicates an incomplete precipitation of the cerium cations. Since cerium was not incorporated inside the layers and had undergone oxidation to Ce^{4+} during precipitation or washing and drying (as discussed below), it was included in the

chemical formulae as a 'CeO_2' component.

4.3.1.2 XRD analysis

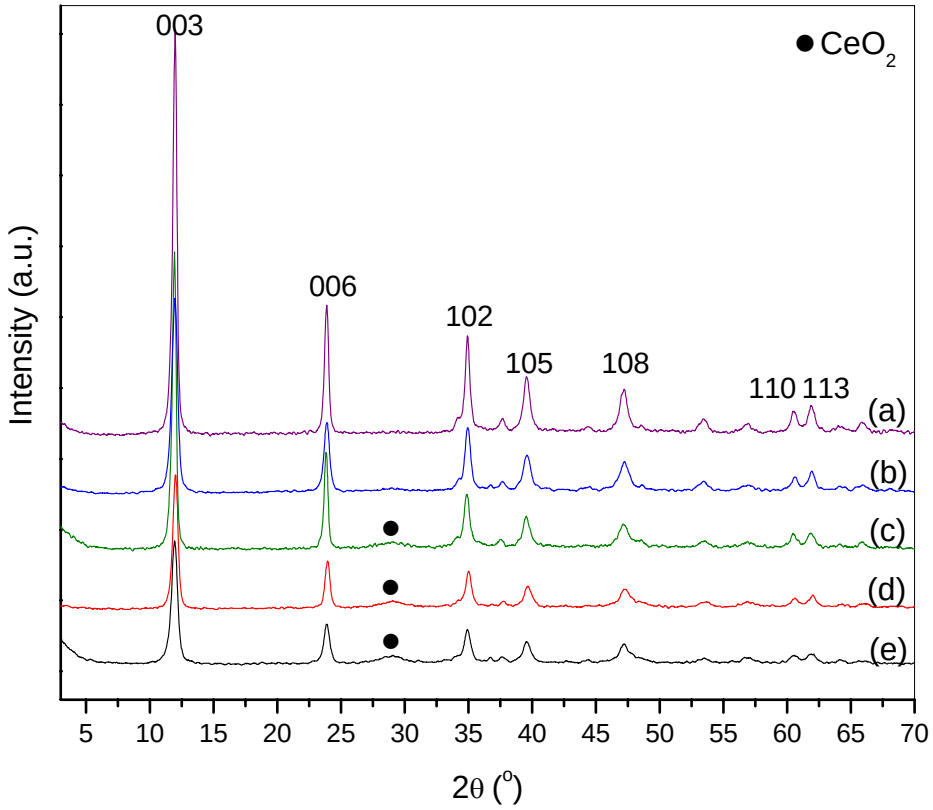

Fig. 4-1 XRD patterns of CeX-CuZnAl-LDHs prepared with different contents of Ce^{3+} in the synthesis mixture: a) Ce0 b) Ce5 c) Ce10 d) Ce15 e) Ce20

XRD powder patterns of CeX-CuZnAl-LDHs prepared with different contents of Ce(III) in the synthesis mixture are shown in Fig. 4-1. The expected amounts of Ce in these samples from (a) to (e) were 0%, 5%, 10%, 15% and 20%, respectively. The series of samples Ce5 to Ce20 all showed the characteristic basal and non-basal reflections of a crystalline LDH phase, comparable to those of the pure CuZnAl-LDH (Fig. 4-1 (a)), suggesting that similar LDH structures were prepared. In addition however, a broad

peak was observed around 28°, the intensity of which increased with the amount of cerium in the synthesis mixture. This peak can be assigned to the (111) reflection of a very poorly crystalline CeO_2 phase [39]. Thus XRD data suggest that the products consist of a mixture of CeO_2 and LDH phases and that cerium has not been incorporated in the layers. Since the radius of the Ce^{3+} ion is significantly larger than that of Al^{3+} it appears that it is unable to isomorphously substitute Al^{3+} ions on layer sites. Furthermore, Ce^{3+} tends not to adopt octahedral coordination, with coordination numbers of 8 or 9 being common, which further reduces the likelihood of its being incorporated in the layers. It appears that during the preparation process (probably during the washing and drying steps), the majority of Ce^{3+} ions were oxidized to Ce^{4+} species. This is commonly observed, especially when Ce^{3+} ions are dispersed on a solid surface [35]. Even if the Ce^{4+} ions were formed earlier, during the actual precipitation of the LDH phase, it is unlikely that they would be incorporated into the layers. Although smaller than Ce^{3+} ions, they are still significantly larger than Al^{3+} and also tend to show high coordination numbers. Furthermore, Leroux *et al.* [36] have reported that the incorporation of tetravalent cations in LDH layers is unfavorable, and that rather an amorphous or poorly crystalline $M^{4+}O_2$-like oxide phase is formed, impregnating the LDH crystallites. The first metal coordination sphere at the tetravalent ion K-edge was mainly dominated by the M^{4+}-M^{4+} correlation, confirming their absence from the layers of the LDH. Though XRD suggests the amount of CeO_2 in Ce20 materials is larger than in Ce10 materials, the analytical data in Table 4-1 indicate the content of Ce element in calcined samples is almost the same. It is explained that after thermal treatment, some crystalline CeO_2 are

present and it is difficult to dissolve and then measure them in ICP, so that the measured value of Ce content may be less than the actual one.

Table 4-2 Some XRD data and calculated parameters for CeX-LDHs prepared with different contents of cerium in the synthesis mixture

Sample	Ce0-LDH	Ce5-LDH	Ce10-LDH	Ce15-LDH	Ce20-LDH
d(003)/nm	0.7399	0.7408	0.7431	0.7374	0.7417
d(006)/nm	0.3729	0.3727	0.3735	0.3718	0.3726
d(009)/nm	0.2569	0.2568	0.2574	0.2563	0.2570
d(110)/nm	0.1529	0.1528	0.1530	0.1528	0.1529
FWHM[003]/(^{o})	0.37	0.53	0.35	0.47	0.54
FWHM[006]/(^{o})	0.46	0.43	0.37	0.46	0.77
Lattice parameter *a*/nm	0.3057	0.3056	0.3068	0.3056	0.3058
Lattice parameter *c*/nm	2.2196	2.2223	2.2292	2.2123	2.2250
Crystallite size in *a* direction/nm	19.8	21.0	24.9	19.7	11.8
Crystallite size in *c* direction/nm	21.4	14.9	22.4	16.7	14.5

The doublet recorded between 60 and 65º (2θ) is a characteristic feature of the diffraction pattern of LDH phases. These peaks correspond the diffraction by (110) and (113) planes. Unit lattice parameters are usually calculated for a hexagonal cell on the basis of rhombohedral R-3m symmetry [18,37]. The lattice parameter *a* is related to the (110) spacing according to $a = 2d(110)$, and represents the average metal - metal distance in the brucite-like layers [38]; it is therefore affected by the partial substitution of metal ions with different radii. The lattice parameter *c* is related to the basal spacing d(003) by $c = 3d(003)$, and depends on the size and charge of the anion between the

LDH layers. The values of crystallite size in the *a* or *c* direction can be calculated from the Scherrer equation [37]. The results of these calculations for LDH samples with different contents of cerium are reported in Table 4-2. If the large cerium ions were incorporated in the LDH layers, the value of the lattice parameter *a* should increase monotonically with cerium content. This is not the case, confirming that the cerium cations were not incorporated in octahedral coordination sites in the layers. For the sample with the largest loading of cerium, the LDH crystallites were reduced in size suggesting that the co-existence of significant quantities of almost amorphous CeO_2 separates the LDH crystals and restricts their growth. The broad, weak nature of the peak due to CeO_2 indicates that crystallite sizes of the CeO_2 phase are very small and the material is highly dispersed, but the exact size is difficult to estimate. Similar results have been reported by Cantu *et al* [39] using SEM and EDX analysis of Ce-containing MgAlFe-LDH materials; they proposed that the co-precipitation of CeO_2 and LDH phases favoured the formation of small CeO_2 particles and their high dispersion over the bulk LDH phase. Therefore, the CeX-LDH samples involve a mixture of relatively large crystallites of the LDH phase mixed with much smaller crystallites of cerium oxide. The size of the CeO_2 crystallites is not affected by subsequent calcination processes, because the temperature chosen for calcination of the LDH phase was well below that required to cause sintering of the CeO_2.

4.3.1.3 IR spectroscopy

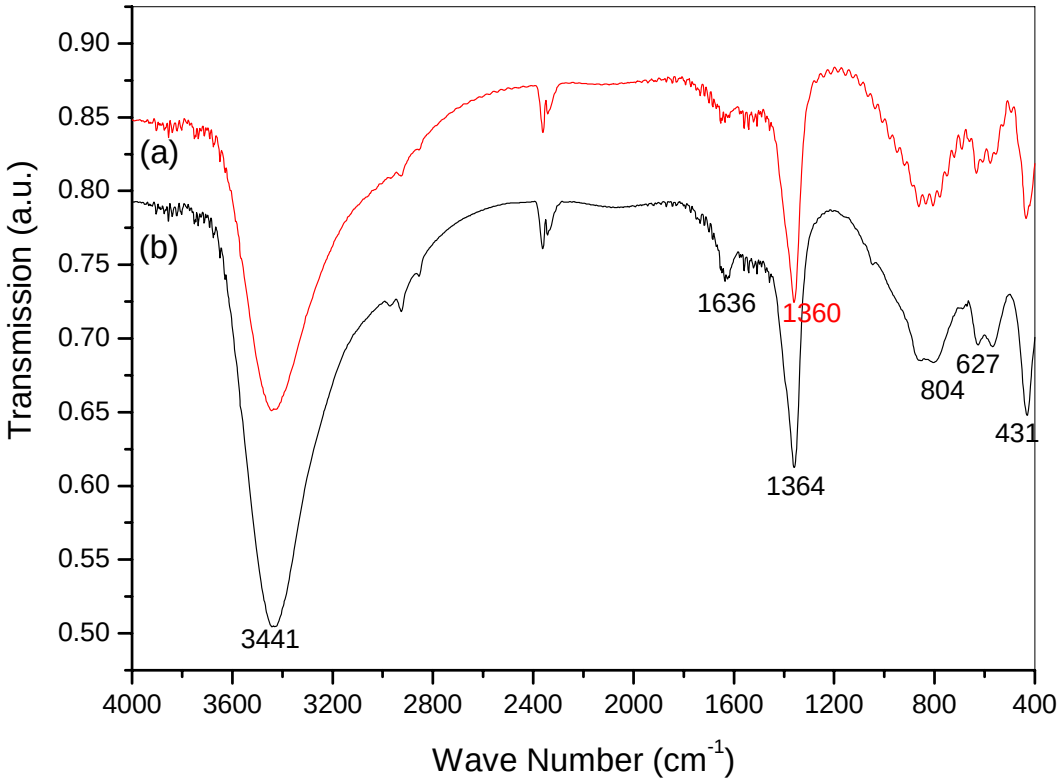

Fig. 4-2 IR spectra of CeX-LDHs prepared with different contents of Ce in the synthesis mixture: (a) Ce0-LDH; (b) Ce10-LDH

The FT-IR spectra of Ce0-LDH and Ce10-LDH samples, shown in Fig. 4-2, are very similar, and resemble those of other LDH phases [18, 40] with CO_3^{2-} as the counter anion. The strong and broad adsorption band centered at around 3441 cm^{-1} is due to O-H stretching bands, $\upsilon(OH_{str})$, arising from metal-hydroxyl groups and hydrogen-bonded interlayer water molecules; another absorption band corresponding to a water deformation, $\delta(H_2O)$, was recorded close to 1636 cm^{-1}; there were three IR active absorption bands arising from vibrations of CO_3^{2-} ion in the interlayer, namely the υ_3 (asymmetric stretching), υ_2 (out-of-plane deformation), and υ_4 (in-plane deformation) vibrations observed at around 1364 cm^{-1}, 857 cm^{-1}, and 686 cm^{-1}

respectively; the bands observed in the low-frequency region of the spectrum correspond to lattice vibration modes and can be attributed to cation-oxygen (M-O) vibrations at around 804 cm^{-1}, 627 cm^{-1} and O-M-O vibrations at around 431 cm^{-1}. There were no significant differences in the M-O stretching region in the spectra of Ce0-LDH and Ce10-LDH materials, confirming that Ce was not incorporated inside the LDH layers.

4.3.1.4 TG-DTA analysis

The TG-DTA profiles for Ce0-LDH and Ce10-LDH samples were studied and the curves were very similar to those previously reported by several authors for LDH materials [41]. The DTA profiles showed two endothermic peaks [42-44]: the peak at low temperature can be assigned to the removal of interparticle pore water, crystallization water, weakly bonded hydroxyls, and its position varies according to the particle size and texture of the sample [45]; the endothermic peak at high temperature corresponds to the dehydroxylation of the layers and decomposition of interlayer carbonate anions which leads to structure collapse and the formation of poorly crystallized mixed metal oxides [46].

4.3.1.5 BET analysis

The XRD powder patterns of Ce0-LDH and Ce10-LDH after calcination at 500 °C for 3 h are shown in Fig. 4-3. The thermal treatment completely destroys the layered structure in each case because no characteristic reflections of an LDH phase were present in the patterns. Some broad reflections of poorly crystalline metal oxide phases were observed, in agreement with the TG-TGA results. It can be seen that these broad

diffraction peaks are different when Ce was introduced into the LDH material. In the XRD pattern of Ce0-CLDH (Fig. 4-3 (a)), some weak peaks of very poorly crystalline Zn^{2+} and Cu^{2+} oxides can be observed, whereas for the Ce-containing Ce10-CLDH (Fig. 4-3 (b)), the pattern is dominated by the reflection centred at about 28^{o} (2θ) of a poorly crystalline CeO_2 phase.

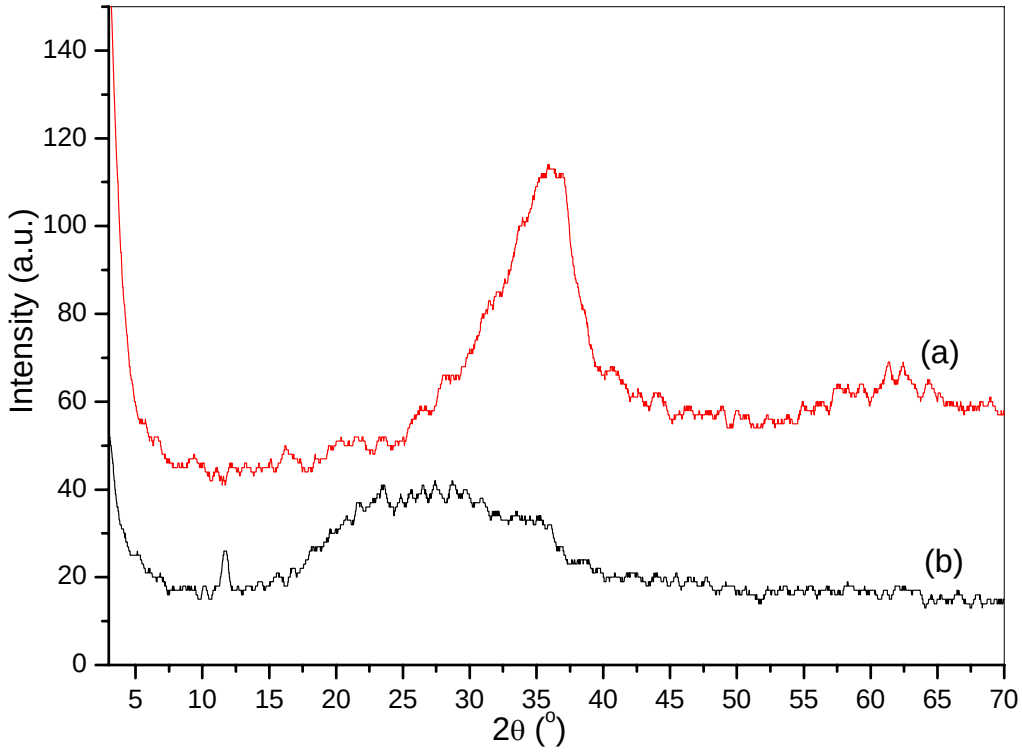

Fig. 4-3 XRD patterns of samples Ce0-CLDH (a) and Ce10-CLDH (b) calcined at 500 °C for 3 h

The specific surface area and pore size distribution of Ce0-CLDH, Ce10-CLDH and Ce20-CLDH were studied using the N_2 adsorption/desorption method. Their isotherms, shown in Fig. 4-4, are of type IV which is characteristic of mesoporous materials. The hysteresis loops are of type H3 in the IUPAC classification, which is commonly observed for adsorbents containing silt-shaped pores [50], and is consistent

with the morphology of the calcined solids. During calcination, mesoporosity is generated by both interparticle stacking and layer stacking defects [45], the relative proportions of which determine the range and uniformity of the pore distribution.

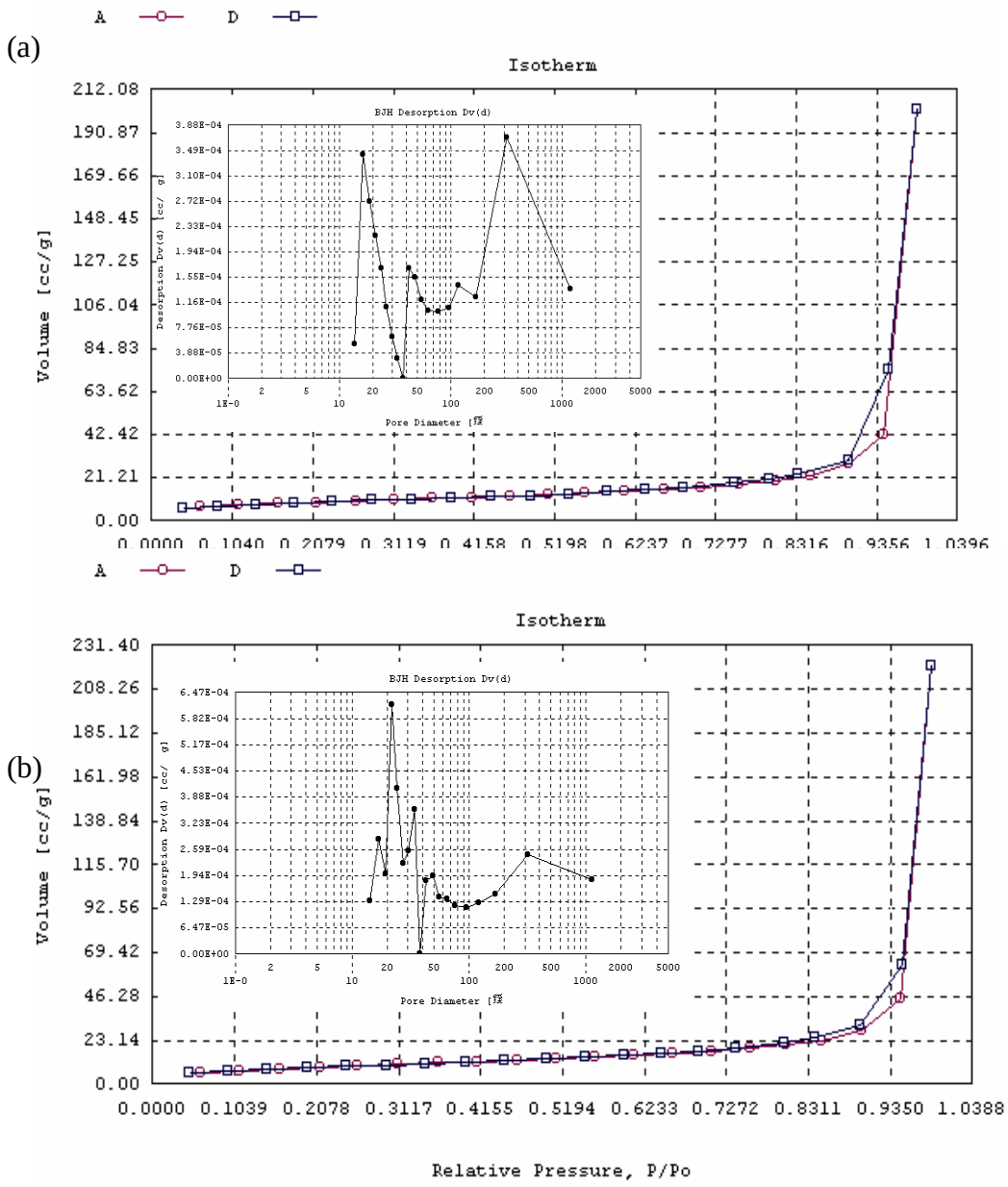

Fig. 4-4 N_2 adsorption-desorption isotherms for the calcined samples Ce0-CLDH (a) and Ce10-CLDH (b)

The insets in Fig. 4-4 show the pore size distributions of Ce0-CLDH (a) and Ce10-CLDH (b), in which it can be seen that the pore volume of smaller pores (less than 50 Å) increased with the incorporation of Ce. This suggests that cerium oxide particles were high dispersed over the bulk CLDH phase, since the formation of CeO_2 clusters would be expected to block these small pores. The specific surface areas of Ce0-CLDH, Ce10-CLDH and Ce20-CLDH were 32.6 m^2/g, 32.9 m^2/g, 42.4 m^2/g, respectively. The former two samples had similar surface areas, but the last one has a significantly higher value. This is consistent with the XRD data, which suggest that Ce20-CLDH has the smallest crystallite size.

4.3.2 CuZnAl-Ce(dipic)-LDHs and their calcined products

The CuZnAl-Ce(dipic)-LDH materials prepared by the ion-exchange method were calcined under different conditions and the products were characterized and compared with the calcined NO_3-LDH precursors without Ce.

4.3.2.1 XRD analysis

Before calcination, CuZnAl-Ce(dipic)-LDH samples showed the typical XRD pattern of an LDH structure. Calcination resulted in the formation of nonstoichiometric mixed metal oxides whose phase and crystallinity were influenced by their precursor chemical composition and the calcination temperature [4]. From the results of *in situ* variable temperature XRD described in Chapter 3, it was clear that the calcination of Ce-containing LDHs at 500 °C led to the destruction of LDH network, giving rise to mostly amorphous metal oxides. In contrast, the XRD pattern of calcined CuZnAl-LDH showed that well-crystalline metal oxides were formed under the same conditions. The

thermal decomposition of Ce-containing CuZnAl-LDH at 500 °C, which led to loss of interlayer $[Ce(dipic)_3]^{3-}$ anions and layer hydroxyl groups, only afforded a small quantity of crystalline mixed metal oxides. An increase in calcination temperature to 700 °C enhanced the crystallinity of the M(II)-O phases, as evidenced by the sharpening of these peaks. When the calcination temperature was further increased to 800 °C, crystallization of $CuAl_2O_4$ and $ZnAl_2O_4$ spinels occurred, together with the formation of divalent metal oxides. In addition, sharper peaks whose positions were coincident with those of CeO_2 were also observed with intensities related to the content of Ce in the precursor. The results indicated that the presence of Ce could retard the formation of metal oxide and spinels [48], since the reflection intensities of crystalline metal oxides or spinels were weaker in calcined Ce-containing CLDHs than in CuZnAl-CLDHs calcined at the same temperature.

4.3.2.2 IR spectroscopy

The FT-IR spectrum of the calcined CuZnAl-Ce(dipic)-LDH product obtained by heating at 500 °C for 6 h was markedly different from that of the precursor. It showed two weak bands around 1630 and 3400 cm^{-1}, which may be assigned to the hydrogen-bonded hydroxyl groups of water molecules reversibly adsorbed on the oxide surface [49]. Compared with the CuZnAl-Ce(dipic)-LDH precursor, the intensity of these bands was lower as a result of removal of physisorbed and interlayer water and the dehydroxylation of the layers. Significant changes were also observed in the low frequency region of the spectrum associated with changes in lattice structure and the intensity of cation-oxygen vibration bands showed a significant increase. As expected,

IR absorption bands arising from $[Ce(dipic)_3]^{3-}$ and CO_3^{2-} anions were reduced in intensity because of decomposition of the interlayer anions. The band around 1505 cm^{-1} can be attributed to the lower symmetry environment associated with carbonate adsorbed from the air, which is confirmed by the presence of the ν_1 vibration of carbonate around 1050 cm^{-1}.

4.3.2.3 BET analysis

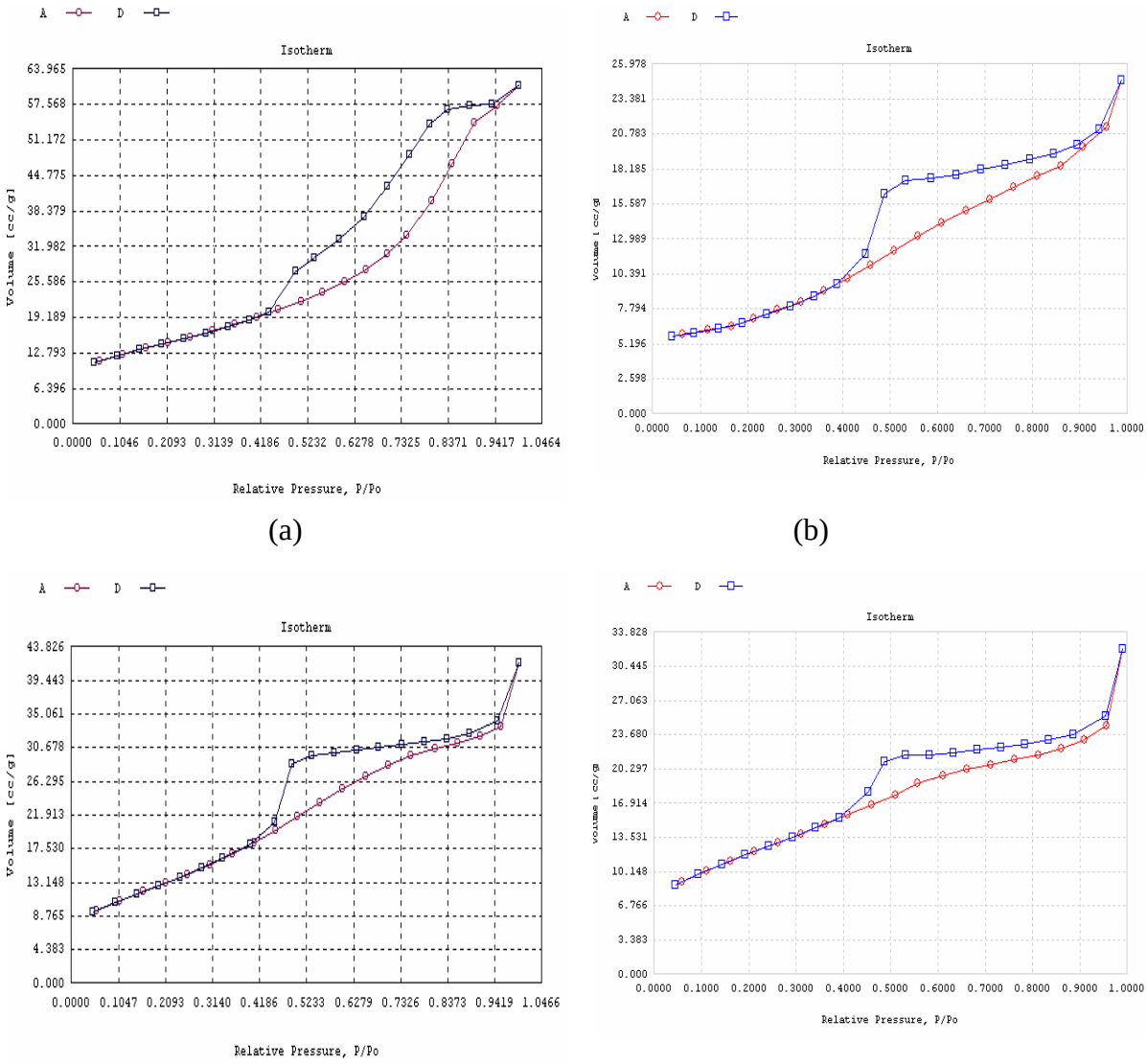

Fig. 4-5 N_2 adsorption-desorption isotherms for the calcined CuZnAl-Ce(dipic)-LDH products

prepared under different conditions together with those of the non-Ce containing material

(a) CuZnAl-500-6h (b) CuZnAl-Ce-500-6h-1/6 (c) CuZnAl-Ce-500-6h (d) CuZnAl-Ce-500-3h

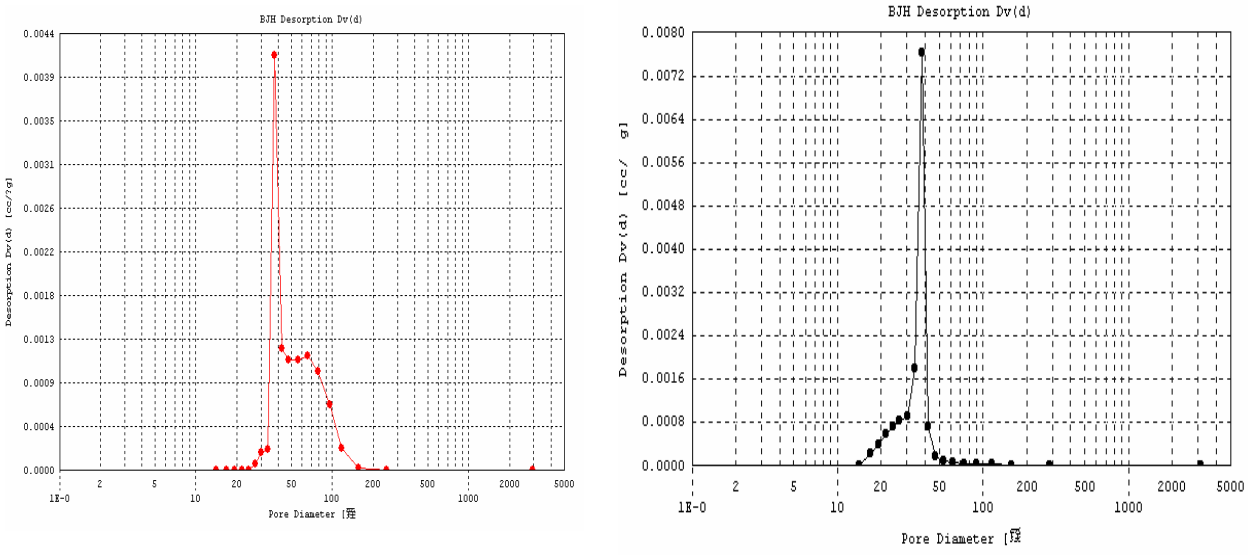

(a) (b)

Fig. 4-6 Pore size distribution curves for the non-Ce containing material CuZnAl-500-6h (a) and the CuZnAl-Ce-500-6h (b)

Nitrogen adsorption-desorption experiments were carried out in order to determine the surface areas and pore size distributions of the materials. Since calcination at higher temperatures destroys the layered structure of LDHs, this can be expected to lead to changes in specific surface area and pore structure. If volatile species such as CO_2 or NO/NO_2 are generated by decomposition of the interlayer anion on heating, surface area values will be increased. As shown in Fig. 4-5, each material obtained by the thermal decomposition of intercalated LDHs showed an isotherm typical of type IV in the IUPAC classification [50], indicative of a mesoporous material [51]. The shapes of the hysteresis loops differ however, indicating different pore characteristics. This results

from the nature of interlayer anions of precursors, which leads to the formation of different decomposition pattern. The N_2 adsorption-desorption isotherms in Fig. 4-5(a), (b) and (c) are for samples CuZnAl-500-6h, CuZnAl-Ce-500-6h-1/6 and CuZnAl-Ce-500-6h, respectively, in which Ce/Al ratios increase from 0 to stoichiometric 1/1. With increasing Ce content, the hysteresis loops became more and more narrow in the high pressure region, suggesting some micropores were present in addition to mesopores, some of which result from the interparticle pores [52,53]. For the sample CuZnAl-Ce-500-3h (Fig. 4-5(d)) with a reduced calcination temperature, a similar phenomenon was observed.

Fig. 4-6 illustrates the pore size distributions of calcined CuZnAl-Ce(dipic)-LDH and the non-Ce containing material after heating at 500 °C for 6 h. The sharpness of the inflection reflects the uniformity of pore sizes and the height indicates the pore volume. The pore size curve for sample CuZnAl-500-6h shows a maximum in the region 3.5 - 4.5 nm, and a broad distribution from 4.5 nm to 15 nm, which results from the irregular stacking of oxide particles. The pore size distribution curve for sample CuZnAl-Ce-500-6h has a maximum in the region 3 - 5 nm with a small quantity of micropores (<2 nm), which reflects the evolution of volatile species formed by thermal decomposition of the interlayer anions.

Table 4-3 Specific surface areas for the calcined $[Ce(dipic)_3]^{3-}$-LDHs prepared under different conditions and the non-Ce containing materials for comparison

Sample	Conditions	Surface area (m^2/g)
Zn_2Al-NO_3-LDH	300 ^oC; 6 h	18.6
	500 ^oC; 6 h	44.3
	700 ^oC; 6 h	18.3
Zn_2Al-Ce(dipic)-LDH	300 ^oC; 6 h	11.0
	500 ^oC; 6h	51.6
	700 ^oC; 6 h	32.8
CuZnAl-NO_3-LDH	300 ^oC; 6 h	15.0
	500 ^oC; 6 h	51.4
	700 ^oC; 6 h	18.8
CuZnAl-Ce(dipic)-LDH	300 ^oC; 6 h	5.0
	500 ^oC; 6 h	47.6
	700 ^oC; 6 h	1.6
CuZnAl-Ce(dipic)-LDH (different conditions)	500 ^oC; 6 h; Ce/Al = 1:3	49.4
	500 ^oC; 6 h; Ce/Al = 1:6	24.7
	500 ^oC; 3 h; Ce/Al = 1:1	43.0
	500 ^oC; 3 h; Ce/Al = 1:3	81.9
	500 ^oC; 3 h; Ce/Al = 1:6	38.4

Table 4-3 lists the specific surface area values of the calcined $[Ce(dipic)_3]^{3-}$-CuZnAl-LDHs, $[Ce(dipic)_3]^{3-}$-ZnAl-LDHs and the corresponding non-Ce containing materials. The intercalated $[Ce(dipic)_3]^{3-}$-LDHs possess poor porosity characteristics. They exhibit low surface areas of about 1 - 5 m^2/g, and no microporosity. Whether interlayer micropores are present or not depends on the interpillar distance. In these samples, the increase in interlayer spacing was not accompanied by a sufficient

increase in interpillar distance, resulting in an interlayer space completely filled by the anions. The mesopores are created by the irregular stacking of different arrangements of parallel-assembled layers. The size of these stacks gives an indication of the LDH crystallinity, which was controlled by the electrostatic interactions between interlayer anions and the layers. Stronger bonds lead to larger stacks, and a greater number of mesopores [51].

All of materials showed a maximum in the BET surface area after calcination at 500 °C, and the mesoporous structures were preserved at this temperature. This may be explained as follows: at 300 °C, the LDH structure was not completely destroyed and the surface area represents only the outside surface of the irregular stacked layers; at 700 °C, the formation of new metal oxide and spinel phases leads to a reduction in the surface area. For ZnAl-Ce(dipic)-LDH calcined at 500 °C for 6 h, the BET surface area was 51.6 m^2/g, larger than that of its non-Ce containing analogue (44.3 m^2/g) calcined under the same conditions. On calcination, the decomposition of guest $[Ce(dipic)_3]^{3-}$ anions and the dehydroxylation of host layers generates NO/NO_2, CO_2 and H_2O. The release of volatile species may destroy the parallel-assembled layers, produce many irregular channels and subsequently increase the surface area of the calcined product [54, 55]. The difference in surface areas between ZnAl- and CuZnAl- calcined materials was due to varying extents of crystallization of metal oxides. For CuZnAl-Ce(dipic)-LDH calcined at 500 °C for 6 h, the BET surface area was 47.6 m^2/g, smaller than that of the LDH-NO_3 precursor (51.4 m^2/g) calcined under the same conditions. Though some irregular channels were generated by the decomposition and volatilization of the organic

anions, as indicated by the pore size distribution in Fig. 4-6, the interaction between Cu and Ce promotes the formation of a Cu-Ce-O solid solution, which leads to an observed decrease in surface area. The surface areas of the calcined CuZnAl-Ce(dipic)-LDH materials depend on the Ce/Al ratio. The maximum was 81.9 m^2/g, for the sample CuZnAl-Ce-500-3h-1/3, in which the Ce/Al ratio was equal to the stoichiometric value of 1/3. In the sample CuZnAl-Ce-500-3h, excess Ce complex was transformed into cerium oxides physically mixed with other metal oxides so that the quantity of the Cu-Ce-O solid solution may be increased and consequently the surface area decreased. In the sample CuZnAl-Ce-500-3h-1/6, the amount of Ce complex was insufficient for complete ion-exchange, so that the amount of Ce-Cu-O solid solution and interlayer organic anions were reduced. The number of channels generated by decomposition of volatile species plays an important role in determining the surface area. The data in Table 4-3 show that surface area decreased with increase in the calcination time from 3 h to 6 h. This suggests that the prolonged calcination time favors the formation of a Ce-Cu-O solid solution and other composite metal oxides.

4.3.2.4 XPS analysis

In order to determine the effect of cerium incorporation on the chemical states of copper and cerium in mixed metal oxides obtained from $[Ce(dipic)_3]^{3-}$-LDH precursors with different Ce contents, the Cu 2p, Ce 3d and O 1s regions were analyzed by XPS. Signals from the mixed oxide phases were assigned on the basis of the literature as reported in the following figures and tables.

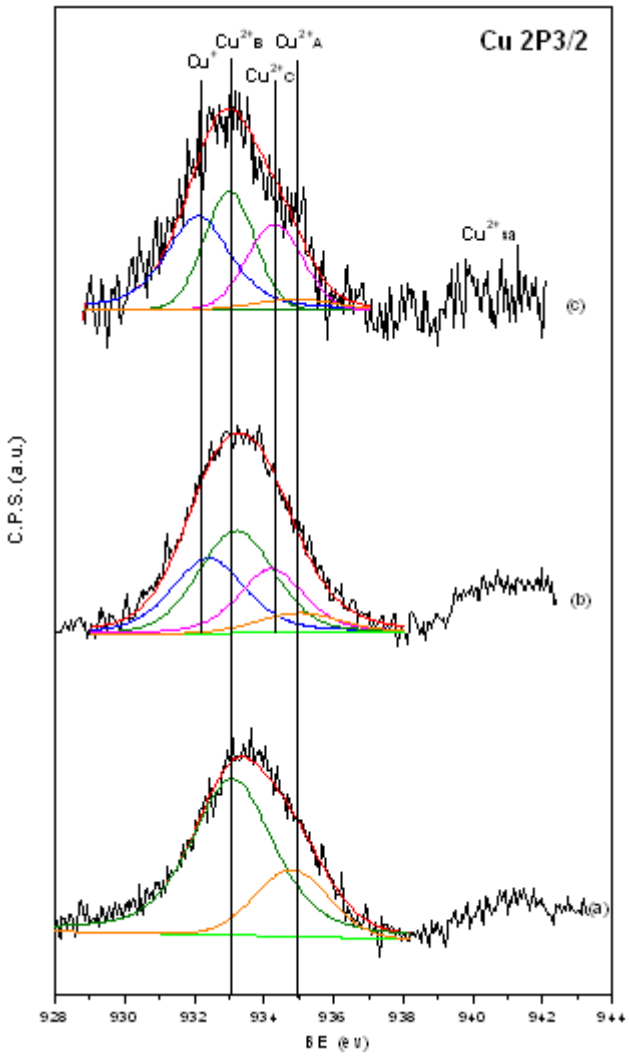

Fig. 4-7 XPS of the Cu $2p_{3/2}$ regions in the calcined CuZnAl-Ce(dipic)-LDHs with different Ce/Al molar ratios: (a) 0; (b) 1/6; (c) 1/1

Table 4-4 XPS characteristics of Cu $2p_{3/2}$ region for CuZnAl-Ce(dipic)-CLDHs with different Ce/Al molar ratios

Ce/Al ratio	Binding energy (eV)				Peak intensity[b] (%)			
	Cu^{+}	Cu^{2+}_{B} (Cu-O)	Cu^{2+}_{C} (Cu-Ce-O)	Cu^{2+}_{A} (Spinel)	$I_{(Cu^{+})}$	$I_{(Cu^{2+}_{B})}$	$I_{(Cu^{2+}_{C})}$	$I_{(Cu^{2+}_{A})}$
0	—	933.1 (2.8)[a]	—	934.8 (2.5)	—	76.4	—	23.6
1/6	932.4(2.5)	933.2 (2.6)	934.2 (2.2)	935.0 (2.8)	30.7	38.7	23.0	7.6
1/1	932.1(2.2)	933.0 (1.7)	934.3 (1.9)	934.9 (2.7)	39.4	31.0	25.1	4.5

a Numbers in parentheses refer to FWHM in eV.

b Intensity of the peak in percentage of the total Cu $2p_{3/2}$ area.

Fig. 4-7 shows the Cu 2p spectra for three calcined CuZnAl-Ce(dipic)-LDHs in which experimental $[Ce(dipic)_3]^{3-}$/CuZnAl-LDH (Ce/Al) molar ratios were 0, 1/6 and 1/1 (the stoichiometric Ce/Al ratio in the intercalated LDH precursor is 1/3). When Ce/Al = 0, two peaks can be observed at 934.8 and 933.1 eV, which can be attributed to Cu^{2+} cations in the spinel $CuAl_2O_4$ (A) and oxide CuO (B) structure respectively [18], with satellite lines between 940 and 945 eV. For Ce-containing samples, four peaks were observed, close to 932.1, 933.0, 934.3 and 934.9 eV respectively, which demonstrate that the presence of cerium has led to modifications in the surface composition of these systems. One of the additional peaks, around 934.3 eV is in the range expected for Cu^{2+}, implying the presence of a different coordination environment of Cu^{2+} (C). This could result from a surface interaction between copper and cerium, and the consequent formation of a Cu-Ce-O solid solution [56]. The other additional peak around 932.1 eV can be assigned to Cu^{+} on the basis of the literature data [56]. In general, the lower the oxidation state, the lower the value of Cu 2p3/2 BE. Thus it appears that the presence of cerium leads to an increase in the relative stability of Cu^{+} cations [57].

XPS data are listed in Table 4-4. For all the samples, the two peaks attributed to Cu^{2+} cations in the spinel (A) and oxide (B) structures could be observed but their percentages decreased markedly with increasing Ce content. The decrease in proportion of Cu^{2+} (A) cations from 23.6 (Ce/Al = 0) to 4.5% (Ce/Al = 1/1), is in agreement with the *in situ* variable temperature XRD analysis, which suggested that the presence of

cerium oxide could delay the formation of the $CuZn_2Al_4$ spinel structure. With the introduction of cerium oxides, the proportions of Cu^+ and Cu^{2+} (C) cations increased to 39.4 and 25.1%, respectively, and so became the major components. This suggests that Cu could interact strongly with adjacent Ce in a Cu-Ce-O solid solution, and this so-called Cu-Ce synergistic effect may have an important influence on the catalytic abilities of these samples.

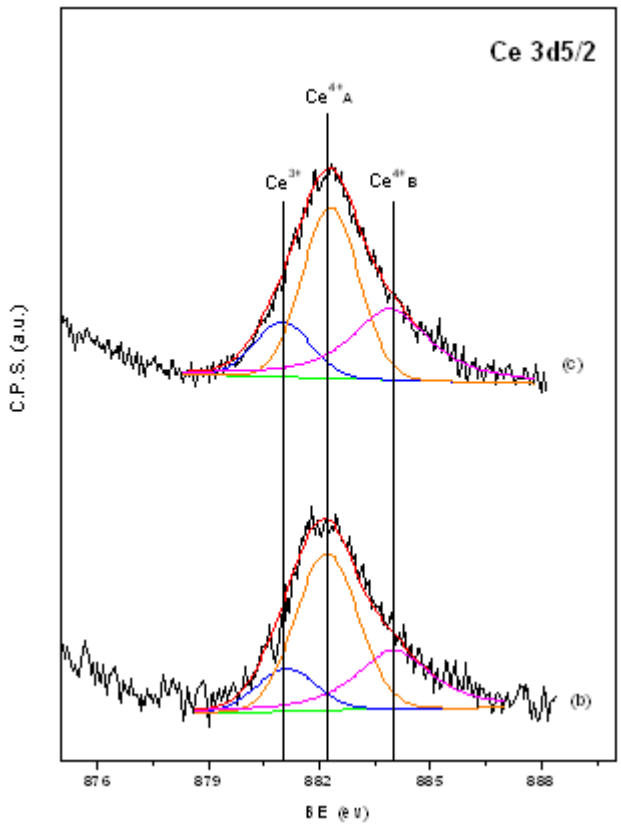

Fig. 4-8 XPS of the Ce $3d_{5/2}$ regions in the calcined CuZnAl-Ce(dipic)-LDHs with different Ce/Al molar ratios: (a)0/1 (omitted) (b) 1/6; (c) 1/1

Table 4-5 XPS characteristics of Ce $3d_{5/2}$ region for CuZnAl-Ce(dipic)-CLDHs with different Ce/Al molar ratios

Ce/Al ratio	Binding energy (eV)			Peak intensity[b] (%)		
	Ce^{3+}	$Ce^{4+}{}_A$ (Ce-O)	$Ce^{4+}{}_B$ (Cu-Ce-O)	$I(Ce^{3+})$	$I(Ce^{4+}{}_A)$	$I(Ce^{4+}{}_B)$
1/6	881.0 (1.9)[a]	882.2 (2.0)	884.0 (2.4)	13.9	53.2	32.9
1/1	881.0 (1.8)	882.3 (1.8)	883.9 (2.5)	13.5	48.5	38.0

a Numbers in parentheses refer to FWHM in eV.

b Intensity of the peak in percentage of the total Ce $3d_{5/2}$ area.

The analysis of the Ce $3d_{5/2}$ region for two Ce-containing CuZnAl-Ce(dipic)-CLDHs with different Ce contents is shown in Fig. 4-8 and XPS characteristics are listed in Table 4-5. Both spectra showed three peaks at around 881.0, 882.3 and 883.9 eV, accompanied by some satellite lines at higher BE values. The peaks at around 882.3 and 883.9 eV can be assigned unambiguously to Ce^{4+} cations (V_0 peak) [58] in different sites of which the former, corresponding to Ce^{4+} species in ceria (A), showed a higher intensity. The higher value of the BE of the other peak is indicative of a change in the environment of Ce^{4+} cations (B), and may result from the Cu-Ce interaction in a Cu-Ce-O solid solution [56]. The peak at around 881.0 eV can be assigned to Ce^{3+} cations (u_1 peak) [58], indicating incomplete oxidation of Ce has occurred. In Table 4-5, it can be seen that the oxidation state +4 was predominant, about 86% (Ce^{4+} (A) + Ce^{4+} (B)). With increasing Ce content, the relative quantities of surface atom number fractions of the two types of Ce^{4+} showed a significant variation: the number of Ce^{4+} (A) cations decreased and the number of Ce^{4+} (B) cations increased, consistent with the formation of larger quantities of Cu-Ce-O solid solution.

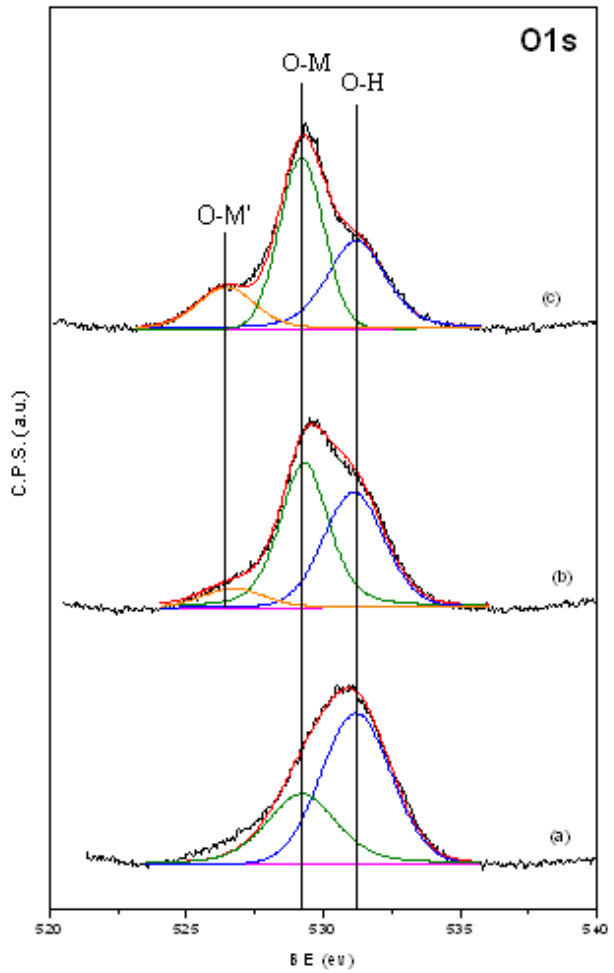

Fig. 4-9 XPS of the O 1s regions in the calcined CuZnAl-Ce(dipic)-LDHs with different Ce/Al molar ratios: (a) 0; (b) 1/6; (c) 1/1

Table 4-6 XPS characteristics of O 1s region for CuZnAl-Ce(dipic)-CLDHs with different Ce/Al molar ratios

Ce/Al ratio	Binding energy (eV)			Peak intensity[b] (%)	
	O_I (O-M')	O_I (O-M)	O_{II} (O-H)	$I(O_I)$	$I(O_{II})$
0	—	529.2 (3.0)[a]	531.2 (3.0)	35.3	64.7
1/6	526.7(2.7)	529.3 (2.1)	531.1 (2.6)	57.2	42.8
1/1	526.5(2.5)	529.2 (1.9)	531.2 (2.5)	63.2	36.8

a Numbers in parentheses refer to FWHM in eV.

b Intensity of the peak in percentage of the total O 1s area.

Spectra of the O 1s region are shown in Fig. 4-9, together with the relevant two fitted peaks, O_I and O_{II}, representing two different kinds of surface oxide species. Their relative abundances are listed in Table 4-6. Following the literature [18], O_I at around 529.2 eV can be assigned to lattice oxygen bound to metal cations, and the other O_I with the low BE at around 526.5 eV may result from lattice oxygen in a Cu-Ce-O solid solution, while O_{II} with the high BE at around 531.1 eV can be assigned to surface oxygen, mainly hydroxyl groups. It can be seen that the signal intensity of O_{II} decreased noticeably with the increasing content of cerium oxides, which suggests that oxygen atoms of the hydroxyl groups present on the surface of the metal oxides are partially converted into lattice oxygen. The enhancement of intensity of O_I peaks can also be related to the incorporation of ceria [56]. The additional lattice oxygen may take part in oxidation processes and thus have a beneficial effect on the catalytic activity of the material.

4.4 Catalytic properties

4.4.1 CeX-CLDHs prepared by the co-precipitation method

4.4.1.1 Catalyst activity and selectivity

Oxidation of aqueous phenol solution with hydrogen peroxide over calcined CeX-LDHs was investigated at room temperature. Analysis of the oxidation products by HPLC indicated the presence of hydroquinone (HQ) and catechol (CTC) as well as deep oxidation products such as dicarboxylic acids.

Table 4-7 Conversion and product distribution of phenol oxidation over CeX-CuZnAl-LDHs calcined at 500 ^{o}C for 3 h

Sample	Conversion /%	Conversion$^{\#}$ /(% /0.028 g Cu)	Product distribution/wt%		
			CTC	HQ	Others
Ce0-CLDH	74.3	74.3	1.4	1.0	97.6
Ce10-CLDH	55.6	61.5	0	0	100
Ce20-CLDH	48.0	57.9	0	0	100

Phenol: 50 ml, 100 mg/L; Catalyst: 0.1 g; H_2O_2: 0.5 ml; room temperature and pressure; time: 1 h; CTC: catechol; HQ: hydroquinone; others: low molecular weight carboxylic acids

Conversion$^{\#}$: calculated conversion according to the equation: conversion*$m_{(Cu\ in\ Ce0\text{-}CLDH)}/m_{(Cu\ in\ CeX\text{-}CLDH)}$

The conversion and product distribution were examined by HPLC and the results are summarized in Table 4-7. The amounts of untreated phenol, catechol and hydroquinone were measured, and the quantity of other degradation products such as light molecular weight carboxylic acids was calculated according to the molar quantities of PhOH, HQ and CTC. Because the quantity of catalyst put into the mixed solution was fixed, the amount of active components varied and it is therefore more useful to calculate the conversion based on the actual content of Cu in the catalyst (denoted as conversion$^{\#}$ in Table 4-7). The Ce-containing catalysts had no obvious advantages in terms of the conversion$^{\#}$ of phenol compared with calcined CuZnAl-LDH (Ce0-CLDH), which indicates that Ce in CeX-CLDHs prepared by the co-precipitation method do not promote the catalytic activity and Cu still provides the main active center [53]. The CeX-LDH precursors consist of two mixed phases - CuZnAl-LDH and CeO_2. Although after calcination CeO_2 was dispersed uniformly throughout the oxide mixture, there was

no enough strong interaction between Cu and Ce comparable to the synergistic effect like in the Cu-Ce-O solid solution due to the difference in structure and composition, so that Ce does not act as a promoter for the catalytic activity of Cu in this series of Ce-containing catalysts.

Although the presence of the rare earth element did not improve the catalyst activity, it did enhance the extent of deep oxidation of phenol and control the product distribution. The only products in the oxidation of phenol over the Ce-containing catalysts were light molecular weight carboxylic acids like acetic acid, but in the calcined CuZnAl-LDH system, catechol and hydroquinone could be observed in the products though their amounts were small. This indicated that the presence of cerium could enhance the oxidation degree of phenol avoiding the formation of intermediate products so that it played a role in the complete degradation of phenol. This may be related to the ability of CeO_2 to produce more active oxygen centers such as lattice oxygen.

4.4.1.2 Catalyst stability

It is very important in studying the catalytic stability to investigate the loss of Cu ions into the supernatant liquid remaining after CWO. The common reasons for the loss of metal ions from catalysts in CWO are acidic leaching due to the presence of low molecular weight carboxylic acids formed in the reaction process; and reactive leaching attributed to oxygen loss which weakens the interactions between the different ions in the composite metal oxides.

Table 4-8 Concentration of leaching metal ions in the supernatant liquids after phenol oxidation reactions over CeX-CLDHs

Sample	Concentration in filtrate (mg/L)			
	Cu	Zn	Al	Ce
Ce0-CLDH	0.37	26.26	0	-
Ce10-CLDH	0.06	10.26	0	0
Ce20-CLDH	0.36	18.57	0	0

Table 4-8 lists the leaching extent of different metal ions into the filtered liquors remaining after completion of the phenol oxidation reaction. In comparison with the calcined CuZnAl-LDH, the leaching extent of Cu, Zn and Al from Ce-containing catalysts decreased significantly. In the case of Ce10-CLDH, the loss of copper was <1/6 of that from Ce0-CLDH and the zinc was also stabilized against leaching. At the same time, leaching of Ce was not detected. Therefore, the presence of Ce reduced the extent of leaching of the active component Cu and other metal elements, which offers an advantage in terms of improving the catalyst stability. This may be explained as follows: the solvated cerium in the co-precipitation process induced the delamination of CuZnAl-LDH structure and then was impregnated on the surface of very small grains, so that the interaction between CuO and CeO_2 was stronger than that in the simply physical mixture but it was weaker than that in the Cu-Ce-O solid solution. It was this interaction that fixed Cu ions and prevented them from leaching. The advantageous effect of rare earth elements in terms of reducing the loss of Cu has previously been reported in the literature for other systems such as $Ce_{1-x}Cu_xO_{2-y}$ [59], where it was also observed that the presence of cerium in mixed metal oxides could prevent the formation

of carbonaceous deposits in oxidation reactions.

In summary, although the Ce-containing catalysts did not obviously improve the catalytic activity for phenol oxidation, they showed better catalytic selectivity and stability than the calcined CuZnAl-LDH. Cu acts as the main catalyst providing the majority of active centres, and Ce acts as a promoter improving the catalyst characteristics, corresponding to the interaction between CuO and CeO_2. On the basis of our results, Ce10-CLDH was found to be the best catalyst for phenol oxidation, having good selectivity and stability, whilst simultaneously maintaining high catalytic activity.

4.4.2 CuZnAl-Ce(dipic)-CLDHs prepared by the ion-exchange method

4.4.2.1 Catalyst activity and selectivity

Table 4-9 Conversion and product distribution of phenol oxidation over calcined $[Ce(dipic)_3]^{3-}$-LDHs prepared under different conditions

Sample	Calcination conditions			Conversion of phenol/%	Product distribution /wt.%		
	Ce/Al	Temp./^{o}C	Time/h		HQ	CTC	Others
Without Cat.	-	-	-	4.1	21.7	78.3	0
CuZnAl-500-6h	0	500	6	12.2	0.5	0	99.5
CuZnAl-Ce-500-6h-1/6	1/6	500	6	22.6	29.1	5.3	65.6
CuZnAl-Ce-500-6h	1/1	500	6	35.9	43.6	3.2	53.2
ZnAl-Ce-500-6h	1/1	500	6	11.7	8.1	0	91.9
CuZnAl-500-3h	0	500	3	11.4	1.2	0	98.8
CuZnAl-Ce-500-3h-1/6	1/6	500	3	17.8	25.9	1.6	72.5
CuZnAl-Ce-500-3h	1/1	500	3	20.7	41.0	27.6	31.4
CuZnAl-700-6h	0	700	6	9.8	33.5	0	66.5
CuZnAl-Ce-700-6h	1/1	700	6	26.2	15.3	5.2	79.5

Phenol: 20 ml, 100 mg/L; Catalyst: 0.04 g; H_2O_2: 0.2 ml; room temperature and pressure; time: 1 h; CTC: catechol; HQ: hydroquinone; others: low molecular weight carboxylic acids

Oxidation of aqueous phenol solution with hydrogen peroxide over the calcined LDHs was investigated under the same conditions as for CeX-LDHs (Section 4.4.1). The conversions of phenol (PhOH) and the product distribution obtained over different catalysts are summarized in Table 4-9. The nature of the interlayer anions in the LDH precursor is known to have a significant influence on the properties of the calcined product, including the distribution of chemical states of metal species and the surface basicity [60]. In Table 4-9, it can be seen that the contents of the different metal elements, calcination temperature and time all had an influence on the catalytic performance. The conversion of phenol increased with increasing Ce content in the calcined LDHs, with CuZnAl-Ce-500-6h showing the highest catalytic activity (35.9% conversion), approximately three times that of CuZnAl-500-6h. The conversions exhibited a similar trend in a series of Ce-containing LDH samples calcined at 500 °C for 3 h. The presence of Ce in the metal oxides improved the catalytic activity. It should be noted that the absolute conversions of phenol calculated in terms of the content of Cu in the Ce-containing catalysts were much higher. For comparative purposes, ZnAl-Ce-500-6h was also studied and the conversion was close to that over CuZnAl-500-6h. This indicated that under these experimental conditions cerium oxide had some catalytic activity, due to its reducibility and high oxygen storage capacity [48]. On the basis of the structural characteristics of the calcined LDHs, it was concluded that the high catalytic

activity of CuZnAl-Ce-500-6h may be related to the formation of a mixture of divalent metal oxides and a Cu-Ce-O solid solution. However, since the specific surface area of CuZnAl-Ce-500-6h was lower than that of either CuZnAl-500-6h or ZnAl-Ce-500-6h but the activity was much higher, this implied the synergistic effect between Cu-Ce in the solid solution played an important role in increasing catalytic activity. The percentage of HQ in the product distribution also increased markedly with increasing Ce content. This indicated that Ce containing catalysts had a good catalytic selectivity to HQ, rather than to low molecular weight carboxylic acids.

Rare earth oxide additives have previously been used as textural and structural promoters for supported copper oxide catalysts. In phenol oxidation reactions, the major active catalytic centers are found to be copper sites. Copper clusters provide surface sites for phenol adsorption and cerium oxides modify the chemical environment of copper ions via surrounding oxygen ions. A catalytic process includes diffusion, adsorption, reaction, desorption and final diffusion steps. In the case of calcined LDHs, the diffusion should be fast because the pore size (>3 nm) is larger than the size of the phenol molecule (<0.5 nm) and the adsorption or reaction step should be rate limiting. Thus the catalytic activity will depend on the degree of dispersion of Cu ions, the number of Cu sites per unit surface area, the amount of active oxygen and the spatial orientation of the phenol molecules. In the case of CuZnAl-500-6h, catalytically active Cu centers were densely packed on the surface so that adsorption sites of phenol molecules were close together, which inhibited the reaction step. The ion-exchange method using $[Ce(dipic)_3]^{3-}$ anions resulted in a uniform dispersion of Ce between the

layers. After calcination, the inclusion of Ce in the composite metal oxides reduced the number of Cu sites per unit surface area, increased the short-range ordering, and promoted the effective adsorption of phenol molecules, which enhanced the catalytic efficiency of Cu ions [61]. The other important advantage of incorporation of Ce into calcined CuZnAl-LDH was the formation of a Cu-Ce-O solid solution.

The strong synergism displayed by the Cu-Ce-O solid solution significantly modifies the low-temperature redox activity of copper, and increases lattice oxygen lability [62-64]. In oxidation reactions, the formation of reactive oxygen species of the type O^- or O_2^- plays a very important role and the properties of cerium oxides including high oxygen storage capacity and formation of defects such as oxygen vacancies favors the formation of these radicals [65, 66]. Doping of Ce is reported to cause an increase in the oxygen conductivity proportional to the increase in oxygen vacancy concentration [67]. This facilitates the transfer of oxygen from the bulk to the surface [68] thus providing more surface oxygen, which results in a more effective redox process.

In the case of calcined LDHs, the interaction between Cu and Ce resulted in the stabilization of copper oxide against spinel formation [69], as seen by the reduced amount of copper aluminate in CuZnAl-Ce-CLDHs as compared with CuZnAl-CLDHs after calcination at 800 °C. Cerium addition is known to improve the dispersion and thermal stability of copper ions [70-72]. It is also known that the surface electronic state of copper plays an important role in catalytic processes such as deep and selective oxidation and dehydrogenation. The presence of cerium oxides has been reported to cause a marked change in the electronic state and coordination structure of surface

copper ions [7,73,74] and stabilizes ionic states of copper (Cu^{+} and Cu^{2+}). Moreover, the reducibility of Cu^{2+} to Cu^{+} is significantly enhanced by the presence of cerium. The Cu^{+} ion has an ionic radius of 0.115 nm, which is close to the ionic radius of the 8-coordinate Ce^{4+} ion (0.111 nm) so that the formation of a solid solution is possible. Since cerium oxides have an intrinsic mixed valence ground state, the following redox equilibrium may occur during the formation of the solid solution [59]:

$$Ce^{3+} + Cu^{2+} = Ce^{4+} + Cu^{+},$$

thus stabilizing the presence of Cu^{+} in the structure.

$[Ce(dipic)_3]^{3-}$-LDHs calcined at 500 and 700 °C were compared in the phenol oxidation, with the sample calcined at 500 °C showing a higher conversion (35.9%), consistent with the greater specific surface area of the former catalyst. A maximum in surface area was observed for the sample CuZnAl-Ce-500-6h. The influence of the specific surface area on the oxidation of aqueous phenol solution has been emphasized in other work [4, 75]. In the case of the calcined LDHs, after calcination at 700 °C the conversion was low, which could possibly be due to the crystal phase transformation coupled with the decrease in the specific surface area. Moreover, aggregation of copper clusters occurred on further heating the Cu-Ce-O solid solution, leading to crystal growth of cerium oxide, and decrease in number of active oxygen species, which can also be considered as possible reasons for the activity loss.

The conversions of phenol over $[Ce(dipic)_3]^{3-}$-LDHs calcined at 500 °C for 6 h and 3 h were also compared, with the sample calcined for 3 h showing lower conversions. For example, the conversions over CuZnAl-Ce-500-3h and CuZnAl-Ce-500-3h-1/6

were 20.7% and 17.8% respectively, but over CuZnAl-Ce-500-6h and CuZnAl-Ce-500-6h-1/6 they were 35.9% and 22.6%. Furthermore, the catalytic selectivity to the oxidation product HQ was lower in the case of samples calcined for 3h. This suggests that the short calcination process reduced the amount of Cu-Ce-O solid solution formed, which led to a decrease in the amounts of copper clusters and lattice oxygen. Hence the reduction in the synergistic effect between Cu and Ce results in the observed decrease in catalytic activities.

4.4.2.2 Catalyst stability

Table 4-10 Concentration of leaching metal ions in the supernatant liquids after phenol oxidation reaction over calcined $[Ce(dipic)_3]^{3-}$-LDHs

Sample	Concentration in filtrate (mg/L)			
	Al	Cu	Zn	Ce
CuZnAl-500-6h	0.03	0.04	6.58	-
CuZnAl-Ce-500-6h	0.39	0.73	4.56	0.91
ZnAl-Ce-500-6h	0.16	-	0.41	0
CuZnAl-500-3h	0.04	0.06	3.96	-
CuZnAl-Ce-500-3h	0.08	0.10	4.30	0.04
CuZnAl-700-6h	0.27	0.13	2.62	-
CuZnAl-Ce-700-6h	0.19	0.54	5.70	1.95

The concentrations of metal elements of CuZnAl-Ce(dipic)-CLDHs in the aqueous solution remaining after CWO were measured by ICP and the results are listed in Table 4-10. Generally, compared with that observed for a pure CuO catalyst, the leaching of metal elements from CLDH catalysts was slight [5], and the small differences between

calcined CuZnAl-LDHs containing Ce or not were within experimental error. The catalysts prepared from LDH precursors thus clearly exhibited good catalytic stabilities. The incorporation of Ce in CuZnAl-Ce(dipic)-CLDHs did not bring any advantages in preventing Cu and other metals from leaching out. This suggested that reactive leaching was the main process responsible for metal ion loss. The interactions between Cu and Ce ions results in the formation of poorly crystalline metal oxides, in which M-O bonds are easily broken following oxygen participation in the oxidation reactions, so that metal elements are readily lost. With an increase in the calcination temperature to 700 °C, the amount of leaching metal elements in Ce-containing catalysts was reduced, which can be explained by formation of more crystalline metal oxides.

4.4.3 Comparison in catalytic properties of two Ce-containing CuZnAl-CLDHs prepared by different methods

Overall, Ce-containing CuZnAl-CLDH materials prepared by co-precipitation or ion-exchange methods were both promising systems for the catalytic degradation of phenol. The main features of these systems were: 1) the possibility of varying the composition; 2) the enhanced textural and redox properties at low temperatures; 3) the efficient control over product distributions; 4) the stability under reaction conditions.

However, the catalytic abilities of two types of Ce containing CuZnAl-CLDHs in the oxidation of phenol were different. The CeX-CLDH samples prepared by the co-precipitation method exhibited similar catalytic activities to the calcined CuZnAl-CO_3-LDH, with high catalytic selectivities to deep oxidation products like light carboxylic acids, and good catalytic stabilities. However, for the CuZnAl-Ce-CLDH

catalysts prepared by the ion-exchange method, the conversions of phenol were much larger than their calcined precursor without any cerium (CuZnAl-NO_3-CLDH). In terms of the product distribution however, intermediate oxidation products like catechol and hydroquinone were predominant. The incorporation of Ce in this type of catalysts showed no inhibiting effects on the leaching of metal elements.

The difference in catalytic ability depended strongly on the method of preparation and on catalyst composition. This indicates that the various textural and structural characteristics including the specific surface area and the nature of the Cu-Ce interaction were important. In general, the preparation method can affect the activity for at least two reasons. The first is the difference in specific surface area and the other is the type and strength of M-O-M' bonds. Moreover, the catalyst composition can influence the degree of interaction and the contents of the active elements. For a series of CeX-LDH samples, CeO_2 was impregnated uniformly on the surface of very small LDH grains and the molar amount relative to Al (Ce/Al) was small, about 10%. After calcination, the specific surface areas were smaller than in Ce(dipic)-CLDH samples calcined under the same conditions, which may be caused by the liberation of volatile species from the decomposition of interlayer organic anions in the latter samples. Furthermore, the Cu-Ce interaction in mixed oxides was generated due to the high dispersion of ceria on the surface of LDH particles, but the Cu-Ce synergistic effect was not present consistent with the absence of a Cu-Ce-O solid solution. Thus the Cu-Ce interaction does not lead to enhanced catalytic abilities, but does alter the catalytic selectivities of copper ions and inhibit the leaching of metal elements. However, for the

series of Ce(dipic)-LDH samples, the Ce-complex was located in the interlayer galleries and the molar amount relative to Al was large, about 30%. After thermal treatment, the Cu-Ce interaction was stronger than in CeX-CLDHs due to the intercalation of Ce in the LDH structure, and so that Cu-Ce synergistic effect was generated with the formation of a Cu-Ce-O solid solution. The synergism of Cu-Ce leads to a significant increase in the catalytic activity and changes the product distribution. Moreover, in this type of Ce(dipic)-CLDH catalysts more Ce ions were present so that the number of copper ions per unit area was small, which may enhance the dispersion degree of Cu and increase the catalytic efficiency of active centres.

4.4.4 Mechanism of oxidation reaction of phenol

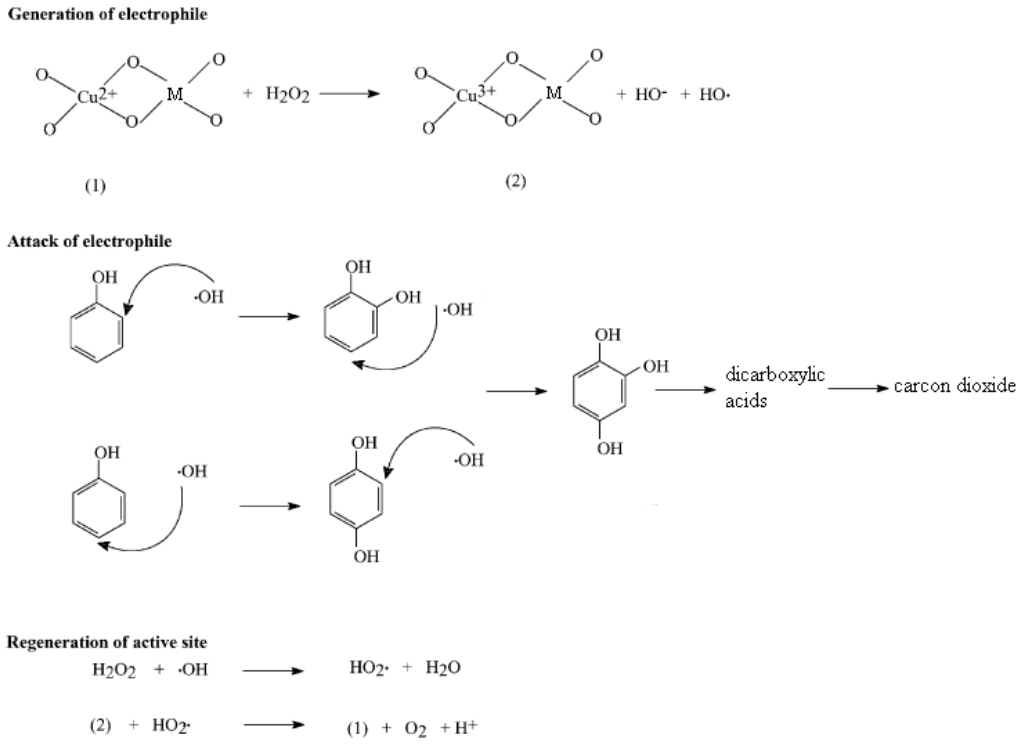

Scheme 4-1 Reaction pathway for the catalytic oxidation reaction of phenol

The phenol oxidation process is generally supposed to proceed in accordance with the parallel-consecutive mechanism [76], represented in Scheme 4-1. Some intermediate oxidation products like hydroquinone (HQ), catechol (CTC), hydroxyhydroquinone (HHQ) and light carboxylic acids are identified in the liquid phase. Phenol oxidation is initiated by the attack of hydroxyl radicals at *ortho* or *para* positions of phenol leading to HQ or CTC. The reaction continues proceeding with HHQ as a common intermediate. HHQ is then oxidized into light carboxylic acids, even carbon dioxide and water.

The main mechanism of the catalytic oxidation reaction of aqueous phenol solution over calcined CuZnAl-Ce(dipic)-LDHs is considered to be a free-radical mechanism [2,3,76] in which hydroxyl radicals ($OH^{\cdot}$) are believed to come from two sources. The major pathway involves hydroxyl radical generation through oxidation of Cu^{2+} ions by H_2O_2 as shown in Scheme 4-1. The O-O bond in an H_2O_2 molecule is broken by virtue of electron transfer from Cu^{2+} ions giving Cu^{3+}, $OH^{\cdot}$ and OH^-. Thus copper is the active center in the catalyst. The second, minor pathway, involves the formation of hydroxyl radicals through the combination between the lattice oxygen (O^-) of cerium oxide and an H atom removed from the phenolic OH group. These $OH^{\cdot}$ and other active oxygen forms participate further in the next steps of the surface oxidation so that the formation of various intermediate compounds may be explained by the presence of different types of active sites on the catalyst surface. The introduction of cerium to the copper oxide system promotes the formation of new active sites- hydroxyl radicals and lattice oxygens. Furthermore, Ce can obviously enhance the catalytic activity of Cu through the Cu-O-Ce bonds, the so-called synergistic effect in the Cu-Ce solid solution. In effect,

Ce acts as a promoter. According to the catalytic data in Table 4-9, the incorporation of Ce into Cu catalysts using the ion-exchange method significantly enhances the catalytic activities and increases the amount of HQ in oxidation products. Experimental conditions for the preparation of CLDHs should be optimized in order to give deep oxidation products (e.g. dicarboxylic acids) when the materials are used in the CWO reaction of phenol.

4.5 Conclusions

1. The incorporation of a rare earth element - Ce into CuZnAl-LDH was carried out using a co-precipitation method at pH10 in aqueous solution. The results obtained by ICP, XRD, TG/DTA, and BET demonstrated that cerium could not be inserted into the LDH layers, because of its large ionic radius and preference for large coordination numbers. The products consisted of two phases - CuZnAl-LDH and CeO_2, with CeO_2 being uniformly dispersed on the surface of the small LDH particles. Moreover, the influence of varying the experimental conditions such as Ce content and aging time was investigated and some optimized conditions were chosen.

2. Two types of CuZnAl-LDHs containing Ce elements were prepared by co-precipitation or ion-exchange methods and subsequently calcined under different conditions to yield a series of novel catalysts, which were characterized in detail by a variety of physicochemical techniques.

3. Studies with CeX-CLDH samples calcined at 500 °C for 3 h indicated that the incorporation of CeO_2 influenced the properties of CuZnAl-LDH materials. With the

incorporation of CeO_2, the thermal stability of the divalent metal oxides increased, and the specific surface area also increased. The pore size distribution analysis suggested that cerium oxide particles were highly dispersed over the bulk.

4. Studies with CuZnAl-Ce(dipic)-CLDH samples indicated that thermal treatment at 500 °C for 6 h led to the destruction of LDH network, and the formation of mixed metal oxides and a composite Cu-Ce-O solid solution. Cerium addition improved the thermal stability of copper in the catalysts.

5. The pore size analysis indicated that CuZnAl-Ce(dipic)-CLDHs were mesoporous materials, commonly observed for CLDHs. Experimental conditions such as calcination temperature, time and Ce/Al molar ratio affected the specific surface area. Increase in calcination temperature above 500 °C resulted in a decrease in surface area, attributed to the presence of a spinel phases. Prolonged calcination times up to 6 h reduced the surface area, due to the formation of a Cu-Ce-O solid solutions. A Ce/Al molar ratio equal to the stoichiometric value was found to be optimal because the decomposition of organic anions favoured a high specific surface area.

6. The presence of Ce in the mixtures of CuZnAl-LDH and CeO_2 phases prepared using the co-precipitation method allowed an interaction with active centre - Cu. After calcination, CeO_2 was effective as a promoter in phenol oxidation reaction but no Cu-Ce-O solid solution was formed. The presence of cerium oxide enhanced deep oxidation of phenol, improved catalyst selectivity, reduced leaching of metal elements and increased catalyst stability.

7. The presence of Ce in the interlayer anions in CuZnAl-Ce(dipic)-LDHs prepared

using an ion-exchange method led to a strong interaction with the active component - Cu. After calcination, the Cu-Ce synergistic effect in a Cu-Ce-O solid solution increased catalyst abilities. An increase in Ce content significantly enhanced the catalytic activity and influenced the product distribution. Catalysts with different layer cations or calcined at different temperatures and times were studied and the results indicated catalyst ability was related to two competing factors, the specific surface area and the quantity of Cu-Ce-O solid solution.

8. The catalytic abilities of two types of Ce-containing CuZnAl-CLDHs in the oxidation of phenol were different. The difference depended strongly on the preparation method and catalyst composition.

9. The phenol catalytic oxidation process is believed to proceed in accordance with the parallel-consecutive steps mechanism, and intermediate oxidation products include HQ, CTC, HHQ and light carboxylic acids. The main mechanism over CuZnAl-Ce(dipic)-CLDHs was a free-radical mechanism. Cu ions acted as main catalyst providing the majority of hydroxyl radicals. Ce ions acted as a promoter providing some hydroxyl radicals and other active oxygen forms (like O^- and O_2^-). Moreover, Ce influenced the chemical environment of Cu by formation of Cu-O-Ce bonds, which can be described as the synergistic effect of Cu and Ce.

References:

1. L. Keith, W. Telliard, EST Special Report: Priority Pollutants: I-a perspective view, *Environ. Sci. Technol.*, 1979, 13, 416-423.
2. St. G. Christoskova, M. Stoyanova, M. Georgieva, Low-temperature iron-modified

cobalt oxide system: Part 2. Catalytic oxidation of phenol in aqueous phase, *Appl. Catal. A: Gen.*, 2001, 208, 243-249.

3. K. Z. Zhu, C. B. Liu, X. K. Ye, Y. Wu, Catalysis of hydrotalcite-like compounds in liquid phase oxidation: (I) phenol hydroxylation, *Appl. Catal. A: Gen.*, 1998, 168, 365-372.
4. A. Dubey, V. Rives, S. Kannan, Catalytic hydroxylation of phenol over ternary hydrotalcites containing Cu, Ni and Al, *J. Mol. Catal. A: Chem.*, 2002, 181, 151-160.
5. F. Arena, R. Giovenco, T. Torre, A. Venuto, A. Parmaliana, Activity and resistance to leaching of Cu-based catalysts in the wet oxidation of phenol, *Appl. Catal. B: Environ.*, 2003, 45, 51-62.
6. C. Hettige, K. R. R. Mahanama, D. P. Dissanayaka, Cyclohexane oxidation and carbon deposition over metal oxide catalysts, *Chemosphere*, 2001, 43, 1079-1083.
7. P. W. Park, J. S. Ledford, The influence of surface structure on the catalytic activity of cerium promoted copper oxide catalysts on alumina: oxidation of carbon monoxide and methane, *Catal. Lett.*, 1998, 50, 41-48.
8. J. T. Kummer, Catalysts for automobile emission control, *Prog. Energy Combust. Sci.*, 1980, 6, 177-199.
9. F. Severino, J. Brito, O. Carias, J. Laine, Comparative study of alumina-supported CuO and $CuCr_2O_4$ as catalysts for CO oxidation, *J. Catal.*, 1986, 102, 172-179.
10. A. Q. M. Boon, F. van Looij, J. W. Geus, Influence of surface oxygen vacancies on the catalytic activity of copper oxide: Part 1. Oxidation of carbon monoxide, *J. Mol. Catal.*, 1992, 75, 277-291.
11. L. Agudo, J. M. Palacios, J. L. G. Fierro, J. Laine, F. Severino, Activity and structural changes of alumina-supported CuO and $CuCr_2O_4$ catalysts during carbon monoxide oxidation in the presence of water, *Appl. Catal.*, 1992, 91, 43-55.
12. Q. M. Boon, H. M. Huisman, J. W. Geus, Influence of surface oxygen vacancies on the catalytic activity of copper oxide: Part 1. Oxidation of methane, *J. Mol. Catal.*, 1992, 75, 293-303.
13. U. S. Ozkan, R. F. Kueller, E. Moctezuma, Methanol oxidation over nonprecious

transition metal oxide catalysts, *Ind. Eng. Chem. Res.*, 1990, 29, 1136-1142.

14. H. Rajesh, U. S. Ozkan, Complete oxidation of ethanol, acetaldehyde and ethanol/methanol mixtures over copper oxide and copper-chromium oxide catalysts, *Ind. Eng. Chem. Res.*, 1993, 32, 1622-1630.
15. F. Kapteijn, S. Stegenga, N. J. J. Dekker, J. W. Bijsterbosch, J. A. Moulijn, Alternatives to Noble Metal Catalysts for Automotive Exhaust Purification, *Catal. Today*, 1993, 16, 273-287.
16. T. J. Huang, T. C. Yu, Calcination conditions on copper/alumina catalysts for carbon monoxide oxidation and nitric oxide reduction, *Appl. Catal.*, 1991, 71, 275-282.
17. V. N. Goetz, A. Sood, J. R. Kittrell, Catalyst Evaluation for the simultaneous reduction of sulfur dioxide and nitric oxide by carbon monoxide, *Ind. Eng. Chem. Prod. Res. Develop.*, 1974, 13, 110-114.
18. F. Li., L. H. Zhang, D. G. Evans, X. Duan. Structure and surface chemistry of manganese-doped copper-based mixed metal oxides derived from layered double hydroxides, *Colloid Surf. A: Physicochem. Eng. Aspects*, 2004, 244, 169-177.
19. A. Pintar, J. Levec, Catalytic liquid-phase oxidation of refractory organics in waste water, *Chem. Eng. Sci.*, 1992, 47(9-11), 2395-2400.
20. J. Barrault, C. Bouchoule, K. Echachoui, N. Frini-Srasra, M. Trabelsi, F. Bergaya, Catalytic wet peroxide oxidation (CWPO) of phenol over mixed (Al-Cu) -pillared clays, *Appl. Catal. B: Environ.*, 1998, 15, 269-274.
21. S. Valange, Z. Gabelica, M. Abdellaoui, J. M. Clacens, J. Barrault, Synthesis of copper bearing MFI zeolites and their activity in wet peroxide oxidation of phenol, *Microporous Mesoporous Mater.*, 1999, 30, 177-185.
22. S. P. Newman, W. Jones, in: C. N. R. Rao, W. Jones (Eds.), Supramolecular Organization and Materials Design, Cambridge University Press, Cambridge, UK, 2001, 295.
23. S. Velu, C. S. Swamy, Alkylation of phenol with methanol over magnesium-aluminium calcined hydrotalcites, *Appl. Catal. A: Gen.*, 1994, 119, 241-252.

24. R. S. Drago, K. Jurczyk, N. Kob, Catalyzed decomposition of N_2O on metal oxide supports, *Appl. Catal. B: Environ.*, 1997, 13, 69-79.
25. H. Dandl, G. Emig, Mechanistic approach for the kinetics of the decomposition of nitrous oxide over calcined hydrotalcites, *Appl. Catal. A: Gen.*, 1998, 168, 261-268.
26. F. M. Cabello, D. Tichit, B. Coq, A. Vaccari, N. T. Dung, Hydrogenation of acetonitrile on nickel-based catalysts prepared from hydrotalcite-like precursors, *J. Catal.*, 1999, 167, 142-152.
27. S. K. Agarwal, J. J. Spivey, J. B. Butt, Deep oxidation of hydrocarbons, *Appl. Catal. A: Gen.*, 1992, 81, 239-255.
28. R. E. Bedford, W. J. La Barge, US Patent 5,063,193, 1991.
29. G. G. Jernigan, G. A. Somorjai, Carbon monoxide oxidation over three different oxidation states of copper: Metallic copper, copper(I) oxide, and copper(II) oxide - A surface science and kinetic study, *J. Catal.*, 1994, 147, 567-577.
30. W. Liu, M. Flytzani-Stephanopoulos, Total oxidation of carbon monoxide and methane over transition metal fluorite oxide composite catalysts: I Catalyst composition and activity, *J. Catal.*, 1995, 153, 304-316.
31. W. Liu, M. Flytzani-Stephanopoulos, Total oxidation of carbon monoxide and methane over transition metal fluorite oxide composite catalysts: II Catalyst characterization and reaction kinetics, *J. Catal.*, 1995, 153, 317-332.
32. G. Centi, S. Perathoner, D. Biglino, E. Giamello, Adsorption and reactivity of NO on copper-on-alumina catalysts: I. Formation of nitrate species and their influence on reactivity in NO and NH_3 conversion, *J. Catal.*, 1995, 152, 75-92.
33. J. M. Fernandez, C. Barriga, M. A. Ulibarri, F. M. Labajos, V. Rives, New hydrotalcite-like compounds containing yttrium, *Chem. Mater.*, 1997, 9, 312-318.
34. S. Miyata, Anion-exchange properties of hydrotalcite-like compounds, *Clays Clay Miner.*, 1983, 31, 305-311.
35. E. Abi-aad, R. Bechara, J. Grimblot, A. Aboukais, Preparation and characterization of CeO_2 under an oxidizing atmosphere. Thermal analysis, XPS, and EPR study, *Chem. Mater.*, 1993, 5, 793-797.
36. M. Intissar, J. C. Jumas, J. P. Besse, F. Leroux, Reinvestigation of the layered

double hydroxide containing tetravalent cations: Unambiguous response provided by XAS and Mossbauer spectroscopies, *Chem. Mater*, 2003, 15, 4625-4632.

37. F. Millange, R. I. Walton, D. O'Hare, Time-resolved in situ X-ray diffraction study of the liquid-phase reconstruction of Mg-Al-carbonate hydrotalcite-like compounds, *J. Mater. Chem.*, 2000, 10(7), 1713-1720.
38. M. C. Gastuche, G. Brown, M. M. Mortland, Mixed magnesium-aluminum hydroxides 1. Preparation and characterization of compounds formed in dialysed systems, *Clay Miner.*, 1967, 7, 177-192.
39. M. Cantu, E. Lopez-Salinas, J. S. Valente, SOx removal of calcined MgAlFe hdrotalcite-like materials: Effect of the chemical composition and the cerium incorporation method, *Environ. Sci. Technol*, 2005, 39, 9715-9720.
40. J. T. Kloprogge, R. L. Frost, Fourier transform infrared and Raman spectroscopic study of the local structure of Mg-, Ni-, and Co- hydrotalcites, *J. Solid State Chem.*, 1999, 146, 506-515.
41. T. Sato, H. Fujita, T. Endo, M. Shimada, Synthesis of hydrotalcite-like compounds and their physico-chemical properties, *React. Solids*, 1988, 5, 219-228.
42. G. W. Brindley, S. Kikkawa, Thermal behaviour of hydrotalcite and of anion-exchange forms of hydrotalcite, *Clays Clay Miner.*, 1980, 28, 87-91.
43. M. J. Hernandez, M. A. Ulibarri, J. L Rendon; C. J. Serna, Thermal stability of Ni, Al double hydroxides with various interlayer anions, *Thermochim. Acta*, 1984, 81, 311-318.
44. J. M. Fernandez, C. Barriga, M. A. Ulibarri, F. M. Labajos, V. Rives, Preparation and thermal stability of manganese-containing hydrotalcite: $[Mg_{0.75}Mn^{II}_{0.04}Mn^{III}_{0.21}(OH)_2](CO_3)_{0.11} \cdot nH_2O$, *J. Mater. Chem.*, 1994, 4, 1117-1121.
45. S. K. Yun, T. J. Pinnavaia, Water content and particle texture of synthetic hydrotalcite-like layered double hydroxides, *Chem. Mater.*, 1995, 7, 348-354.
46. S. Miyata, Physico-chemical properties of synthetic hydrotalcites in relation to composition, *Clays Clay Miner.*, 1980, 28(1), 50-56.
47. J. Valente, F. Figueras, M. Gravelle, P. Khumbar, J. Lopez, J. P. Besse, Basic

properties of the mixed oxides obtained by thermal decomposition of hydrotalcites containing different metallic compositions, *J. Catal.*, 2000, 189, 370-381.

48. S. Velu, K. Suzuki, Selective production of hydrogen for fuel cells via oxidative steam reforming of methanol over CuZnAl oxide catalysts: effect of substitution of zirconium and cerium on the catalytic performance, *Topic Catal.*, 2003, 22(3-4), 235-244.
49. Y. Takita, J. Lunsford, Surface reactions of oxygen ions. 3. Oxidation of alkanes by ozonide (1-) ion on magnesium oxide, *J. Phys. Chem.*, 1979, 83, 683-688.
50. M. Kruk, M. Jaroniec, Gas adsorption characterization of ordered organic-inorganic nanocomposite materials, *Chem. Mater.*, 2001, 13, 3169-3183.
51. J. He, B. Li, D. G. Evans, X. Duan, Synthesis of layered double hydroxides in an emulsion solution, *Colloids Surf. A: Physicochem. Eng. Aspects*, 2004, 251, 191-196.
52. V. Rives, Characterization of layered double hydroxides and their decomposition products, *Mater. Chem. Phys.*, 2002, 75, 19-25.
53. L. H. Zhang, F. Li., D. G. Evans, X. Duan, Structure and surface characteristics of Cu-based composite metal oxides derived from layered double hydroxides, *Mater. Chem. Phys.*, 2004, 87, 402-410.
54. M. D. Arco, E. Cebadera, S. Gutiérrez, C. Martín, M. J. Montero, V. Rives, J. Rocha, M. A. Sevilla, Mg, Al layered double hydroxides with intercalated indomethacin: Synthesis, characterization, and pharmacological study, *J. Pharm. Sci.*, 2004, 93, 1649-1658.
55. J. H. Meng, Studies of assembly, supramolecular structure and properties of sorbic acid, lactic acid and glyphosate intercalated layered double hydroxides, PhD Thesis, Beijing University of Chemical Technology, 2005.
56. A. Aboukais, A. Galtayries, E. Abi-Aad, D. Courcot, J. Grimblot, Spectroscopic and surface potential variations study of a CuCe oxide catalyst using H_2S as a probe molecule, *Colloids Surf. A: Physicochem. Eng. Aspects*, 1999, 154, 335-342.
57. M. Fernandez-Garcia, E. Gomez Rebollo, A. Guerrero Ruiz, J. C. Conesa, J. Soria, Influence of ceria on the dispersion and reduction/oxidation behaviour of

alumina-supported copper catalysts, *J. Catal.*, 1997, 172**,** 146-159.

58. F. Larachi, J. Pierre, A. Adnot, A. Bernis, Ce 3d XPS study of composite $CexMn_{1-x}O_{2-y}$ wet oxidation catalysts, *Appl. Surf. Sci.*, 2002, 195, 236-250.
59. H. Stanko, B. Jurka, L. Janez, Wet oxidation of phenol on $Ce_{1-x}Cu_xO_{2-y}$ catalyst, *J. Catal.*, 1999, 184, 39-48.
60. L. H. Zhang, J. Zhu, X. R. Jiang, D. G. Evans, F. Li, Influence of nature of precursors on the formation and structure of Cu-Ni-Cr mixed oxides from layered double hydroxides, *J. Phys. Chem. Solids*, 2006, (in press).
61. S. Velu, K. Suzuki, T. Osaki, Selective production of hydrogen by partial oxidation of methanol over catalysts derived from CuZnAl layered double hydroxides, *Catal. Lett.*, 1999, 62(2-4), 159-167.
62. W. Liu, M. Flytzani-Stephanopoulos, Transition metal-promoted oxidation catalysis by fluorite oxides: A study of CO oxidation over Cu-CeO_2, *Chem. Eng. J.*, 1996, 64, 283-294.
63. C. E. Hori, H. Permana, K. Y. S. Ng, A. Brenner, K. More, K. M. Rahmoeller, D. Belton, Thermal stability of oxygen storage properties in a mixed CeO_2-ZrO_2 system, *Appl. Catal. B: Environ.*, 1998, 16, 105-117.
64. I. S. Metcalfe, S. Sundaresan, Oxygen storage in automobile exhaust catalyst, *Chem. Eng. Sci.*, 1986, 41, 1109-1112.
65. A. Trovarelli, C. de Leitenburg, M. Boaro, G. Dolcetti, The utilization of ceria in industrial catalysis, *Catal. Today*, 1999, 50, 353-367.
66. B. Li, K. Domen, K. Maruya, T. Onishi, Dioxygen adsorption on well-outgassed and partially reduced cerium oxide studied by FT-IR, *J. Am. Chem. Soc.*, 1989, 111, 7683-7687.
67. P. J. Gellings, H. J. M. Bouwmeester, Solid state aspects of oxidation catalysis, *Catal. Today*, 2000, 58, 1-53.
68. T. Bunluesin, E. S. Putna, R. J. Gorte, A comparison of CO oxidation on ceria-supported Pt, Pd, and Rh, *Catal. Lett.*, 1996, 41, 1-5.
69. M. Ferrandon, B. Ferrand, E. Bjornbom, F. Klingstedt, A. Kalantar Neyestanaki, H. Karhu, I. J. V Ayrynen, Copper oxide–platinum/alumina catalysts for volatile

organic compound and carbon monoxide oxidation: Synergetic effect of cerium and lanthanum, *J. Catal.*, 2001, 202**,** 354-366.

70. Y.-F. Yu-Yao, J. T. Kummer, Low-concentration supported precious metal catalysts prepared by thermal transport, *J. Catal.*, 1987, 106, 307-312.
71. R. Dictor, S. Roberts, Influence of ceria on alumina-supported rhodium: observation of rhodium morphology made using FTIR spectroscopy, *J. Phys. Chem.*, 1989, 93, 5846-5850.
72. F. Le Normand, L. Hilaire, K. Kili, G. Krill, G. Maire, Oxidation state of cerium in cerium-based catalysts investigated by spectroscopic probes, *J. Phys. Chem.*, 1988, 92, 2561-2568.
73. B. Wen, M. Y. He, E. Schrum, C. Li, NO reduction and CO oxidation over Cu/Ce/Mg/Al mixed oxide catalyst in FCC operation, *J. Mol. Catal. A: Chem.*, 2002, 180, 187-192.
74. A. N. Pestryakov, A. A. Davydov, The influence of modifying additions of La and Ce oxides on electronic state of surface atoms and ions of supported copper, *Appl. Surf. Sci.*, 1996, 103, 479-483.
75. A. Alejandre, F. Medina, P. Salagre, A. Fabregat, J. E. Sueiras, Characterization and activity of copper and nickel catalysts for the oxidation of phenol aqueous solutions, *Appl. Catal. B Environ.*, 1998, 18, 307-315.
76. D. Duprez, F. Delanoe, J. Barbier Jr, P. Isnard, G. Blanchard, Catalytic oxidation of organic compounds in aqueous media, *Catal. Today*, 1996, 29, 317-322.
77. G. Y. Fu, Y. M. Bao, C. Li, Synthesis and Characterization of Hydrotalcite Like - Containing Rare Earth Europium, J. Inner Mongolias Teacher’s College Nationalities, 1999, 14(2), 148-150.
78. Y. M. Bao, L. S. Li, S. J. Ma, D. C. Xiong, G. Y. Fu, S. H. Feng, R. R. Xu, Synthesis and Characterization of Hydrotalcite - Like $[Cd_xMg_{6-x}Al_2(OH)_{16}]^{2+}[S.2H_2O]^{2-}$, Chem. J. Chin. Univ., 1996, 17(3), 355-358.

Chapter 5

Conclusions

1. Nanometer-size LDHs materials with narrow size distributions and uniform platelet configurations can be readily synthesized using a continuous co-precipitation technique under steady-state conditions. The steady-state technique was found to offer two main advantages over the standard routes. One is that it shortens the preparation time by working without an aging step, whilst allowing control over the characteristics of the LDHs. The other is that it has the potential to be easily used in large-scale production in the future.

2. The effects of varying the operating conditions on the structural and textural properties of the resulting LDHs were studied, including total cation concentration, solvent, residence time, pH and intercalation anion. The LDHs products were found to exhibit poor crystallinity and small crystallite sizes. The total cation concentration and use of mixed water-organic solvents were found to be the most significant factors and their effects were explained primarily through the changes in supersaturation, but the role of viscosity of the preparation medium was also highlighted. The optimal operating conditions were found to be: a total cation concentration of 3.0×10^{-2} mol/l, a mixed solvent of EG/H_2O or PEG/H_2O (80/20), and a residence time of 15 min at pH 9.

3. Ce-containing LDHs with $[Ce(dipic)_3]^{3-}$ complex anions in the interlayer galleries were prepared by an ion-exchange method but were found to be always mixed with carbonate - containing LDHs. Intercalation of $[Ce(dipic)_3]^{3-}$ anions in the host layer structure was demonstrated by an increase in interlayer spacing. For some host matrixes, the $[Ce(dipic)_3]^{3-}$ complex underwent partial decomposition into $dipic^{2-}$ during the intercalation process, resulting in formation of $dipic^{2-}$-intercalated LDHs as co-product.

4. The ion-exchange process was investigated using a series of adsorption experiments and optimized through varying the experimental conditions. The adsorption of $[Ce(dipic)_3]^{3-}$ complexes on LDHs was found to proceed in two steps: saturation of the external sites followed by an interlayer exchange process occurring at high equilibrium concentrations. After studying the influence of varying some preparation parameters, the best results were obtained with a layer cation ratio $M^{2+}/M^{3+} = 2$, a $[Ce(dipic)_3]^{3-}$ concentration around 5 mmol/l and an exchange period around 10 h at room temperature.

5. Another Ce-containing LDHs was synthesized by an ion-exchange process involving $[Ce(DTPA)]^{2-}$ complexes with LDHs precursor. This $[Ce(DTPA)]^{2-}$-intercalated material showed characteristics of well-crystallized LDHs with an interlayer spacing of 1.46 nm, suggesting a vertical orientation of the complex in the interlayer galleries.

6. Eu-containing LDHs were prepared by an anion-exchange process with $[Eu(dipic)_3]^{3-}$

anions and their luminescence properties were investigated. The $[Eu(dipic)_3]^{3-}$-intercalated LDHs showed similar structural characteristics to $[Ce(dipic)_3]^{3-}$-LDHs. Immobilization led to enhanced thermal stability and luminescence properties of the $[Eu(dipic)_3]^{3-}$ complex. It was shown that Eu^{3+} can be used as a structural probe to study the interaction between the complex and the layered host on the basis of the changes in its luminescence properties.

7. Thermal behavior of the above materials was analyzed in terms of dehydration and dehydroxylation of the layers at low temperatures followed by decomposition of the intercalated species at higher temperatures. The decomposition temperature and process were found to be dependent on the nature of layer cations and interlayer anions. The presence of cerium was found to exert a significant influence on the thermal behavior of the materials. The presence of a uniform distribution of cerium oxides in the calcined products resulted in an increase in the temperature at which spinel phases were formed. The enhanced thermal stability of divalent metal oxides, especially CuO, should be important in terms of catalysis.

8. Ce-containing LDHs were calcined under different conditions to yield novel mesoporous CLDHs materials. The effects of varying the experimental conditions such as layer metal composition, calcination temperature, time and Ce/Al molar ratio on specific surface area were investigated. Studies with CuZnAl-Ce(dipic)-CLDHs indicated that thermal treatment at 500 °C for 6 h resulted in the complete destruction of

the LDHs network, and the formation of mixed metal oxides and a composite Cu-Ce-O solid solution.

9. The incorporation of cerium into CuZnAl-LDHs was also attempted using a co-precipitation method at pH 10. It was demonstrated that cerium is not inserted into the LDHs layers under these conditions, and the products consist of two phases - CuZnAl-LDHs and CeO_2, with CeO_2 being uniformly dispersed on the surface of the small LDHs particles. Incorporation of CeO_2 leads to an increase in the specific surface area and thermal stability of the metal oxides.

10. The two types of Ce-containing CuZnAl-LDHs synthesised by co-precipitation and ion-exchange methods were calcined to prepare catalysts for wet oxidation of organic compounds. Their catalytic performance was studied using phenol oxidation as a probe reaction. The presence of cerium in the mixture of CuZnAl-LDHs and CeO_2 prepared using the co-precipitation technique led to enhanced deep oxidation of phenol, improved catalyst selectivity, and reduced extent of leaching of metal elements, with a consequent increase catalyst stability. It was proposed that after calcination, cerium is involved in a weak interaction with the active centre (Cu) due to its high dispersion over the bulk, so that CeO_2 is effective as a catalyst promoter even though no Cu-Ce-O solid solution is formed.

11. The presence of cerium in the interlayer anions of CuZnAl-Ce(dipic)-LDHs

prepared using an ion-exchange technique results in an increase in the catalytic activity of the calcined material and influences the product distribution in phenol oxidation. It was proposed that after calcination, Ce is involved in a strong interaction with Cu due to the formation of a Cu-Ce-O solid solution, and the resulting Cu-Ce synergistic effect results in a significant enhancement in catalyst ability. Catalysts with different layer cations or calcined under different conditions were studied, and the results indicated that the catalytic ability is determined by two competing factors, the specific surface area and the quantity of Cu-Ce-O solid solution.

12. It was shown that the significant differences between the two types of Ce-containing CuZnAl-CLDHs materials could be rationalized in terms of the textural and structural characteristics of the materials, principally specific surface area and Cu-Ce interaction.

Acknowledgments

At Université Blaise Pascal, first and foremost I would like to thank my French supervisors Prof. Claude Forano and Prof. Marie de Roy for giving me the opportunity to do this research and for providing me with a positive and fruitful academic environment. Their guidance, encouragement, support, time, suggestions and comments during my studies are all greatly appreciated.

Thanks to Drs. Vanessa Prévot, Christine Taviot-Guého, Fabrice Leroux, Andre de Roy, Philippe Boutinaud, Christophe Vial, Rachide Segni, Stéphanie Vial, Erwan Gerand and the members of the Laboratoire des Matériaux Inorganiques for their knowledge, assistance and inspiration during my work and their friendship and kindness during my time in France. They made my stay in France extremely interesting and rewarding.

At Beijing University of Chemical Technology, first and foremost I would like to thank my Chinese supervisor Prof. Xue Duan for allowing me to work under his supervision to accomplish my thesis. I appreciate the enthusiasm, breadth of knowledge and conscientiousness in science he has shown to me.

I would like to express my sincere thanks to Prof. David G. Evans for his requirement of a serious and rigorous research manner, his priceless advice in many aspects and especially for his patient reading of my numerous revisions of the thesis.

I also would like to thank Prof. Feng Li for helping me a great deal. His continuous

support, encouragement, critical suggestions and comments in numerous discussions have been very valued.

Thanks also to my teachers in China: Drs. Hui Zhang, Jing He, Dianqing Li, Wensheng Yang, Lan Yang, Renjie Li, Fazhi Zhang, Min Wei, Qinghong Xu, Lianying Wang, and Xu Xiang for their help and discussions throughout my studies.

A very, very special thanks goes to my husband Yapeng Jin for all the support, time and patience he has given me whilst working on my thesis. I am not sure I would have attained my goal without his help. I feel so lucky to have met him in my life.

And last, but certainly not least, a big heart-felt thank you to all of my family and friends: Grandpa, Mom, Dad, Yongjun Feng, Liyi Zhang, Yan Zhou, Ye Tian, Xian Zhang and everyone else - I really appreciate your love and unending support.

This thesis had been made possible due to financial support from a France Government Scholarship.

Zheng CHANG

July, 2006

Publications

1. Z. Chang, D. G. Evans, X. Duan, C. Vial, J. Ghanbaja, V. Prevot, M de Roy, C. Forano, Synthesis of [Zn-Al-CO_3] layered double hydroxides by a coprecipitation method under steady-state conditions, *Journal of Solid State Chemistry*, 2005, 178, 2766-2777.

2. Z. Chang, D. G. Evans, X. Duan, P. Boutinaud, M de Roy, C. Forano, Preparations and Characterizations of Rare Earth-containing Layered Doubled Hydroxides, *Journal of Physics and Chemistry of solids*, 2006, 67, 1054-1057.

3. Chang Z., Li F., Evans D. G., Forano C., De Roy M., Duan X., The effects of rare earth element - Ce on structure and catalytic ability of Cu-based layered doubled hydroxides, *Industrial Catalysis*, 2005, 13, 472-476.